AFRL-AFOSR-VA-TR-2021-0014

Anisotropic and Active Metasurfaces

Sievenpiper, Daniel
UNIVERSITY OF CALIFORNIA, SAN DIEGO
230 W 41ST STREET FL 7
NEW YORK, NY, 92093-0621
US

02/11/2021
Final Technical Report

Air Force Research Laboratory
Air Force Office of Scientific Research
Arlington, Virginia 22203
Air Force Materiel Command

REPORT DOCUMENTATION PAGE

Form Approved
OMB No. 0704-0188

1. REPORT DATE *(DD-MM-YYYY)*	**2. REPORT TYPE**	**3. DATES COVERED** *(From - To)*
11-02-2021	Final	15 Dec 2015 - 14 Sep 2020

4. TITLE AND SUBTITLE
Anisotropic and Active Metasurfaces

5a. CONTRACT NUMBER

5b. GRANT NUMBER
FA9550-16-1-0093

5c. PROGRAM ELEMENT NUMBER

6. AUTHOR(S)
Daniel Sievenpiper

5d. PROJECT NUMBER

5e. TASK NUMBER

5f. WORK UNIT NUMBER

7. PERFORMING ORGANIZATION NAME(S) AND ADDRESS(ES)
UNIVERSITY OF CALIFORNIA, SAN DIEGO
230 W 41ST STREET FL 7
NEW YORK, NY 92093-0621
US

8. PERFORMING ORGANIZATION REPORT NUMBER

9. SPONSORING/MONITORING AGENCY NAME(S) AND ADDRESS(ES)
AF Office of Scientific Research
875 N. Randolph St. Room 3112
Arlington, VA 22203

10. SPONSOR/MONITOR'S ACRONYM(S)
AFRL/AFOSR RTB1

11. SPONSOR/MONITOR'S REPORT NUMBER(S)
AFRL-AFOSR-VA-TR-2021-0014

12. DISTRIBUTION/AVAILABILITY STATEMENT
A Distribution Unlimited: PB Public Release

13. SUPPLEMENTARY NOTES

14. ABSTRACT
During this program we have had several major accomplishments. We completed our work on arbitrary patterning techniques for anisotropic impedance surfaces which we began under a prior program. In this effort, we developed ways to generate impedance surface is that are anisotropic, and in which the direction of anisotropy and the magnitude of the various tensor components can be varied arbitrarily across the surface. This has proven to be useful for certain kinds of scattering problems, such as avoiding holes. In the course of this work, we also discovered a new kind of interface wave that appears at the boundary between two different impedance surfaces that have complementary impedance values. For example, joining an inductive surface with a capacitive surface can produce such a mode. We have named these interface waves "line waves" because they occur along a one-dimensional line, Analogous to surface waves, but reduced by one dimension. These modes were found to have unusual properties including polarization that is locked to the direction of propagation, providing some immunity to backscattering. This introduced us to the emerging field of photonic topological insulators, which are closely related to line waves. We have put significant effort into developing an understanding these structures, and their relationship with other kinds of metasurfaces. We have simulated an fabricated several examples of both spin and valley type structures. We have also studied the effects of disorder and have developed new structures that demonstrate spin momentum locking without requiring a nontrivial interface.

15. SUBJECT TERMS

16. SECURITY CLASSIFICATION OF:			**17. LIMITATION OF ABSTRACT**	**18. NUMBER OF PAGES**	**19a. NAME OF RESPONSIBLE PERSON**
a. REPORT	**b. ABSTRACT**	**c. THIS PAGE**			ARJE NACHMAN
U	U	U	UU	31	**19b. TELEPHONE NUMBER** *(Include area code)* 426-8427

Anisotropic and Active Metasurfaces

Daniel Sievenpiper, University of California, San Diego

AFOSR Final Performance Report FA9550-16-1-0093

Abstract

During this program we have had several major accomplishments. We completed our work on arbitrary patterning techniques for anisotropic impedance surfaces which we began under a prior program. In this effort, we developed ways to generate impedance surface is that are anisotropic, and in which the direction of anisotropy and the magnitude of the various tensor components can be varied arbitrarily across the surface. This has proven to be useful for certain kinds of scattering problems, such as avoiding holes. In the course of this work, we also discovered a new kind of interface wave that appears at the boundary between two different impedance surfaces they have complementary impedance values. For example, joining an inductive surface with a capacitive surface can produce such a mode. We have named these interface waves “line waves” because they occur along a one-dimensional line, Analogous to surface waves, but reduced by one dimension. These modes were found to have unusual properties including polarization that is locked to the direction of propagation, providing some immunity to backscattering. This introduced us to the emerging field of photonic topological insulators, which are closely related to line waves. We have put significant effort into developing an understanding these structures, and their relationship with other kinds of metasurfaces. We have simulated an fabricated several examples of both spin and valley type structures. We have also studied the effects of disorder and have developed new structures that demonstrate spin momentum locking without requiring a nontrivial interface. This reinforces the idea that non scattering modes in photonic topological insulators are actually a kind of chiral waveguide. Thus, we have also begun studying chiral metasurfaces, and have found that they can support self-collimated waves which appear to have some resistance to scattering from discontinuities such as bends.

Anisotropic Surfaces

During the initial stages of this program, we focused on concluding our efforts on arbitrary impedance surface pattern generation, as shown in figure 1. Beginning with a desired impedance function, we would define a set of unit cells using a pattern of dots which represent the center of each cell. We then move each dot according to the local gradient of the desired impedance function. This pushes some of the dots closer together, representing smaller cells, and pulls other dots farther apart, representing larger cells. If the spacing varies with direction, the result is an anisotropic surface. We also developed a technique for verifying the surface impedance that is represented by one of these arbitrary patterns. By extracting an equivalent rectangle for each cell using mathematics that is similar to the mechanical moment of inertia, we can generate an impedance curve from which we can extract the impedance tensor for each cell. We have verified that the cell generation technique can accurately reproduce the desired impedance function.

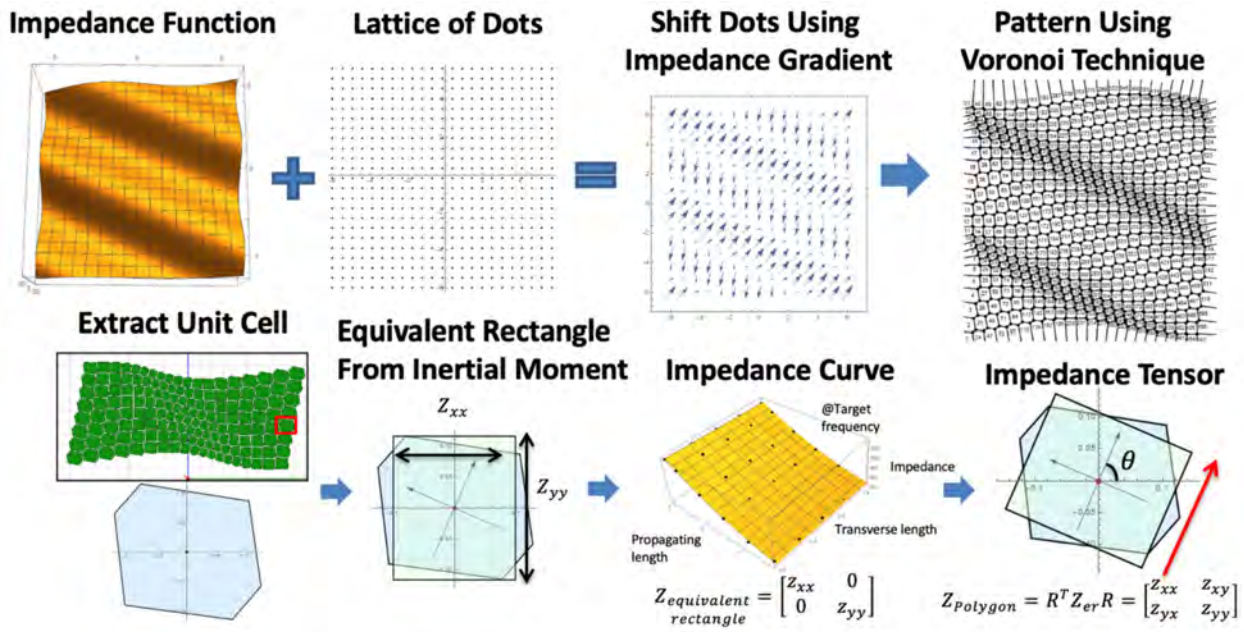

Figure 1. An example of our technique for generating arbitrary anisotropic impedance surfaces. beginning with an impedance function, we adjust the locations of a lattice of dots according to the local gradient of the desired function, resulting in a new set of dots with variable spacing , representing a set of unit cells. The cells are generated from the dots using the Voronoi function. We have also verified that the patterns generated using this technique accurately reproduced the desired surface impedance tensor.

We have used our pattern generation technique to create a number of functional surfaces, as shown in figure 2. For example, we can cause a surface wave to smoothly move around a 90-degree curve by bending the low impedance direction along that shape. A wave excited by a small sectoral horn or surface wave launching structure can be seen to clearly follow the curved path. We can also cause a wave to shift laterally, relative to its direction of propagation, by simply stretching the unit cells along the desired direction.

This technique can also be used to produce a variety of other useful patterns. For example, a radially symmetric structure with higher impedance in the center can be used as a planar lens. Such a structure can focus an incoming surface wave to a point on the lens or can be used to collimate radiation from a small source. In addition, we can also build a structure that behaves as an “anti-lens”, thus causing waves to avoid a region. This can be used, for example, to cause surface waves to bend around a particular region, such as where a scattering center may exist such as a hole in the ground plane. In figure 3, we demonstrate this method, plotting the fields in the vertical plane near a hole in an ordinary ground plane, compared to the patterned ground plane. On the ordinary ground plan, when the surface waves encountered the hole, they are highly scattered, both into the surrounding space and also through the hole. However, when the region around the hole is patterned using this technique, the waves are bent around the hole and are not scattered by it.

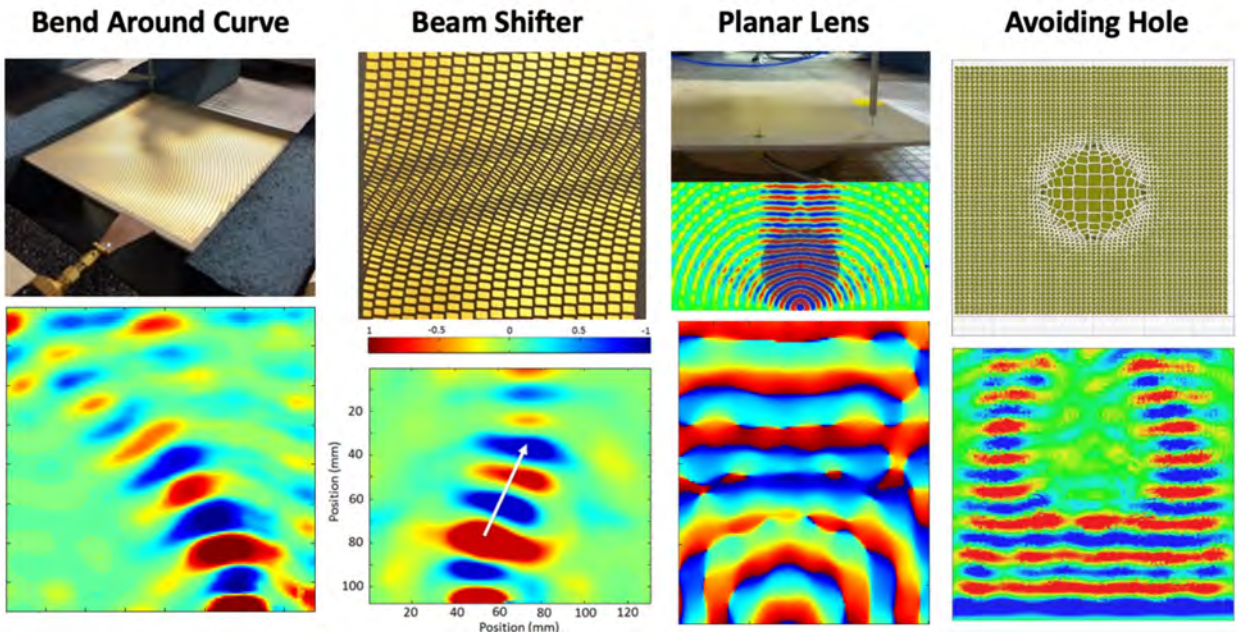

Figure 2. Examples of some of these structures that we can build using our patterning technique include surface is that can cause waves to bend or shift in desired directions, as well as planar lens structures, or "anti-lens" patterns which can cause waves to avoid a particular region, such as a hole. The data shown here include a combination of simulated and measured results. We are able to measure the fields of propagating surface waves on these patterned impedance surfaces using a planer nearfield scanner, in which a small probe is scanned over the surface to detect the magnitude and phase of the propagating wave.

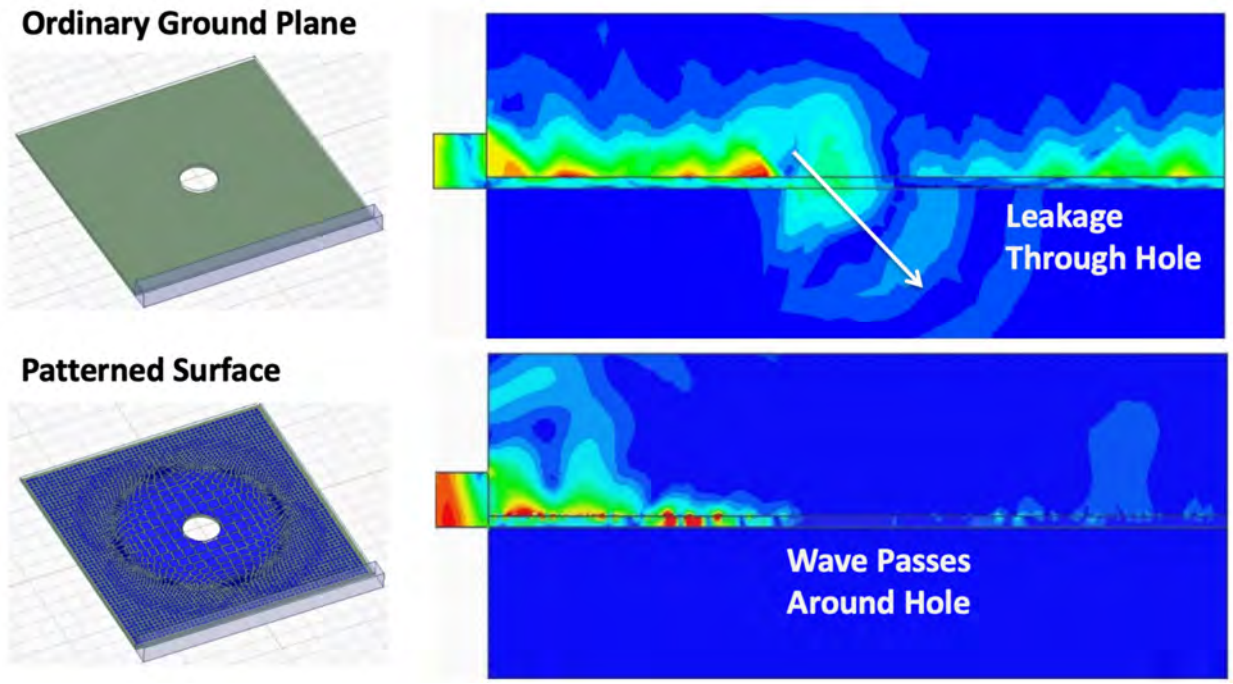

Figure 3. An example of an application for our patterning technique, in which a wave is made to avoid a hole, to reduce scattering by that hole. on the ordinary ground plane, a surface wave is highly scattered when it encounters a hole, and this results in leakage into the hole, to the other side of the ground plane. When the region around the hole is patterned with an "anti-lens" pattern, the wave is guided around the hole and does not encounter it, thereby reducing scattering.

Line Waves

One of our more interesting developments in this program is the discovery of line waves. We had hypothesized that there could be waves that exist at the interface between two surfaces, just like surface waves exist at the boundary between two volumes. We had previously searched for such waves but had been unable to find them. After looking again, we found that we had been simply looking in the wrong place, and that with the correct relationship between the impedance values on each side of the interface, these waves could be found. They only occur when the impedances on the two sides of the interface have complementary values, such as capacitive on one side and inductive on the other side. An example of these waves is shown in figure 4. They have several interesting properties. First, the fields have a singularity at the center. Numerically, the fields actually diverge to infinity. In the simplest form, when we assume a magnetic conductor on one side and an electric conductor on the other side, the field profile is a modified Bessel K function. For other impedance values a solution can also be found, but it is more complicated.

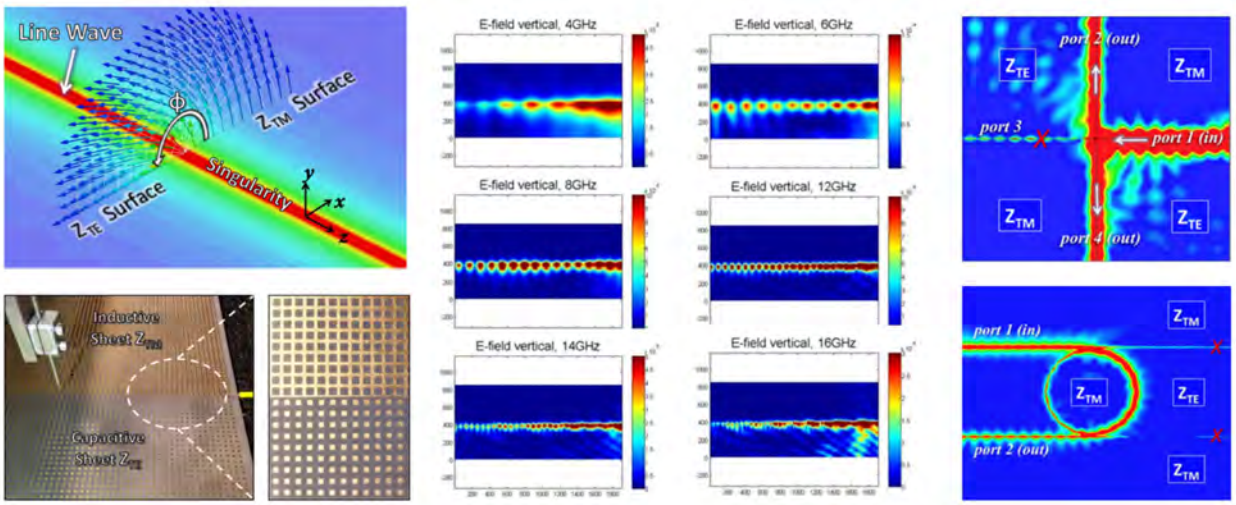

Figure 4. A depiction of the inline waves which were discovered under this program, and one possible implementation using an interface between an inductive grid and a capacitive complementary grid. It turns out that any two complementary metallic patterns can also support similar waves. These modes exist over a broad bandwidth, at least several octaves, and can be used to build a variety of structures that are analogous to common microwave or optical devices, such as a magic T interface or a ring resonator with coupling transmission lines.

Line waves are closely related to photonic topological insulators, in that both structures provide for unidirectional propagation and are resistant to backscattering. Photonic topological insulators are based on bandgap structures, and therefore have limited bandwidth. However, line waves do not require a bandgap and thus can cover several octaves of bandwidth in a single structure. They can also be used to build a variety of devices that are similar to conventional microwave or optical components such as a magic T interface or a ring resonator. Examples are shown in Figure 4. One fortunate outcome of us investigating this area is that it has led us into the field of photonic topological insulators as well, in which we have made significant progress, including implementing several of these as metasurfaces, as well as using other techniques to build planar dielectric structures.

Photonic Topological Insulators

Closely related to line waves, photonic topological insulators typically involve joining two structures to create an interface. The structure is typically must have one of several important differences on either side of the interface in order to create a bound mode which spans the bandgap and is topologically protected. This generally provides the interface mode with protection from backscattering due to what is often called spin orbit coupling. This essentially means that the polarization of the mode is linked to the direction of propagation, so scattering that does not involve polarization conversion will generally also not cause back reflection. Common ways to achieve these modes include reversing the symmetry on either side of the interface in some way or flipping the relative ordering of modes such as dipole and quadrupole modes on either side of the bandgap. Two of the common types shown in figure 5 are the spin type and the valley type. In the case of the spin type PTI, we use a combination of inductive and capacitive sheets, similar to how we create line waves. In this case, a pair of complementary sheets that are closely spaced will result in a bandgap. If the arrangement of the sheets is reversed across a boundary, so that the inductive side is lined up with the capacitive side, and vice versa, this results in a pair of unidirectional modes that do not couple to each other. This can be used to guide waves around sharp corners and achieve other interesting devices. The valley type structure is perhaps more surprising because the unit cells are identical on the two sides of the interface, but merely flipped in plane.

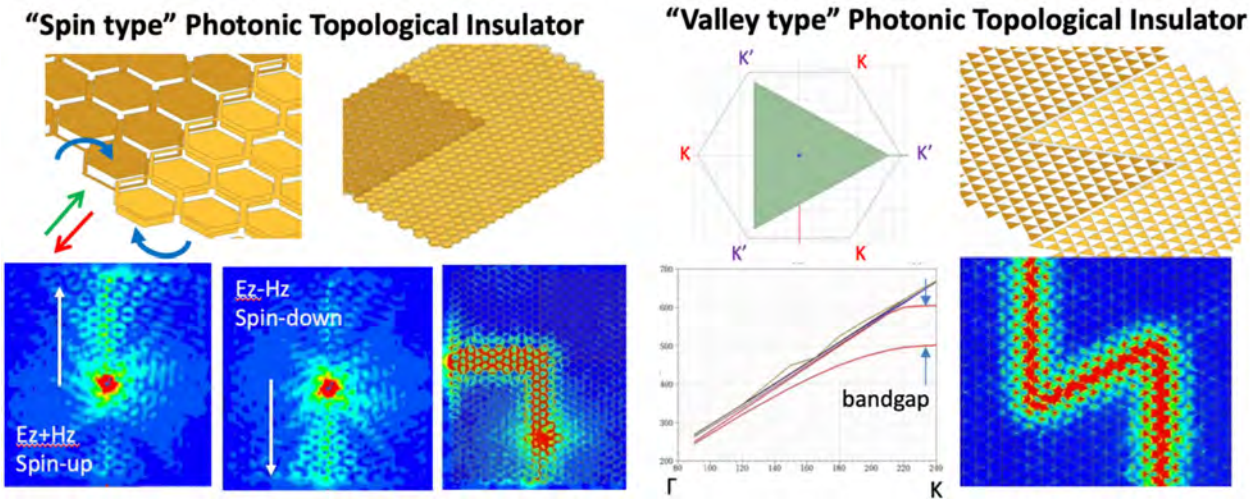

Figure 5. Two examples of photonic topological insulators realized using metallic metasurfaces. For the spin type structure, we use a combination of inductive and capacitive grids they are closely spaced. On opposite sides of the interface, the position of the two grids are swapped. This forms a spin momentum locked mode that is largely immune to backscattering. The valley type structure uses a single metallics sheet patterned with triangles That are pointing in opposite directions on opposite sides of the interface.

One important development for bringing photonic topological insulators into practical applications is a transition between conventional waveguides and topological waveguides. Figure 6 shows an example of an optimized transition structure between the spin type photonic topological insulator and antipodal waveguide which can be transitioned to various conventional waveguides including microstrip. through optimization of the transition region we have achieved less than one dB loss per transition.

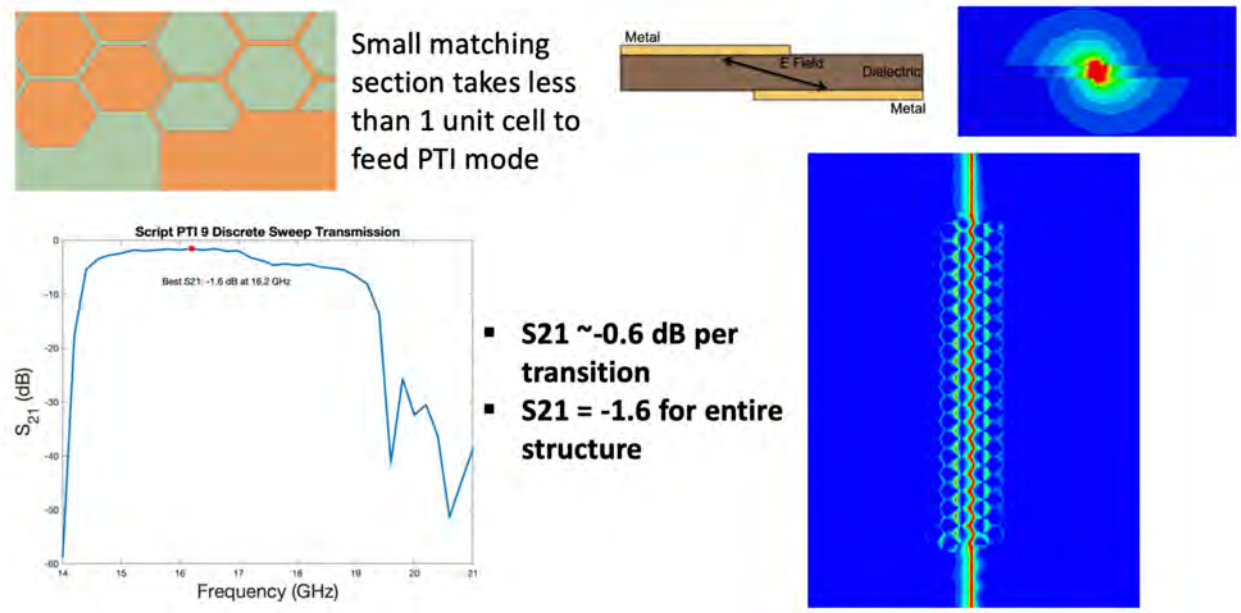

Figure 6. A transition between a conventional waveguide and a topological waveguide. By optimizing the metal geometry at the junction, we can match the mode profile in the two waveguides and optimize transmission to less than one dB per transition.

One of the intriguing ideas that we explored was the concept of an endpoint for a topological waveguide. All of the designs in the literature always involve two regions of different materials that are joined together, such that there are always two ends. since these waveguides resist reflections, it occurred to us that it would be interesting to study what would happen if we could create a single ended waveguide that stops at some point. Figure 7 shows one of the conventional photonic topological insulators built using two different sizes of dielectric rods. The two rods can be labeled A and B. On one side of the interface, the A rods are larger, and the B rods are smaller. The geometry is reversed on the other side of the interface. To create the endpoint, we gradually change the diameter of the two rods around a central point. In the direction opposite the waveguide the two rods are the same diameter. We were surprised to find that energy was not reflected back at this endpoint, but rather propagates through the structure, from right to left as shown in figure 7. Furthermore, the wave spreads out, but the entire wavefront is phase locked such that it forms a flat phase front.

This can be understood through the band diagram shown in Figure 8. At the K points in the Brillouin zone, two bands come together and form singular points known as Dirac points. at these points the wave is propagating forward in the K direction (in terms of phase velocity, which is responsible for the observed phase locking) but it is also traveling outward in all directions from the Dirac point (in terms of group velocity which determines the spread of energy). This behavior is known as diffusive transport. It can be used to create broad area radiators in which the phase profile is locked by the internal periodicity of the structure rather than the overall shape of the waveguide or feed geometry.

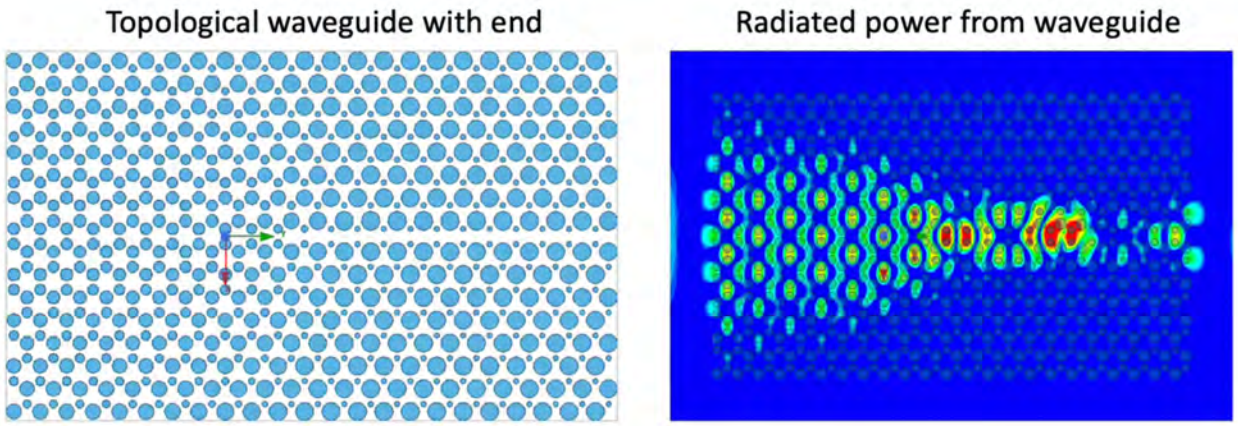

Figure 7. The concept of an end point for a topological waveguide. The guide is formed by switching the sizes of two alternating dielectric pillars that form the lattice on opposite sides of an interface. The two diameters are smoothly varied around a central point such that the diameters are equal in the direction opposite the waveguide. When excited by a source inside the guide, energy is not reflected back at the end point, but instead travels forward as a phase locked wavefront.

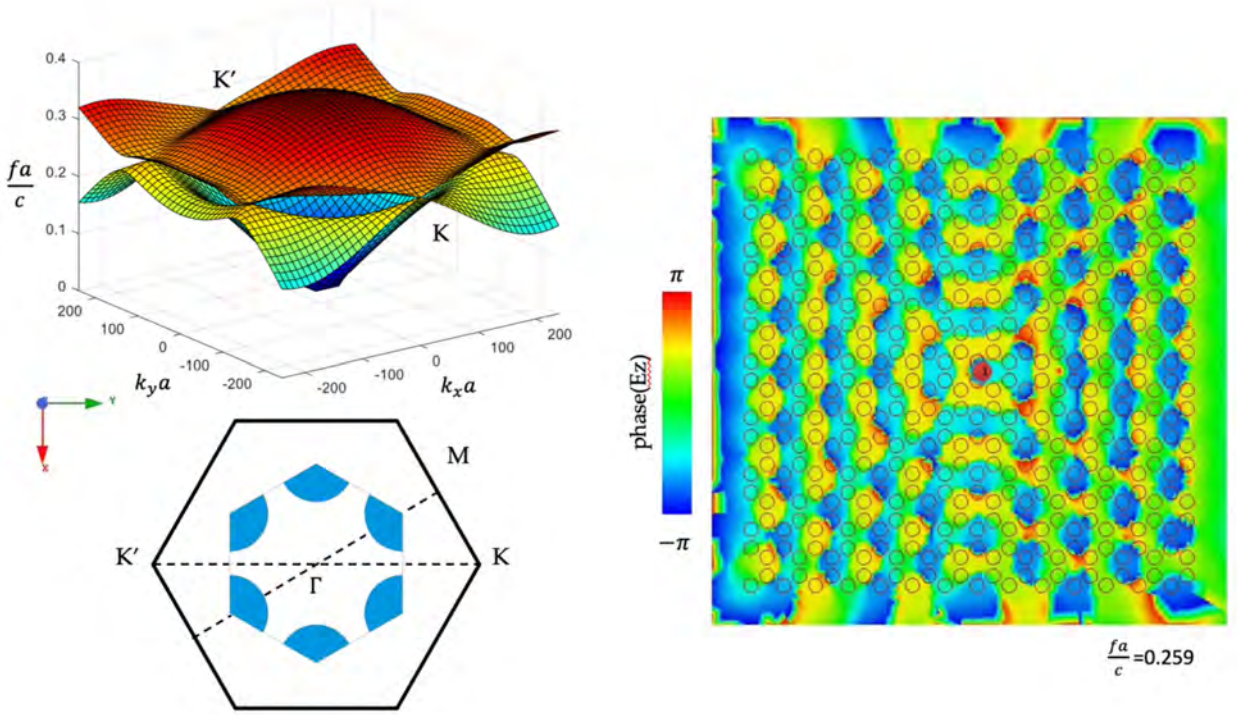

Figure 8. An explanation for why we observe a mode that spreads out laterally, but is phase locked across the entire mode profile. At the k points in the Brillouin zone, two bands come together to form singular points, called Dirac points. at these points, the phase velocity represents a wave that is traveling in a specific direction, but the group velocity can be in all directions, known as diffusive transport. This is why the wave spreads out but remains phase locked.

We have also studied a variety of amorphous structures, as shown in Figure 9. We have found that if we randomly move the locations of dielectric rods, the bandgap will gradually close up. We can quantify this closing through a density of states calculation. As long as the band gap remains open, the structure can still support unidirectional propagation, even in the presence of significant deviation from the original periodic lattice.

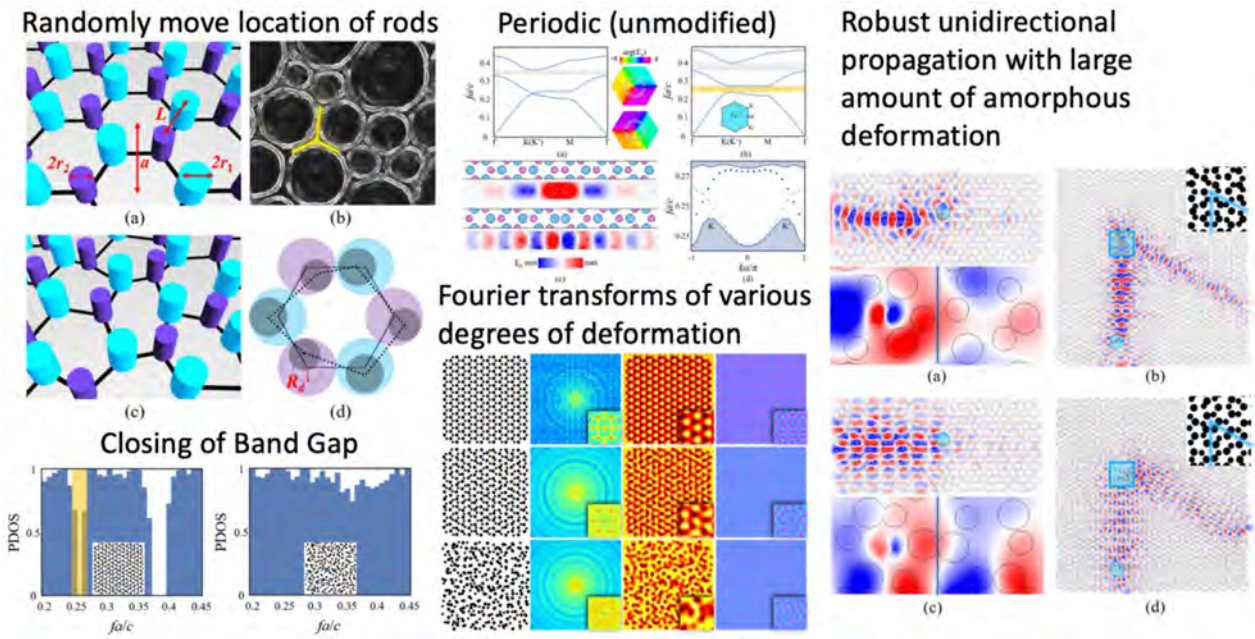

Figure 9. An example of the behavior of a photonic topological insulator under amorphous deformation. As the locations of dielectric rods are varied from their original positions, the band gap gradually closes. However, as long as it remains open, the structure can support unidirectional propagation without backscattering even under significant deformation of the lattice.

We also studied a new type of waveguide in which we shift the lattice in the longitudinal direction on opposite sides of an interface, as shown in Figure 10. We find that for certain degrees of shift, an interface mode is formed that supports unidirectional propagation of spin momentum locked modes, just like photonic topological insulators, but in this case the geometry is identical on opposite sides of the interface. This can be considered as a kind of chiral waveguide, leading us to study other types of chiral metasurfaces.

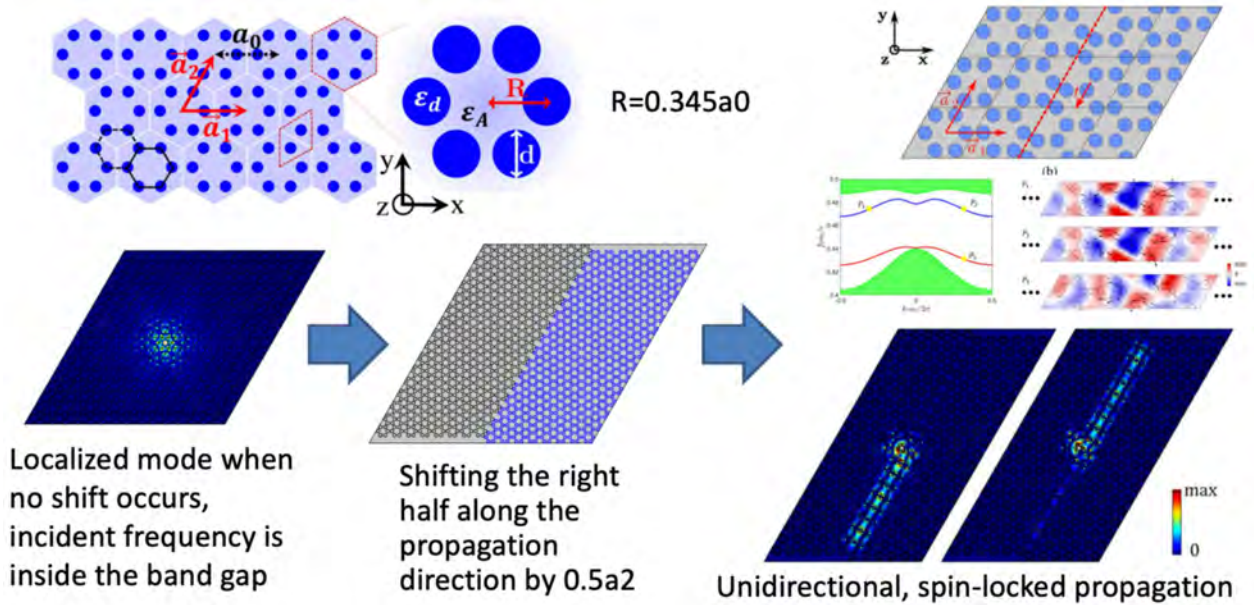

Figure 10. By shifting the lattice longitudinally on opposite sides of an interface, we can also create a spin momentum locked mode even though the structure is identical on both sides. This supports the hypothesis that topologically protected interface modes in photonic topological insulators are actually just a form of chiral waveguide.

Chiral Metasurfaces

Based on our observation of chiral waveguides discussed above, we have also investigated chiral metasurfaces, such as shown in figure 11. A simple L-shaped aperture forms a chiral unit cell for waves propagating diagonally along the L-shaped opening. When excited with one degree of handedness, the wave will propagate forward, while the other degree of hand in this will cause a wave to propagate backward. Thus, this surface is analogous to the chiral waveguides and other photonic topological insulators discussed above. It also has the unexpected feature that the wave is collimated, even when excited with a small point source. This can be understood by examining the equifrequency contours shown in figure 12. All of the chiral structures including the Omega patches, L-shaped slots, and Z- shaped slots show a region where the equifrequency contours become flat. It is in this region where the wave is collimated. The non-chiral structure Shows curvature throughout all regions of the equifrequency contours, and thus does not support self-collimated waves.

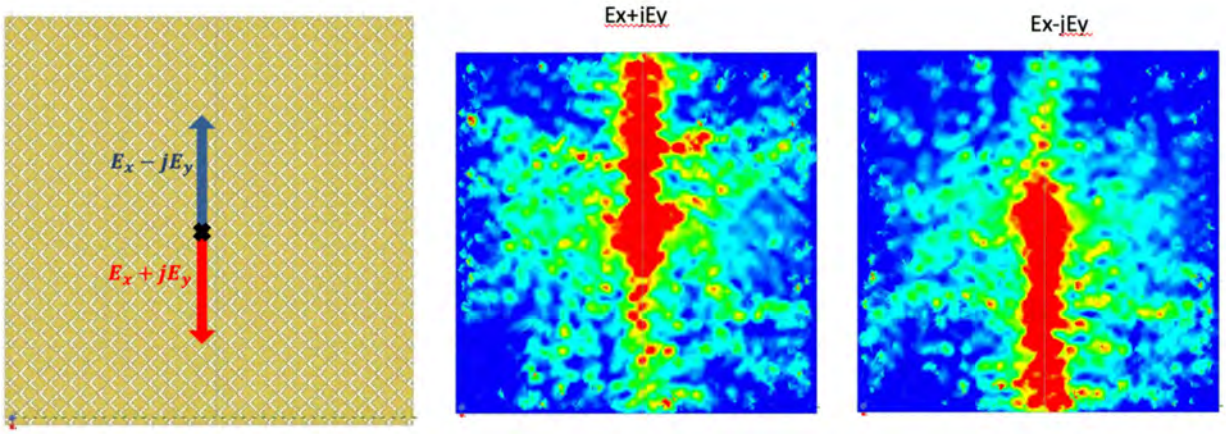

Figure 11. An example of a chiral metasurface built with L-shaped apertures, and examples of self-collimated waves.

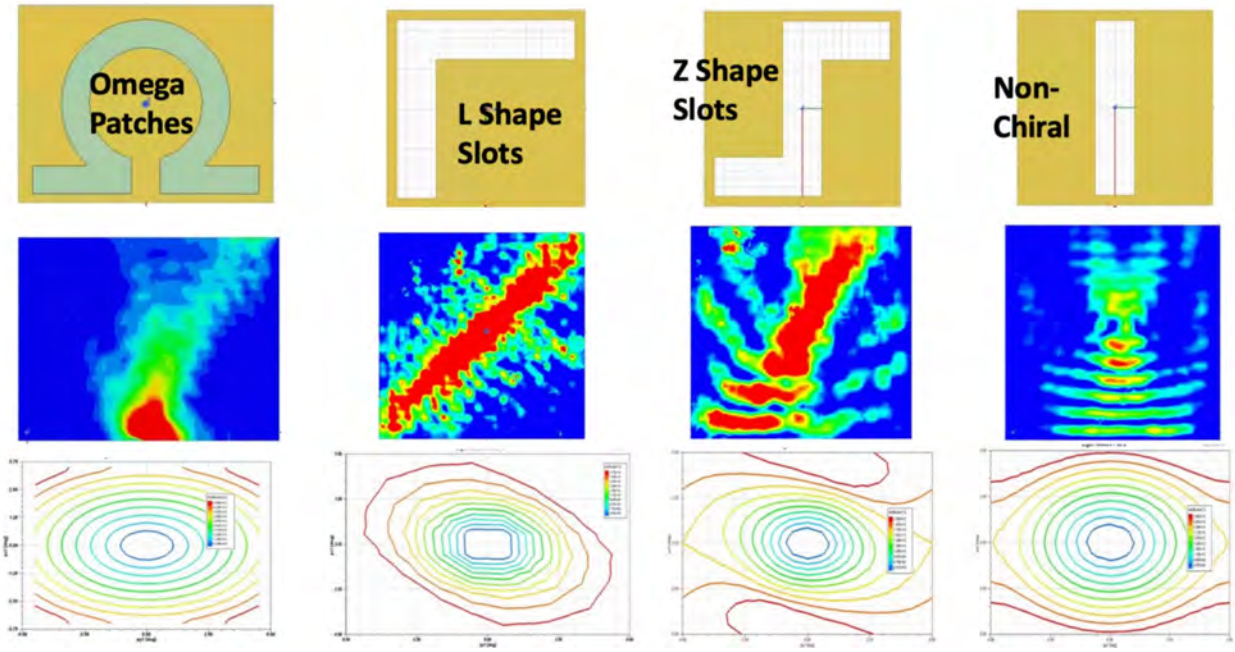

Figure 12. The self-collimation can be attributed to flat regions on the equifrequency contours of chiral structures.

We have begun to investigate whether chiral metasurfaces will be useful for scattering applications. In figure 13 we show an example of the chiral metasurface based on L-shaped apertures. We can excite it with several possible sources including a source in which the spin is normal to the plane of propagation, or normal to the surface (chiral spin). Note that for the case of chiral spin, the wave propagates across the bend in the surface with negligible backscattering, but in the ordinary spin case the observed backscattering is significant

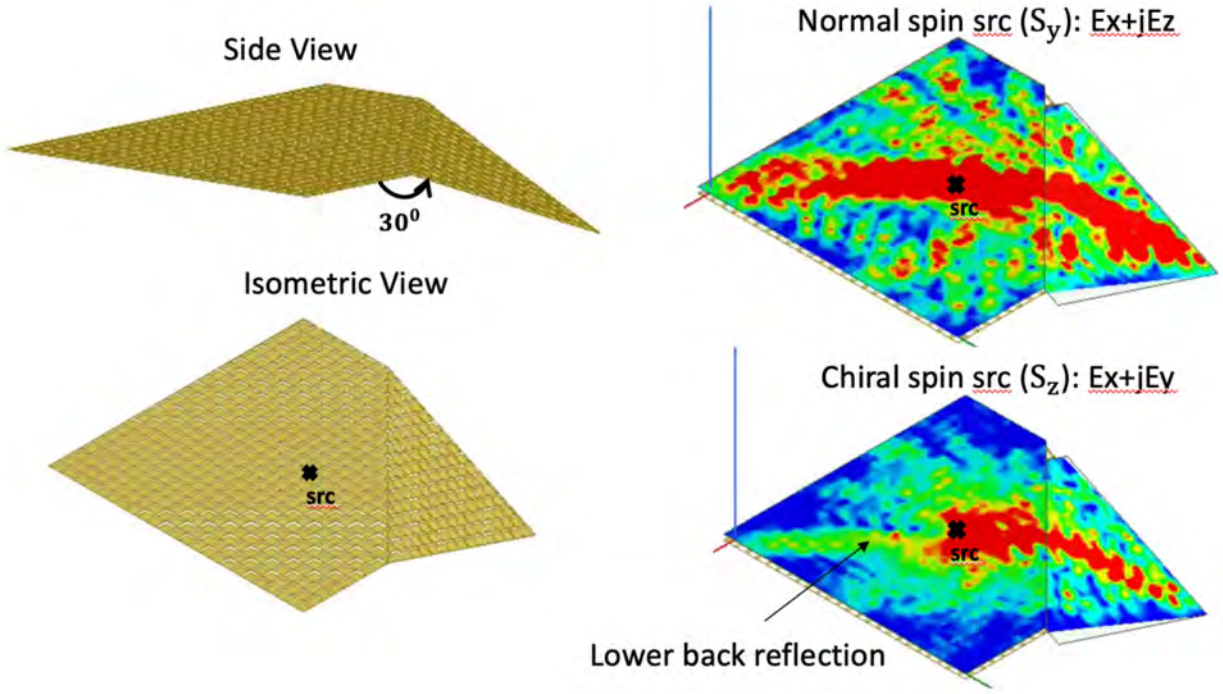

Figure 13. Two examples of wave propagation on a chiral metasurface with a bend. when excited with a source having ordinary spin we observe significant backscattering. When excited with a source having chiral spin, the wave propagates over the bend with negligible backscattering.

Further details on all of these studies can be found in the publications resulting from this program, the most relevant of which are attached to this report.

Publications Resulting from this Program:

H. Hou, J. Long, J. Wang, D. Sievenpiper, "Reduced Electromagnetic Edge Scattering using Inhomogeneous Anisotropic Impedance Surfaces", IEEE Transactions on Antennas and Propagation, IEEE Transactions on Antennas and Propagation, vol. 65, no. 3, pp. 1193-1201, 2017

M. Li, S. Xiao, D. Sievenpiper, "Polarization-Insensitive Holographic Surfaces with Broadside Radiation", IEEE Transactions on Antennas and Propagation, vol. 64, no. 12, pp. 5272-5280, December 2016

J. Lee, D. Sievenpiper, "Patterning Technique for Generating Arbitrary Anisotropic Impedance Surfaces", IEEE Transactions on Antennas and Propagation, vol. 64, no. 11, pp. 4725-4732, December 2016

M. Li, S. Xiao, J. Long, D. Sievenpiper, "Surface Waveguides Supporting both TM Mode and TE Mode with the Same Phase Velocity", IEEE Transactions on Antennas and Propagation, vol. 64, no. 9, pp. 3811-3819, Sept. 2016

Y. Li, A. Li, D. Sievenpiper, "Theoretical Design and Analysis of Wideband Active Hard Electromagnetic Surfaces Using Non-Foster Circuit Loaded Anisotropic Metasurfaces", Journal of Physics D 51, 075101 (2018)

C. Wang, E. Li, D. Sievenpiper, "Surface Wave Coupling and Antenna Properties in Two Dimensions", IEEE Transactions on Antennas and Propagation, vol. 65, no. 10, pp. 5052-5060, 2017

D. Bisharat, D, Sievenpiper, "Guiding Waves Along an Infinitesimal Line Between Impedance Surfaces", Physical Review Letters 119, 106802 (2017)

J. Lee, D. Sievenpiper, "Method for Extracting the Effective Tensor Surface Impedance Function from Nonuniform, Anisotropic, Conductive Patterns", IEEE Transactions on Antennas and Propagation, vol. 67, no. 5, pp. 3171-3177 (2019)

C. Wang, D. Bisharat, S. Kim, E. Li, D. Sievenpiper, "Simulation Analysis of Electromagnetic Surface Wave Suppression by Soft Surfaces, Including Effects of Resistive and Active Elements", IEEE Antennas and Wireless Propagation Letters, vol. 17, no. 12, pp. 2394-2398, 2018

D. Bisharat, D. Sievenpiper, "Manipulating Line Waves in Flat Graphene for Agile Terahertz Applications", Nanophotonics 2018; 7(5): 893–903

Z. Xu, X. Kong, R. Davis, D. Bisharat, Y. Zhou, X. Yin, D. Sievenpiper, "Topological Valley Transport Under Long-Range Deformations", Physical Review Research 2, 013209 (2020)

X. Kong, Y. Zhou, G. Xiao, D. Sievenpiper, "Spin-Momentum Locked Modes on Anti-Phase Boundaries in Photonic Crystals", Optics Express 28, 2070-2078 (2020)

O. Quevedo-Teruel, H. Chen, A. Diaz Rubio, G. Gok, A. Grbic, G. Minatti, E. Martini, S. Maci, G. Eleftheriades, M. Chen, N. Zheludev, N. Papasimakis, S. Choudhury, Z. Kudyshev, S. Saha, H. Reddy, A. Boltasseva, V. Shalaev, A. Kildishev, D. Sievenpiper, C. Caloz, A. Alu, Q. He, L. Zhou, G. Valerio, E. Rajo-Iglesias, Z. Sipus, F. Mesa, R. Rodríguez-Berral, F. Medina, V. Asadchy, S. Tretyakov, C. Craeye, "Roadmap on Metasurfaces", Journal of Optics 21, 073002 (2019)

Z. Xu, J. Shi, R. Davis, S. Wang, Y. Zhou, X. Yin, D. Sievenpiper, "Rainbow trapping with long oscillation lifetimes in gradient magnetoinductive metasurfaces", Physical Review Applied, 12, 024043 (2019)

Z. Du, A. Li, X. Zhang, D. Sievenpiper, "A Simulation Technique for Radiation Properties of Time-Varying Media Based on Frequency- Domain Solvers", IEEE Access, 7, 112375 (2019)

D. Bisharat, D. Sievenpiper, "Electromagnetic-Dual Metasurfaces for Topological States Along a One-Dimensional Interface", Laser & Photonic Reviews, 1900126

Z. Xu, X. Yin, D. F. Sievenpiper, "Adiabatic Mode-Matching Techniques for Coupling Between Conventional Microwave Transmission Lines and One-Dimensional Impedance-Interface Waveguides", Physical Review Applied, Physical Review Applied 11, 044071 (2019)

X. Kong, D. Bisharat, G. Xiao, D. Sievenpiper, "Analytic Theory of an Edge Mode Between Impedance Surfaces", Physical Review A 99, 033842 (2019)

Reduced Electromagnetic Edge Scattering Using Inhomogeneous Anisotropic Impedance Surfaces

Haijian Hou, Jiang Long, *Student Member, IEEE*, Junhong Wang, *Senior Member, IEEE*, and Daniel F. Sievenpiper, *Fellow, IEEE*

***Abstract*— Electromagnetic scattering characteristics highly depend on the geometry and material property of the scatterers. In particular, electromagnetic wave scattering occurs at the discontinuity of the propagation path, such as the edge of a scatterer. In this paper, the edge scattering from a triangular object is largely reduced by patterning the triangular surface with inhomogeneous and anisotropic impedance surface. Because surface waves propagate toward the direction with the lower surface refractive index on an anisotropic surface, the direction of the wave propagation can be controlled by designing the distribution of the refractive index. Consequently, the proposed anisotropic impedance surfaces can make the current flows toward or away from the edge so that the edge scattering can be reduced or redirected to a different angle. For demonstration, anisotropic unit cells are analyzed and designed. Also, the anisotropic impedance surfaces are simulated, fabricated, and measured. Here we propose two types of impedance profiles, which are capable of changing the surface current direction either toward or away from the scattering edge. The experimental measurement demonstrates a 7–10 dB edge scattering reduction.**

***Index Terms*— Anisotropic surface impedance, electromagnetic metamaterials, metasurface, radar cross sections (RCSs), scattering.**

I. Introduction

ARTIFICIAL impedance surfaces (AISs) have a surface impedance which is controlled by the geometry and arrangement of subwavelength metallic patches on a grounded dielectric substrate. They are part of a class of structures generally called metasurfaces, which include electromagnetic bandgap (EBG), surfaces, high impedance surfaces, artificial materials, and so forth. Many applications have been explored, including antennas, lenses, and waveguides. When used in antenna applications, they can be used to improve gain, reduce side lobes, and improve isolation by reducing the surface wave coupling between the multiple antennas. For example, low radar cross section (RCS) has been demonstrated using microstrip antennas combined with an EBG structure [1]–[3]. In lens applications, AISs have been implemented to control the pattern of refractive index, which leads to the design of fish eye lenses and Luneburg lenses [4]–[7]. Also, a surface waveguide can be created by using a strip of high index AIS surrounded by low index surfaces [8]. Moreover, anisotropic impedance surfaces have been used to achieve lower RCS by using the concepts such as cloaking, transformation optics, control of scattering or guiding of wave propagation, and rotation of the electromagnetic field [9]–[14].

When a wave impinges upon a surface such as a metallic sheet, reflection from the surface and scattering from the edges are induced. For antenna engineers, it is crucial to reduce the energy scattered from the edges in order to control the radiation pattern [15]. In this paper, we are primarily focused on the scattering of the transverse magnetic (TM) surface waves. Other related researches have involved patterning a hard and soft surface onto a metal sheet to create an artificial boundary which is able to change the direction of backward scattering [16]. In this paper, a novel approach is proposed to reduce the scattering from edges by using anisotropic impedance surfaces [17]–[19] to redirect the surface wave propagate toward or away from the edges.

The scattering properties of an object are controlled by the combination of material property and geometry, such as by using absorbing materials, or configuring its shape so that waves are scattered to specific angles. For antennas, this can involve designing the size and shape of the ground plane to achieve specific radiation pattern goals, leading to designs that are not necessarily optimum from the perspective of other engineering tradeoffs, such as size, weight, or aerodynamics. The basic concept of this paper is that we can control the specular reflection from a particular edge by tailoring the surface impedance around that edge with inhomogeneous anisotropic impedance surfaces. Specifically, it is known that the reflected wave can be reduced by changing the angle of the incident wave. To change the incident angle, we can not only physically change the edge orientation, but also change the wave propagation direction relative to the edge geometry. The latter provides an additional tool for the electromagnetic designers beyond simply changing the geometry of the surface. In this paper, we demonstrate this concept with a simple triangular scatterer by reducing specular reflection from the hypotenuse.

When a plane wave impinges on a metal surface, current is excited on the surface, creating radiation from the edges [20], [21]. As shown in Fig. 1(a), when an incident

Manuscript received January 25, 2016; revised November 24, 2016; accepted December 9, 2016. Date of publication January 4, 2017; date of current version March 1, 2017. This work was supported in part by the Air Force Office of Scientific Research under Contract FA9550-16-1-0093 and in part by the National Natural Science Foundation of China (NSFC) Project under Grant 61271048 and Grant 61331002.

H. Hou is with Beijing Jiaotong University, Beijing 100011, China, and also with the Applied Electromagnetics Research Group, University of California at San Diego, La Jolla, CA 92093 USA (e-mail: 12111005@bjtu.edu.cn).

J. Long is with Skyworks Solution Inc., Woburn, MA 01801 USA (e-mail: jilong@ucsd.edu).

J. Wang is with Beijing Jiaotong University, Beijing 100011, China (e-mail: wangjunh@bjtu.edu.cn).

D. F. Sievenpiper is with the Applied Electromagnetics Research Group, University of California at San Diego, La Jolla, CA 92093 USA (e-mail: dsievenpiper@eng.ucsd.edu).

Color versions of one or more of the figures in this paper are available online at http://ieeexplore.ieee.org.

Digital Object Identifier 10.1109/TAP.2016.2647681

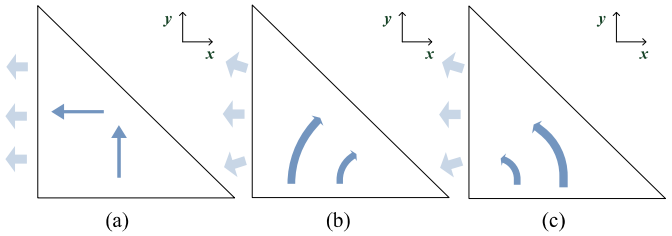

Fig. 1. Scattering manipulation. A plane wave enters the three different models including metal and anisotropic impedance surfaces. Different scattering behaviors are created by controlling the incidence angle on the hypotenuse edge of the triangle. (a) Bare metal. (b) Anisotropic AIS guiding surface waves toward the hypotenuse edge. (c) Anisotropic AIS guiding surface waves away from the edge.

plane wave propagating along the positive y-direction, strong scattering peak toward $-x$-direction is produced owing to the reflection at the hypotenuse of the triangle surface. Fig. 1 illustrates the concept of this paper: when the wave is steered toward the edge, we would expect the scattered energy to be stronger toward directions normal to that edge. When the wave is steered away from the edge, it hits the edge closer to a grazing angle, and it is thus expected that the scattered energy will be directed toward the grazing angles. Here, a simple triangle structure was chosen because it is straightforward to identify the scattering peak, which enables us to study patterning techniques to control the scattering behavior.

In order to reduce the scattering peak of a triangle structure, the geometric reflection from its hypotenuse needs to be altered. Because the reflection angle is determined by the phase progression of the surface waves along the edge, it can be controlled by changing the direction of the incident surface waves relative to the orientation of the hypotenuse without modifying the physical geometry of the hypotenuse. This can be realized by an anisotropic AIS, which is able to guide the surface waves toward or away from the hypotenuse, the edge causing the reflection. Surface waves on impedance surfaces can be controlled either by building discrete waveguides, or by using anisotropy. On an anisotropic surface, the waves will tend to follow the direction of lowest impedance, or refractive index, according to the principle of least time [22]. Specifically, the surface wave is guided toward the edge as illustrated in Fig. 1(b) when the low refractive index is rotated toward the edge. On the contrary, when the low refractive index is rotated away from the edge, surface waves avoid the edge as shown in Fig. 1(c). In either case, the waves hit the edge at a different angle either near normal or grazing and both can reduce the scattering toward the regular specular angle. In this paper, we study both cases, and demonstrate that both cases are effective at controlling scattering from the edge.

The remainder of this paper is organized as follows. Section II discusses the theory of anisotropic AISs and design of the unit cell. Characteristic parameters of the proposed anisotropic AIS are also discussed in Section II. Based on these characteristics, both discontinuous and continuous patterns are introduced in Section III. For the discontinuous case, the surface is divided into several sections. For the continuous case, the impedance is varied smoothly across the surface. Simulation and measurement results are presented

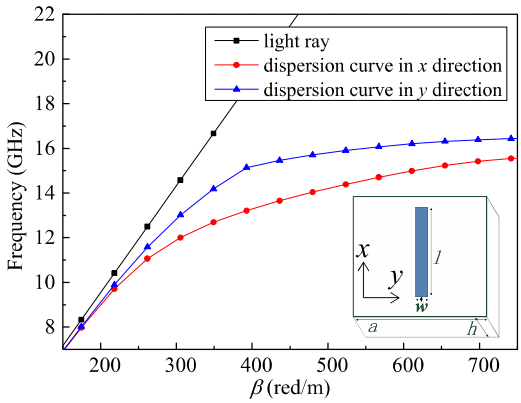

Fig. 2. Unit cell model and dispersion curves. Configuration parameters: the length of unit cell $a = 4$ mm, length of dipole short edge $w = 0.3$ mm, length of dipole long edge $l = 3$ mm, height of substrate $h = 1.27$ mm. The permittivity of the substrate is 10.2 and the permeability of the substrate is 1. The black line represents free-space propagation, and dispersion curves below this light line correspond to bound surface wave modes.

and discussed in Sections IV and V. In Section IV, the RCS of anisotropic AIS and a simple copper triangle are compared and analyzed. In Section V, surface wave results are calculated using near-field measurement results, and scattering characteristics are obtained by far-field measurement

II. Anisotropic Impedance Unit Cell

A. Anisotropic Surface Unit Cell

An anisotropic AIS is created by covering a grounded dielectric substrate with a pattern of metallic shapes [23]–[26]. In this paper, a dipole shaped rectangle is printed on Rogers 6010 substrate with a copper ground. This particular pattern is chosen because of its simplicity, its ease in creating a high degree of anisotropy, and the fact that it can be rotated in any direction within its square unit cell. In Fig. 2, the unit cell is shown in Cartesian coordinates, in which the short edge of the copper rectangle is in y-direction with length $l = 0.3$ mm and the long edge is in x-direction with $w = 3$ mm. The period of the unit cells is 4 mm, which is longer than the diagonal of the copper patch, so adjacent patches does not touch each other no matter how they are rotated.

The impedance of the anisotropic AIS is a function of the geometry of the unit cell, the substrate permittivity, as well as the incident wave direction. In this paper, a rectangle shaped unit cell is discussed and its behavior is similar to the dipole unit cell which can be used to make hard and soft surfaces [24] each a kind of highly anisotropic impedance surface. A TM polarized surface wave sees high impedance when propagating along the longitudinal edge of the rectangle patch, whereas low impedance is seen by TM waves when the wave is traveling in transverse direction [18], [24].

As discussed in Fig. 1, strong scattering occurs at the hypotenuse of a triangle shaped surface. In order to reduce the scattering from the edge, an anisotropic AIS can be used to control the direction of surface wave propagation, either toward or away from that edge. The rectangle patches, as the unit cell shown in Fig. 2, are patterned over the entire triangle region with various orientations. The rectangular patches are

rotated as a function of position on the surface to guide the surface waves to follow a controlled path along the surface. If rectangles are rotated gradually, the TM waves turn toward low impedance direction. If the rectangles are rotated abruptly, the surface waves may be reflected from the discontinuous boundaries between regions [16].

B. Dispersion

Since the TM surface wave mode is of interest, we analyzed the surface impedance by analyzing the refractive index for the TM mode [18]. The surface wave is bound to the surface when its propagation constant is larger than that in free space, or when the dispersion curve lies below the light line, as indicated in Fig. 2. The effective refractive index seen by the surface waves can be calculated [18]

$$n = k_t c/\omega \tag{1}$$

where k_t is the wavenumber of the surface wave, c is the speed of light, and ω is the angular frequency.

The dispersion characteristics shown in Fig. 2 are calculated using the eigenmode solver in Ansys HFSS. Periodic boundaries are applied to the four vertical walls of the simulation volume. Top and bottom faces are set with perfect electric boundaries. The height of the upper boundary to the unit cell is 25 mm. The red line represents the dispersion curve along the long edge of the dipole, i.e., x-direction, whereas the blue line shows the dispersion curve in short edge direction which is y-direction. It can be seen from Fig. 2 that impedance along x-axis gives high impedance (red curve), and in contrast, low impedance is achieved in y-axis (blue curve). The "light line" plotted in black corresponds to the speed of light in free space. The operating frequency is chosen at 15 GHz where the two primary directions have a large index contrast. For this structure, the effective refractive index varies from 1.2 in the y-direction to 2.0 in the x-direction.

For isotropic materials, k, B, and D are perpendicular, but for anisotropic materials, D and E are not always in parallel with each other. In dispersive materials, the group velocity and phase velocity of surface waves are different. Also, the direction of power flow or Poynting vector S and the direction of phase progression k may be different [31]. In the measured results, the propagation direction is determined by the wavefront, and the power flow is determined by the E field.

III. Pattern Design

Two patterning approaches are discussed in this section. One way is to pattern the rectangular unit cells onto the surface using discontinuous homogeneous regions. Alternatively, the other way is to pattern unit cells continuously, creating an inhomogeneous and smoothly varying impedance. Both of these methods are explored because anisotropic impedance surfaces are often difficult to pattern into arbitrary impedance functions while retaining high anisotropy due to the fact that the symmetry of the metal patches is lower than that of a simple square or triangular lattice. In other words, elongated metal shapes cannot be easily formed into smoothly curved paths. Thus, discrete regions of different impedances are much simpler to design in many cases, but may yield lower performance due to reflections from their interfaces. Here a simple square lattice with a dipole unit cell is chosen because it can be easily patterned into discontinuous or continuous patterns, and the results can be extrapolated to more complex unit cells.

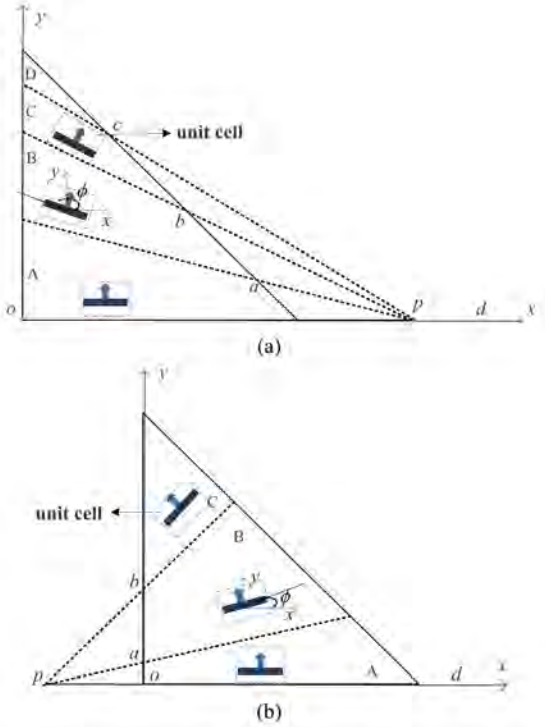

Fig. 3. Discontinuous design. The whole surface is divided into several sections. The rectangles are the homogeneous in each sector. (a) Anisotropic AIS guides the surface wave toward the hypotenuse edge. (b) Anisotropic AIS guides surface wave away from the edge.

A. Discontinuous Pattern

The simplest way to steer the surface waves toward or away from the edge is to refract them at a series of interfaces between discrete but homogeneous anisotropic regions. In these discontinuous cases, as shown in Fig. 3, the triangle is divided into several sections. Identical unit cells are used to fill up each section. Therefore, the entire triangular shape is patterned "discretely," which is the reason why we call it discontinuous patterns. For simplicity, a common point outside of the triangle is arbitrarily chosen, based on which three lines with the elevation angle from the horizontal direction as $\phi = 170°$, $160°$, and $150°$, respectively, are made to intersect with the triangular shape, dividing it into four sections. The common point p is shown in Fig. 3(a). $\angle apd$ is $170°$, $\angle bpd$ is $160°$, and $\angle cpd$ is $150°$. In Fig. 3, boundaries between sections are drawn in dotted line, and hypotenuse edges of triangles are drawn in solid line. Three unit cells are given as typical examples in Fig. 3, and the boundaries of the unit cells are drawn in dotted line. The bottom edge of each unit cell is in parallel with the section boundaries. If two different unit cells are overlapped on boundaries, in Fig.3, unit cells in

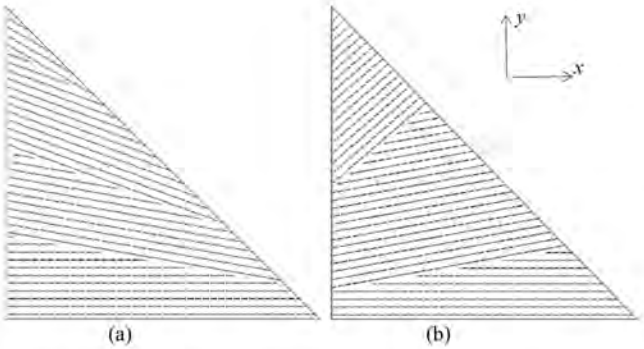

Fig. 4. Configuration of discontinuous designs. (a) Anisotropic AIS guiding surface waves toward the hypotenuse edge. (b) Anisotropic AIS guiding surface waves away from the edge.

region A are overrode by unit cells in region B, unit cells in region B are overrode by unit cells in region C, and so on. The rectangular metal patches in each section are identical in size and shape, but are oriented at different angles of 180°, 170°, 160°, and 150° in regions A, B, C, and D, respectively (the original position: the short edge of rectangle is in y-direction and the long edge is in x-direction in Fig. 2). Therefore, the longer edges of rectangular metal patches in each section are in parallel with section boundaries. As can be seen, the longer edges of the rectangular metal patches in region B are in parallel with the boundaries between region A, and region B. Thus, the low impedance direction approximates a continuous curve toward the hypotenuse of the triangle. The light blue arrows indicate direction of low surface refractive index.

In Fig. 3(b), the design is similar but the waves are intended to curve away from the edge. With the similar manner described above, the triangle is divided into three sections and the boundaries between them are at $\phi = 10°$ and 40°. $\angle apd$ is 10°, and $\angle bpd$ is 40°. The rectangles in each section are oriented to 0°, 10°, and 40° in regions A, B, and C, respectively, for this surface (the original position: the short edge of rectangle is in y-direction and the long edge is in x-direction in Fig. 2). The configuration of discontinuous designs are shown in Fig. 4.

Both of these are intended to be discontinuous approximations to the smoothly varying continuous surfaces to be described below. In both cases, the angles of the patches and the locations of the boundaries were chosen to minimize the scattering from the hypotenuse edge of the triangle. These discontinuous patterns produce extra reflections at their boundaries, as will be shown in Section IV. To reduce the reflections, continuous patterns are discussed in next section.

B. Continuous Pattern

As an alternative to the discontinuous case, a surface with the angle of low refractive index varies smoothly and continuously is also investigated. The unit cell studied here, in which a small rectangular dipole is arranged on a square lattice, is amenable to either type of patterning approach. However, more complex unit cells may be difficult to pattern in a continuous manner. Thus, it is important to understand and quantify the advantages relative to the discontinuous case.

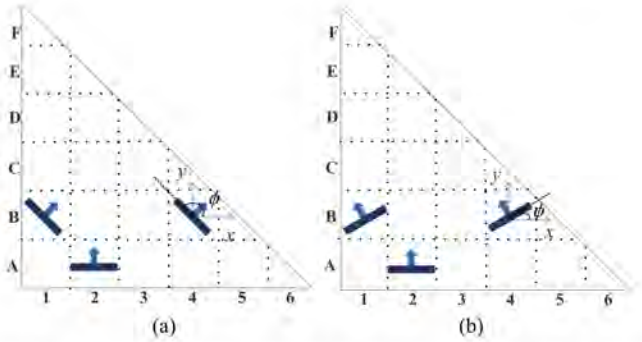

Fig. 5. Continuous design. The whole surface is divided into a square grid. The rotation angle of each cell varies according to the cell location. (a) Anisotropic AIS guiding surface waves toward the hypotenuse edge. (b) Anisotropic AIS guiding surface waves away from the edge.

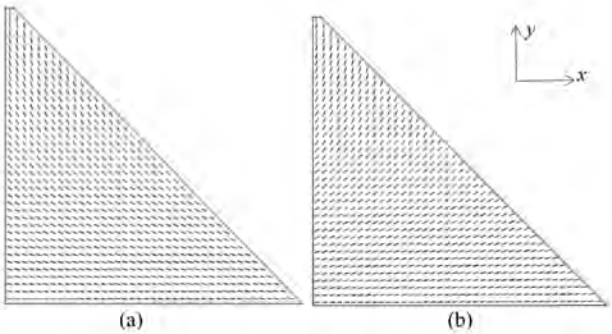

Fig. 6. Configuration of continuous design. (a) Anisotropic AIS guiding surface waves toward the hypotenuse edge. (b) Anisotropic AIS guiding surface waves away from the edge.

In order to reduce the reflections at the boundaries, continuous patterns are described in this section. In Fig. 5(a) and (b), the right angle vertices of the triangles are located on origin of our coordinate system. Instead of grouping the unit cells by several sections, all the unit cells are patterned in a much finer manner: dipole angle rotates by the row index. For example, as illustrated in Fig. 5(a) and (b), the triangle is filled up with six rows of unit cells, with row index A to F, and six columns with column index from one to six. Within each square, there is a single dipole unit cell. The direction of the diploe, described as the blue arrow in Fig. 5, rotates row by row, while maintains the same within each row. In Fig. 5(a), the metal patches are gradually rotated toward the hypotenuse edge, while in Fig. 5(b) they are gradually rotated away from it. For the case where the surface waves are directed to the hypotenuse [Fig. 5(b)], starting from the bottom row A, where the blue arrow is about perpendicular to the bottom edge, the direction of the blue arrow rotates gradually, and eventually get horizontal to the bottom edge as the last row (F as illustrated in Fig. 5). In contrast, the diploe direction also gets perpendicular to the bottom edge. For the case, the surface wave is directed away from the hypotenuse. The rotation step for each row is uniform. Therefore, in the following experimental demonstration, a surface with 40 rows of unit cells is designed, and the rotation step is 2.25°. The configuration of continuous designs is shown in Fig. 6.

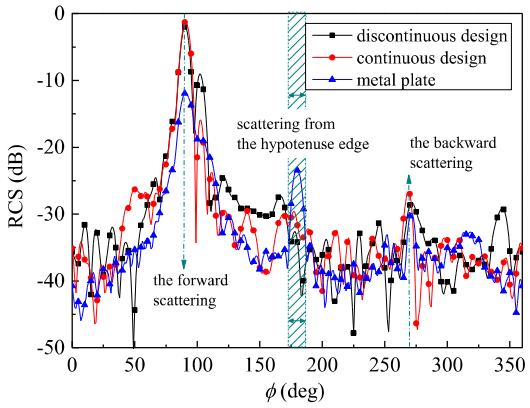

(a)

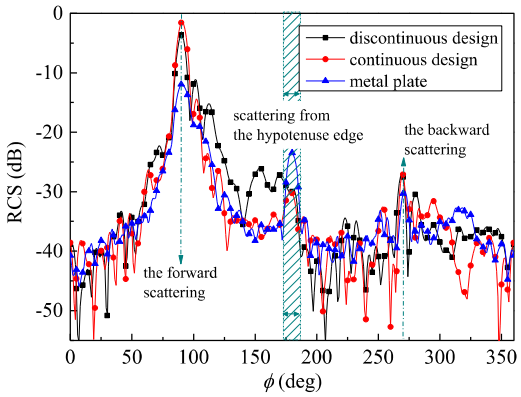

(b)

Fig. 7. Bistatic RCS of the bare metal triangle and the anisotropic impedance surfaces at 15 GHz. (a) Anisotropic AIS guiding surface waves toward the hypotenuse edge. (b) Anisotropic AIS guiding surface waves away from the edge.

With both patterns, the direction of surface wave propagation is curved and the scattering from the hypotenuse edge is reduced. Simulation results are discussed in the next section to compare the discontinuous pattern and the continuous pattern.

IV. Scattering Simulation

In this section, two aforementioned patterned triangle scatterers and a bare metal scatterer are examined by bistatic RCS simulation. Although the full bistatic RCS is simulated for the purpose of identifying other scattering characteristics, our primary concern is the scattering from the hypotenuse edge, and how much reduction is achieved by the proposed patterned surfaces. In this section, all of the triangular surfaces are 163 mm in width and 160 mm in length, and the unit cells are as described in Section II, and patterned as described in Section III. The surfaces are simulated using HFSS. Because the models are too complex to draw by hand, HFSS-MATLAB scripting is used to create the anisotropic impedance surface.

The scattering from a copper triangle is analyzed first. The bistatic RCS is shown in Fig. 7 and the relation between surface current and scattering is discussed. For the anisotropic AIS cases, the bistatic RCS is compared with the copper triangle, and the relation between current and scattering is discussed. Finally, the discontinuous case and continuous case are compared and discussed.

A. Bare Metal Surface

In this case, a simple copper triangle oriented in the xy plane is analyzed, and $\theta = 0°$ represents the z-direction, normal to the surface. In these simulations, a plane wave impinges on the copper triangle at an elevation angle of $\theta = 80°$ and azimuth angle of $\phi = 270°$. θ and ϕ are the parameters in the spherical coordinates. The bistatic RCS at $\theta = 80°$ elevation is the blue line shown in Fig. 7(a) and (b). We chose to analyze the RCS of all of the surfaces at a slight elevation angle (i.e., 10° from grazing) because the scattering from a thin metal sheet is negligible for TM polarization at grazing incidence. Note the three peaks in the scattering plot at $\phi = 90°$, $\phi = 180°$, and $\phi = 270°$. These correspond to forward scattering, reflection from the hypotenuse edge, and backward scattering, respectively. We are not concerned with the large forward scattering peak at $\phi = 90°$, nor the smaller backward scattering peak at $\phi = 270°$, but only with the peak at $\phi = 180°$ representing the edge which we are attempting to control. As we will discuss below, both patterning methods are able to provide reduction of the specular reflection from the hypotenuse edge, with varying degrees of additional scattering to other directions.

B. Patterned Metal Surfaces

Fig. 7(a) compares the metal triangle with two patterned triangles using the discontinuous and continuous patterning methods, both of which intend to bend the surface currents toward the hypotenuse edge. For both cases, the patterned surfaces show reduced scattering compared to the metal surface, with a reduction of about 8 dB for the continuous pattern and 10 dB for the discontinuous case. Fig. 7(b) shows the same results but for the cases where the patterned surfaces are intended to bend the surface currents away from the hypotenuse edge. In these cases, both approaches reduce the bistatic RCS at $\phi = 180°$ by about 7 dB, demonstrating both approaches (steering the wave toward or away from the edge) change the phase progression along that edge, and thus reduce the specular reflection at $\phi = 180°$. However, two points are noted: 1) All four cases still show lobes at or near $\phi = 180°$, and the location and level of these lobes can significantly affect the actual degree of improvement. Thus, one should be careful to draw conclusions based on one curve being 1–2 dB above another, and instead we should discuss the overall trend. Because the scattering to any angle is a result of the integrated reflection from the entire surface, small variations can determine whether different components add or cancel at a particular angle. Thus, these RCS plots must be compared with other simulation approaches and measurement results to verify and quantify this approach and 2) Overall, both types of patterning approaches show the same trends, but the discontinuous surfaces have a higher degree of diffuse scattering, particularly at angles below $\phi = 45°$ in Fig. 7(a), and between $\phi = 90°$ and 180° in both figures. The scattering in Fig. 7(a) below $\phi = 45°$ is due to the orientation of the

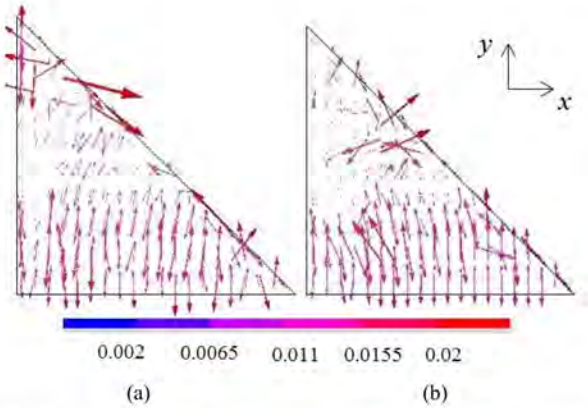

Fig. 8. Surface currents on the discontinuous anisotropic impedance surfaces designed to guide the surface currents at 15 GHz (a) toward the edge or (b) away from the edge. Note the regions of high field at the boundaries between regions.

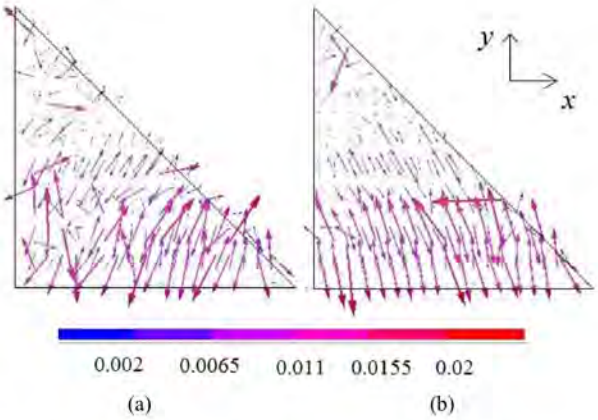

Fig. 9. Surface currents on the continuous anisotropic impedance surfaces designed to guide the surface currents at 15 GHz (a) toward the edge or (b) away from the edge. Note that the fields are much more uniform than in the discontinuous case.

edges in the discontinuous structure. The continuous structure also shows a lobe near $\phi = 45°$ which may be because we have bent the surface waves in precisely that direction. However, as with the prior point above, assigning particular lobes to specific regions of the surface can be difficult due to the complex nature of scattering from an electrically large object. The main point to take away from this data is that using anisotropic impedance surfaces to change the angle at which surface waves impinge on an edge can affect the scattering from that edge, and that there appears to be a slight advantage to using slowly varying impedance functions in terms of not generating other artifacts from discontinuities.

The differences between the discontinuous and continuous designs can also be seen in the simulated field plots in Figs. 8 and 9. The incident plane wave is the same as in Fig. 7. The discontinuous designs in Fig. 8 show regions of high fields at the boundaries between regions, which are likely to cause scattering, and which are not seen in the continuous designs in Fig. 9.

V. Measurements

The anisotropic impedance surfaces are fabricated as shown in Fig. 10. The unit cells are printed on 1.27 mm thick Rogers

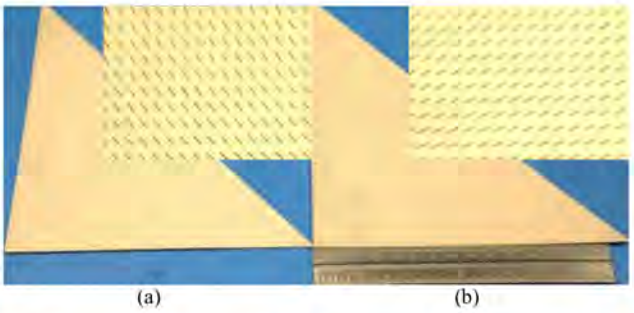

Fig. 10. Anisotropic impedance surface fabrication. The samples are 163 mm in width and 160 mm in length. (a) Surface for steering toward the edge. (b) Surface for steering away from the edge.

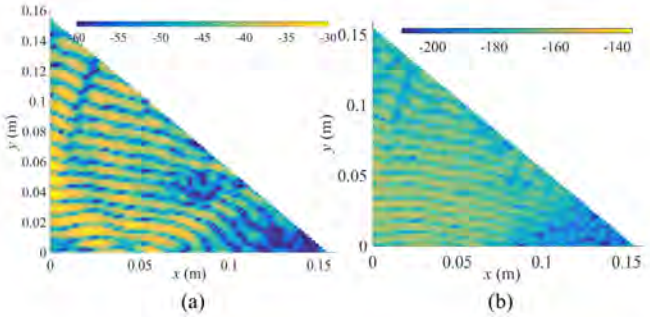

Fig. 11. Near-field plot of the surface waves on the patterned surface designed to steer the waves toward the hypotenuse at 15 GHz. (a) Raw measured data. (b) Transformed data.

6010 which has a relative dielectric constant of 10.2, with a metal ground plane on the back side.

A. Near-Field Measurement

If a surface charge density wave radiates into the far field, the magnitude of wave vector parallel to the propagation direction should be lower than the magnitude of the wave vector in free space [31]. If not, the wave decays in the direction perpendicular to the surface, and is described as a bound wave.

A surface wave was launched on each surface using an H-plane sectoral horn antenna placed near the edge of the surface. Near-field data are collected using a probe connected to an Agilent E5071C vector network analyzer, and the probe is scanned over the surface at a height of 2–3 mm, with data taken every 2 mm over the surface. Figs. 11(a) and 12(a) show the raw measurement results for the E-field in the z-direction.

The probe measures the E_z field including both surface wave and incident wave over the anisotropic surface. In order to distinguish the surface wave from the incident wave, measurement data are transformed to the k domain. The coefficient of imaginary propagation constant in the z-direction in the k domain can be used and transformed to the spatial domain by taking its Fourier transform. If the E-field on the xy plane ($z = d$) is known, the E-field above the $z = d$ plane can be calculated by the following equations [27]:

$$E_z = \iint A_z(k_x, k_y) e^{-j(k_x x + k_y y)} dk_x dk_y \quad (2)$$

$$A_z(k_x, k_y) = \frac{1}{4\pi^2} \iint E_z(x, y) e^{j(k_x x + k_y y)} dx dy. \quad (3)$$

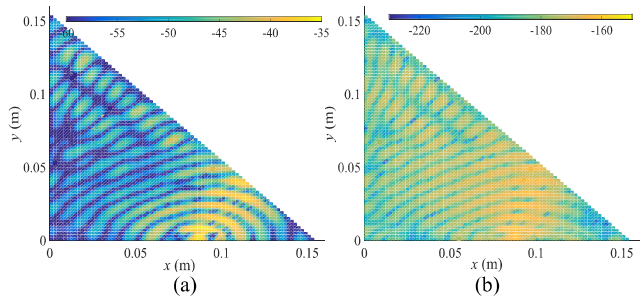

Fig. 12. Near-field plot of the surface waves on the patterned surface designed to steer the waves away from the hypotenuse at 15 GHz. (a) Raw measured data. (b) Transformed data.

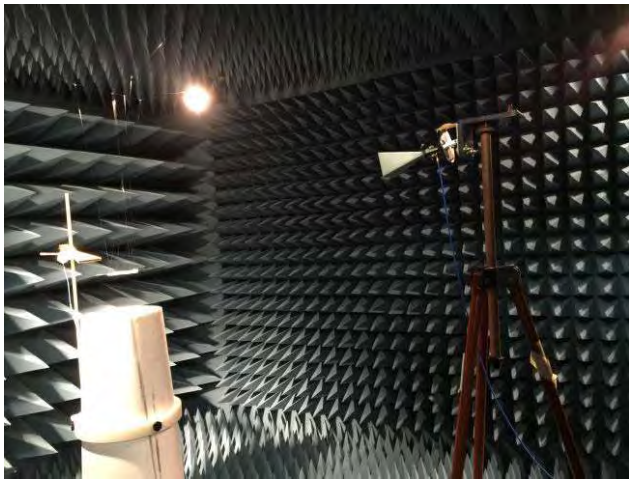

Fig. 13. Far-field measurement setup for bistatic RCS measurements. The source horn antenna is fixed on a tripod and the receive horn antenna is rotated around the surface under test.

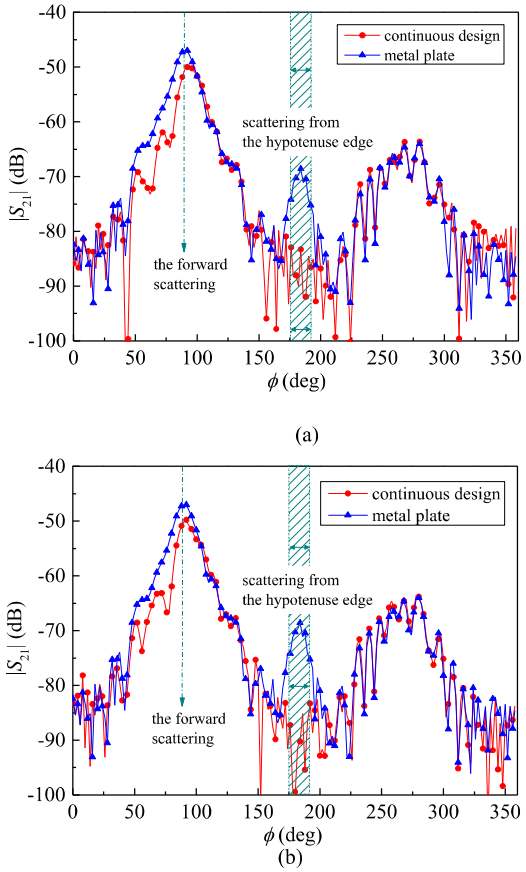

Fig. 14. S_{21} measurement at 15 GHz results for (a) surface designed to steer toward the hypotenuse edge and (b) surface designed to steer away from the hypotenuse edge.

This has the effect of filtering out the data that do not correspond to a bound surface wave, and removes the interference caused by free space waves which are also excited by the feed horn, resulting in cleaner plot of only the surface wave. The method is similar to the near-field to far-field transformation [28]–[30]. In the results shown in Figs. 11(b) and 12(b), curved surface waves can be clearly observed.

B. Bi-Static RCS Measurements

The bistatic RCS measurements were performed in an anechoic chamber with the setup shown in Fig. 13 using an Agilent E5071C vector network analyzer (VNA), a rotating platform, and a pair of horn antennas, one of which was an H-plane sectoral horn. Although this test was not ideal, and large facilities exist for performing bistatic RCS measurements, those are not available to us at reasonable cost. Thus, these experiments represent a quick and simple method to obtain an approximate bistatic RCS in a relatively small chamber. Remarkably, they provide results that are qualitatively and quantitatively in line with the simulations in Fig. 7. To perform this measurement, the surface to be tested was hanging in the chamber at a fixed location by a thin dielectric wire. The source horn was stationary, about 1.5 m from the surface, and this generates the incident plane wave. It was placed on an adjustable tripod so that the angle of the incident wave can be controlled. The receive antenna was mounted on an arm which was attached to a rotating pedestal, and rotated around the stationary surface under test. The measurement is limited by the directionality of the receive antenna because it is within the main beam of the source antenna, so the side-lobes from itself can contribute to the measured RCS of the surface at certain angles. It is also limited by the distance of the receive antenna from the surface which is not strictly within the far field. (Note that the distance between the source horn and target is 1.5 m, the distance between the receive horn and target is 0.5 m, and the distance of far field is 2.56 m). Nonetheless, this is a direct, if limited, measurement of the bistatic RCS, and thus provides useful data that are not available from simulations or other indirect measurement methods.

The plots in Fig. 14 show the S_{21} data from the measurement with the receiver antenna rotating over a complete circle. The blue line indicates the scattering from the copper triangle surface and the red line indicates the scattering from the anisotropic impedance surface. Compared to the copper triangle surface, the scattering from both patterned surfaces is reduced significantly in the direction corresponding to reflection from the hypotenuse edge, at 180°. Moreover, the relative improvement is on the order of what has been seen in the simulations, roughly 10 dB.

We must be careful not to draw inappropriate conclusions from Fig. 14, because it is not a true bistatic RCS measurement, and is confounded by the limitations discussed above. For this reason, it cannot be compared directly to Fig. 7. For example, the magnitude of the peak at $\phi = 90°$ is a function of the gain of the two horns and their separation, not a direct indication of the magnitude of the RCS, which would require a calibrated target. Furthermore, the large set of lobes at $\phi = 270°$ may be due as much to the back lobe of the receive horn as any properties of the surface. Reflections from the back wall of the chamber would also be maximized at this angle. The $\phi = 180°$ case is the angle where the receive horn is oriented orthogonally to the transmit horn, so it is expected to have a low gain in that direction, and reflections from the chamber walls would be at a minimum. Thus, in spite of the limitations of this measurement, the distinct elimination of the scattering peak at $\phi = 180°$ in both patterned surfaces, corresponding to the angle of specular reflection from the hypotenuse edge, may be taken as additional confirmation that this method provides a useful way to manipulate reflection from edges.

VI. Conclusion

An anisotropic impedance surface method is proposed for reducing specular reflection from edges by steering surface waves to change the direction at which they impinge on the edge. As an example, a triangular surface designed with a clearly identifiable scattering peak from the hypotenuse edge, and inhomogeneous anisotropic impedance surfaces are designed to reduce scattering from that edge. A simple unit cell containing a rectangular metallic dipole element is chosen which provides high anisotropy and can be rotated to any direction without interfering with neighboring cells. A triangular sample is patterned with anisotropic impedance surfaces based on both discontinuous and continuous designs. Simulation data suggest that both approaches provide similar reduction in specular reflection from the edge, but the discontinuous design suffers from higher scattering at other angles compared to the continuous design. This is verified by field plots on the surface which show hot spots at the discontinuities between regions. Fabricated samples clearly demonstrate steering of the surface waves in near-field scans. For both types of surfaces, steering the waves either toward or away from the hypotenuse edge shows a clear reduction of the scattering peak from that edge in simple bistatic RCS measurements. This represents a new approach that can be incorporated into designs of antennas, reflectors, or other structures to manipulate specular reflections for applications such as reducing coupling between antennas, eliminating unwanted lobes, or otherwise manipulating the radiation properties of structures. It is worth noting that energy that is diverted from specular scattering can end up as diffuse scattering, spread over other angles. Thus, designs which incorporate this technique must be careful to control for the range of angles at which the waves impinge on any edges, and the effect on the overall scattering profile. Furthermore, this paper only provides a narrowband solution based on a passive AIS, but there is current research aimed at building broadband impedance surfaces using active circuit approaches [33].

Acknowledgment

The authors would like to thank their colleague R. Quarfoth for the contribution to the measurement.

References

[1] J. Zhang, J. Wang, M. Chen, and Z. Zhang, "RCS reduction of patch array antenna by electromagnetic band-gap structure," *IEEE Antennas Wireless Propag. Lett.*, vol. 11, pp. 1048–1051, 2012.

[2] W. Xu, J. Wang, M. Chen, Z. Zhang, and Z. Li, "A novel microstrip antenna with composite patch structure for reduction of in-band RCS," *IEEE Antennas Wireless Propag. Lett.*, vol. 14, pp. 139–142, 2015.

[3] W. Chen, C. A. Balanis, and C. R. Birtcher, "Checkerboard EBG surfaces for wideband radar cross section reduction," *IEEE Trans. Antennas Propag.*, vol. 63, no. 6, pp. 2636–2645, Jun. 2015.

[4] H. Ming, Y. Shuwen, G. Fei, R. Quarfoth, and D. Sievenpiper, "A 2-D multibeam half Maxwell fish-eye lens antenna using high impedance surfaces," *IEEE Antennas Wireless Propag. Lett.*, vol. 13, pp. 365–368, 2014.

[5] M. Bosiljevac, M. Casaletti, F. Caminita, Z. Sipus, and S. Maci, "Non-uniform metasurface luneburg lens antenna design," *IEEE Trans. Antennas Propag.*, vol. 60, no. 9, pp. 4065–4073, Sep. 2012.

[6] R. Yang, Z. Lei, L. Chen, Z. Wang, and Y. Hao, "Surface wave transformation lens antennas," *IEEE Trans. Antenna Propag.*, vol. 62, no. 2, pp. 973–977, Feb. 2014.

[7] B. Fuchs, O. Lafond, S. Rondineau, and M. Himdi, "Design and characterization of half Maxwell fish-eye lens antennas in millimeter waves," *IEEE Trans. Microw. Theory Techn.*, vol. 54, no. 6, pp. 2292–2300, Jun. 2006.

[8] R. Quarfoth and D. Sievenpiper, "Artificial tensor impedance surface waveguides," *IEEE Trans. Antennas Propag.*, vol. 61, no. 7, pp. 3597–3606, Jul. 2013.

[9] Y.-Q. Li, H. Zhangm, Y.-Q. Fu, and N.-C. Yuan, "RCS reduction of ridged waveguide slot antenna array using EBG radar absorbing material," *IEEE Trans. Antennas Propag. Lett.*, vol. 7, pp. 473–476, 2008.

[10] H.-K. Jang, J.-H. Shin, and C.-G. Kim, "Low RCS patch array antenna with electromagnetic bandgap using a conducting polymer," in *Proc. Int. Conf. Electromagn. Adv. Appl. (ICEAA)*, Sep. 2010, pp. 140–143.

[11] J. C. I. Galarregui, A. T. Pereda, J. L. M. de Falcón, I. Ederra, R. Gonzalo, and P. de Maagt, "Broadband radar cross-section reduction using AMC technology," *IEEE Trans. Antennas Propag.*, vol. 61, no. 12, pp. 6136–6143, Dec. 2013.

[12] M. Paquay, J. C. Iriarte, I. Ederra, R. Gonzalo, and P. D. Maagt, "Thin AMC structure for radar cross-section reduction," *IEEE Trans. Antennas Propag.*, vol. 55, no. 12, pp. 3630–3638, Dec. 2007.

[13] A. M. Patel and A. Grbic, "Transformation electromagnetics devices based on printed-circuit tensor impedance surfaces," *IEEE Trans. Microw. Theory Techn.*, vol. 62, no. 5, pp. 1102–1111, May 2014.

[14] R. Quarfoth and D. Sievenpiper, "Surface wave scattering reduction using beam shifters," *IEEE Antennas Wireless Propag. Lett.*, vol. 13, pp. 963–966, 2014.

[15] F. C. Smith, "Edge coatings that reduce monostatic RCS," *IEE Proc. Radar, Sonar Navigat.*, vol. 149, no. 6, pp. 310–314, Dec. 2002.

[16] R. Quarfoth and D. Sievenpiper, "Alteration of electromagnetic scattering using hard and soft anisotropic impedance surfaces," *IEEE Trans. Antennas Propag.*, vol. 63, no. 10, pp. 4593–4599, Oct. 2015.

[17] H. J. Bilow, "Guided waves on a planar tensor impedance surface," *IEEE Trans. Antennas Propag.*, vol. 51, no. 10, pp. 2788–2792, Oct. 2003.

[18] B. H. Fong, J. S. Colburn, J. J. Ottusch, J. L. Visher, and D. Sievenpiper, "Scalar and tensor holographic artificial impedance surfaces," *IEEE Trans. Antennas Propag.*, vol. 58, no. 10, pp. 3212–3221, Oct. 2010.

[19] A. M. Patel and A. Grbic, "Modeling and analysis of printed-circuit tensor impedance surfaces," *IEEE Trans. Antennas Propag.*, vol. 61, no. 1, pp. 211–220, Jan. 2013.

[20] J. H. Wang and Y. B. Gan, "In-band scattering of dipole array with edge loaded rectangular reflector," in *Proc. IEEE Antennas Propag. Soc. Int. Symp.*, Jun. 2003, pp. 468–471.

[21] J. M. Usoff and B. A. Munk, "Edge effects of truncated periodic surfaces of thin wire elements," *IEEE Trans. Antennas Propag.*, vol. 42, no. 7, pp. 946–953, Jul. 1994.

[22] D. J. Gregoire and A. V. Kabakian, "Surface-wave waveguides," *IEEE Antennas Wireless Propag. Lett.*, vol. 10, pp. 1512–1515, 2011.

[23] E. Doumanis, G. Goussetis, J. L. Gómez-Tornero, R. Cahill, and V. Fusco, "Anisotropic impedance surfaces for linear to circular polarization conversion," *IEEE Trans. Antennas Propag.*, vol. 60, no. 1, pp. 212–219, Jan. 2012.

[24] S. Maci and P. Kildal, "Hard and soft gangbuster surface," in *Proc. Int. Symp. Electromagn. Theory (URSI EMTS)*, pp. 290–292, 2004.
[25] S. Maci, M. Caiazzo, A. Cucini, and M. Casaletti, "A pole-zero matching method for EBG surfaces composed of a dipole FSS printed on a grounded dielectric slab," *IEEE Trans. Antennas Propag.*, vol. 53, no. 1, pp. 70–81, Jan. 2005.
[26] J. A. Aas, "Plane-wave reflection properties of two artificially hard surfaces," *IEEE Trans. Antennas Propag.*, vol. 39, no. 5, pp. 651–656, May 1991.
[27] R. Yang, S. Zhang, J. Jin, C. Lu, and W. Yu, *Advanced Electromagnetic Theory*. Beijing, China: Higher Education Press, 2008, pp. 218–219.
[28] R. A. Marr, U. H. W. Lammers, T. B. Hansen, T. J. Tanigawa, and R. V. McGahan, "Bistatic RCS calculations from cylindrical near-field measurements—Part II: Experiments," *IEEE Trans. Antennas Propag.*, vol. 54, no. 12, pp. 3857–3864, Dec. 2006.
[29] T. B. Hansen, R. A. Marr, U. H. W. Lammers, T. J. Tanigawa, and R. V. McGahan, "Bistatic RCS calculations from cylindrical near-field measurements—Part I: Theory," *IEEE Trans. Antennas Propag.*, vol. 54, no. 12, pp. 3846–3856, Dec. 2006.
[30] O. M. Bucci and C. Gennarelli, "Use of sampling expansions in near-field-far-field transformation: The cylindrical case," *IEEE Trans. Antennas Propag.*, vol. 36, no. 6, pp. 830–835, Jun. 1998.
[31] A. M. Patel and A. Grbic, "The effects of spatial dispersion on power flow along a printed-circuit tensor impedance surface," *IEEE Trans. Antennas Propag.*, vol. 62, no. 3, pp. 1464–1469, Mar. 2014.
[32] S. Sun, Q. He, S. Xiao, Q. Xu, X. Li, and L. Zhou, "Gradient-index meta-surfaces as a bridge linking propagating waves and surface waves," *Nature Mater.*, vol. 11, no. 5, pp. 426–431, 2012.
[33] J. Long and D. Sievenpiper, "Low-profile and low-dispersion artificial impedance surface in the UHF band based on non-foster circuit loading," *IEEE Trans. Antennas Propag.*, vol. 64, no. 7, pp. 3003–3010, Jul. 2016.

Haijian Hou received the B.S. degree in communication engineering from Beijing Jiaotong University, Beijing, China, in 2012, where she is currently pursuing the Ph.D. degree in engineering.

Her current research interests include scattering in time domain from metamaterials, FSS, and antennas.

Jiang Long (S'11) received the B.S. and M.S. degrees from Zhejiang University, Hangzhou, China, in 2007 and 2010, respectively, and the Ph.D. degree from the University of California, San Diego, CA, USA, in 2015.

He is currently an RF Engineer with Skyworks Solution Inc., Woburn, MA, USA. His current research interests include nonfoster circuits in antenna/microwave applications, including nonfoster circuit loaded active fast-wave waveguides, broadband metasurfaces, broadband antennas, and active microwave components.

Dr. Jiang was awarded the IEEE MTT-S Graduate Fellowship in 2015.

Junhong Wang (M'02–SM'03) was born in Jiangsu, China, in 1965. He received the B.S. and M.S. degrees in electrical engineering from the University of Electronic Science and Technology of China, Chengdu, China, in 1988 and 1991, respectively, and the Ph.D. degree in electrical engineering from Southwest Jiaotong University, Chengdu, in 1994.

In 1995, he joined the Department of Electrical Engineering, Beijing Jiaotong University, Beijing, China, as a Faculty Member, where he became a Professor in 1999. From 1999 to 2000, he was a Research Associate with the Department of Electric Engineering, City University of Hong Kong, Hong Kong. From 2002 to 2003, he was a Research Scientist with the Temasek Laboratories, National University of Singapore, Singapore. He is currently with the Key Laboratory of all Optical Network and Advanced Telecommunication Network, Ministry of Education of China, Beijing Jiaotong Univeristy, and also with the Institute of Lightwave Technology, Beijing Jiaotong University. His current research interests include numerical methods, antennas, scattering, and leaky wave structures.

Daniel F. Sievenpiper (M'94–SM'04–F'09) received the B.S. and Ph.D. degrees in electrical engineering from the University of California, Los Angeles, CA, USA, in 1994 and 1999, respectively.

He was the Director of the Applied Electromagnetics Laboratory, HRL Laboratories, Malibu, CA, USA, where he was involved in artificial impedance surfaces, conformal antennas, tunable and wearable antennas, and beam steering methods. He is currently a Professor with the University of California, San Diego, CA, USA, where he is involved in antennas and electromagnetic structures. He has authored or co-authored more than 100 technical publications and holds more than 70 issued patents.

Dr. Sievenpiper was awarded the URSI Issac Koga Gold Medal in 2008. He has been an Associate Editor of the IEEE *Antennas and Wireless Propagation Letters* since 2010.

Polarization-Insensitive Holographic Surfaces With Broadside Radiation

Mei Li, *Student Member, IEEE*, Shao-Qiu Xiao, *Member, IEEE*, and Daniel F. Sievenpiper, *Fellow, IEEE*

***Abstract*— Scalar holographic surfaces (HSs) with a unique polarization-insensitive property are presented. The proposed HSs are constructed by sinusoidally modulated loop-wire unit cells, which can support both TE mode and TM mode propagation with the same phase velocity. The modulation principle in terms of refractive index is presented, which is convenient for HS designs concerning both TE and TM modes. A scalar polarization-sensitive HS using square patches exhibits a mismatch in the E- and H-plane beamwidths due to the sin (φ) circumferential illumination of the x-directed dipole, resulting in a low aperture efficiency. Two novel scalar HS designs using loop-wire configuration in square lattice and hexagonal lattice are proposed which exhibit the polarization-insensitive property with nearly circularly symmetric E- and H-plane beamwidths when illuminated by an x-directed dipole. Both simulations and measurements are carried out in this paper, which agree well with each other.**

***Index Terms*— Holographic surfaces (HSs), leaky-wave antennas, metasurfaces, modulated surfaces.**

I. Introduction

A HOLOGRAPHIC surface (HS) is a kind of modulated artificial surface based on the interference pattern between the currents generated by a source, which can be a small feed or a plane wave impinging on the surface, and the desired fields, which can be radiating leaky waves or bound surface waves [1]. HSs are usually constituted by a series of modulated conducting strips [2]–[6] or subwavelength, electrically small periodic unit cells [1]. By properly engineering the geometrical dimensions of the unit cells, the effective surface impedance can be modulated. Due to the simple manufacture process using standard printed-circuit techniques, HSs have the advantages of low cost, low profile, lightweight, and conformability, and thus have gained increasing attention in recent years.

One predominant application of HSs is holographic antennas and also known as impedance modulated surfaces, which are essentially leaky-wave antennas with radiation performance of high gain and pencil beams. In 1959, Oliner and Hessel [7] studied the propagation characteristics and field distributions of waves guided by a sinusoidally modulated reactance surface. A printed, 1-D leaky-wave antenna with a sinusoidally modulated surface reactance was designed in [5]. 2-D holographic antennas using scalar and tensor holographic artificial impedance surfaces were proposed in [1], demonstrating that a tensor impedance surface can provide control over polarization. Minatti *et al.* [8], [10], Faenzi *et al.* [9], and Pereda *et al.* [11] have done intensive study on circularly polarized holographic antennas including using scalar impedance surfaces with a spiral modulation as well as tensor impedance surfaces to properly polarize the aperture field. In [11], two synchronized modes (TE and TM modes) with the same phase velocity are generated by selecting an appropriate tensor modulated surface and an LHCP or RHCP antenna is then obtained when the circular waveguide-feed is excited with two mutually orthogonal TE_{11} modes in phase-quadrature. It is reported in [12] that by varying the relative phase of the sinusoidal modulation of the different regions of a scalar impedance HS, it is possible to obtain a desired pencil beam with a desired polarization. Besides the application of holographic antennas, HSs can also be applied to the field of surface-wave manipulation. A focusing HS, which can convert the incoming propagating waves to surface waves and then focus on a spot, is presented in [13]. This mechanism can be seen as the inverse process of a holographic antenna. HSs have also been reported to be used in the aspect of near-field focusing [14] and radar cross section reduction [15].

Scalar impedance surfaces generally support the propagation of either a TM or a TE lower order surface-wave mode at a given frequency. For a vertically polarized (TM) surface-wave excitation, for instance, a circularly symmetric E- and H-plane beamwidth can be achieved when the HS, as shown in Fig. 1, is constituted by a scalar artificial surface supporting TM surface waves (namely, TM-type HS) [10]. However, for a horizontally polarized incidence wave originating from an x- or y-directed infinitesimal electric dipole, the radiation pattern of one plane (E- or H-plane) exhibits noticeably wider beamwidth than that of the other plane (H- or E-plane), regardless of whether

Manuscript received July 27, 2016; revised September 9, 2016; accepted September 14, 2016. Date of publication October 19, 2016; date of current version December 5, 2016. This work was supported in part by AFOSR under Grant FA9550-16-1-0093, in part by the China Scholarship Council, and in part by the National High Technology Research and Development Program under Grant 2015AA7124075A.

M. Li is with the College of Communication Engineering, Chongqing University, Chongqing 400044, China, and also with the Department of Electrical and Computer Engineering, University of California at San Diego, La Jolla, CA 92093 USA (e-mail: li.mei@cqu.edu.cn).

S.-Q. Xiao is with the School of Physical Electronics, University of Electronic Science and Technology, Chengdu 610054, China (e-mail: xiaoshaoqiu@uestc.edu.cn).

D. Sievenpiper is with the Electrical and Computer Engineering Department, University of California at San Diego, La Jolla, CA 92130 USA (e-mail: dsievenpiper@eng.ucsd.edu).

Color versions of one or more of the figures in this paper are available online at http://ieeexplore.ieee.org.

Digital Object Identifier 10.1109/TAP.2016.2618853

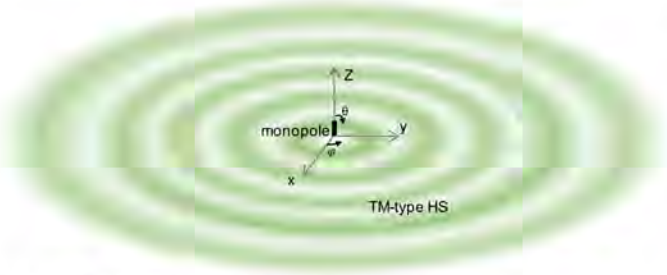

Fig. 1. TM-type HS with z-directed monopole excitation.

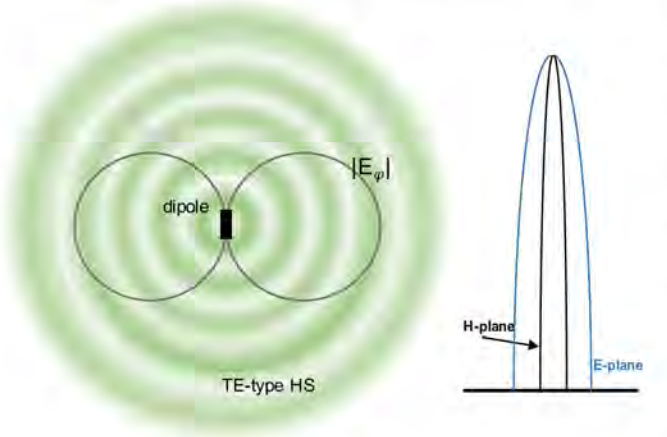

(a) (b)

Fig. 2. TE-type HS with horizontal dipole excitation. (a) Sin(φ) circumferential illumination of the HS by the x-directed electric dipole. (b) E- and H-plane radiation patterns with different beamwidths.

the HS is composed of a TM- or TE-type scalar impedance surface [3], [16]. Fig. 2 shows a sinusoidally modulated HS composing of a TE-type scalar metasurface excited by a small, x-directed electric dipole. The HS is thereby sin(φ) circumferentially illuminated by the dipole. As a result, the radiation pattern in the E-plane is much wider than that of H-plane [as shown in Fig. 2(b)], which would result in a low aperture efficiency. This part of work will be illustrated in detail in Section III. With the aid of tensor impedance surfaces, it is possible to obtain a rotationally symmetric pencil beam from a horizontal, linearly polarized excitation [11]. Instead of using tensor HSs, this paper focuses on utilizing scalar metasurfaces to realize this radiation property aiming to improve the aperture efficiency. The unit cell structure of the scalar metasurfaces is based on the polarization-insensitive, double-layered, and loop-wire configuration proposed in [17], which can support both TM and TE modes with the same phase velocity.

This paper is organized as follows. Section II presents the modulation principle of the HSs in terms of refractive index. Based on this modulation principle, a polarization-sensitive HS consisting of metallic square patches is proposed and analyzed when excited by an x-directed small electric dipole in Section III. Polarization-insensitive HS using loop-wire unit cells arranged in square lattice and hexagon lattice are proposed in Sections IV and V, respectively. The characteristics of these two HSs are investigated both by simulation and measurement. Then, conclusions are drawn in Section VI.

II. Modulation Principle of Holographic Surfaces

Instead of modulating the surface impedance to synthesize an HS, as is widely used in [1], here, the propagation constant is sinusoidally modulated by the following expression:

$$\beta = \beta_0 + m\cos\left(\frac{2\pi}{a}\rho\right) \tag{1}$$

where β_0 is average propagation constant and also represents the unperturbed value of β with $m = 0$, m is the modulation factor, a is the period of the modulation, and ρ is the radial distance from the center point in a cylindrical coordinate system.

Because of the one-to-one mapping of propagation constant values with modulated geometry, the HSs obtained by sinusoidally modulated propagation constant correspond to a sinusoidally modulated periodic surface. Based on Floquet theory, the propagation constant of a periodic structure can be written as follows:

$$\beta_{tp} = \beta_{t0} + \frac{2\pi p}{a} = \beta_0 + \Delta\beta + \frac{2\pi p}{a} \tag{2}$$

where p $(0, \pm 1, \pm 2 \ldots)$ is the index of the Floquet mode, β_{t0} is the propagation constant of the Floquet mode with an index of $p = 0$, and $\Delta\beta$ is perturbation of β caused by the non-zero modulation m. β_{t0} is close to β_0 when the modulation of the surface is small [5]. Therefore

$$\beta_{tp} \approx \beta_0 + \frac{2\pi p}{a}. \tag{3}$$

The beam direction θ_0 can be determined from

$$\sin(\theta_0) = \frac{\beta_{t(-1)}}{k_0} = \frac{\beta_0 - \frac{2\pi}{a}}{k_0}. \tag{4}$$

Considering the case of normal radiation (equally, plane waves normally illuminating the surface), there is $\theta_0 = 0°$. Therefore, it can be obtained that $a = (2\pi/\beta_0)$, and (1) can be rewritten as

$$\beta = \beta_0 + m\cos(\beta_0\rho). \tag{5}$$

Dividing k_0, i.e., the wavenumber in the free space, to both sides of the equation, we have

$$\frac{\beta}{k_0} = \frac{\beta_0}{k_0} + \left(\frac{m}{k_0}\right)\cos(\beta_0\rho). \tag{6}$$

Let $n = \beta/k_0$, $X = \beta_0/k_0$, and $M = m/k_0$. Then

$$n = X + M\cos(Xk_0\rho) \tag{7}$$

where n represents effective refractive index, X represents the average refractive index and determines the period of the modulation, and M is the modulation depth. X and M can be properly chosen in each individual HS design. Note that $X > 1$ in (7) should be met such that no other spatial harmonics radiate besides the $p = -1$ harmonic. Meanwhile, M should be small enough to be consistent with (3).

Equation (7) provides the modulation principle in terms of effective refractive index to synthesize an HS and will

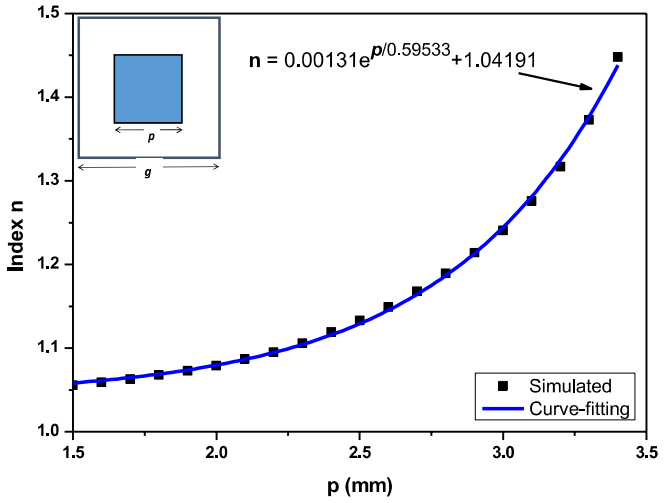

Fig. 3. Effective refractive index as a function of length p at 15 GHz. Scatters show the result of HFSS calculations, and the line is obtained by curve-fitting. The lattice constant of the unit cell is $g = 3.5$ mm.

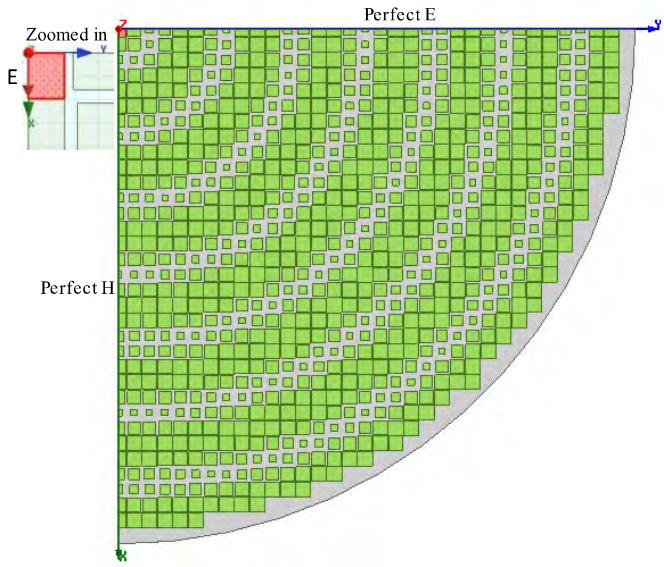

Fig. 4. Quarter of the HS in circular layout with a radius of $R = 5.87\lambda_0$, where λ_0 corresponds to the free-space wavelength at a frequency of 15 GHz. Symmetric boundaries (i.e., perfect E and perfect H) are used to simplify the simulation. A lumped port with the electric field E aligned with the x-axis (shown in the red shadow) is assigned at the center. X and M in (7) take the value 1.252 and 0.196, respectively.

be employed to synthesize all of the HS proposed in this paper. Using index instead of surface impedance to express the modulation formula offers the following convenience: On the one hand, the conventional calculation process from index to surface impedance and then to modulated geometry is simplified. Here, index is directly mapped to the modulated geometry. The need for intermediate surface impedance calculation is avoided. One the other hand, regardless of TE or TM mode, X and M in (7) stay the same so as to guarantee the phase matching of these two kinds of modes, i.e., $X_{\mathrm{TE}} = X_{\mathrm{TM}}$ and $M_{\mathrm{TE}} = M_{\mathrm{TM}}$, as demonstrated in Sections IV and V. In contrast, when the modulation principle is expressed in terms of surface impedance, the average impedance X [1] of TE and TM modes is different and so is the corresponding modulation depth M [1].

III. Polarization-Sensitive Holographic Surface Design Using Square Patches

In this section, an HS constructed by subwavelength conductive square patches is designed by using (7). Those square patches are printed on the top layer of a bare dielectric with a relative permittivity of 2.2 and thickness of 1.575 mm. It is known that arrays constructed by discrete patches without a ground plane predominantly support TE-type surface waves. Fig. 3 plots the simulated effective refractive index n as a function of the patch length $p$at a frequency of 15 GHz for a periodically infinite array. The geometry of the unit cell and nonlinear curve fit are also provided in Fig. 3. ANSYS HFSS was used for simulation in this paper.

An HS in circular layout with a radius of R is proposed in this paper. As shown in Fig. 4, a quarter of the HS with symmetric boundaries is modeled to simplify the simulation. The HS is generated using (7) with the values of $X = 1.252$ and $M = 0.196$. In order to investigate the performance of the proposed surface, a lumped port with E-field aligned with the x-axis is assigned at the center to excite the surface.

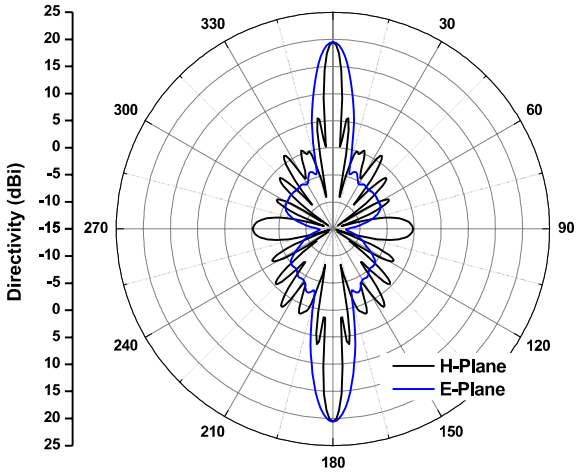

Fig. 5. Radiation patterns of the HS constituted by conductive patches. The directivity is 20.6 dBi at $\theta = 180°$ direction and 19.5 dBi at $\theta = 0°$ direction. The slight difference in directivity is due to the presence of dielectric. The return loss due to impedance mismatch is not included in the radiation patterns.

Radiation patterns and field distributions are analyzed to examine the surface performance. Fig. 5 shows the radiation patterns of the HS. As can be seen from Fig. 5, the patterns in the H- and E-plane differ greatly in beamwidth. A narrow beam is shaped in the H-plane, while a much broader beam is formed in the E-plane, which is consistent with the analysis in Fig. 2. As a result, the aperture efficiency $((D\lambda^2)/(4\pi A)$, where D is the directivity and A is the physical size of the HS) of the HS is 8.72% when considering the backward beam ($\theta = 180°$) only and 15.27% when considering both the forward ($\theta = 0°$) and backward beams.

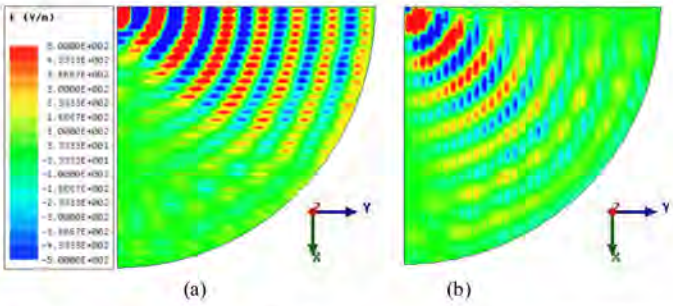

Fig. 6. Field distributions of (a) E_x component and (b) E_y component on a reference plane with a distance of 1 mm above the HS.

The field distributions of the E_x and E_y components along the HS are investigated to get a better understanding of the radiation mechanism. Assume the electric field of the excitation has the form of $E_0\vec{x}$. In the cylindrical coordinates system, there is

$$\vec{e_x} = \vec{e_\rho}\cos(\varphi) - \vec{e_\varphi}\sin(\varphi). \tag{8}$$

For a TE-type HS, only E_φ component can propagate along the HS. Therefore, the fields on the HS are as follows:

$$E_\varphi = -E_0\sin(\varphi) \text{ (as the plot shown in Fig. 2)} \tag{9a}$$

$$E_\rho = 0. \tag{9b}$$

Since

$$\vec{e_\varphi} = -\vec{e_x}\sin(\varphi) + \vec{e_y}\cos(\varphi). \tag{10}$$

Therefore, according to (9a), (9b), and (10), E_x and E_y components on the HS have the following forms:

$$E_x = -E_\varphi\sin(\varphi) = E_0\sin^2(\varphi) = \frac{E_0}{2}(1-\cos(2\varphi)) \tag{11}$$

$$E_y = E_\varphi\cos(\varphi) = -\frac{E_0}{2}\sin(2\varphi). \tag{12}$$

The field distributions of the E_x and E_y components on a reference plane with a distance of 1 mm above the HS are shown in Fig. 6. As can be seen from Fig. 6(a), E_x component is concentrated around the y-axis ($\varphi = 90°$) and is nearly zero along the x-axis ($\varphi = 0°$), which is consistent with (11). According to Fig. 6(b), the E_y component has the maximum at the $\varphi = 45°$ direction and the minimum at the $\varphi = 0°$ and $\varphi = 90°$ directions, which perfectly agree with (12).

To sum up, an x-directed dipole on a TE-type HS would result in a much wider beamwidth in the E-plane than that in the H-plane. Similarly, an x-directed dipole on a TM-type HS would result in a wider beamwidth in the H-plane compared to that in the E-plane. Therefore, it can be concluded that HSs supporting only the TM or TE mode would result in a low aperture efficiency in the cases of horizontal dipole excitation due to their polarization-sensitive property. In order to overcome this disadvantage, polarization-insensitive metasurfaces that simultaneously support both TM and TE modes are utilized to achieve a pencil beam with nearly circularly symmetric E- and H-plane beamwidths in the following sections. Other methods to improve the aperture efficiency include using tapered modulation, as reported in [18].

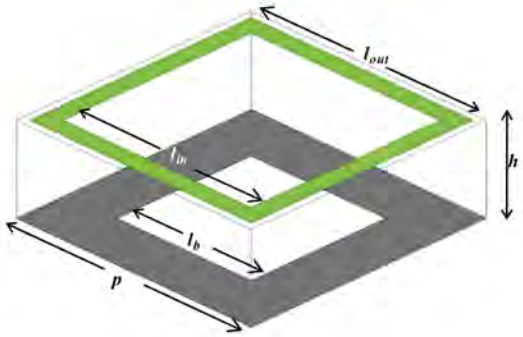

Fig. 7. Loop-wire unit cell in square lattice.

IV. Polarization-Insensitive Holographic Surface Design Using Loop-Wire Cells in Square Lattice

A. Unit Cell Design

In general, scalar metasurfaces dominantly support either the TM or TE mode at a given frequency, and limitations exist due to such polarization sensitivities. It is reported in [17] that surface waveguides composed of two frequency-selective surfaces (FSSs) layers whose dominant modes are TE and TM, respectively, can be designed to exhibit the property of supporting both TE and TM modes with the same phase velocity at a given frequency. Specifically, a square loop-wire configuration, as shown in Fig. 7, can achieve such polarization-insensitive property. A conductive square loop and a conductive wire-grid are printed at the top and bottom layer of a dielectric with a thickness of $h = 1.575$ mm and relative permittivity of $\varepsilon_r = 2.2$. The square lattice constant of the unit cell is $p = 3.5$ mm. The outer edge length of the square ring is kept as a constant of $l_{\text{out}} = 3.3$ mm. The lengths of the inner edges of the square loop and the wire-grid are l_{in} and l_b, respectively.

The square loop-wire unit cells with the same dimensions as shown in Fig. 7 are utilized to synthesize the polarization-insensitive HS. In order to enable the phase matching of TE and TM modes, it is necessary to guarantee that propagation constants of TE and TM modes are the same. The modulation principle of such an HS becomes

$$n_{\text{TE}} = n_{\text{TM}} = X + M\cos(Xk_0\rho). \tag{13}$$

The next step is to determine the effective refractive index as a function of the geometric parameters of the unit cell. Note that, compared to a purely TE- or TM-type HS as that in Section III, one additional requirement needs to be met: the dispersion curves of the TE and TM modes must overlap at the HS operation frequency, satisfying $n_{\text{TE}} = n_{\text{TM}}$. By properly choosing the values of l_{in} and l_b, the refractive index of TE and TM modes can be tuned simultaneously, as shown in Fig. 8. For illustration, Fig. 8 plots indexes versus frequency for three particular sets of (l_{in}, l_b) values, where green points show the desired indexes satisfying $n_{\text{TE}} = n_{\text{TM}}$ at the operation frequency. In the same manner, we can obtain a series of indexes and the corresponding (l_{in}, l_b) values, which will be used to calculate the index functions versus geometric

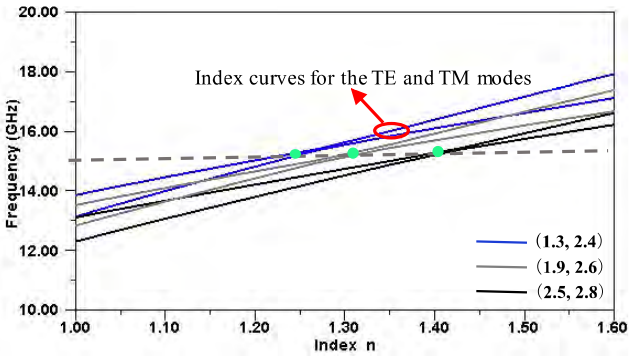

Fig. 8. Indexes versus frequency for three different sets of (l_{in}, l_b). For each set, the two curves show the index overlap of the TE and TM modes. The operation frequency of the HS is 15 GHz. Three green points indicate the desired indexes satisfying $n_{\mathrm{TE}} = n_{\mathrm{TM}}$ at the operation frequency.

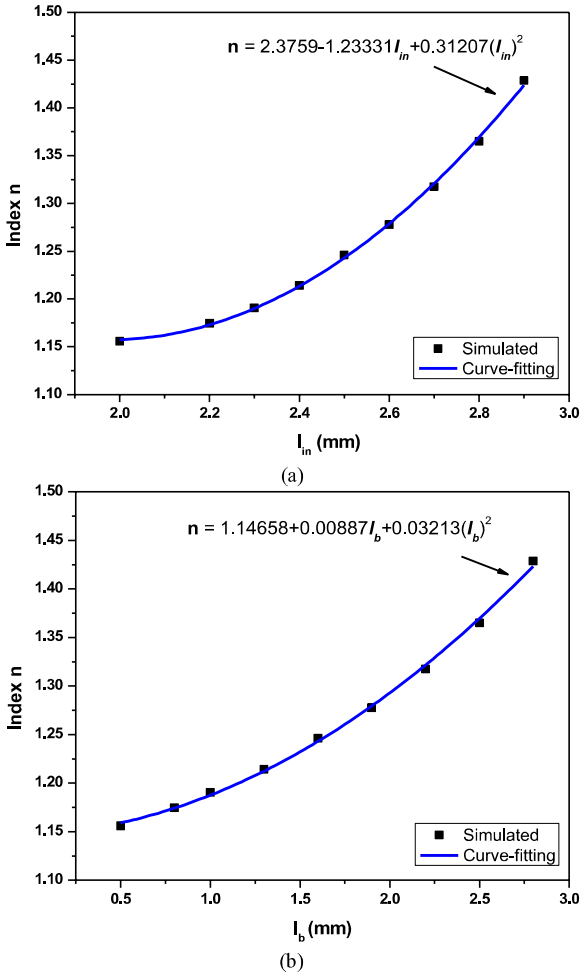

Fig. 9. Index versus lengths (a) l_{in} and (b) l_b of the loop-wire unit cell in square lattice.

parameters, as will be shown in Fig. 9. It is worth noting that, l_{in} and l_b have a dominant effect on the dispersion curves of the TE mode and TM mode, respectively, which is intuitive because the loop FSS dominantly supports the TE mode and wire-grid FSS dominantly supports the TM mode.

The index n, i.e., $n = n_{\mathrm{TE}} = n_{\mathrm{TM}}$, as a function of l_{in} and l_b at a frequency of 15 GHz is given

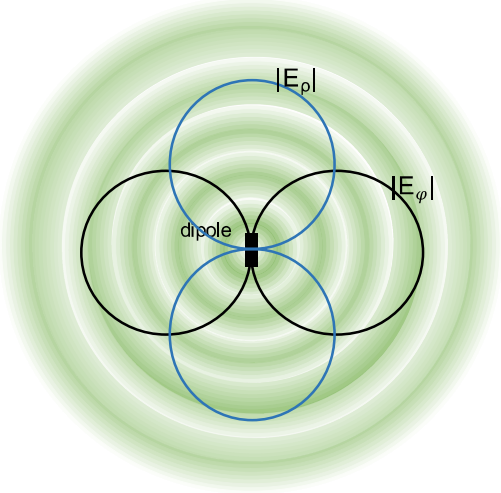

Fig. 10. Circumferential illumination of an HS by the x-directed electric dipole. The HS supports both TE and TM modes.

in Fig. 9(a) and (b), respectively. The scatter points are obtained from HFSS simulations by the same way as shown in Fig. 8, and the blue curves are obtained by nonlinear curve fit. For a given index, the values of l_{in} and l_b can be uniquely determined by solving these two fitting functions. Therefore, both layers are sinusoidally modulated for each HS constituted by this type of unit cells.

B. Holographic Surface Design

The field distributions on a polarization-insensitive HS excited by a small x-directed electric dipole are shown in Fig. 10. Because the HS can support both TE and TM modes, both E_ρ and E_φ can propagate on the surface. Assume the excitation of the x-directed dipole has the same expression as that in Section III, i.e., $E_0\vec{x}$. According to (8)

$$E_\rho = E_0\cos(\varphi) \quad \text{and} \quad E_\varphi = -E_0\sin(\varphi). \tag{14}$$

Fig. 10 shows the field distributions of E_ρ and E_φ on the HS structure. As a result, circularly symmetric E- and H-plane beamwidths can be achieved because the amplitude of the circumferential illumination of the dipole is constant.

A sinusoidally modulated HS constituted by loop-wire unit cells is designed by using function (13) with $X = 1.3$ and $M = 0.13$. A quarter of the HS in square lattice is shown in Fig. 11. Symmetric boundaries are used to simplify the simulation. As shown in Fig. 11, both the top layer (loops) and the bottom layer (grid-wires) are sinusoidally modulated. The HS works at a frequency of 15 GHz. The radius of the simulated HS is $R = 6\lambda_0$ (λ_0 is the free-space wavelength at 15 GHz.). To examine the electromagnetic properties of the proposed HS, a lumped port with polarization aligned with the x-axis is assigned at the center of the bottom layer of the HS structure.

The performance of the proposed HS is examined by HFSS simulations. Fig. 12 shows the radiation patterns of the proposed HS. As can be seen from Fig. 12, the E- and H-plane patterns are nearly the same, especially for the forward

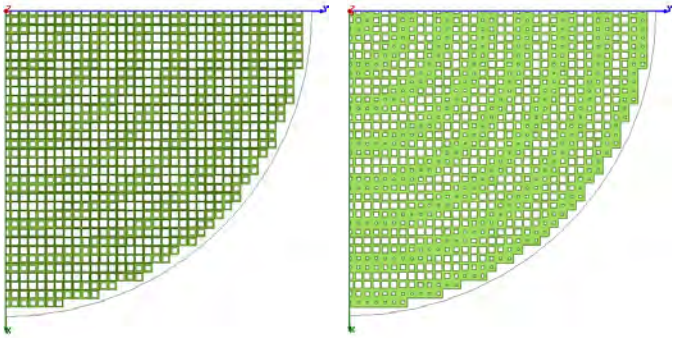

(a) (b)

Fig. 11. Quarter of the modulated HS composed of loop-wire unit cells in square lattice. (a) Top layer pattern. (b) Bottom layer pattern. Symmetric boundaries are used to simplify the simulation. X and M in (13) are 1.3 and 0.13, respectively.

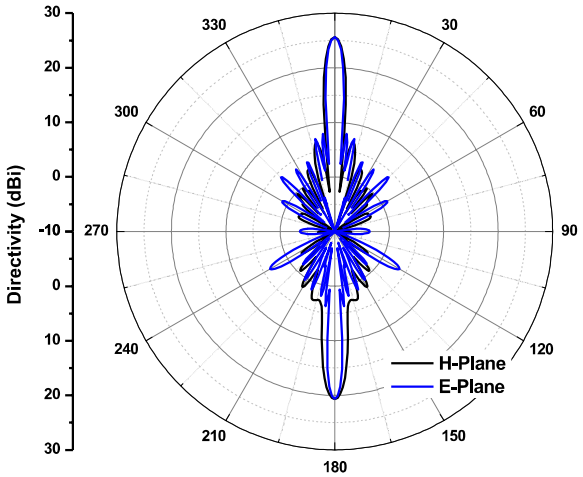

Fig. 12. Simulated radiation patterns with a maximum directivity of 25.6 dBi at $\theta = 0°$ direction and 20.7 dBi at $\theta = 180°$ direction. The return loss due to impedance mismatch is not included in the radiation patterns.

beam ($\theta = 0°$). However, for the backward beam ($\theta = 180°$), the beamwidth in the H-plane is noticeably wide compared to that in the E-plane. This is due to the lumped port excitation, which is directly attached to bottom layer, i.e., the wire-grid layer. As is mentioned before, the wire-grid layer would have a strong effect on the TM mode and therefore, for the backward beam, the beamwidth of the H-plane pattern is wider than that of the E-plane pattern. In the whole, such a pencil beam demonstrates that a rotationally symmetric E- and H-plane beamwidth can be achieved when the HS can support both TE and TM modes simultaneously. Therefore, a high aperture efficiency can be predicted. In fact, the aperture efficiency is 25.5% when considering the forward beam only and 33.7% when including both the forward and the backward beams, which demonstrates a great improvement compared with the aperture efficiency reported in Section III.

The field distributions of E_x and E_y components of an HS supporting both TE and TM modes can be derived as follows.

Since

$$\vec{e_\rho} = \vec{e_x}\cos(\varphi) + \vec{e_y}\sin(\varphi). \tag{15}$$

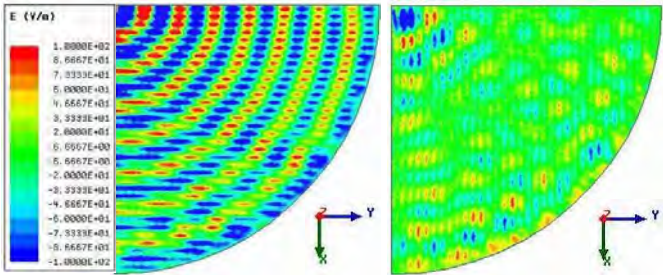

(a) (b)

Fig. 13. Field distributions of (a) E_x and (b) E_y components at a distance of 1 mm above the surface.

According to (10), (14), and (15), the E_x and E_y components on the HS structure have the following forms:

$$E_x = -E_\varphi \sin(\varphi) + E_\rho \cos(\varphi) = E_0 \tag{16}$$

$$E_y = E_\varphi cos(\varphi) + E_\rho \sin(\varphi) = 0. \tag{17}$$

Expressions (16) and (17) manifest that the E_x component remains constant at the HS surface with the same magnitude as the excitation and is independent of the azimuthal angle φ, while the E_y component is always zero.

Fig. 13 plots the field distributions of E_x and E_y components on a reference plane at a distance of 1 mm above the HS. As can be seen from Fig. 13(a), contrasting with those in Fig. 6(a), the E_x component is distributed along the whole surface, as is consistent with (16). Meanwhile, the E_y component is very weak over the whole surface, which agrees well with (17). Therefore, for the proposed polarization-insensitive HS, an x-directed dipole can fully illuminate the HS, which contributes to its high aperture efficiency.

Fabrication and measurements are carried out to verify the simulations. In simulation, the HS is excited by a lumped port. Similarly, in experiment, the HS is excited by an SMA probe with the inner conductor soldered to one edge of the wire-grid (bottom layer) and the outer conductor soldered to the other edge of the wire-grid along the x-axis. Fig. 14 shows the measured radiation patterns, which agree well with those in Fig. 12. The fabricated HS panel is also provided in Fig. 14. As can be seen from Fig. 14, the beamwidths in the E- and H-plane are nearly the same. Compared with simulation, a slightly higher side lobe level appears around θ from 90° to 120° due to the SMA probe feed on the bottom layer.

V. Polarization-Insensitive Holographic Surface Design Using Loop-Wire Cells in Hexagonal Lattice

A. Unit Cell Design

Square and hexagonal lattices are two commonly seen lattice types. The effects of these two lattice types on dispersion curves have been investigated by using the loop-wire configuration in [17], which demonstrates that surface waveguides with a hexagonal lattice exhibit better performance in the aspect of dispersion isotropy than those with a square lattice. In this section, an HS using hexagonal loop-wire unit cells, which can support both TE and TM modes propagation, is

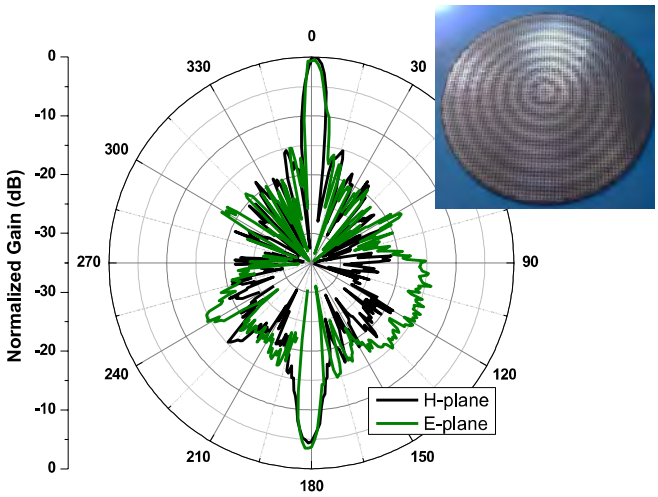

Fig. 14. Fabricated HS panel and its measured radiation patterns.

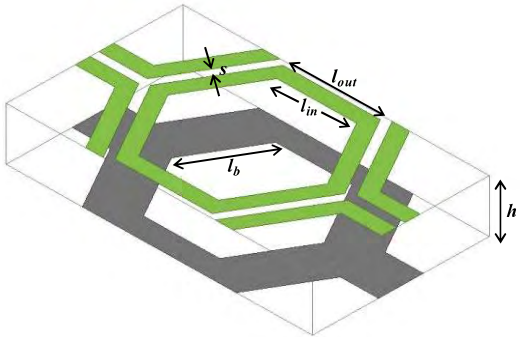

Fig. 15. Loop-wire unit supercell in hexagonal lattice.

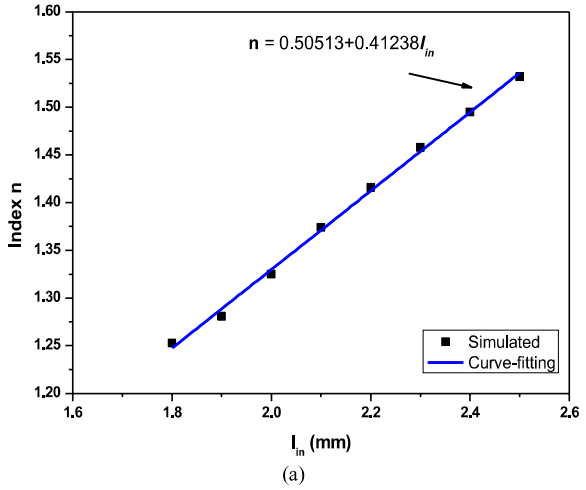

(a)

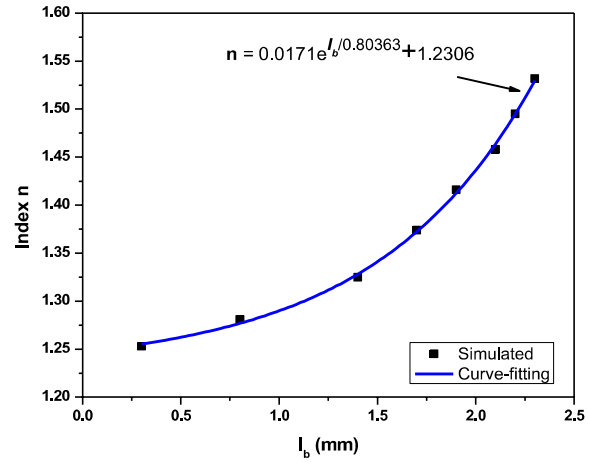

(b)

Fig. 16. Index versus lengths (a) l_{in} and (b) l_b of the loop-wire unit cell in hexagonal lattice at a frequency of 13.5 GHz.

proposed following the same design procedure as that in Section IV. For the sake of calculation, as shown in Fig. 15, a rectangular unit supercell instead of a hexagonal one is chosen for simulation. As shown in Fig. 15, a rectangular supercell consisted of hexagonal unit cells in terms of discrete loop-FSS for the top layer and continuous wire-FSS for the bottom layer is presented. A conductive hexagonal loop and a conductive wire-grid are printed at the top and bottom layer of a dielectric with a thickness of $h = 1.575$ mm and relative dielectric constant of $\varepsilon_r = 2.2$. The outer edge length of the square ring is kept as a constant of $l_{\text{out}} = 2.8$ mm. The lengths of the inner edges of the square loop and the wire-grid are l_{in} and l_b, respectively. The gap between two adjacent loops is $s = 0.25$ mm.

Next, the relationship between index and geometric parameters of the hexagonal loop-wire unit cell needs to be determined. The index of the TE mode and the TM mode can be tuned simultaneously (i.e., $n_{\text{TE}} = n_{\text{TM}}$) when lengths l_{in} and l_b are properly chosen. The index n ($n = n_{\text{TE}} = n_{\text{TM}}$) versus lengths l_{in} and l_b at a frequency of 13.5 GHz is given in Fig. 16(a) and (b), respectively, where the points are obtained from HFSS simulations and blue curves are obtained by curve fitting.

B. Holographic Surface Design

An HS in hexagonal lattice is designed using the hexagonal unit cells presented in Fig. 15 in this section. It is worth mentioning that the working principle of this HS is the same as that of the square lattice, which is analyzed in Section IV. Due to the loop-wire configuration, both of them are able to support both TE and TM modes at the operation frequency, and therefore pencil beams with circularly symmetric beamwidth in both the E- and H-plane can be obtained. In this section, the detailed analysis of the proposed HS is omitted for concision. The proposed HS, as shown in Fig. 17, is generated by using function (13) with $X = 1.41$ and $M = 0.13$. A lumped port at the bottom layer with polarization aligned with x-direction is used to illuminate the surface. The HS works at a frequency of 13.5 GHz. The radius of the simulated HS is $R = 5.59\lambda_0$ (λ_0 is the free-space wavelength at 13.5 GHz).

The simulated radiation performance is shown in Fig. 18. As can be seen in Fig. 18, a pencil beam is achieved both in the E- and H-plane. Especially for the forward beam ($\theta = 0°$), the beamwidths of the patterns in both planes are nearly the same. Due to the bottom-layer excitation, the beamwidth of the H-plane is slightly larger than that in the E-plane for

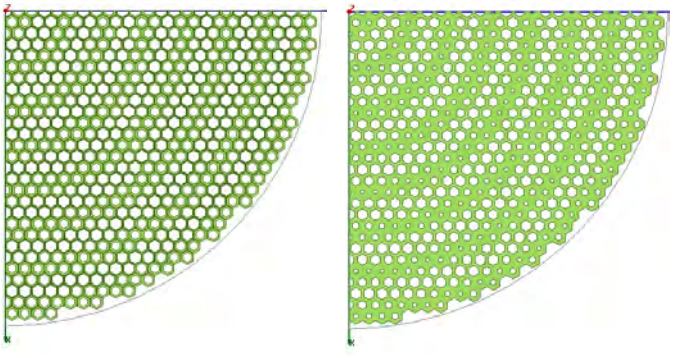

(a) (b)

Fig. 17. Quarter of the proposed HS with symmetric boundaries in hexagonal lattice. (a) Top layer pattern. (b) Bottom layer pattern. X and M in (13) are 1.41 and 0.13, respectively.

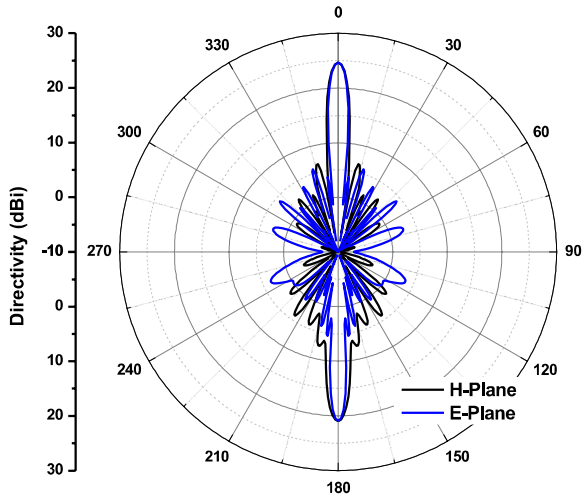

Fig. 18. Simulated radiation patterns with a maximum directivity of 24.7 dBi at $\theta = 0°$ direction and 20.9 dBi at $\theta = 180°$ direction. The return loss due to impedance mismatch is not included in the radiation patterns.

the backward beam ($\theta = 180°$). The same phenomenon can be found in Fig. 12. The corresponding aperture efficiency of the proposed HS is 23.8% when considering the forward beam only and 33.9% when considering both the forward beam and the backward beam. Almost the same aperture efficiencies are achieved for the HS in square lattice and that in hexagonal lattice. Therefore, both polarization-insensitive HS designs using loop-wire configuration in square and hexagonal lattice exhibit pencil beams and improved aperture efficiencies compared with a traditional scalar HS which has the drawback of polarization sensitivity.

Fig. 19 shows the fabricated panel of the proposed HS as well as the measured radiation patterns. As can be seen from Fig. 19, a narrow pencil beam is formed in the broadside direction. Compared with the simulated results, the beamwidth in the H-plane is slightly wider because of the errors resulting from the measurement setup and fabrication. Compared with simulations, a noticeably higher sidelobe appears in the lower hemisphere due to the SMA probe excitation, which is directly soldered to the center wire-grid cell on the bottom layer.

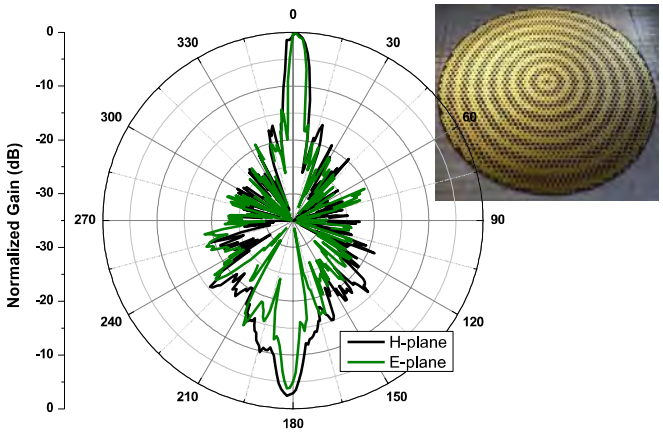

Fig. 19. Fabrication HS panel in hexagonal lattice and measured radiation patterns.

In the whole, the measurements agree well with the simulations.

VI. Conclusion

Traditional scalar HSs are able to support a TE or TM lower order Floquet mode, and have the drawback of polarization sensitivity, which results in a mismatch between the E- and H-plane beamwidths when excited by a horizontal dipole, and thus a low aperture efficiency. In this paper, loop-wire unit cells, which can support both TE and TM modes with the same phase velocity are utilized to design polarization-insensitive HSs. Instead of modulating the surface impedance to synthesize an HS, the refractive index is sinusoidally modulated in this paper, which provides convenience to the design of HSs for simultaneous TE and TM modes. Two HS designs using square and hexagonal loop-wire cells are proposed and experimentally studied to validate the characteristics of polarization insensitivity. Simulation and measurements show that pencil beams are achieved in the E- and H-plane of these two HS. This demonstrates that the proposed HS are insensitive to the polarization of coming waves and able to support both TE and TM modes. This kind of HS has the potential to be used in applications such as energy scavenging, because they can focus incoming waves to the center point of the antenna regardless of their polarization.

Acknowledgment

The authors would like to thank R. Quarfoth, the researcher at HRL Laboratories, and A. Li at UCSD for contributions during the work.

References

[1] B. H. Fong, J. S. Colburn, J. J. Ottusch, J. L. Visher, and D. F. Sievenpiper, "Scalar and tensor holographic artificial impedance surfaces," *IEEE Trans. Antennas Propag.*, vol. 58, no. 10, pp. 3212–3221, Oct. 2010.

[2] F. Caminita, M. Nannetti, and S. Maci, "Holographic surfaces realized by curvilinear strip gratings," in *Proc. 2nd Eur. Conf. Antennas Propag. (EuCAP)*, Nov. 2007, pp. 1–4.

[3] C. Rusch, J. Schäfer, H. Gulan, P. Pahl, and T. Zwick, "Holographic mmW-antennas with TE_0 and TM_0 surface wave launchers for frequency-scanning FMCW-radars," *IEEE Trans. Antennas Propag.*, vol. 63, no. 4, pp. 1603–1613, Apr. 2015.
[4] T. Su, Q. Zhang, R. Chen, and C. Sun, "Novel design of surface-wave holographic antenna miniaturization," *IEEE Antennas Wireless Propag. Lett.*, vol. 14, pp. 1077–1080, 2015.
[5] A. M. Patel and A. Grbic, "A printed leaky-wave antenna based on a sinusoidally-modulated reactance surface," *IEEE Trans. Antennas Propag.*, vol. 59, no. 6, pp. 2087–2096, Jun. 2011.
[6] S. K. Podilchak, L. Matekovits, A. P. Freundorfer, Y. M. M. Antar, and M. Orefice, "Controlled leaky-wave radiation from a planar configuration of width-modulated microstrip lines," *IEEE Trans. Antennas Propag.*, vol. 61, no. 10, pp. 4957–4972, Oct. 2013.
[7] A. A. Oliner and A. Hessel, "Guided waves on sinusoidally-modulated reactance surfaces," *IRE Trans. Antennas Propag.*, vol. 7, no. 5, pp. 201–208, Dec. 1959.
[8] G. Minatti, F. Caminita, M. Casaletti, and S. Maci, "Spiral leaky-wave antennas based on modulated surface impedance," *IEEE Trans. Antennas Propag.*, vol. 59, no. 12, pp. 4436–4444, Dec. 2011.
[9] M. Faenzi *et al.*, "Realization and measurement of broadside beam modulated metasurface antennas," *IEEE Antennas Wireless Propag. Lett.*, vol. 15, pp. 610–613, 2016.
[10] G. Minatti *et al.*, "Modulated metasurface antennas for space: Synthesis, analysis and realizations," *IEEE Trans. Antennas Propag.*, vol. 63, no. 4, pp. 1288–1300, Apr. 2015.
[11] A. T. Pereda *et al.*, "Dual circularly polarized broadside beam metasurface antenna," *IEEE Trans. Antennas Propag.*, vol. 64, no. 7, pp. 2944–2953, Jul. 2016.
[12] S. Pandi, C. A. Balanis, and C. R. Birtcher, "Design of scalar impedance holographic metasurfaces for antenna beam formation with desired polarization," *IEEE Trans. Antennas Propag.*, vol. 63, no. 7, pp. 3016–3024, Jul. 2015.
[13] X. Wan, Y. B. Li, B. G. Cai, and T. J. Cui, "Simultaneous controls of surface waves and propagating waves by metasurfaces," *Appl. Phys. Lett.*, vol. 105, no. 12, pp. 121603:1–121603:5, 2014.
[14] J. L. Gómez-Tornero, D. Blanco, E. Rajo-Iglesias, and N. Llombart, "Holographic surface leaky-wave lenses with circularly-polarized focused near-fields—Part I: Concept, design and analysis theory," *IEEE Trans. Antennas Propag.*, vol. 61, no. 7, pp. 3475–3485, Jul. 2013.
[15] Y. Liu, Y. Hao, K. Li, and S. Gong, "Wideband and polarization-independent radar cross section reduction using holographic metasurface," *IEEE Antennas Wireless Propag. Lett.*, vol. 15, pp. 1028–1031, Oct. 2015.
[16] A. Sutinjo, M. Okoniewski, and R. H. Johnston, "A holographic antenna approach for surface wave control in microstrip antenna applications," *IEEE Trans. Antennas Propag.*, vol. 58, no. 3, pp. 675–682, Mar. 2010.
[17] M. Li, S. Xiao, J. Long, and D. F. Sievenpiper, "Surface waveguides supporting both TM mode and TE mode with the same phase velocity," *IEEE Trans. Antennas Propag.*, vol. 64, no. 9, pp. 3811–3819, Sep. 2016.
[18] J. S. Colbum, D. F. Sievenpiper, B. H. Fong, J. J. Ottusch, J. L. Visher, and P. R. Herz, "Advances in artificial impedance surface conformal antennas," in *Proc. IEEE Antennas Propag. Soc. Int. Symp.*, Jun. 2007, pp. 3820–3823.

Mei Li (S'15-M'16) received the B.S. degree in electronic information science and technology from the Chengdu University of Information Technology, Chengdu, China, in 2010, and the Ph.D. degree in radio physics from the University of Electronic Science and Technology of China, Chengdu, in 2016.

From 2014 to 2016, she was with the Applied Electromagnetics Research Group, University of California at San Diego, San Diego, CA, USA, as a Visiting Graduate. Her current research interests include reconfigurable antennas, phased arrays, artificial electromagnetic structures, and holographic metasurfaces.

Shao-Qiu Xiao (M'05) received the Ph.D. degree in electromagnetic field and microwave engineering from the University of Electronic Science and Technology of China (UESTC), Chengdu, China, in 2003.

In 2004, he joined UESTC as an Assistant Professor. From 2004 to 2006, he was with the Wireless Communications Laboratory, National Institute of Information and Communications Technology, Tokyo, Japan, as a Researcher focusing on the planar antenna and smart antenna design and optimization. From 2006 to 2010, he was with UESTC as an Associate Professor, and is currently a Professor. He has authored or co-authored more than 160 technical journals, conference papers, books, and book chapters. His current research interests include planar antenna and phased array, microwave passive circuits, and time reversal electromagnetics.

Daniel F. Sievenpiper (M'94–SM'04–F'09) received the B.S. and Ph.D. degrees in electrical engineering from the University of California at Los Angeles, Los Angeles, CA, USA, in 1994 and 1999, respectively.

He was the Director of the Applied Electromagnetics Laboratory at HRL Laboratories, Malibu, CA, USA. He is currently a Professor with the University of California at San Diego, San Diego, CA, USA. He holds more than 70 issued patents and has authored 80 technical publications. His research interests included artificial impedance surfaces, conformal antennas, tunable and wearable antennas, and beam steering methods. His current research interests include antennas and electromagnetic structures.

Dr. Sievenpiper was a recipient of the URSI Issac Koga Gold Medal, in 2008. Since 2010, he has been an Associate Editor of the *IEEE Antennas and Wireless Propagation Letters*.

Patterning Technique for Generating Arbitrary Anisotropic Impedance Surfaces

Jiyeon Lee, *Student Member, IEEE*, and Daniel F. Sievenpiper, *Fellow, IEEE*

***Abstract*— Anisotropic impedance surfaces have been demonstrated to be useful for a variety of applications ranging from antennas, to surface wave guiding, to control of scattering. To increase their anisotropy requires elongated unit cells which have reduced symmetry and thus are not easily arranged into arbitrary patterns. We discuss the limitations of existing patterning techniques, and explore options for generating anisotropic impedance surfaces with arbitrary spatial variation. We present an approach that allows a wide range of anisotropic impedance profiles, based on a point-shifting method combined with a Voronoi cell generation technique. This approach can be used to produce patterns which include highly elongated cells with varying orientation, and cells which can smoothly transition between square, rectangular, hexagonal, and other shapes with a wide range of aspect ratios. We demonstrate a practical implementation of this technique which allows us to define gaps between the cells to generate impedance surfaces, and we use it to implement a simple example of a structure which requires smoothly varying impedance, in the form of a planar Luneberg lens. Simulations of the lens are verified by measurements, validating our pattern generation technique.**

***Index Terms*— Anisotropic surface, artificial material, luneberg lens, metasurface, patterning, surface impedance, surface waves.**

I. Introduction

An ARTIFICIAL impedance surface is a metasurface which is fabricated with periodic metallic patches on a grounded dielectric substrate. It has been used for various applications including control of surface waves [1], [2], scattering [3], conformal antennas [4], and waveguides [5]–[7]. Their electromagnetic properties are defined by the thickness of the substrate, and the capacitance between patches, which together determine the effective surface impedance. Varying the cell size and shape allows the impedance to be controlled. Vertical conducting vias are sometimes also used, but they are only necessary if very high impedance values are needed, or to completely block surface waves [8]. Initial impedance surfaces consisted of simple square or hexagonal cells. However, reducing the symmetry of the cells allows the surface to have anisotropic impedance properties. This is important for applications such as surface wave cloaking, interference reduction between RF apertures, control over polarization, and conversion between transverse magnetic (TM) and transverse electric surface waves.

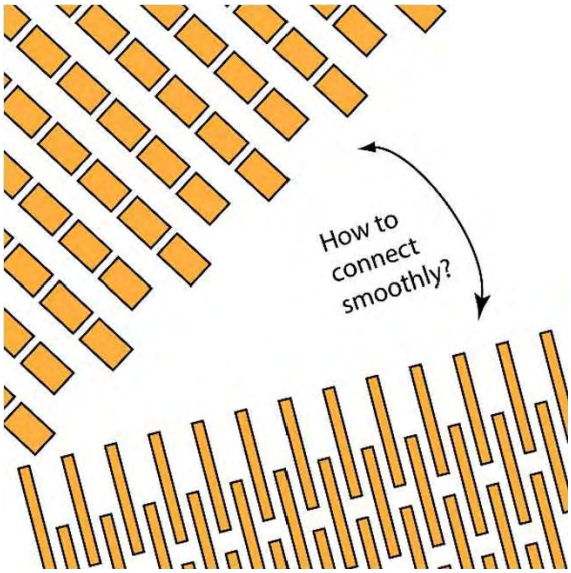

Fig. 1. Primary challenge in current artificial impedance surface research is how to pattern impedance surfaces to produce arbitrary impedance profiles when the surface is highly anisotropic or has impedance that varies dramatically with position.

Until recently it was not possible to create smoothly varying, highly anisotropic impedance functions because of the difficulty of patterning regions in which the cell size, shape, and orientation varied. Illustrated in Fig. 1, there was no available method to smoothly connect these regions with different impedance values and with different primary directions, aside from drawing each cell manually, which is impractical. The challenge is how to pattern elongated unit cells which allow high anisotropy, but to also create arbitrary and smoothly varying impedance patterns. All previous work in this area used discrete regions of different impedance values or directions [3], [5].

Several existing approaches to patterning anisotropic surfaces can be found in the literature, and examples are shown in Fig. 2. The first anisotropic impedance surface [9] shown in Fig. 2(a) used slices in a lattice of square patches, that are rotated to an arbitrary angle. For example, if the slices are oriented along the y-direction, the structure has twice as many capacitive gaps along x as along y, due to the extra capacitance of the slice. Thus, the maximum anisotropy of

Manuscript received August 3, 2015; revised April 24, 2016; accepted July 6, 2016. Date of publication September 13, 2016; date of current version October 27, 2016. This work was supported by the Air Force Office of Scientific Research under Grant FA9550-16-1-0093.

The authors are with the University of California at San Diego, La Jolla, CA 92093-0407 USA (e-mail: y0l001@ucsd.edu).

Color versions of one or more of the figures in this paper are available online at http://ieeexplore.ieee.org.

Digital Object Identifier 10.1109/TAP.2016.2608935

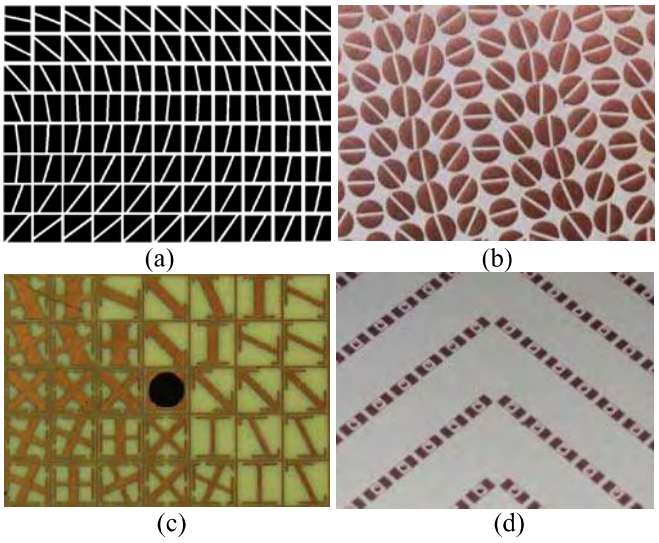

Fig. 2. Examples of anisotropic surfaces include (a) square or (b) circular patches with slices rotated to an arbitrary angle, or (c) other patterns confined to a square lattice, as well as (d) lower symmetry cells that cannot be arranged into arbitrary patterns.

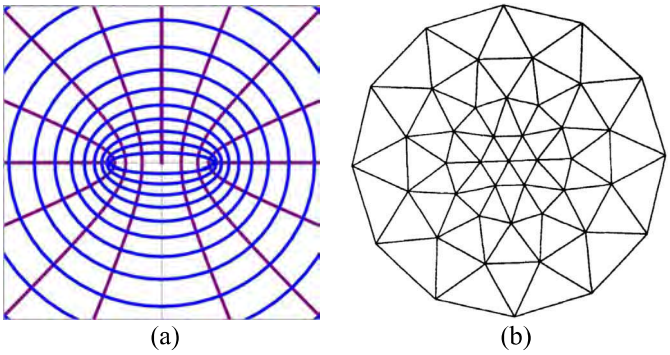

Fig. 3. Other possible approaches to patterning smoothly varying impedance surfaces include (a) conformal mapping and (b) mesh generation techniques. Neither of these produces anisotropic impedance surfaces with the properties needed for applications.

such a structure is roughly 2:1. A structure based on circular patches [10] shown in Fig. 2(b) is similar and suffers from the same limitation. In Fig. 2(c), the structure [11] involved capacitive regions connected by inductive bars that are rotated to arbitrary angles. If the angle of rotation varies too rapidly between adjacent cells, the capacitive regions do not line up. It is also limited by the use of a square grid. Fig. 2(d) shows that elongated unit cells [3] can provide a high range of anisotropy, however, these require a rectangular grid. Any design that reduces symmetry of the lattice itself cannot be patterned to include an arbitrarily varying angle of anisotropy.

Other approaches exist for creating smoothly varying and arbitrary geometrical patterns, however, they do not have the required properties for artificial impedance surfaces. Conformal mapping [12], [13], illustrated in Fig. 3(a) is one option which is commonly used for defining effective permeability or permittivity in transformation optics applications [14]. It could potentially be applied to generating cells for impedance surfaces. However, it has the limitation that the cell size, shape, and orientation would be highly dependent on the divergence of the local impedance function. As illustrated in Fig. 3(a), as the lines diverge, the cells get larger in the direction perpendicular to the lines, which also sets their orientation. This is true of any patterning technique that relies on defining cell boundaries by continuous lines. Thus, while conformal mapping is useful for determining impedance profiles to achieve certain functional properties, it is not appropriate for defining the unit cells to create those impedance profiles. Our approach to be described below provides more freedom in defining impedance surfaces that have dramatic changes in impedance over short distances.

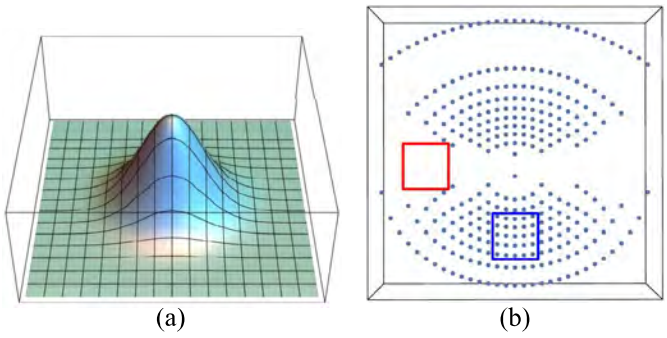

Fig. 4. Another method called the point density approach involves choosing points with a density based on (a) function whose slope represents the local impedance function. (b) Resulting set of points represents the centers of the cells, but their location depends on the path over which one traverses the original function. Discrepancies are indicated at the red and blue squares.

Mesh generation techniques have been developed for physical modeling codes for many years, and typically produce patterns such as shown in Fig. 3(b) [15]. These could potentially be applied to patterning impedance surfaces as well. However, they are generally designed to provide a specific average cell density, without concern for the details of the cell shape. For impedance surfaces the cell shape is very important for determining the anisotropic impedance values.

We explored another option that we called the point density method as illustrated in Fig. 4. The idea is to start with a function in Fig. 4(a), the slope of which represents the local impedance. By traversing that function, we can define a point which represents the center of a unit cell each time the function reaches an integer value, or at some other uniform interval of z-axis and another axis among x- and y-axis. The problem with this approach is that it is highly dependent on the path over which one traverses the function. As shown in Fig. 4(b) it does not produce a unique set of unit cells. This is one example of many path-dependent approaches that we determined were unable to produce patterns which required properties for impedance surfaces.

In this paper, we introduce a new patterning technique based on a point shifting method with cells defined using the Voronoi technique. In Section II, we describe the details of how the method is implemented, and illustrate the range of patterns that can be created. In Section III, we demonstrate that it can produce useful structures by building an example of a smoothly varying impedance function, in the form of a well-known planar Luneburg lens [16]–[18]. Measurements show

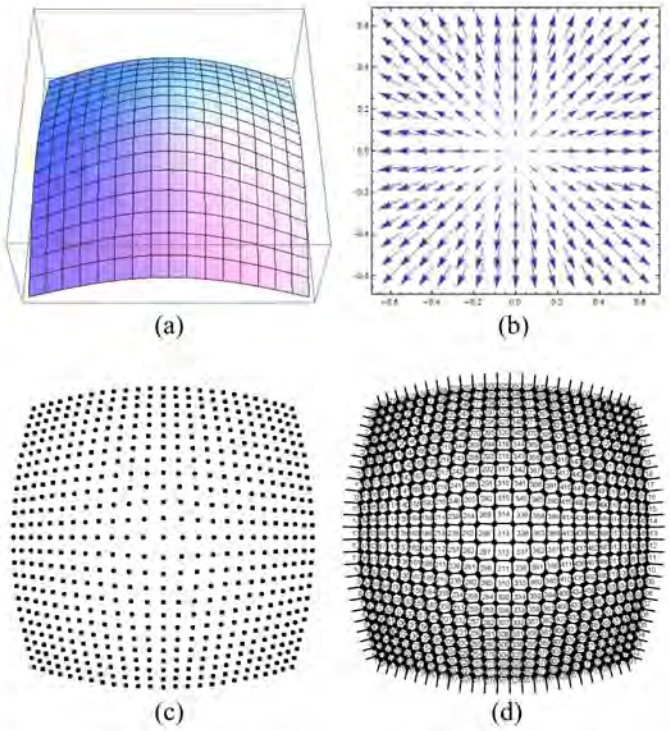

Fig. 5. (a) Starting function with a local maximum. (b) Set of gradient vectors which define the movement of points. (c) Final set of points. (d) Unit cells generated by the Voronoi method.

that the field profile matches the simulations, verifying that this method produces the intended impedance profile.

II. Patterning Process

We developed a patterning technique to produce arbitrary anisotropic surfaces which we call the point shifting method. For our patterning method, we define a function that is related to the desired surface impedance in each direction, which is related to the cell size in that direction. We currently choose this starting function based on knowledge of the desired cell profile. We then define a uniform grid of points with a period equal to the average cell size. Next, we shift each point in proportion to the gradient vector of the starting function. This is illustrated in Fig. 5(a) which shows a function with a local maximum, and in Fig. 5(b) which shows each point moving with a direction and magnitude that is in proportion to its gradient vector. The result is that the distance between neighboring points is expanded near local maxima, and compressed near local minima. In regions with constant slope, the points all shift by the same amount, resulting in no change in the distance between them. Fig. 5(c) shows the final lattice of points for this example. Anisotropic cells are created by compressing or stretching the distance between points in one direction relative to the other. Thus, the anisotropy in the final lattice of points is defined by the anisotropy of the curvature in the starting function. The cells are generated from the grid of points using a Voronoi technique, as shown in Fig. 5(d).

A Voronoi diagram is an approach for dividing regions based on a set of points and the Euclidean distance between those points [19]. To create a 2-D Voronoi diagram, one draws

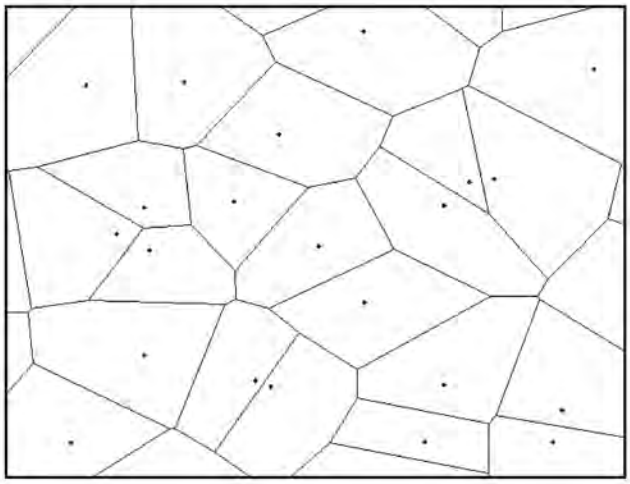

Fig. 6. Voronoi diagram for a random set of points. Each cell is defined as the region that is closer to each point than to any of its neighbors.

a midline between each pair of neighboring points, which is perpendicular to a line drawn from one point to the other. For each point, the collection of midlines to each of its neighbors defines the cell associated with that point. This is the same method used to define Brillouin zones for crystals [20]. Fig. 6 shows an example of Voronoi diagram for a random set of points. The Voronoi function is available in codes such as Mathematica and MATLAB.

The relationship between the properties of the Voronoi cells and the surface impedance is defined by the details of the cell geometry. For a fixed substrate thickness and dielectric constant, higher impedance can be obtained using larger cells, or smaller gaps [1]. The surface impedance is defined as the ratio of the tangential electric and magnetic fields. It can be direction-dependent in the case of anisotropic surfaces, and the impedance along a particular direction is primarily determined by the length and gap width in that direction [5]. Varying only the gap width limits the range of available impedance values, but allowing the cell size to vary provides a wider design space. Furthermore, more complex anisotropic structures cannot be designed without either elongated unit cells (which cannot be patterned into arbitrary functions with any existing techniques) or more complicated cell geometries [11]. For this reason, we are developing a patterning technique that allows for continuous variation of cell size, shape, and orientation.

After an array of cells is patterned on the *xy* plane, a gap is required between neighboring cells to define an artificial impedance surface. The process of generating a constant gap width starts with calculating the distance between the center point and one side of the cell. Each cell is defined by its center point and vertices. We define a line connecting each pair of vertices, as shown in Fig. 7(a), and then calculate the length of the segment running from the center point and perpendicular to this line, as shown in Fig. 7(b). The next step is calculating the ratio between the distance calculated in Fig. 7(b) and half of the assigned gap which is shown in Fig. 7(c) as a blue line. After the ratio is obtained, it can be used to calculate the coordinates of new vertexes for each cell. Each vertex is moved

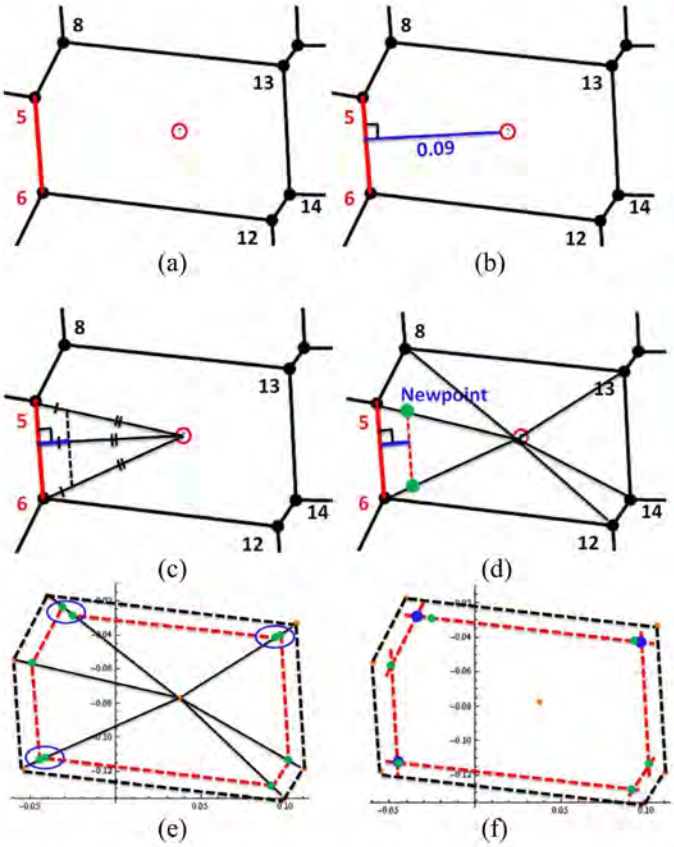

Fig. 7. (a) Cell defined by a center point and vertices. (b) Segment shown in blue from the center point to a line connecting two vertices shown in red. (c) Half the intended gap width is shown in blue. (d) Vertices are moved toward the center point by a distance that is proportional to the gap width. (e) Errors are introduced due to the varying angles between adjacent sides. (f) Errors are corrected by placing new vertices at the intersections between lines defined by each side. The final cell has constant gap width.

toward the center of the cell by a distance that is defined by the ratio calculated above, as shown in Fig. 7(d). This process is used to create each new side of the cell, as shown in Fig. 7(e). However, the varying angles between sides create errors in the definition of the new cell which must be corrected. The solution is to take the intersections of lines created from the new sides to generate corrected vertices, shown as blue dots in Fig. 7(f). These new points complete the new cell with a constant gap width. This process is repeated for all cells in the array to generate a file which defines the metallic pattern that forms the artificial impedance surface.

The cells are generally designed to be electrically small at the frequency of interest so that they can be considered in the effective medium limit, and the surface can be described as an effective impedance boundary. Refraction or reflection [1] does not occur at the individual cell boundaries, but rather due to large-scale variation in the effective surface impedance.

Fig. 8 shows the range of properties that can be created using our point shifting method. This approach enables not only smoothly varying impedance functions, but also varying cells with arbitrary shapes, sizes, and direction of anisotropy as a function of position. The patterns in Fig. 8 were generated by starting function with a square grid. However, we have

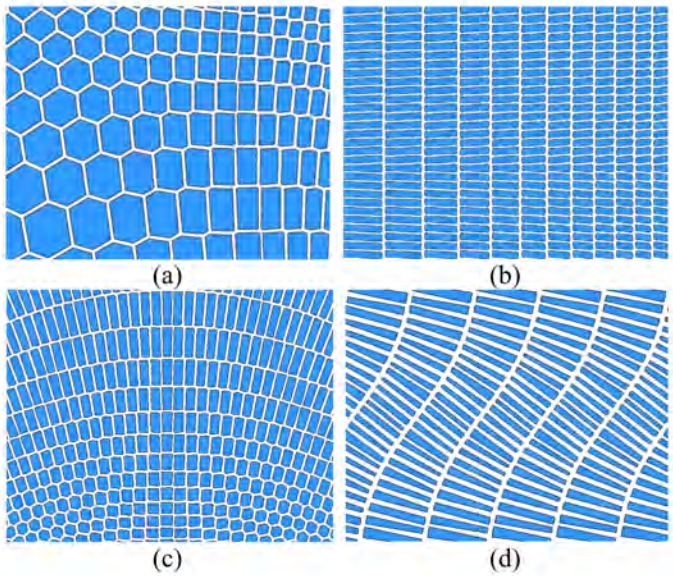

Fig. 8. Examples of various patterns that can be produced by this technique. (a) Varying cell shape. (b) Gradient of impedance. (c) Varying orientation. (d) Extreme variation with high anisotropy.

also developed code to start with a triangular grid, which can produce similar results, allowing a wider range of possible patterns. After having demonstrated the range of properties that are achievable with this method we now use it to create a simple example of a structure which requires a smoothly varying impedance profile, in the form of a planner Luneburg lens. We should note that our method is applicable to general tensor impedance surfaces having a wide range of properties including anisotropy, as illustrated in Fig. 8. However, since canonical anisotropic impedance surface problems are not widely known, for the purpose of demonstrating and validating our patterning method we choose a common problem with a well-defined solution that requires a smoothly varying surface impedance. For this reason, we have selected a planar Luneburg lens design as an example.

III. Luneburg Lens Patterning

A Luneburg lens is a spherically symmetric gradient-index lens [16]. The refractive index n of the lens follows the function:

$$\mathrm{n} = \sqrt{\varepsilon_r} = \sqrt{2 - \left(\frac{r}{R}\right)^2} \tag{1}$$

where r is the radial distance from the center of the lens and R is the radius of the lens. The index n falls from $\sqrt{2}$ to 1 from the center to the edge. It has also been demonstrated in planar form using impedance surfaces [21], [22]. As an example of a practical application of our point shifting method, we generate an inhomogeneous impedance surface with the Luneburg lens profile. We then simulate and measure it to verify that this approach can produce the intended impedance pattern.

A. Patch Simulation Results and Impedance Data

The patterned Luneburg lens consists of patches which set the surface impedance. Therefore we first analyze the

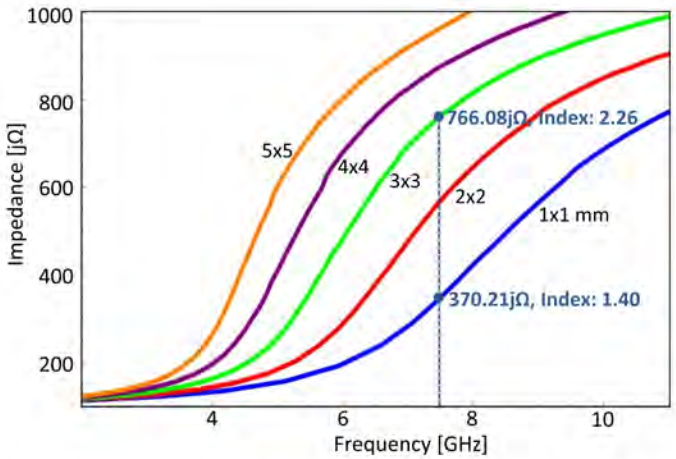

Fig. 9. Simulated impedance versus frequency for various sizes of square unit cells on 2.5 mm Rogers 6010 with 0.25 mm gaps. The indicated impedance range of 766.08 to 370.21 jΩ corresponds to an index ratio of 1.6:1.

impedance as a function of cell geometry to determine the appropriate range of cell sizes for a given substrate and thickness. Assuming grounded 2.5 mm thick Rogers 6010 substrate ($\varepsilon_r = 10.2$), we studied cells ranging in size from 1 to 5 mm, shown in Fig. 9. The gap was 0.25 mm for each case. Although the patches will have various shapes, we studied square patches as a compromise that is representative of a typical patch. We have previously shown that for anisotropic surfaces with rectangular unit cells, the impedance along one direction is independent of the cell size in the orthogonal direction [1], so simulations of square cells provide an understanding of the behavior of rectangular cells as well.

The unit cell structure was simulated in the eigenmode solver in Ansys HFSS version 15.0.3 (a full-wave, commercial software package). The surface impedance for TM waves was calculated as

$$Z_{\mathrm{TM}} = Z_0 \sqrt{1 - \left(\frac{k_{\mathrm{TM}} c}{\omega}\right)^2} \tag{2}$$

based on the dispersion results of the unit cell [8], [23].

Fig. 9 shows the frequency-dependent surface impedance plot of unit cells from 1×1 mm to 5×5 mm. In this plot TM surface impedance can be translated to the index so that the analysis allows us to find an appropriate range of cells which follows the index profile of a Luneburg lens. The effective TM index for surface waves is defined as [24]

$$n_s = \sqrt{1 - \left(\frac{Z_{\mathrm{TM}}}{Z_0}\right)^2}. \tag{3}$$

According to the simulation results we can find appropriate cell sizes which support the surface impedance range for the Luneburg lens index at around 7–8.5 GHz. Fig. 9 shows the result at 7.5 GHz which is selected as the operating frequency of our Luneburg lens pattern. In order to approximate the Luneburg lens profile, we choose a range of cells varying from 1 to 3 mm, which corresponds to an impedance range of 370.21 to 766.08 jΩ. Using (3), this corresponds to an index ratio of approximately 1.6. The next step is to select a starting function for our pattern generation code which will produce a rotationally symmetric array of cells that vary smoothly from 3 mm in the center to 1 mm at the edges.

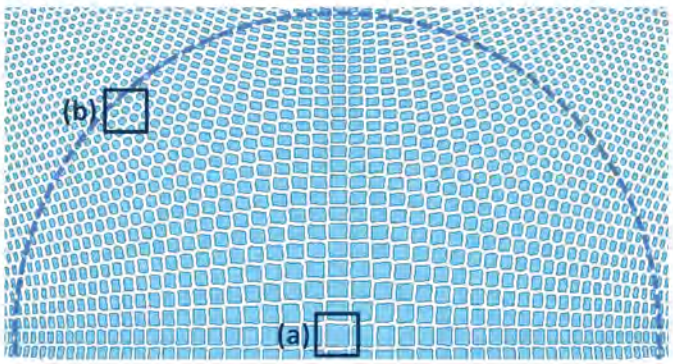

Fig. 10. Luneburg lens pattern used in the simulations. (only half shown) (a) Patches at the center of the lens measured 3 mm. (b) Patches at the edge of the lens measured 1 mm. These produce a 1.6:1 index ratio.

B. Patterns by Point Shifting Method and Simulation Results

We do not have a direct method to produce an arbitrary impedance function. Instead, we begin with a function that has the appropriate properties for our intended application, and then fit that function to produce the range of cell sizes that correspond to the desired impedance range. For example, a planar Luneburg lens requires a function with circular symmetry, and a local maximum in the center. The Luneburg lens pattern was generated by the point shifting method on a 93×93 point array with a starting function f

$$f = \sqrt{1000 e^{-0.2(x^2+y^2)^{0.9}}}. \tag{4}$$

This function was chosen empirically to generate a smoothly varying pattern of cells with rotational symmetry to approximate the Luneburg lens function. A section of the lens, and details of the unit cells from the center and edge are shown in Fig. 10. As shown in Fig. 9, the range of patch sizes varies from 1 to 3 mm from the edge to the center of the lens, and these sizes were chosen to provide an index ratio of 1.4 as required for the Luneberg lens profile. The substrate is the same 2.5 mm thick Rogers 6010 as used in the unit cell analysis. The diameter of the lens is approximately 90 mm and the whole pattern dimensions are 140×140 mm. The pattern consists of 8281 PEC patches and there are 0.5 mm gaps between the cells.

This lens differs from the true Luneburg lens profile in several ways. First, it does not match the function in (1) exactly, it is only an approximation. Second, it does not have a distinct edge, as the cells simply get smaller away from the center at a rate that exponentially approaches the background cell size of approximately 1 mm. Nonetheless, we can define an approximate edge to roughly match the edge of the Luneburg lens function. Third, the cells end about 2 cm past the edge of the lens, and the surrounding material is dielectric clad ground plane, with an impedance of 75.5 jΩ [25]. In spite of these differences, this approach has the advantage that the index varies smoothly, aside from the

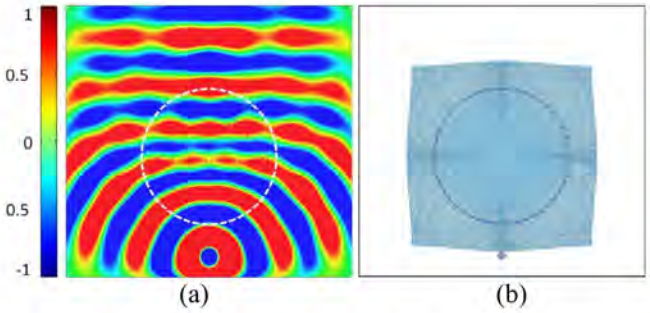

Fig. 11. (a) Normalized electric field at 7.5 GHz. Simulated data showing the field of a collimated surface wave produced from a monopole feed. (b) Area of the lens and surrounding board. The edge of the lens is approximate because it does not have a distinct boundary.

discrete nature of the cells, and we do not need to use shells or rings as in some other planar lens structures [26].

Furthermore, we do not need to match (1) exactly to obtain a structure with measurable lensing effects. Note that the purpose of this paper is not to build a planar Luneburg lens—that has been done many times before. The purpose is to introduce a new patterning technique for producing smoothly varying artificial impedance surfaces. The lens is just an example of a simple, well-known function with practical applications. We include it here to validate that our patterning method can produce structures with predictable and measurable properties.

The Luneburg lens pattern was simulated using the driven modal solver in Ansys HFSS. Fig. 11 shows the field plot at 2 mm above the board at 7.5 GHz. There is a coaxial feed in front of the pattern which generates circular waves that propagate over the lens pattern. The wavefronts are flattened as they pass through the lens pattern. As shown in this figure, the printed impedance surface produces a collimated beam at the output of the lens, as expected, validating our patterning procedure.

IV. Beam Shifting Patterning

In addition to the lens, we have also studied a structure that explicitly requires anisotropy, to demonstrate the usefulness of this structure for generating anisotropic patterns. As an example, we have designed a beam shifting structure. Such structures have been designed previously using anisotropic metasurfaces [3]. However, previous work involved homogeneous impedance surfaces because of the difficulty of patterning inhomogeneous anisotropic surfaces.

The beam shifter can be understood by considering that waves in an anisotropic medium will refract toward the lower index direction [27]. By gradually tilting the direction of low impedance, the wave can be made to follow a desired path.

The beam shifting pattern was generated with starting function f

$$f = \frac{x}{2} - 2\mathrm{Sin}(5x + y). \tag{5}$$

The patterning method resulted in 1154 PEC patches which were printed on a grounded 2.5 mm thick Rogers 6010 substrate. The size of the entire structure is 56 mm × 88 mm.

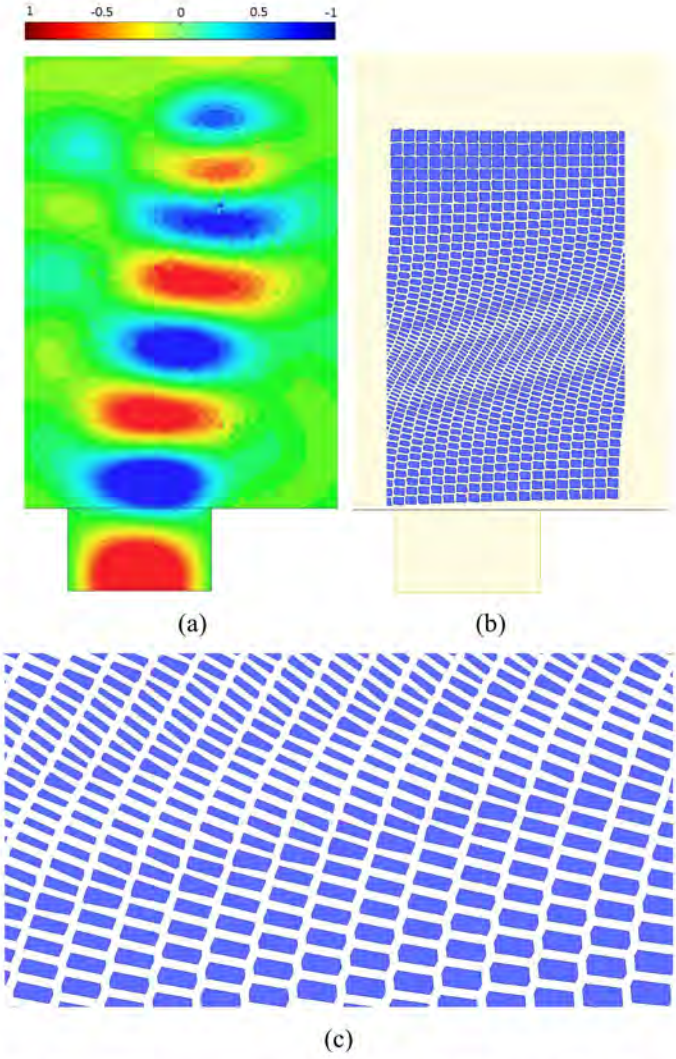

Fig. 12. (a) Normalized electric field at 7 GHz. (b) Pattern on the board with a wave guide source. (c) Enlarged section of the beam shifting surface.

For the elongated patches near the center of the beam shifting structure, the impedance was 260 jΩ in the low direction and 374 jΩ in the high direction. Simulations, shown in Fig. 12, indicate that a beam excited at one end of the structure (such as generated by a waveguide aperture) will be shifted by nearly an entire beamwidth at the other end of the structure. This smoothly varying beam shifting structure represents a pattern that would be impossible to produce using existing techniques. The performance of both the Luneburg lens and the beam shifting surface were verified experimentally, as described in the following section.

V. Experiments

The Luneburg lens pattern was fabricated using printed circuit fabrication technology, and is shown in Fig. 13. The panel is 190 × 180 mm with 8281 copper patches on top of the board, and bottom of the board is a ground. There is a 5 mm diameter hole in front of the pattern for a coaxial feed which is the excitation source. A vertical probe was swept 2 mm above the surface along a 1 mm grid and an Agilent E5071C vector network analyzer recorded the magnitude and

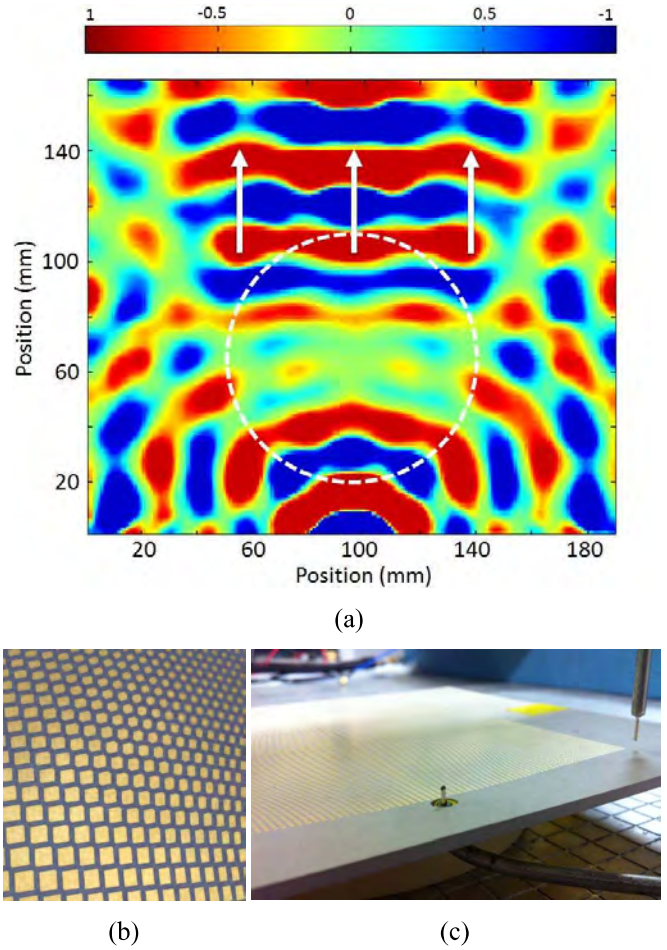

Fig. 13. (a) Normalized near field plot of the surface waves scanned over a 190 × 165 mm area, indicating the collimating capabilities of the lens. The scan starts just beyond the feed point. (b) Closeup photo of the fabricated Luneburg lens pattern. (c) Details of the feed and the measurement technique, including the probe visible at one extreme of the scan region.

the phase of the surface wave. Normalized field results are shown in Fig. 13(a). The circular wavefronts generated by the feed are transformed into flat wavefronts at the opposite side of the lens, as expected. The essential characteristics of the pattern match that shown in Fig. 11, verifying that our technique produces practical impedance surface patterns that match simulation results, and perform a useful function of collimating surface waves. The flat wavefronts emerging from the surface of the lens opposite to the feed are the expected behavior for a Luneburg lens. The additional variations along the edges of the measurement area are artifacts that are indicative of a standing wave pattern which is likely caused by reflections from the edges of the board.

The beam shifting structure was excited by a WR137 waveguide placed adjacent to the surface at one edge. A field map was produced in the same way as for the lens described above, and is plotted in Fig. 14. The beam center is smoothly shifted from 50 to 70 mm along the length of the structure. Note also that the phase fronts begin and end parallel to the front and back edges of the surface, gradually tilt to the right in the central region, following the anisotropic impedance pattern.

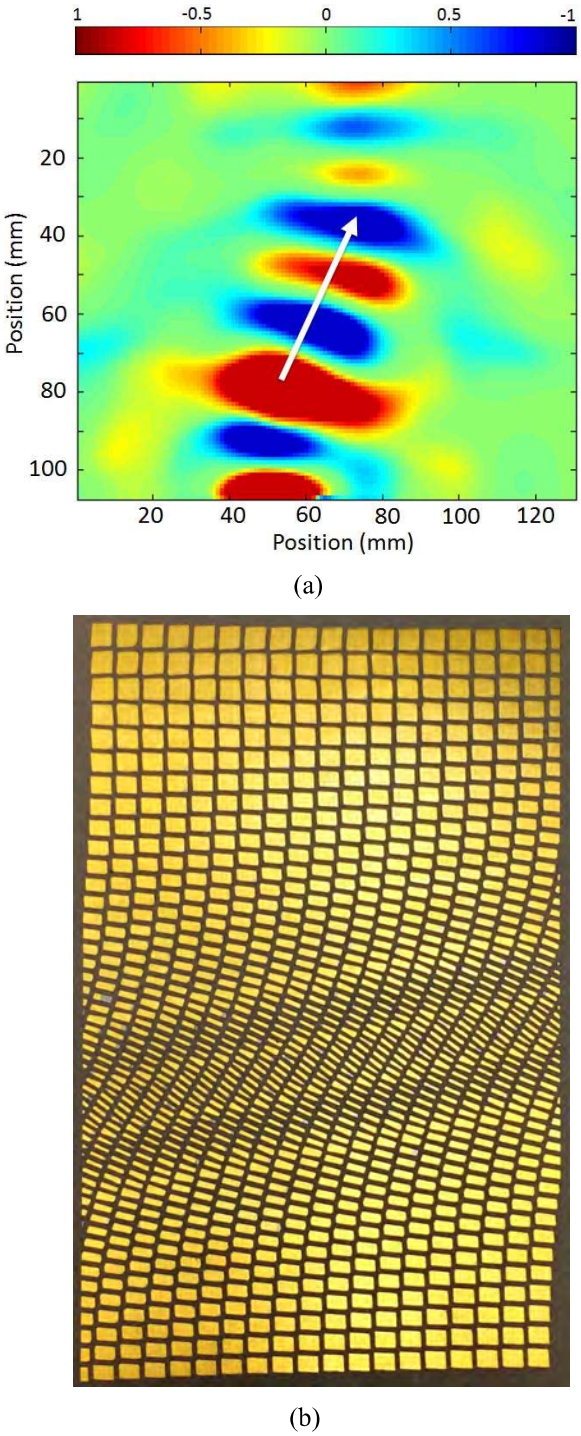

Fig. 14. (a) Normalized near field plot of the surface waves scanned over a 130 × 07 mm area. The arrow represents waves propagating direction to the tilted angle. (b) Fabricated beam shifting pattern.

VI. Conclusion

We have introduced a patterning technique for generating arbitrary impedance surfaces. It provides several advantages over other patterning approaches such as the ability to produce a range of cell sizes, shapes, and orientations, including smoothly varying and highly anisotropic impedance surfaces. Specifically, the ability to produce smoothly varying impedance surfaces with reduced symmetry cells, which are

important for achieving high anisotropy, has been absent from all previous patterning methods. We have illustrated the limitations of existing techniques, as well as other potential approaches such as conformal mapping, and path-dependent methods. We have shown that our technique based on point shifting with Voronoi cell generation can produce impedance surfaces with a wide range of useful properties. We have chosen a simple and practical example to validate our method experimentally, in the form of a planar Luneburg lens as well as an anisotropic beam shifting structure.

We expect that this method will be used to design a wide range of future impedance surface for applications such as planar antennas, scattering control, and interference mitigation. However, there are also several fundamental questions that are topics for future research. First, the starting function is currently chosen empirically to produce a described range of predetermined cell geometries. We need a method to translate the desired impedance function directly to the starting function. Second, the limitations of this method are not known, such as the range of impedance functions that are achievable. Third, aside from certain special cases such as the lens illustrated here, it is not known what impedance function is required to produce a specific surface wave or scattering response. Addressing these issues will allow us to use the method described here to produce arbitrary impedance surfaces for a wide range of applications.

ACKNOWLEDGMENT

The authors would like to thank R. Quarfoth, the researcher at HRL Laboratories for valuable suggestions and contributions during the work.

REFERENCES

[1] R. G. Quarfoth and D. F. Sievenpiper, "Nonscattering waveguides based on tensor impedance surfaces," *IEEE Trans. Antennas Propag.*, vol. 63, no. 4, pp. 1746–1755, Apr. 2015.

[2] A. M. Patel and A. Grbic, "Transformation electromagnetics devices based on printed-circuit tensor impedance surfaces," *IEEE Trans. Microw. Theory Techn.*, vol. 62, no. 5, pp. 1102–1111, May 2014.

[3] R. Quarfoth and D. Sievenpiper, "Surface wave scattering reduction using beam shifters," *IEEE Antennas Wireless Propag. Lett.*, vol. 13, pp. 963–966, 2014.

[4] D. Sievenpiper, J. Colburn, B. Fong, J. Ottusch, and J. Visher, "Holographic artificial impedance surfaces for conformal antennas," in *Proc. IEEE Antennas Propag. Soc. Int. Symp.*, vol. 1B. Jul. 2005, pp. 256–259.

[5] R. Quarfoth and D. Sievenpiper, "Artificial tensor impedance surface waveguides," *IEEE Trans. Antennas Propag.*, vol. 61, no. 7, pp. 3597–3606, Jul. 2013.

[6] C. L. Holloway, E. F. Kuester, J. A. Gordon, J. O'Hara, J. Booth, and D. R. Smith, "An overview of the theory and applications of metasurfaces: The two-dimensional equivalents of metamaterials," *IEEE Antennas Propag. Mag.*, vol. 54, no. 2, pp. 10–35, Apr. 2012.

[7] C. L. Holloway, D. C. Love, E. F. Kuester, J. A. Gordon, and D. A. Hill, "Use of generalized sheet transition conditions to model guided waves on metasurfaces/metafilms," *IEEE Trans. Antennas Propag.*, vol. 60, no. 11, pp. 5173–5186, Nov. 2012.

[8] D. Sievenpiper, L. Zhang, R. F. J. Broas, N. G. Alexopolous, and E. Yablonovitch, "High-impedance electromagnetic surfaces with a forbidden frequency band," *IEEE Trans. Microw. Theory Techn.*, vol. 47, no. 11, pp. 2059–2074, Nov. 1999.

[9] B. H. Fong, J. S. Colburn, J. J. Ottusch, J. L. Visher, and D. F. Sievenpiper, "Scalar and tensor holographic artificial impedance surfaces," *IEEE Trans. Antennas Propag.*, vol. 58, no. 10, pp. 3212–3221, Oct. 2010.

[10] G. Minatti *et al.*, "Modulated metasurface antennas for space: Synthesis, analysis and realizations," *IEEE Trans. Antennas Propag.*, vol. 63, no. 4, pp. 1288–1300, Apr. 2015.

[11] C. Pfeiffer and A. Grbic, "Planar lens antennas of subwavelength thickness: Collimating leaky-waves with metasurfaces," *IEEE Trans. Antennas Propag.*, vol. 63, no. 7, pp. 3248–3253, Jul. 2015.

[12] L. V. Ahlfors, *Conformal Invariants: Topics in Geometric Function Theory*, vol. 371. Providence, RI, USA: AMS, 2010.

[13] U. Leonhardt, "Optical conformal mapping," *Science*, vol. 312, no. 5781, pp. 1777–1780, 2006.

[14] H. Chen, C. T. Chan, and P. Sheng, "Transformation optics and metamaterials," *Nature Mater.*, vol. 9, pp. 387–396, May 2010.

[15] S. H. Lo, "A new mesh generation scheme for arbitrary planar domains," *Int. J. Numer. Methods Eng.*, vol. 21, no. 8, pp. 1403–1426, 1985.

[16] R. K. Luneburg and M. Herzberger, *Mathematical Theory of Optics*. Berkeley, CA, USA: Univ. of California Press, 1964.

[17] G. Peeler and H. Coleman, "Microwave stepped-index Luneberg lenses," *IRE Trans. Antennas Propag.*, vol. 6, no. 2, pp. 202–207, Apr. 1958.

[18] G. Peeler and D. Archer, "A two-dimensional microwave Luneberg lens," *Trans. IRE Prof. Group Antennas Propag.*, vol. 1, no. 1, pp. 12–23, Jul. 1953.

[19] M. de Berg, M. van Kreveld, M. Overmars, and O. C. Schwarzkopf, *Computational Geometry*. Berlin, Germany: Springer-Verlag, 2000.

[20] L. Brillouin, *Wave Propagation in Periodic Structures: Electric Filters and Crystal Lattices*. North Chelmsford, MA, USA: Courier Corporation, 2003.

[21] C. Pfeiffer and A. Grbic, "A printed, broadband Luneburg lens antenna," *IEEE Trans. Antennas Propag.*, vol. 58, no. 9, pp. 3055–3059, Sep. 2010.

[22] K. Sato and H. Ujiie, "A plate Luneberg lens with the permittivity distribution controlled by hole density," *Electron. Commun. Jpn. I, Commun.*, vol. 85, no. 9, pp. 1–12, 2002.

[23] R. Quarfoth and D. Sievenpiper, "Broadband unit-cell design for highly anisotropic impedance surfaces," *IEEE Trans. Antennas Propag.*, vol. 62, no. 8, pp. 4143–4152, Aug. 2014.

[24] R. Quarfoth and D. Sievenpiper, "Anisotropic surface impedance cloak," in *Proc. IEEE Antennas Propag. Soc. Int. Symp. (APSURSI)*, Jul. 2012, pp. 1–2.

[25] R. E. Collin, *Field Theory of Guided Waves*. Hoboken, NJ, USA: Wiley, 1991.

[26] M. Huang, S. Yang, F. Gao, R. Quarfoth, and D. Sievenpiper, "A 2-D multibeam half Maxwell fish-eye lens antenna using high impedance surfaces," *IEEE Antennas Wireless Propag. Lett.*, vol. 13, pp. 365–368, 2014.

[27] D. J. Gregoire and A. V. Kabakian, "Surface-wave waveguides," *IEEE Antennas Wireless Propag. Lett.*, vol. 10, pp. 1512–1515, 2011.

Jiyeon Lee (S'14) received the B.S. degree from Hongik University, Seoul, South Korea, in 2007, and the M.S. degree from the University of California at San Diego, San Diego, CA, USA, in 2013, where she is currently pursuing the Ph.D. degree.

From 2008 to 2011, she was a Software Engineer of Management Information System at SK C&C, Seoul. Her current research interests include artificial impedance surfaces, metamaterials, antenna, and communication circuits.

Daniel F. Sievenpiper (M'94–SM'04–F'09) received the B.S. and Ph.D. degrees in electrical engineering from the University of California at Los Angeles, Los Angeles, CA, USA, in 1994 and 1999, respectively.

He was the Director of the Applied Electromagnetics Laboratory at HRL Laboratories, LLC., Malibu, CA, USA, where his research included artificial impedance surfaces, conformal antennas, tunable and wearable antennas, and beam steering methods. He is currently a Professor with the University of California at San Diego, San Diego, CA, USA. He has more than 70 issued patents and more than 100 technical publications. His current research interests include antennas and electromagnetic structures.

Prof. Sievenpiper was a recipient of the URSI Issac Koga Gold Medal in 2008. Since 2010, he has been an Associate Editor of the IEEE ANTENNAS AND WIRELESS PROPAGATION LETTERS.

Surface Waveguides Supporting Both TM Mode and TE Mode With the Same Phase Velocity

Mei Li, *Student Member IEEE*, Shaoqiu Xiao, *Member IEEE*, Jiang Long, *Student Member, IEEE*, and Daniel F. Sievenpiper, *Fellow, IEEE*

***Abstract*— Two kinds of surface-wave waveguide (SWG) topologies are proposed in this paper with the objective to achieve the property of supporting both transverse magnetic (TM) and transverse electric (TE) modes with the same phase velocity. The first type is composed of two frequency-selective surfaces (FSSs) as layers whose dominant modes are TM mode and TE mode, respectively. For illustration'C the combination of loop-type FSS and wire-grid-type FSS is analyzed and its dispersion characteristics are examined as well. The second class also consists of two layers. For the top layer, there are gaps in one direction and continuous conducting strips in the orthogonal direction. The bottom layer is created from a 90° rotation of the top layer. As a particular illustration, a modified bow-tie-like SWG structure is investigated. The simulated results show that the two proposed SWG structures exhibit the property of supporting both TM mode and TE mode with the same phase velocity over a broad bandwidth. In addition, the effects of lattice types on dispersion diagrams are discussed in this paper. Near field measurements are also carried out to validate the simulations and good agreements are achieved.**

***Index Terms*— Artificial materials, dispersion, periodic structures, surface waves (SWs), surface-wave waveguides.**

I. Introduction

SURFACE waveguides (SWG) are a class of open-boundary structures with the capability of guiding surface waves (SWs), which are intimately bound to the surface of the structure [1]. One of the most commonly studied type is the planar structures consisting of periodic subwavelength elements. Various terminologies, such as artificial impedance surfaces including scalar and tensor impedance surfaces [2]–[6], and metasurfaces [7]–[9], have been used in the literature. Here, we classify them under the broad terminology of SW waveguide (SWG) structures. Due to the capability of controlling the propagation path of SWs [10], [11], SWG have been employed for the applications of electromagnetic scattering alteration, cloaking, absorbing, and self-focusing [12]–[16]. Gradient SWG structures have been used for SW and propagating wave manipulation [17], [18]. SWG structures also have been widely employed for antenna applications in the terms of modulated reactance surfaces [19], [20], holographic surfaces [4], [21], [22], and lenses [23].

A SWG structure can support SW that are polarized in a transverse electric (TE) mode, a transverse magnetic (TM) mode, or a combination of a TM and a TE mode depending on the geometric configuration of the SWG surfaces [4]. Naturally occurring surfaces, such as a conducting plane, support a SW mode of TM type. In general, for a grounded periodic SWG structure consisting of a frequency selective surface (FSS) with electrically small cells printed on the top layer of a grounded dielectric, the dominant SW mode is also TM type no matter whether the FSS elements is a patch type or an aperture type [24]. However, for the ungrounded SWG case, the electromagnetic behavior of the SWG would change dramatically by changing very small electrical connections [25]. It is shown that a TM mode is dominantly supported when the vertexes of a geometrically self-complementary SWG are connected, and a TE mode is dominantly supported when the vertexes are disconnected. Similarly, the dominant SW is TM mode when the unit cell is a square aperture and TE mode when the unit cell is a square patch.

SWG structures that support a dominant TM mode or a TE mode have been studied for years and exploited to design holographic surfaces for applications like leaky-wave radiation and field focusing [4], [17]. However, these structures are generally sensitive to the polarization direction and therefore limitations exist due to such polarization sensitivities. For example, it is a challenge to get a centrally symmetric focused field when the modulated SWG are illuminated by a horizontally polarized field [17]. Regarding holographic antennas when excited by a horizontally polarized field, a narrow symmetric beam is hard to achieve [26]. As a result, the aperture efficiency of holographic antennas is reduced. Therefore, one significant challenge is to create a SWG structure that is insensitive to polarization. Since an incident wave can always be decomposed into TM and TE waves, supposing we have a SWG structure that can support both TM mode and TE mode with the same phase velocity, then the incident wave can

Manuscript received December 8, 2015; revised April 19, 2016; accepted June 8, 2016. Date of publication August 5, 2016; date of current version September 1, 2016. This work was supported in part by the National Science Foundation under Grant ECCS-1306055, the China Scholarship Council (CSC), in part by National High Technology Research and Development Program under Grant 2015AA7124075A, and in part by AFOSR Grant FA9550-16-1-0093.

M. Li is with the School of Physical Electronics, University of Electronic Science and Technology, Chengdu 610054, China, and also with the Department of Electrical and Computer Engineering, University of California at San Diego, La Jolla, CA 92093 USA (e-mail: limei.email@gmail.com).

S. Xiao is with the School of Physical Electronics, University of Electronic Science and Technology, Chengdu 610054, China (e-mail: xiaoshaoqiu@uestc.edu.cn).

J. Long was with the University of California, San Diego, La Jolla, CA 92093 USA. He is now with Skyworks Solution Inc., Woburn, MA 01801 USA (e-mail: longjiang.dragon@gmail.com).

D. F. Sievenpiper is with the University of California, San Diego, La Jolla, CA 92093 USA (e-mail: dsievenpiper@eng.ucsd.edu).

Color versions of one or more of the figures in this paper are available online at http://ieeexplore.ieee.org.

Digital Object Identifier 10.1109/TAP.2016.2583471

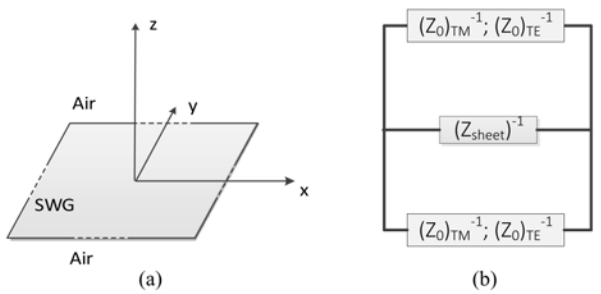

Fig. 1. Equivalent transmission line for transverse resonance analysis. (a) Infinite large SWG impedance sheet placed in the free space. (b) Transmission-line model for the SWG.

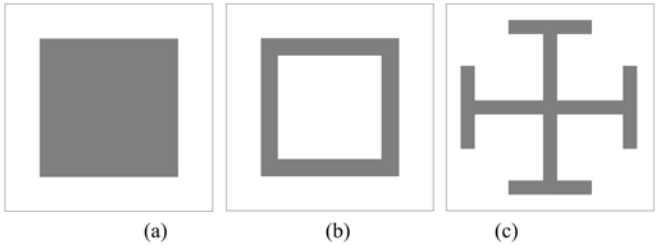

Fig. 2. FSS elements supporting TE modes. (a) Square patch. (b) Square loop. (c) Jerusalem cross.

propagate along the surface regardless of its polarization. In other words, such an SWG structure is insensitive to the polarization direction.

In this paper, we introduce two categories of SWG structures that can support both TM mode and TE mode with the same phase velocity. The proposed SWG structures are constructed by two printed layers separated by a thin dielectric substrate. The two layers of the first SWG type are formed by sub-wavelength periodic elements. The two layers can dominantly support TM mode and TE mode, respectively. For the second type of SWG structures, the bottom layer is simply a 90° rotation of the top layer with respect to the normal direction of the surface. In terms of the configuration of each layer, there are gaps in one direction and continuous conducting strips in the orthogonal direction. When examining the SW propagation characteristics of an SWG structure, the analysis results in dispersion diagrams, and another goal in this paper is to obtain TM and TE dispersion curves that are close to each other as much as possible. It is demonstrated by both simulations and measurements that the two types of SWG structures can support both TM and TE modes with the same phase velocity over a quite broad bandwidth.

This paper is organized as follows. Section II presents the theoretical analysis of a SWG structure suspended in free space using a transmission line model and the transverse resonance condition. Section III presents a SWG category constructed by two layers whose dominant modes are TM mode and TE mode, respectively. As an illustration, a loop-wire unit cell is designed and its dispersion property is investigated as well. Then in Section IV, the configuration of the second kind of SWG is depicted and a modified bow-tie-like unit cell is studied for verification. Section V investigates the effects of lattice types on dispersion curves. As last, conclusions are drawn in Section VI.

II. Theoretical Analysis of Surface Waveguide

Here, the attention is concentrated on SWG structures suspended in free space without a ground plane, as shown in Fig. 1(a). SWG structures are capable of supporting a SW mode, which is intimately bound to the surface of the structure [1]. The field is characterized by an exponential decay $e^{-k_{z0}z}$ away from the surface and having the usual propagation function $e^{-jk_x x}$ (assuming the SW mode propagates along the $+x$ direction). Here, $k_{z0}^2 = {k_x}^2 - k_0^2$, $k_{z0} > 0$ and k_0 is the wave number in the free space above the surface. The TM and TE wave impedances are therefore calculated by [27]

$$(Z_0)_{\mathrm{TM}} = \frac{E_x}{H_y} = -j\eta_0 \frac{k_{z0}}{k_0} \tag{1}$$

$$(Z_0)_{\mathrm{TE}} = -\frac{E_y}{H_x} = j\eta_0 \frac{k_0}{k_{z0}} \tag{2}$$

where η_0 is the wave impedance in the free space above the surface.

Surface impedance boundary conditions are found to be very helpful in analyzing wave propagation properties along scalar or tensor impedance surfaces [3], [4], even though not describing the details of the field distribution near the surface. Fig. 1(b) shows the transmission-line model of the SWG structure, where, Z_{sheet} represents the surface impedance of the SWG structure. According to the transverse resonance condition [28], for a TM mode, there is

$$(Z_0)_{\mathrm{TM}}^{-1} + (Z_{\mathrm{sheet}})^{-1} + (Z_0)_{\mathrm{TM}}^{-1} = 0. \tag{3}$$

Using (1) and (2) in (3) leads to

$$Z_{\mathrm{sheet}} = 2j\eta_0 \frac{k_{z0}}{k_0}. \tag{4}$$

Expression (4) manifests that in order to support a TM mode propagation along a SWG structure, the surface impedance should have inductive reactive term. By the same manner, it can be proved that in order to support a TE SW, the reactive part of the surface impedance must be capacitive. This gives a physical insight into the working mechanism of a SWG structure consisting of electrically small periodic elements, which can be analyzed by an equivalent circuit model.

III. Unit Cell Design of Loop-Wire Structure

A. Topology Configuration

The first SWG topology contains two subwavelength FSS whose dominant modes are TE and TM modes, respectively. Fig. 2 shows three of the most common FSS unit-cell geometries whose dominant modes are TE mode: square patch, square loop, and Jerusalem cross structure. The gaps between adjacent conducting patches or wires create a dominant capacitive response at low frequencies and therefore, as analyzed in Section II that a capacitive response is needed to support TE mode propagation, the dominant mode of these elements is TE mode.

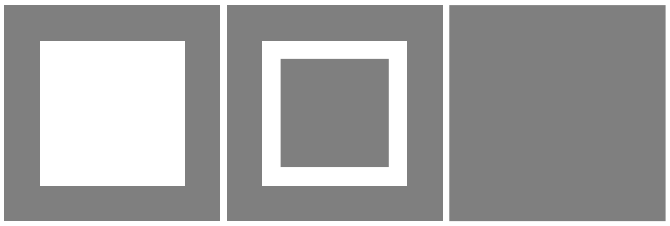

(a) (b) (c)

Fig. 3. Some typical FSS elements supporting TM modes. (a) Wire grid. (b) Ring slot. (c) Conducting ground.

Two typical FSS unit cells whose dominant modes are TM mode are shown in Fig. 3(a) and (b): wire grid and ring slot structure. They are the complementary geometries of the square patch and square loop FSS [as shown in Fig. 2(a) and (b)] whose surface impedances are capacitive. Therefore, according to the Babinet principle, their surface impedances are inductive. In fact, the inductance mainly comes from the continuous conducting strips. Especially, the dominant mode for a metal ground [as shown in Fig. 3(c)] is also TM type due to its inductive property.

It is demonstrated in the following content that a composite structure of a capacitive FSS and an inductive FSS would exhibit the property that the dispersion curves of the TM mode and the TE mode overlap at certain frequencies. In other words, the double-layer structure can support both TM mode and TE mode with the same phase velocity. Therefore, the combination of any FSS type from Fig. 2 and one Fig. 3 can achieve this property. As expected, by choosing proper dimensions, a grounded patch FSS, that is a combination of Figs. 2(a) and 3(c), can exhibit the same dispersion characteristics.

B. Unit Cell Design

The loop-wire unit cell design is illustrated in Fig. 4 (a). A square loop and a wire-grid are printed on the two sides of a 0.508-mm-thick Rogers RT/duroid 5880 substrate (εr = 2.2) with lattice dimension $p = 3.5$ mm. Fig. 4(b) illustrates a square portion of the surface containing a few unit cells. Such a loop-wire configuration has been exploited for a miniaturized-element FSS focusing on its reflection/transmission properties [29], [30]. In this paper, the emphasis is on the SWG property and thus the analysis leads to dispersion diagrams. A full-wave electromagnetic simulation software Ansys HFSS version 15.0 is utilized to examine the performance of the SWG structures.

C. Measured and Simulated Results

In simulation, only a single unit needs to be analyzed to interpret the properties of a periodic structure by assigning master-slave boundaries in the eigenmode solver. In experiment, a finite size surface consisting of 53 × 75 cells was fabricated and tested to represent the infinitely large periodic structure. A photograph of a section of the surface is shown in Fig. 5.

A near field scanner was used to do the dispersion measurement. The measurement setup for the TM mode and the TE mode are different, as is shown in Fig. 6(a) and (b), respectively. A trapezoidal microstip-line connected to one

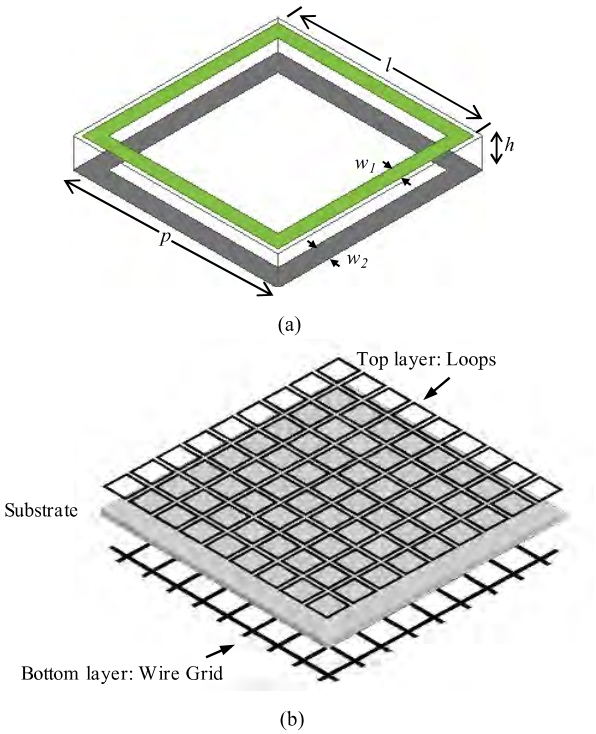

Fig. 4. Loop-wire unit cell and a small portion of its SWG. (a) Loop-wire unit cell geometry: $p = 3.5$ mm, $l = 3.4$ mm, $h = 0.508$ mm, $w_1 = 0.225$ mm, and $w_2 = 0.25$ mm. (b) SWG consisting of the loop array on one side and wire grid on the other side.

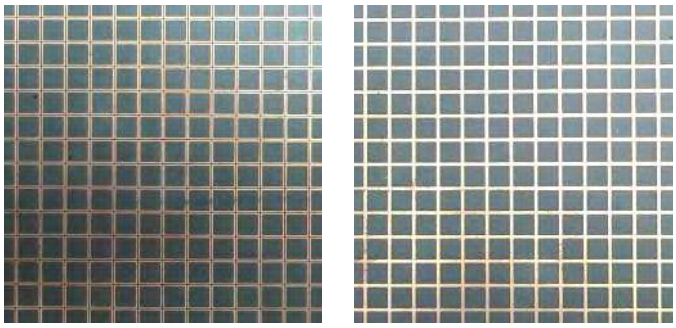

(a) (b)

Fig. 5. Photograph of a session of the finite-size surface. (a) Top side: loop FSS. (b) Bottom side: wire-grid FSS.

port of an Agilent E5071C vector network analyzer (VNA) was adopted to excite the TM mode. A vertical probe, which is scanned across the surface, was connected to the second port of the VNA so as to record the E_z field distributions. With regard to the measurement setup of TE mode, as shown in Fig. 6(b), a waveguide port was connected to one port of the VNA to excite the TE mode and a horizontal probe was connected to the second port of the VNA to record the E_y field distributions.

S_{21} of the E_z and E_y fields were recorded along a x-direction line of 150 mm with 500-um increments in the experiment. By implementing the fast Fourier transform algorithm (FFT) to the measured S_{21} along the 150-mm line, the wavenumber of the TM mode and TE mode can be extracted for the whole frequency range. Fig. 7 gives the measured and simulated dispersion diagrams of the unit-cell design with the direction of propagation along the x-direction.

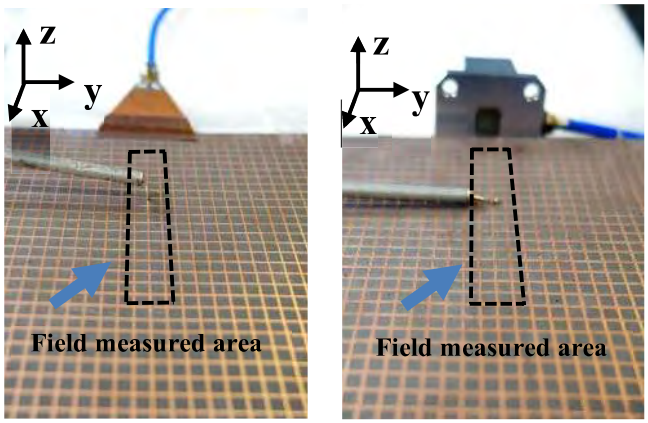

(a) (b)

Fig. 6. Near field measurement setup for (a) TM mode and (b) TE mode.

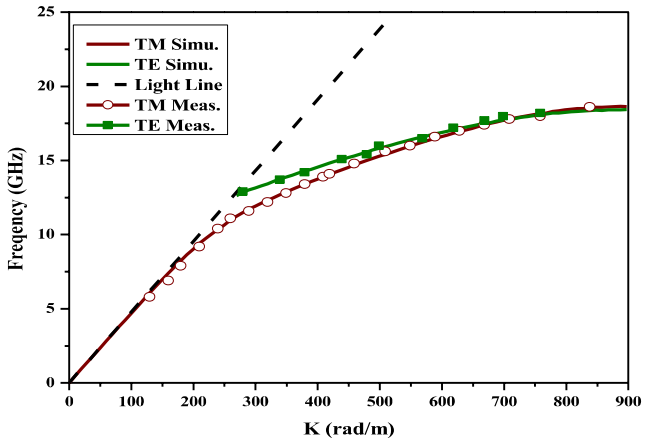

Fig. 7. Dispersion diagram of the loop-wire unit cell.

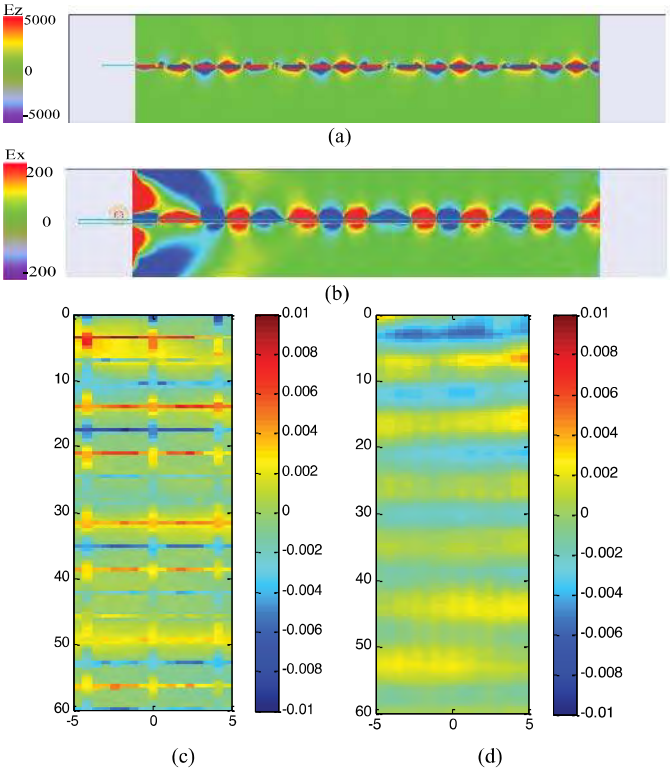

Fig. 8. Field distributions at 18 GHz of (a) simulated E_z for TM mode and (b) simulated E_y for TE mode in the xz plane, (c) measured E_z for TM mode and (d) measured E_y for TE mode close to the xy plane (at a height around 0.2 mm).

Excellent agreement is achieved between the simulation and the measurement. Due to the symmetric geometry, the same dispersion curves would be obtained when waves propagate along the y-direction. According to the simulation, the dispersion curves of the TM mode and TE mode overlap around 18 GHz, which means TM mode and TE mode have the same phase velocity.

To get a better understanding of the SW propagation property along the surface, both TM and TE field distributions of the proposed SWG structure are investigated. Fig. 8(a) and (b) shows the simulated TM mode and TE mode distributions in the xz plane, respectively. It shows obviously that the TM mode and the TE mode are tightly bound to the SWG surfaces. The TM mode and the TE mode distributions close to the xy plane are measured and shown in Fig. 8(c) and (d). As can be seen from Fig. 8(d), for the TE mode, the wavelength can be estimated from the field distributions. For the TM mode, due to the appearance of higher order modes like evanescent modes that are picked up by the vertical probe scanning above the surface at a height around 0.2 mm, the wavenumber is hard to tell from the E_z field distributions. Therefore, the FFT is utilized for both TM and TE wavenumber calibrations.

IV. Unit Cell Design of Double-Layer Modified Bow-Tie-Like Structure

A. Topology Configuration

For an array of continuous, conducting narrow strips, the impedance is either inductive (responsible for the TM mode) or capacitive (responsible for the TE mode), depending on whether the incident wave is polarized parallel to or perpendicular to the edges of the strips, respectively [1]. Fig. 9(a) shows a double-layer unit cell with 90° rotational symmetry in the xy plane. A small section of a SWG constructed by this kind of unit cell is shown in Fig. 9(b). For each layer, there are gaps in one direction and continuous strips in the orthogonal direction. Fig. 9(c) shows an example of the dispersion diagram for this kind of unit cell, which demonstrates that there is a point where the TM mode and TE mode overlap, indicating that the TM mode and TE mode have the same phase velocity. Based on this topology, two unit cells are proposed, as shown in Fig. 10, which give similar dispersion diagrams as that shown in Fig. 9(c). The step-like unit cell shown in Fig. 10(a) derives directly from the topology plotted in Fig. 9(a). In order to realize a miniaturization design, bow-tie-like unit in Fig. 10(b) is proposed based on Fig. 10(a). Fig. 11(b) shows the dispersion diagram for the particular bow-tie-like structure, as shown in Fig. 10(b). In order to get better performance that TM mode and TE mode give the same phase velocity during a broader bandwidth, a modified bow-tie-like structure is proposed in Section IV-B.

B. Unit Cell Design

The configuration of the bi-layer modified bow-tie-like structure and its detailed parameters are shown in Fig. 11.

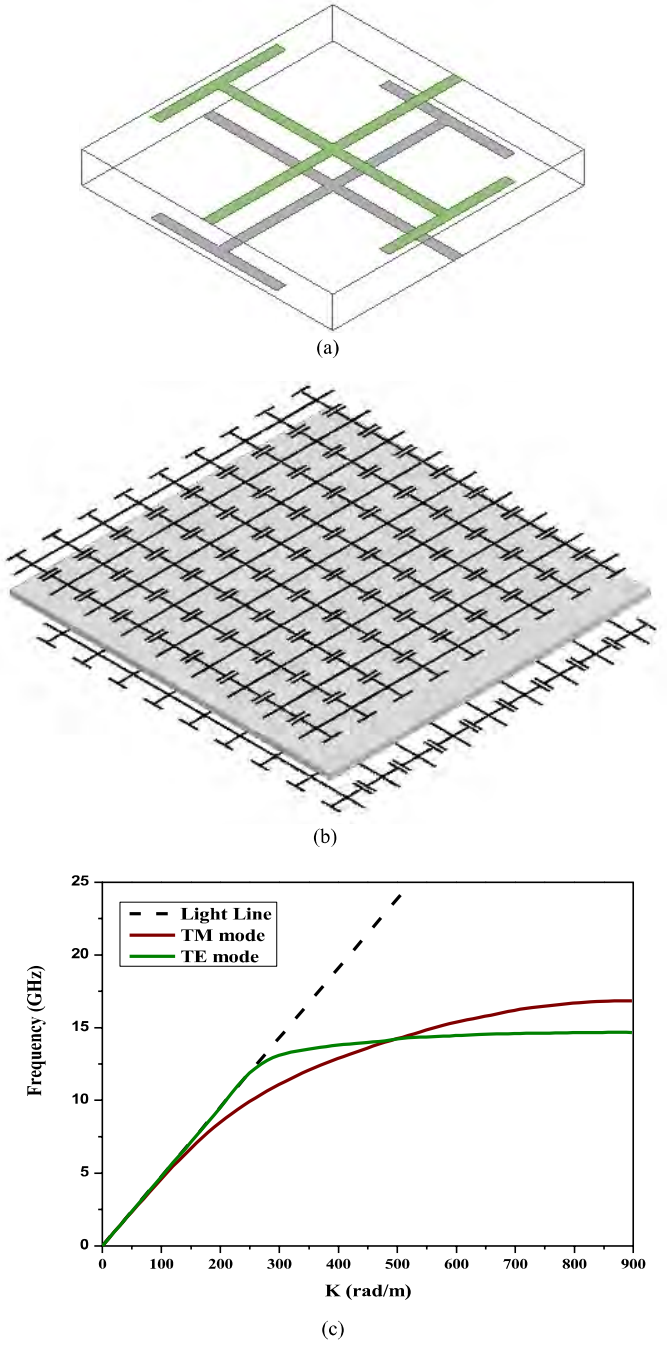

Fig. 9. Double-layer SWG and its dispersion diagram. (a) Unit cell configuration. (b) Small section of the SWG surface. (c) Example of its dispersion curves.

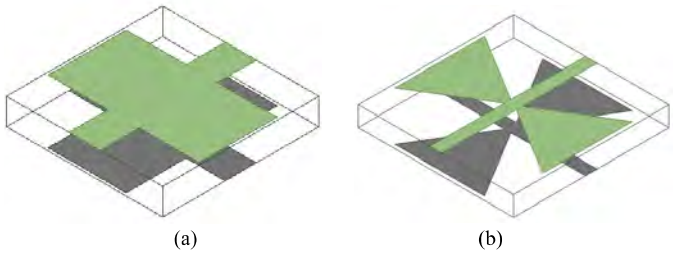

Fig. 10. Double-layer SWG unit cells. (a) Step-like unit cell. (b) Bow-tie-like unit cell.

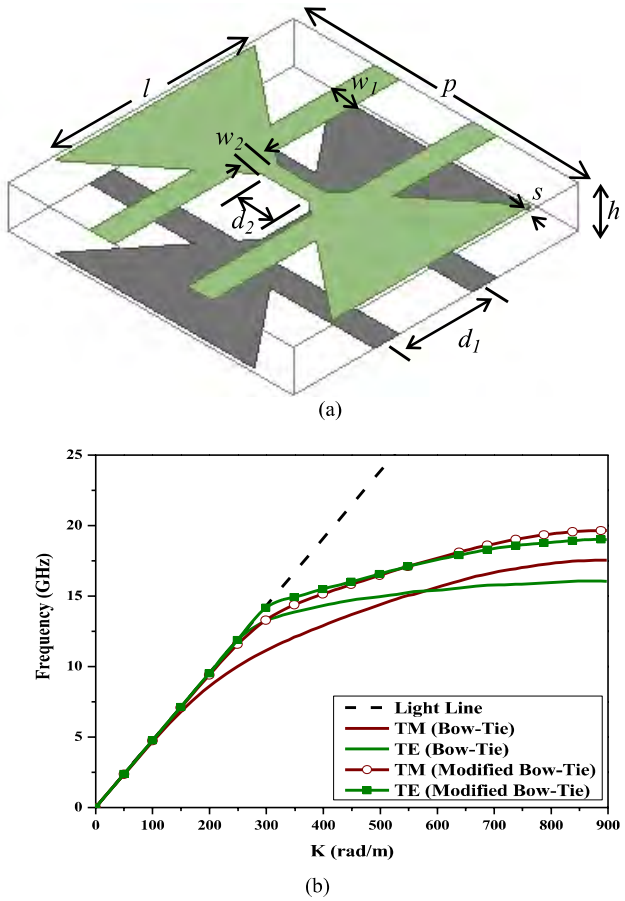

Fig. 11. Modified bow-tie-like unit cell and simulated dispersion curves. (a) Unit cell configuration: $p = 3.5$ mm, $h = 0.508$ mm, $l = 2.45$ mm, $d_1 = 1.2$ mm, $d_2 = 0.576$ mm, $s = 0.05$ mm, $w_1 = 0.3$ mm, and $w_2 = 0.2$ mm. (b) Simulated dispersion curves: the solid line corresponding to the structure in Fig. 10(b) and the line + symbol corresponding to the structure in Fig. 11(a).

Compared with the structure shown in Fig. 10(b), the central metal strip was replaced by twin wires separated with a distance of $d_1 = 1.2$ mm. Fig. 11 shows the simulated dispersion curves of the two unit cells. The dimensions of the parameters of bow-tie-like structure are kept same as that of the modified bow-tie-like structure shown in Fig. 11(a). As can be seen from Fig. 11(b), the modified bow-tie structure exhibits better performance, because the two modes have almost the same phase velocity over a broad bandwidth than that of the bow-tie-like structure.

According to the parametric study, the spacing between the twin wires, d_1, has a great effect on the cross of TM and TE modes and in what level the two modes overlap. Fig. 12 shows the dispersion diagrams with different values of d_1. As can be seen in Fig. 12, d_1 has a dramatic effect on the dispersion curve of the TE mode, whose slope increases with the increase of d_1.

C. Measured and Simulated Results

A prototype sample of the modified bow-tie-like SWG with 53×75 cells was fabricated and tested using the near field scanner. Fig. 13 shows a small section of the fabricated sample. The measurement setup for the TM mode and TE mode measurement are kept almost the same as that in Section III-C except for a horizontal probe, as shown in Fig. 14(b), was used for the TE mode excitation. The E_z and E_y fields are recorded by a vertical probe and a horizontal probe, respectively.

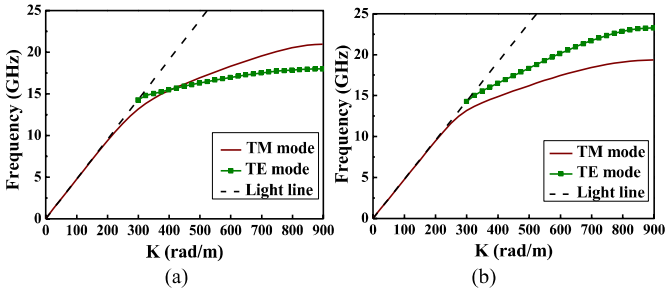

Fig. 12. Dispersion curves with different d_1. (a) $d_1 = 0.8$ mm. (b) $d_1 = 2$ mm.

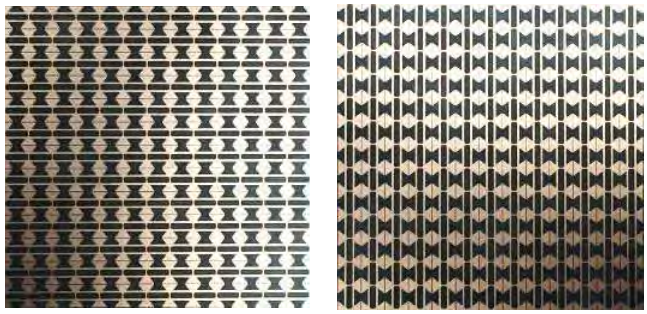

Fig. 13. Photograph of a session of the finite-size surface. (a) Top side. (b) Bottom side.

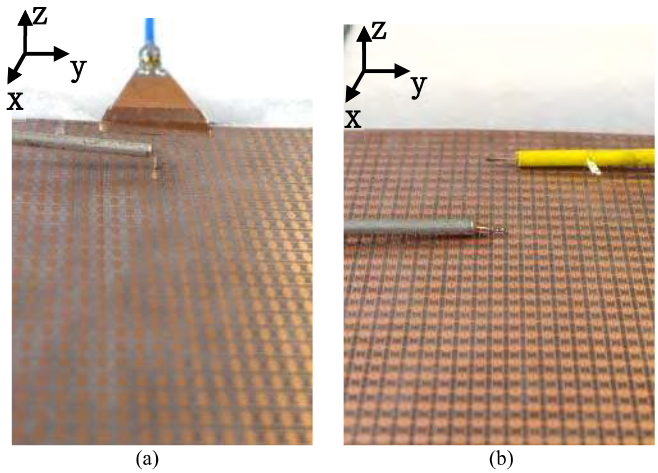

Fig. 14. Near field measurement setup for (a) TM mode measurement and (b) TE mode measurement.

The measured wavenumbers are calculated by applying the FFT algorithm to the recorded S_{21} of the E_z and E_y field distributions along a x-direction line of 150 mm at 500-um increments. Fig. 15 shows the measured dispersion curves as well as the simulated ones for comparison. The measurement and the simulation exhibits good consistency. According to the simulation, the TM mode and TE mode give the same phase velocity around 18 GHz. In addition, the dispersion curves of the two modes closely overlap. The field distributions are also simulated and measured, which demonstrates that TM and TE modes are tightly bound to the SWG surface. For the sake of brevity, the detailed TM and TE field distributions are not shown here.

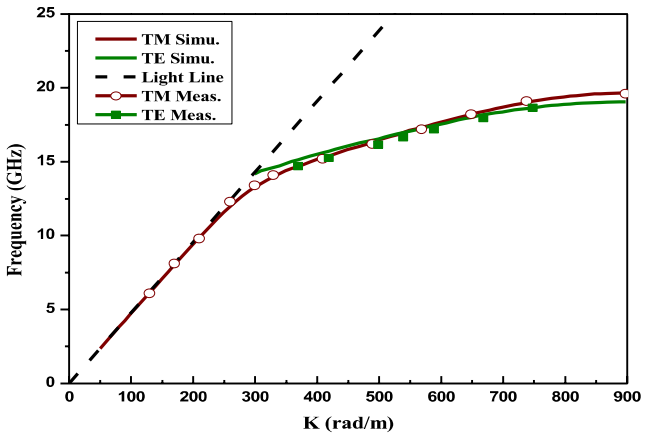

Fig. 15. Dispersion diagram of the bi-layer modified bow-tie-like unit cell.

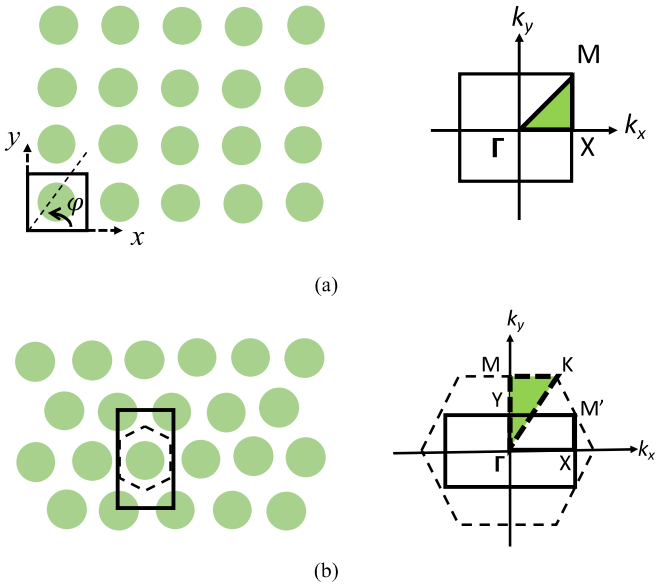

Fig. 16. Lattice types and their Brillouin zones. (a) Square lattice. (b) Hexagonal lattice.

V. Effects of Lattice Types on Dispersion Curves

A 2-D square and hexagonal lattices are two commonly seen lattice types, which have been widely studied in the field of photonic crystals and electromagnetic bandgap structures. It has been reported that the geometry of photonic crystal lattice types would significantly affect the bandgap characteristics [31], [32], and laser characteristics, such as threshold conditions and lasing spectra [33]. The lattice structures and Brillouin zones for these two types are shown in Fig. 16, where the green shadow triangles indicate the irreducible Brillouin zones. For the sake of calculation, as shown in Fig. 16(b), a rectangular unit supercell (solid rectangular) instead of a hexagonal one (dashed hexagon) is chosen for simulation and therefore the corresponding first Brillouin zone is the solid rectangular instead of the hexagonal lattice [34]. The irreducible Brillouin zone of the rectangular lattice is indicated by path ΓXM′YΓ. Note that, due to the folding of both reciprocal lattices, scanning along the contour ΓXM′YΓ completely covers the whole Brillouin zone of the hexagonal lattice.

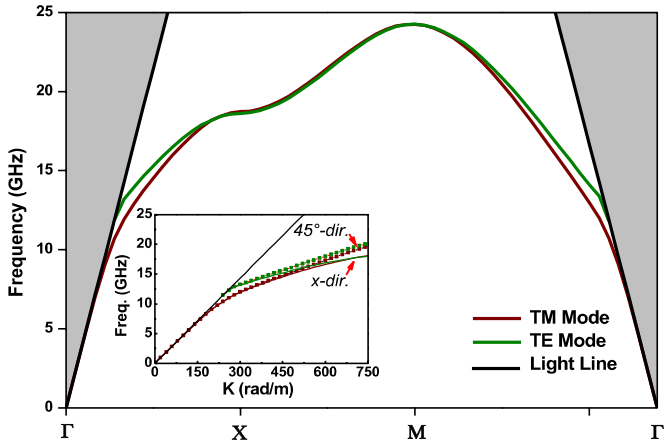

Fig. 17. Dispersion diagram of the first two modes of the loop-wire SWG with square lattice. The subgraph indicates the dispersion curves along the x-direction and the 45° direction.

This paper aims to investigate propagation characteristics of SWGs. Ideally, the proposed SWG surfaces can support both TM- and TE-mode with the same phase velocity in an arbitrary direction along the surface. Due to the symmetric configuration in the xy plane, here, the loop-wire SWG topology is analyzed to study the effects of lattice types on dispersion curves. Two lattice structures, square, and hexagonal lattices, are examined in this paper. The SWG configuration proposed in Section III is a square lattice. Fig. 17 shows the simulated dispersion diagrams of the loop-wire SWG with square lattice in the cases of the first two modes, where the subgraph shows when the two modes propagate in the x-axis [path Γ-X in Fig. 16(a)] and the diagonal [path Γ-M in Fig. 16(a)] directions. The SWG geometry and parameters are kept the same with those presented in Section III. As can be seen from Fig. 17, the dispersion curves in the two directions are aligned with each other in the low frequency range. However, with the increase of frequency, the discrepancy deteriorates. As a result, the dispersion curves of the loop-wire SWG with square lattice exhibit great discrepancy when the SWs propagate in different directions along the SWG surface.

Now, let us examine the loop-wire SWG topology with hexagonal lattice. As shown in Fig. 18(a), a rectangular supercell consisted by hexagonal unit cells in terms of discrete loop-FSS for the top layer and continuous wire-FSS for the bottom layer is presented. A small portion of the corresponding SWG with hexagonal lattice is shown in Fig. 18(b). The dispersion diagram of the first two modes of the supercell is given in Fig. 19. The subgraph illustrates the simulated dispersion curves when the two modes propagate along the y-axis [path Γ-M in Fig. 16(b)] and $\varphi = 60°$ [path Γ-K Fig. 16(b)] directions. According to Fig. 19, the proposed hexagonal loop-wire SWG with hexagonal lattice exhibits almost the same dispersion curves when SWs propagate in different directions of the surface. Therefore, SWGs with hexagonal lattice exhibit better performance in the aspect of dispersion property than those with square lattice.

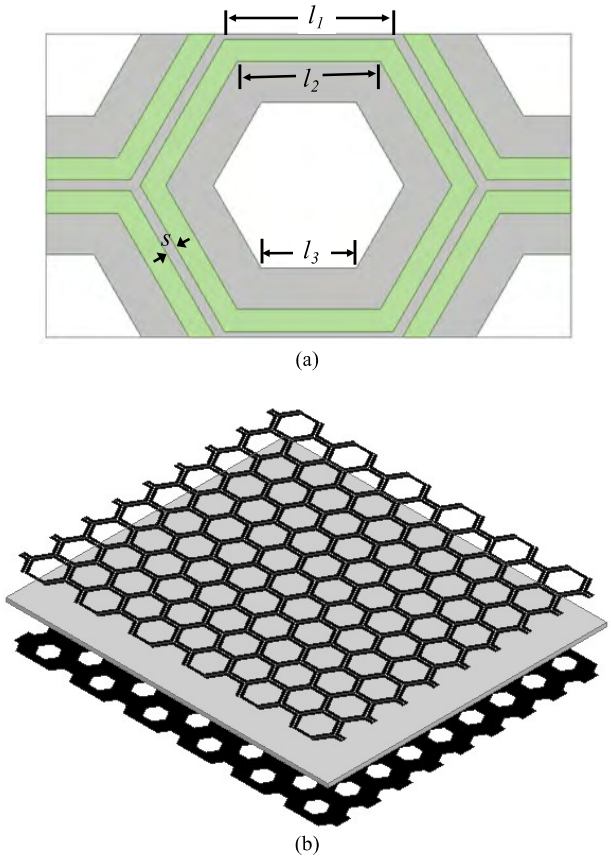

Fig. 18. Hexagonal loop-wire unit supercell and its SWG configuration with hexagonal lattice. (a) Hexagonal loop-wire unit: $l_1 = 2.3$ mm, $l_2 = 1.95$ mm, $l_3 = 1.3$ mm, and $s = 0.075$ mm. (b) Portion of SWG with hexagonal lattice. The thickness of the substrate is 0.508 mm.

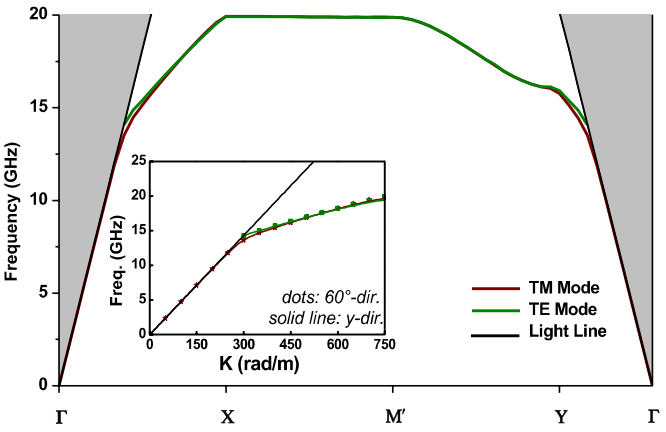

Fig. 19. Dispersion diagram of the first two modes of the loop-wire SWG with hexagonal lattice. The subgraph indicates the dispersion curves along the y-direction and the 60° direction.

Fabrication and measurements have been carried out and the measurement setup is the same as that shown in Fig. 14. The simulated and measured dispersion curves for the TM mode and TE mode that propagate along the y-axis and $\varphi = 60°$ directions are given in Fig. 20(a)–(d), respectively. The same FFT method that described in

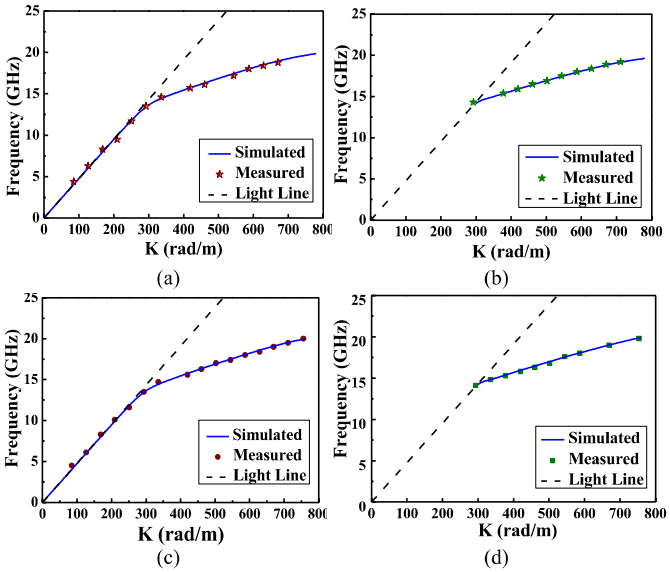

Fig. 20. Measured and simulated dispersion curves of (a) TM mode propagating along the y-axis direction, (b) TE mode propagating along the y-axis direction, (c) TM mode propagating along the $\varphi = 60°$ direction, and (d) TE mode propagating along the $\varphi = 60°$ direction.

Sections III and IV is utilized to obtain the measured dispersion curves. As shown in Fig. 20, the simulation and the measurement agree well with each other.

VI. Conclusion

Two SWG topologies are found to have the property of supporting both TM mode and TE mode with the same phase velocity. The first type consists of two FSS layers whose dominant modes are TM mode and TE mode, respectively. The second type is composed of two layers and the bottom layer comes from a 90° rotation from the top layer. The top layer has gaps in the x-direction and continuous conducting strips in the y-direction. Therefore, in either the x-direction or y-direction, there are gaps on one layer and continuous conducting strips on the other layer. Based on these topologies, SWG structures with various unit-cell shapes can be created to obtain the desired characteristics. Since various FSS shapes can be found to support TM mode or TE mode, according to the first type of the proposed SWG topologies, the combination of any FSS whose dominant mode is TM mode and any one whose dominant mode is TE mode can achieve these characteristics. For the second type, several unit cells are proposed in this paper, and many other shapes can also be created based on this topology. SWG surfaces with these characteristics of supporting both TM and TE mode with the same phase velocity have great potential to be used in many applications like gradient Luneberg lens antennas and holographic surfaces. For instance, a planar holographic surface with central focusing property can be achieved when imposed by a horizontal polarized excitation.

References

[1] R. E. Collin, *Field Theory of Guided Waves*. New York, NY, USA: McGraw-Hill, 1960.

[2] H. J. Bilow, "Guided waves on a planar tensor impedance surface," *IEEE Trans. Antennas Propag.*, vol. 51, no. 10, pp. 2788–2792, Oct. 2003.

[3] B. H. Fong, J. S. Colburn, J. J. Ottusch, J. L. Visher, and D. F. Sievenpiper, "Scalar and tensor holographic artificial impedance surfaces," *IEEE Trans. Antennas Propag.*, vol. 58, no. 10, pp. 3212–3221, Oct. 2010.

[4] A. M. Patel and A. Grbic, "Effective surface impedance of a printed-circuit tensor impedance surface (PCTIS)," *IEEE Trans. Microw. Theory Techn.*, vol. 61, no. 4, pp. 1403–1413, Apr. 2013.

[5] R. G. Quarfoth and D. F. Sievenpiper, "Nonscattering waveguides based on tensor impedance surfaces," *IEEE Trans. Antennas Propag.*, vol. 63, no. 4, pp. 1746–1755, Apr. 2015.

[6] R. Quarfoth and D. Sievenpiper, "Artificial tensor impedance surface waveguides," *IEEE Trans. Antennas Propag.*, vol. 61, no. 7, pp. 3597–3606, Jul. 2013.

[7] S. Maci, G. Minatti, M. Casaletti, and M. Bosiljevac, "Metasurfing: Addressing waves on impenetrable metasurfaces," *IEEE Antennas Wireless Propag. Lett.*, vol. 10, pp. 1499–1502, 2011.

[8] X. Li, S. Xiao, B. Cai, Q. He, T. J. Cui, and L. Zhou, "Flat metasurfaces to focus electromagnetic waves in reflection geometry," *Opt. Lett.*, vol. 37, no. 23, pp. 4940–4942, Dec. 2012.

[9] M. Mencagli, E. Martini, and S. Maci, "Surface wave dispersion for anisotropic metasurfaces constituted by elliptical patches," *IEEE Trans. Antennas Propag.*, vol. 63, no. 7, pp. 2992–3003, Jul. 2015.

[10] D. J. Gregoire and A. V. Kabakian, "Surface-wave waveguides," *IEEE Antennas Wireless Propag. Lett.*, vol. 10, pp. 1512–1515, 2011.

[11] F. Elek, B. B. Tierney, and A. Grbic, "Synthesis of tensor impedance surfaces to control phase and power flow of guided waves," *IEEE Trans. Antennas Propag.*, vol. 63, no. 9, pp. 3956–3962, Sep. 2015.

[12] R. Quarfoth and D. Sievenpiper, "Surface wave scattering reduction using beam shifters," *IEEE Antennas Wireless Propag. Lett.*, vol. 13, pp. 963–966, 2014.

[13] R. Quarfoth and D. Sievenpiper, "Alteration of electromagnetic scattering using hard and soft anisotropic impedance surfaces," *IEEE Trans. Antennas Propag.*, vol. 63, no. 10, pp. 4593–4599, Oct. 2015.

[14] P.-Y. Chen and A. Alù, "Mantle cloaking using thin patterned metasurfaces," *Phys. Rev. B*, vol. 84, p. 205110, Nov. 2011.

[15] H. Wakatsuchi, S. Kim, J. J. Rushton, and D. F. Sievenpiper, "Waveform-dependent absorbing metasurfaces," *Phys. Rev. Lett.*, vol. 111, no. 24, p. 245501, 2013.

[16] Z. Lou, X. Chen, J. Long, R. Quarfoth, and D. Sievenpiper, "Self-focusing of electromagnetic surface waves on a nonlinear impedance surface," *Appl. Phys. Lett.*, vol. 106, no. 21, p. 211102, 2015, doi: 10.1063/1.4921913.

[17] X. Wan, Y. B. Li, B. G. Cai, and T. J. Cui, "Simultaneous controls of surface waves and propagating waves by metasurfaces," *Appl. Phys. Lett.*, vol. 105, no. 12, p. 121603, 2014, doi: 10.1063/1.4896540.

[18] S. Sun, Q. He, S. Xiao, Q. Xu, X. Li, and L. Zhou, "Gradient-index meta-surfaces as a bridge linking propagating waves and surface waves," *Nature Mater.*, vol. 11, no. 5, pp. 426–431, May 2012.

[19] A. A. Oliner and A. Hessel, "Guided waves on sinusoidally–modulated reactance surfaces," *IRE Trans. Antennas Propag.*, vol. 7, no. 5, pp. S201–S208, Dec. 1959.

[20] A. M. Patel and A. Grbic, "A printed leaky-wave antenna based on a sinusoidally-modulated reactance surface," *IEEE Trans. Antennas Propag.*, vol. 59, no. 6, pp. 2087–2096, Jun. 2011.

[21] S. Pandi, C. A. Balanis, and C. R. Birtcher, "Design of scalar impedance holographic metasurfaces for antenna beam formation with desired polarization," *IEEE Trans. Antennas Propag.*, vol. 63, no. 7, pp. 3016–3024, Jul. 2015.

[22] G. Minatti, F. Caminita, M. Casaletti, and S. Maci, "Spiral leaky-wave antennas based on modulated surface impedance," *IEEE Trans. Antennas Propag.*, vol. 59, no. 12, pp. 4436–4444, Dec. 2011.

[23] M. Bosiljevac, M. Casaletti, F. Caminita, Z. Sipus, and S. Maci, "Non-uniform metasurface Luneburg lens antenna design," *IEEE Trans. Antennas Propag.*, vol. 60, no. 9, pp. 4065–4073, Sep. 2012.

[24] O. Luukkonen *et al.*, "Simple and accurate analytical model of planar grids and high-impedance surfaces comprising metal strips or patches," *IEEE Trans. Antennas Propag.*, vol. 56, no. 6, pp. 1624–1632, Jun. 2008.

[25] D. González-Ovejero, E. Martini, and S. Maci, "Surface waves supported by metasurfaces with self-complementary geometries," *IEEE Trans. Antennas Propag.*, vol. 63, no. 1, pp. 250–260, Jan. 2015.

[26] C. Rusch, J. Schäfer, H. Gulan, P. Pahl, and T. Zwich, "Holographic mmW-antennas with TE_0 and TM_0 surface wave launchers for frequency-scanning FMCW-radars," *IEEE Trans. Antennas Propag.*, vol. 63, no. 4, pp. 1603–1613, Apr. 2015.

[27] R. F. Harrington, *Time-Harmonic Electromagnetic Fields*. New York, NY, USA: McGraw-Hill, 1961, pp. 129–132.

[28] R. Sorrentino, "Transverse resonance technique," in *Numerical Techniques for Microwave and Millimeter-Wave Passive Structures*, T. Itoh, Ed. New York, NY, USA: Wiley, 1989, pp. 133–213.
[29] F. Bayatpur and K. Sarabandi, "Single-layer high-order miniaturized-element frequency-selective surfaces," *IEEE Trans. Microw. Theory Techn.*, vol. 56, no. 4, pp. 774–781, Apr. 2008.
[30] K. Sarabandi and N. Behdad, "A frequency selective surface with miniaturized elements," *IEEE Trans. Antennas Propag.*, vol. 55, no. 5, pp. 1239–1245, May 2007.
[31] J. Zha, Z. Y. Zhong, H. W. Zhang, Q. Y. Wen, and Y. X. Li, "Differences of band gap characteristics of square and triangular lattice photonic crystals in terahertz range," *J. Electron. Sci. Technol. China*, vol. 7, no. 3, pp. 268–271, 2009.
[32] P. R. Villeneuve and M. Piche, "Photonic band gaps in two-dimensional square and hexagonal lattices," *Phys. Rev. B*, vol. 46, no. 8, pp. 4969–4972, 1992.
[33] T.-T. Wu, C.-C. Chen, and T.-C. Lu, "Effects of lattice types on GaN-based photonic crystal surface-emitting lasers," *IEEE J. Sel. Topics Quantum Electron.*, vol. 21, no. 1, Jan./Feb. 2015, Art. no. 1700106.
[34] R. Antos and M. Veis, "Fourier factorization with complex polarization bases in the plane-wave expansion method applied to two-dimensional photonic crystals," *Opt. Exp.*, vol. 18, no. 26, pp. 27522–27524, 2010.

Mei Li (S'15) received the B.S. degree in electronic information science and technology from the Chengdu University of Information Technology, Chengdu, China, in 2010, and the Ph.D. degree in radio physics from the University of Electronic Science and Technology of China, Chengdu, in 2016.

She was a Visiting Graduate Student with the Applied Electromagnetics Research Group, University of California at San Diego, La Jolla, CA, USA, from 2014 to 2016. Her current research interests include reconfigurable antennas, phased arrays, artificial electromagnetic structures, and holographic metasurfaces.

Shaoqiu Xiao (M'05) received the Ph.D. degree in electromagnetic field and microwave engineering from the University of Electronic Science and Technology of China (UESTC), Chengdu, China, in 2003.

He joined UESTC as an Assistant Professor in 2004. From 2004 to 2006, he was with the Wireless Communications Laboratory, National Institute of Information and Communications Technology of Japan, Koganei, Japan, as a Researcher with the focus on the planar antenna and smart antenna design and optimization. From 2006 to 2010, he was an Associate Professor with UESTC, where he is currently a Professor. He has authored/co-authored more than 160 technical journals, conference papers, books, and book chapters. His current research interests include planar antenna and phased array, microwave passive circuits, and time reversal electromagnetics.

Jiang Long (S'11) received the B.S. and M.S. degrees from Zhejiang University, Hangzhou, China, in 2007 and 2010, respectively, and the Ph.D. degree from the University of California at San Diego, La Jolla, CA, USA, in 2015.

He is currently an RF Engineer with Skyworks Solution Inc., Woburn, MA, USA. His current research interests include non-Foster circuits in antenna/microwave applications, including non-Foster circuit loaded active fast-wave waveguides, broadband metasurfaces, broadband antennas, and active microwave components.

Dr. Long received the IEEE MTT-S Graduate Fellowship in 2015.

Daniel F. Sievenpiper (M'94–SM'04–F'09) received the B.S. and Ph.D. degrees in electrical engineering from the University of California at Los Angeles, Los Angeles, CA, USA, in 1994 and 1999, respectively.

He was the Director of the Applied Electromagnetics Laboratory with HRL Laboratories, Malibu, CA, USA, prior to 2010, where his research included in artificial impedance surfaces, conformal antennas, tunable and wearable antennas, and beam steering methods. He is currently a Professor with the University of California at San Diego, La Jolla, CA, USA, where his research focuses on antennas and electromagnetic structures. He holds more than 70 issued patents and over 80 technical publications.

Dr. Sievenpiper received the URSI Issac Koga Gold Medal in 2008. Since 2010, he has served as an Associate Editor of the IEEE *Antennas and Wireless Propagation Letters*.

IOP Publishing Journal of Physics D: Applied Physics

J. Phys. D: Appl. Phys. 51 (2018) 075101 (8pp) https://doi.org/10.1088/1361-6463/aaa55b

Theoretical design and analysis of wideband active hard electromagnetic surfaces using non-Foster circuit loaded anisotropic metasurfaces

Yunbo Li, Aobo Li and Daniel Sievenpiper

University of California, San Diego, La Jolla, CA 92093-0407, United States of America

E-mail: dsievenpiper@eng.ucsd.edu

Received 18 October 2017, revised 22 December 2017
Accepted for publication 5 January 2018
Published 25 January 2018

Abstract

The electromagnetic (EM) hard surface which can both support transverse electric and transverse magnetic surface wave modes has the important ability to reduce the EM blockage of metallic obstacles. We propose a method to design an electrically thin hard surface with wide bandwidth by loading with non-Foster elements. The wideband hard surface composed of an anisotropic impedance coating can be considered as a kind of active metasurface. We develop a method to determine the values of the loading non-Foster circuit which can minimize the dispersion of the unit cells. For this method, we derive accurate values for the loading non-Foster elements through theoretical analysis. We also determine the fundamental limitations on the bandwidth due to stability requirements. To verify our theoretical design, we simulate the transmission performance between the two ports on opposite sides of a metallic rhombus-shaped obstacle coated with the non-Foster based metasurface. The simulated results show that the blockage has been largely reduced over a broad bandwidth from 0.2 GHz to 1.5 GHz. Finally, we provide a discussion on how the resistive part of the non-Foster circuit can affect the performance of the wideband hard surface coating.

Keywords: anisotropic metasurface, electromagnetic hard surface, wideband design, non-Foster element

(Some figures may appear in colour only in the online journal)

Introduction

The electromagnetic (EM) hard surface [1] has the ability to guide transverse electric (TE) and transverse magnetic (TM) surface wave modes simultaneously. This is because the hard surface behaves as a perfect electric conductor (PEC) for TM mode illumination and as a perfect magnetic conductor (PMC) for TE mode illumination, so both propagating modes are supported. The electromagnetic soft surface has the opposite behavior, and prevents propagation of both polarizations [2]. Both TE and TM surface waves can smoothly pass around an obstacle coated with the hard surface, as illustrated in figure 1(a). Thus, the hard surface is usually used to reduce the electromagnetic blockage due to obstacles [3–5], such as the struts of a reflector antenna, which is shown in figure 1(b).

An artificial EM cloak [6–8] designed by the theory of transformation optics may have an analogous function to the hard surface. However, the design of the metamaterial-based cloaks suffers from large volume and requires complex effective permittivity and permeability. Recently, the mantle cloak [9–14] based on the theory of scattering cancelation has been proposed. The mantle cloak is very thin, but it can only conceal an electrically small object. Compared with these cloak

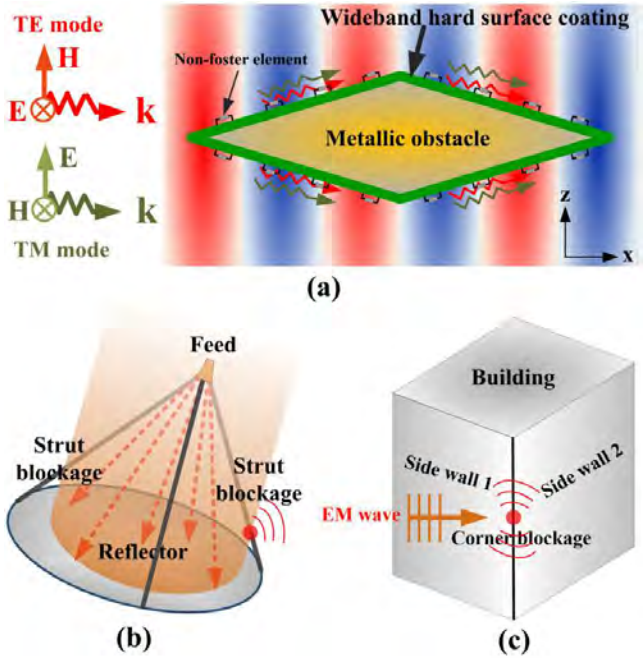

Figure 1. The schematic diagram of the non-Foster based wideband hard surface and its potential applications. (a) The performance of the hard surface. The hard surface can be applied in (b) reducing the strut blockage of the reflector antenna to improve aperture efficiency, and (c) reducing the corner blockage of buildings or other obstacles to increase communication quality.

designs, the hard surface can conceal large objects with an electrically thin coating, and for both polarizations simultaneously. However, it is limited in bandwidth.

The original design of the hard surface is illustrated in the corrugated waveguide [15]. The ideal hard surface can be created by a grid of parallel alternating PEC and PMC strips [16, 17]. A more practical design of the hard surface was also proposed [17]. They used the wide metal strips with via holes to simulate the corrugated structure but with a much thinner substrate. When the surface wave propagates along the surface, the metal strips with vias provide zero impedance (PEC) with broad bandwidth for TM surface waves, and the gap between the metal strips provides high impedance (PMC) but with narrow bandwidth for TE surface waves. The realization of high impedance by adding vias is similar to other kinds of high impedance surfaces [18–20]. However, there are no publications on wideband designs for a hard surface. Based on the design using metal strips with vias, the overall boundary condition of the hard surface will have broad bandwidth if the high impedance condition for TE waves can be realized with broad bandwidth. However, PMC surfaces realized using resonant structures are generally highly dispersive. For passive structures, the bandwidth is limited by the thickness and the permeability of the substrate [18, 21]. Thus, loading the surface with active circuits may be useful for increasing the bandwidth without increasing the thickness. The active non-Foster circuit which violates Foster's reactance theorem [22] has many applications for realizing large bandwidth in electromagnetic structures. Due to the negative capacitance and inductance that can be realized with these circuits, they can partly cancel the normal impedance of electromagnetic structures to decrease dispersion. The classic design for non-Foster circuits is proposed [23]. Two cross-coupled transistors are used to realize a negative impedance converter (NIC) which can transform a positive loading impedance into the negative impedance needed for our application. Initially, non-Foster circuits have been used in research to enhance the bandwidth of electrically-small antennas [24, 25]. In addition, broadband fast wave guides [26] and series-fed antenna arrays for squint-free beamforming [27] have been successfully realized. With the rapid increase of interest in metamaterials and metasurfaces, based on effective media theory and circuit concepts, non-Foster circuits can be applied to metamaterials to reduce their dispersion [28–30]. To begin the design, the stability of non-Foster loading should be analyzed [28]. A wideband artificial magnetic conductor (AMC) [32] has been built by loading a passive surface with active non-Foster integrated circuits (ICs). In addition, a wideband, low-dispersion, slow wave metasurfaces has been constructed with non-Foster circuits located on the back side [33].

This paper describes the first method for realizing a wideband electromagnetic hard surface using an anisotropic impedance surface [34–36] loaded with non-Foster elements. In the following sections, we will describe the performance of a wideband hard surface and its performance under dual-polarization illumination. Compared with a recently published non-Foster based wideband cloak [37], our proposed wideband hard surface has the advantage of polarization independence, applicability to electrically large objects, and broader bandwidth. For the design of the wideband unit cell, we realize wideband propagation of TE surface waves using a method similar to [33] and provide a theoretical analysis to determine the loading values for the non-Foster elements. According to the former design [1–3], wide metal strips with vias can have an intrinsically broad bandwidth for TM waves. Adding active circuits to this method, we create an anisotropic impedance surface to realize a hard boundary that supports wideband TM and TE surface waves simultaneously.

Method

To design the wideband hard surface, we first briefly introduce the theory of the EM hard surface. The structure of the metal strips with arrays of vias, which is shown in figure 2(a), is the classical and practical design for the hard surface. If an EM surface wave propagates along the x direction, for the TM mode (electric field in the x and z directions), the wide metal strips and the via array short the electric field, so the surface impedance seen by the TM mode is equal to zero. For the TE mode (electric field in the y direction), combining the inductance due to the grounded substrate and the capacitance provided by the gap between the metal strips, an effective LC resonant circuit is formed which provides high impedance at its resonance frequency. Thus, for waves propagating along the x-direction, the surface behaves as a hard surface [1] and supports propagation of both polarizations.

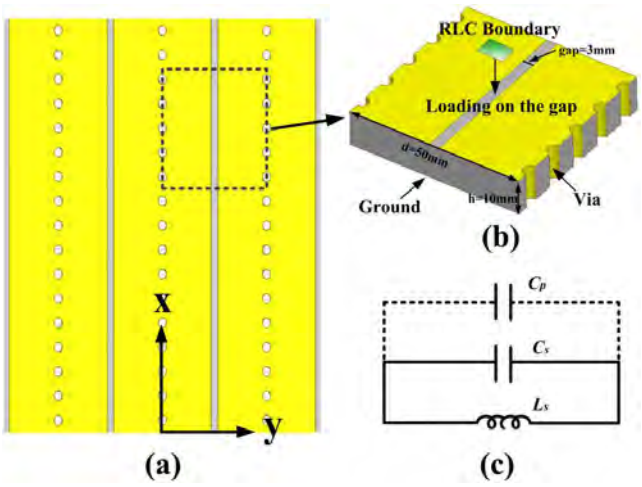

Figure 2. (a) The practical design of the EM hard surface. (b) The unit cell of the hard surface. The yellow area represents metal and the gray area represents the substrate. The loss tangent is considerably small within the operating bandwidth (0.15–0.5 GHz), and is therefore neglected in the analysis. For the design using the synthesized method, an RLC boundary is applied at the gap. (c) The effective circuit of the unit cell when loading capacitors at the gap.

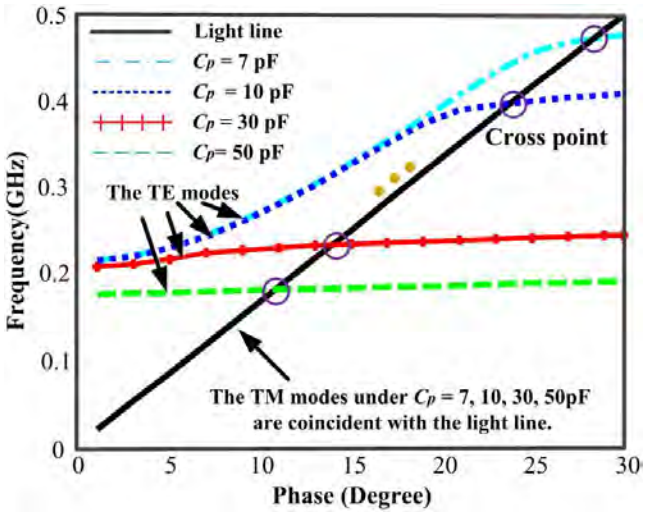

Figure 3. The different dispersive curves for various values of C_p under TE and TM illumination. The black line is the light line which represents propagation along a PEC for the TM mode and along a PMC for the TE mode.

The via array in figure 2(a) has the same function as a vertical metal wall, which would not be practical for fabrication. Thus, the metal strips with via array are similar to a corrugated surface, but this structure is simpler to fabricate. In addition, because the surface impedance seen by the TM mode is already zero over a wide bandwidth, only the TE mode must be controlled with the design of the non-Foster circuit.

To determine the non-Foster circuit parameters, we introduce an RLC boundary at the gap between the metal strips with an impedance representing a positive capacitance, so the effective circuit of the surface is shown in figure 2(c). The C_s and L_s represent the capacitor and the inductor of the original structure respectively. The C_p represents the additional loading capacitor modeled by the RLC boundary in the HFSS solver. The resistor R is initially set to zero, but the effects of ohmic losses will be carefully evaluated later. The added capacitance can also be considered as a test capacitor which can tune the resonance frequency of the TE mode. This is similar to the method used by Zhu and Ziolkowski [25] to match small antennas, and also used by Long in the design of broadband impedance surfaces [33]. We use the eigen-mode solver of HFSS to determine the dispersion curves of the structure for both TE and TM modes, and the results are shown in figure 3 for propagation along the x-axis.

The TM mode dispersion curve is coincident with the light line, and independent of the value of C_p according to the theory of the hard surface which is discussed above. However, the TE mode dispersion curves depend on the value of C_p. The points where the TE dispersion curves cross the light line are shown in figure 3 for various values of loading capacitance. If C_p is replaced by a voltage-tunable varactor, a tunable hard surface could be realized. However, for a wideband design, we extract the frequencies at each crossing point and calculate the relevant impedances corresponding to the loading capacitors. By plotting the variation of required loading impedance with frequency, we find that the required impedance decreases with increasing frequency, corresponds to a non-Foster circuit. By fitting the values at the cross points shown in figure 3, we can obtain the appropriate loading values of the non-Foster circuit, which is composed of a parallel $C_{neg} = -0.3$ pF and $L_{neg} = -15.5$ nH. The fitting results shown in the figure 4 have good agreement with the original data. The extracted values of the non-Foster circuit are not particularly sensitive, allowing for some deviation in our design which will be discussed later. If we replace the RLC boundary at the gap with our extracted non-Foster values, we can realize a wideband design for TE surface waves. Using the eigenmode simulation, we obtain the ultra-wideband dispersion curves which are close to the light line for both the TE and TM modes, shown in figure 5. Thus, we have completed the theoretical wideband hard surface design. The bandwidth is limited at the low frequency end by the dotted line shown in figure 5, and at the high frequency end by the resonance frequency (2.33 GHz) of non-Foster circuit itself.

To verify that the two wideband dispersion curves are actually the TE and TM modes respectively, we have checked the E-field for different phase delays across the unit cell. In figure 6(a), the directions of the E-field are along the y-axis, so the surface wave is a TE mode; in figure 6(b), the directions of the E-field are along the z-direction, and the surface wave is a TM mode.

After having determined the required values for the non-Foster element, we now provide a general theoretical analysis of the design approach. First, we assume the non-Foster element is modeled by a parallel L–C circuit. To realize the wideband TE surface wave mode, the loaded positive capacitor C_p should have the same impedance as the parallel C_{neg} and L_{neg} at the same frequency. Thus,

$$\frac{1}{j\omega_0 C_p} = j\omega_0 L_{neg} \parallel \frac{1}{j\omega_0 C_{neg}} = \frac{j\omega_0 L_{neg}}{1-\omega_0^2 L_{neg} C_{neg}} \qquad (1)$$

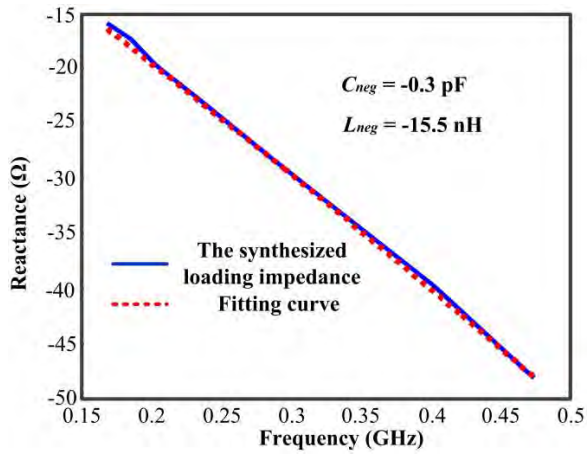

Figure 4. The fitting method to determine the values of the loaded non-Foster element..

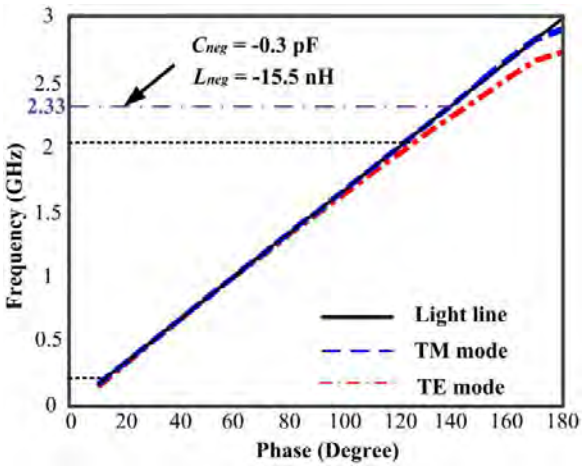

Figure 5. The results of the wideband dispersion curves which are close to the light line under both TE and TM illumination when the surface is loaded with non-Foster elements.

where ω_0 is the angular frequency. In addition, due to the effective circuit model of the surface, the surface impedance for the TE mode when loaded with C_p can be expressed as

$$Z_{TE} = \frac{j\omega_0 L_s}{1 - \omega_0^2 L_s(C_s + C_p)} \tag{2}$$

where L_s and C_s are the original effective parallel inductance and capacitance in the surface respectively. Combining equations (1) and (2), we can obtain the relationship between circuit elements,

$$L_{neg}C_{neg} - L_sC_s = C_p(L_s + L_{neg}) + \frac{\sqrt{L_{neg}(C_{neg} - C_p)}}{Z_{TE}} \tag{3}$$

in which, ω_0 has been eliminated. If Z_{TE} is infinite which means the resonance condition is achieved, equation (3) can be simplified to

$$L_{neg}C_{neg} - L_sC_s = C_p(L_s + L_{neg}). \tag{4}$$

Because C_p can be considered as a test capacitor, if we want to ensure equation (4) is enforced while changing the values of C_p, the conditions given in equation (5) should be satisfied.

$$L_{neg} = -L_s, C_{neg} = -C_s. \tag{5}$$

That means if we want to realize a wideband TE surface wave mode which is close to the light line, we should load the surface with a parallel non-Foster inductor and capacitor which are given by equation (5). Considering the stability conditions [31] for non-Foster circuits, we must ensure that $|L_{neg}| > L_s$ and $|C_{neg}| < C_s$. Thus, in actual design, we can only use values for the non-Foster circuit elements which have small but finite deviations from the theoretical solutions.

If Z_{TE} is not infinite, equation (3) cannot be simplified, and it can be rearranged as

$$C_p^2(L_s + L_{neg})^2 + [\frac{L_{neg}}{Z_{TE}^2} - 2(L_{neg}C_{neg} - L_sC_s)(L_s + L_{neg})] \times C_p + 2(L_{neg}C_{neg} - L_sC_s)^2 - \frac{L_{neg}C_{neg}}{Z_{TE}^2} = 0. \tag{6}$$

If we want to ensure equation (6) while changing the values of C_p, the conditions given in equation (7) should be satisfied.

$$L_{neg} = -L_s = 0 \tag{7}$$

which has no meaning in actual applications. That is to say, we can only determine the values of the parallel negative inductor and capacitor for a TE mode which is close to the light line. For the design of a wideband Z_{TE} which is not infinite, the non-Foster circuit model may be more complex rather than a simple parallel negative inductor and capacitor. The theoretical determination of the loading values of the non-Foster circuit can not only apply in the design of the wideband surface wave structures, but also in the design of other kinds of metasurfaces such as AMCs. We only need to use equation (5) to design a wideband structure considering the non-Foster stability condition. Thus, in figure 4, we only need the resonant crossing points to determine the loading values of the non-Foster circuit, and then we can reasonably realize a wideband design using equations (1) and (5).

We can also discuss the limitation of the bandwidth of the TE mode. Based on the effective parallel L–C circuit model, the TE mode can switch from the fast wave region to the slow wave region near the resonance frequency. After loading the structure with the non-Foster circuit, it still appears as a parallel L–C circuit. Thus, the lower limit of the bandwidth is determined by the resonance frequency of the total circuit model, which is given as

$$\omega_{lower} = \frac{1}{\sqrt{(L_s \parallel L_{neg})(C_s \parallel C_{neg})}}. \tag{8}$$

Note that it is not possible to set the lower limit to zero, because at this point the non-Foster circuit elements match the effective circuit values of the original surface, which is also the limit of stability for the non-Foster circuits. Thus, there is a tradeoff between achieving a broad bandwidth, particularly at the low frequency end, and keeping the non-Foster circuits stable.

The upper limit of the bandwidth is determined by the period of the unit cells. When the size of the unit cell is larger than about ¼ to ½ wavelength, the dispersion curve of the TE mode will start to deviate from the light line. That is

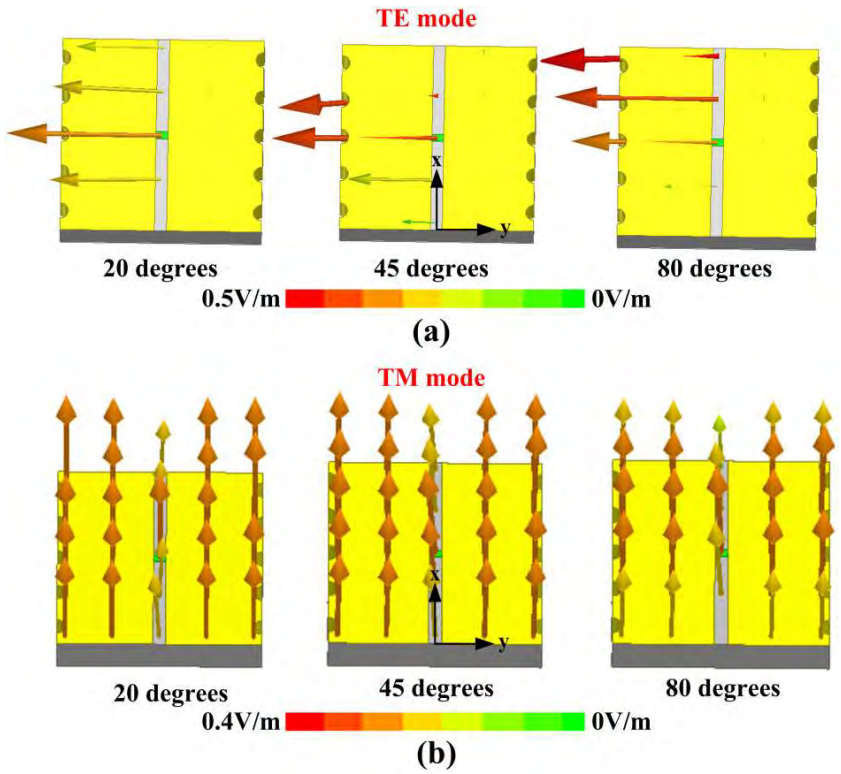

Figure 6. The E-field check for cases of 20, 45, 80 degrees of phase delay. (a) TE mode surface wave. (b) TM modes surface wave.

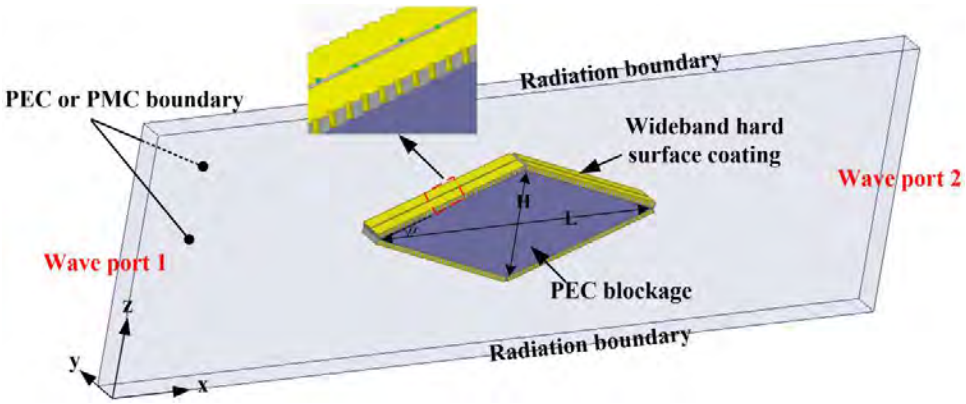

Figure 7. The simulated geometry in HFSS for the driven mode solver. We set $L = 563.8$ mm, H $= 205.2$ mm and $\alpha = 20$ degrees in this simulated structure.

because the effective circuit model will not apply when the spatial variation of the fields across the unit cells is too high. Furthermore, the resonance frequency of the non-Foster circuit itself is the ultimate upper limit, if it is lower than the frequency corresponding to ¼ wavelength per unit cell.

Results and discussions

To verify the wideband design of the hard surface, we have simulated a 2D PEC object coated with the hard surface which is shown in figure 7.

We locate the PEC blockage in the middle of an air box. Since we are interested in the analysis of electrically large objects, a 2D infinitely long structure has been simulated. This would allow us to considerably reduce the computational burden required by full-wave simulations of a large finite-size structure. To imitate a 2D infinitely long strut, we set the boundary on both sides of the air box to PEC or PMC for TE or TM mode illumination respectively. The transmit and the receive ports are wave port 1 and 2 respectively. Wideband hard surfaces loaded with non-Foster elements are coated on the PEC blockage. We then simulate the *E*-field in the air box and the transmission characteristics from port 1 to port 2.

Using our design method, we can find the approximate effective circuit for the structure, which is the parallel combination of $L_s = 15.15$ nH and $C_s = 0.73$ pF, and we set the non-Foster circuit elements to be close to these values according to equation (5). We use 24 unit cells of the non-Foster based wideband hard surface to coat the PEC blockage, with 6 unit cells on each edge. Note that the connections between the

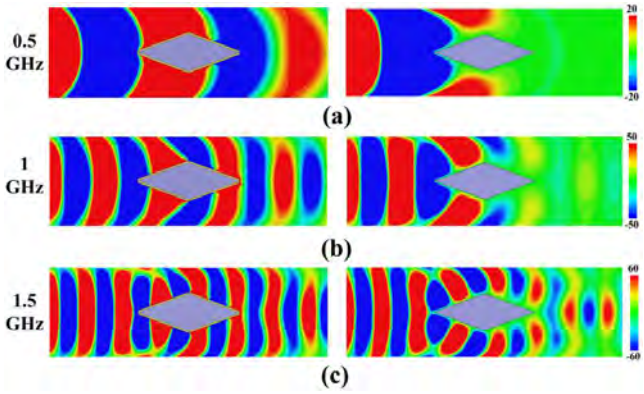

Figure 8. The performance comparison between the coated PEC (left side) and pure PEC (right side) obstacles under the TE mode illumination.

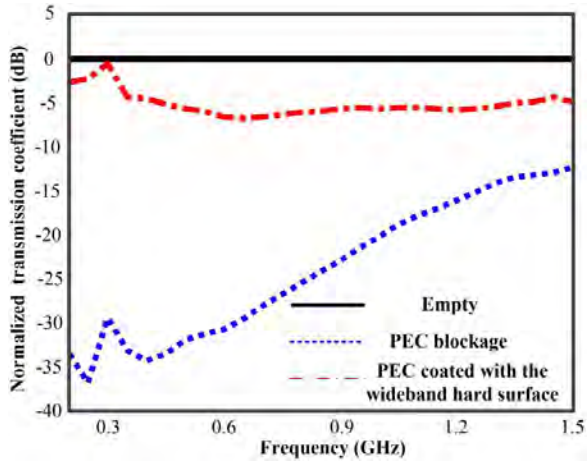

Figure 9. The comparison of the two-port TE-wave transmission coefficients when loaded with the coated PEC and the pure PEC normalized to the empty case (without the obstacle) and simulated over wide bandwidth.

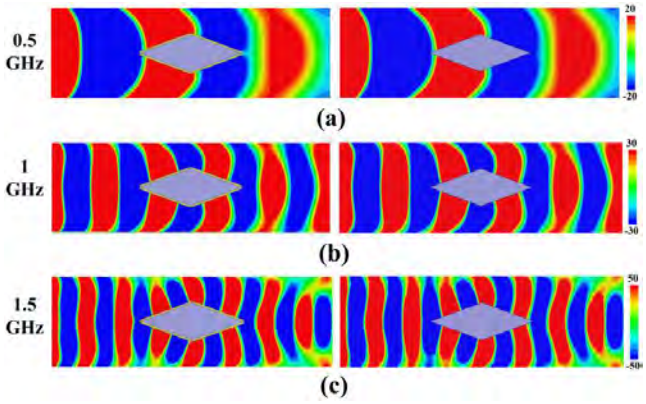

Figure 10. The performance comparison between the coated PEC (left side) and pure PEC (right side) obstacles under the TM mode illumination.

two edges are not smooth nor continuous across the corners, and this may affect ability of the active hard surface to reduce scattering. To maximize the transmission performance, we optimize and sweep the values of the loading non-Foster elements to find the best results. Finally, the parallel combination

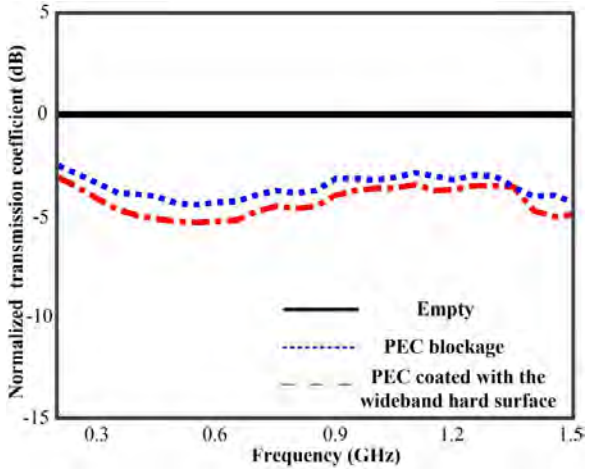

Figure 11. The comparison of the two-port TM-wave transmission coefficients when loaded with the coated PEC and the pure PEC normalized to the empty case (without the obstacle) and simulated over wide bandwidth.

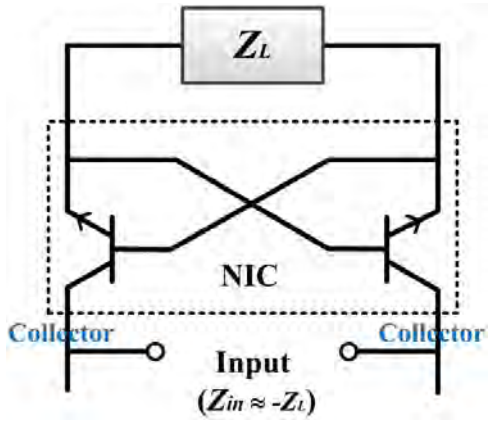

Figure 12. The topology of the SCS type NIC circuit. The Z_L is the load impedance which will be converted to $-Z_L$. The input port is at the collector of the transistors.

of $L_{neg} = -15.5$ nH and $C_{neg} = -0.7$ pF are chosen as the loading values of the non-Foster element.

The results of the *E*-field in the air box with TE mode illumination are shown in figure 8 where we have compared the performance between the coated PEC obstacle and the uncoated one. We can clearly see that the wave can pass smoothly around the PEC obstacle coated with the hard surface at three widely separated frequency points. This is in contrast to the original PEC object which strongly scatters TE waves, causing low transmission between the two ports. Also, we have shown the comparison of the transmission properties between the coated PEC obstacle and the uncoated one from 0.2–1.5 GHz under TE mode illumination in figure 9. We find that the blockage of the PEC obstacle is largely reduced over a wide bandwidth. For the TM mode illumination, the behavior of the hard surface is close to the PEC. The performances of the coated PEC and the uncoated one shown in the figures 10 and 11, respectively, are nearly identical over wide bandwidth as we expect. Thus, the wideband hard surface has been theoretically designed and demonstrated in full-wave simulation.

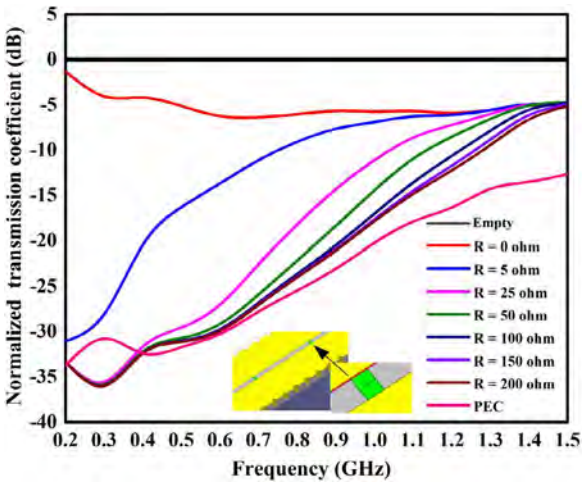

Figure 13. The comparison of the two-port TE-wave normalized transmission coefficients by changing the values of the resistors in the non-Foster circuit under the wideband.

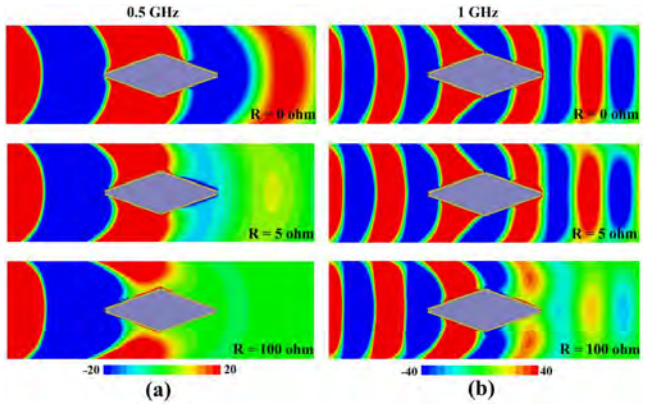

Figure 14. The performance comparison by changing the values ($R = 0$, 5, 100 ohms) of the resistors in the non-Foster circuits at two frequencies (a) 0.5 GHz and (b) 1 GHz.

To load a real non-Foster circuit at the gap between the metal strips, while taking the circuit stability into account, we prefer the floating SCS (short circuit stable) type NIC which is shown in figure 12. Following Linvill's initial idea [23], the input port is set as the two collectors of the BJT-type transistors. Bias circuits are not shown. The NIC circuit can convert Z_L into $-Z_L$ as seen at the input port.

However, in reality Z_{in} which is shown in figure 12 is composed of not only the reactance component, but also with the resistive component which can reduce the transmission performance. To simulate a real NIC circuit, we set two series RLC boundaries (shown in figure 13) in HFSS to be the parallel −L–C and the resistor elements respectively. We show the full-wave simulation results of the normalized transmission coefficient in figure 13, including the influence of the resistor. We can find that if the resistor in the real non-Foster circuit is large ($R = 200$ ohm), the performance of the transmission under TE mode illumination will be reduced. However, small resistor values ($R = 5$ ohm) will not significantly affect the performance. Observing the TE mode *E*-field in the air box in figure 14, by comparing the performances at the two frequencies, we can find that transmission of the TE mode is more significantly affected by any resistance in the circuit at lower frequencies. Thus, the performance of the wideband hard surface is related to the value of Q of the non-Foster circuit design. Because reducing the Q is one way to achieve stability, there is a tradeoff between high performance and stability in the actual design. The transmission performance is not reduced by introducing a resistor in the non-Foster circuit for TM mode illumination because the TM mode primarily sees the continuous metal strips, so it is unnecessary to show the corresponding results here.

Future designs of active hard surfaces based on non-Foster circuits should ideally be based on integrated circuit technology [32]. This is due to the lower parasitics compared to designs based on discrete devices, as well as higher operating frequencies and higher Q that is achievable in a smaller area.

Conclusions

We have proposed a method to realize a wideband hard electromagnetic surface based on the classic design by Kildal by loading it with non-Foster circuit elements. The design method is based on tuning the unit cell with a positive capacitance, and tracking the frequency at which the dispersion curve crosses the light line. This then provides a required reactance versus frequency, which can be implemented with a parallel resonant −L–C non-Foster circuit. The result is a surface which supports both TM and TE waves close to the light line over a broad bandwidth. We have also derived the theoretical formula for the −L and −C elements, and found that they ideally match the original inductance and capacitance of the passive surface. We also determine the bandwidth limitations of the surface, which is governed at the low frequency end by the stability of the non-Foster circuit, and at the high frequency end by the −L–C resonance, and the unit cell size. To verify our design, we simulate a PEC obstacle coated with a wideband active hard surface, and the simulated results show that both TE and TM modes can pass over the obstacle smoothly over a wide bandwidth when the loaded non-Foster elements are ideal. Finally, we show that resistance in non-ideal non-Foster elements can reduce the performance of the wideband hard surface, particularly at the low frequency end of the operating band.

Acknowledgment

This work was supported in part by the Air Force Office of Scientific Research grant FA9550-16-1-0093. National Science Foundation under Grant 1306055.

ORCID iDs

Yunbo Li https://orcid.org/0000-0001-5353-2156
Aobo Li https://orcid.org/0000-0003-4726-2756

References

[1] Kildal P S 1998 *Electron. Lett.* **24** 168
[2] Kildal P-S, Kishk A and Maci S 2005 *IEEE Trans. Antennas Propag.* **53** 1
[3] Kildal P S, Kishk A A and Tengs A 1996 *IEEE Trans. Antennas Propag.* **44** 150
[4] Rajo-Iglesias E, Fernandez J M and Sierra-Castaner M 2009 *IEEE Antennas Wireless Propag. Lett.* **8** 1402
[5] Fernandez J M, Rajo-Iglesias E and Sierra-Castaner M 2009 *Prog. Electromagn. Res.* **99** 179–94
[6] Pendry J B, Schurig D and Smith D R 2006 *Science* **312** 1780
[7] Schurig D *et al* 2006 *Science* **314** 977
[8] Kanté B, Germain D and de Lustrac A *Phys. Rev.* B **80** 201104
[9] Alù A 2009 *Phys. Rev.* B **80** 24115
[10] Chen P Y and Alù A 2011 *Phys. Rev.* B **84** 205110
[11] Liu S, Xu H X, Zhang H C and Cui T J 2014 *Opt. Express* **22** 13403
[12] Wang J, Qu S, Xu Z, Zhang A, Ma H, Zhang J, Chen H and Feng M 2014 *Photonics Nanostruct. Fundam. Appl.* **12** 130–7
[13] Wang J, Qu S, Xu Z, Ma H, Zhang J, Li Y and Wang X 2013 *IEEE Trans. Antennas Propag.* **61** 748
[14] Liu S, Zhang H C, Xu H X and Cui T J 2014 *J. Opt. Soc. Am.* A **31** 9
[15] Kildal P S 1990 *IEEE Trans. Antennas Propag.* **38** 1537
[16] Maci S and Kildal P-S 2004 *Proc. URSI-IEEE AP-S Symp. Monterrey (CA)* p 285
[17] Kildal P S and Kishk A 2003 *Appl. Comput. Electromagn. Soc. J.* **18** 32
[18] Sievenpiper D, Lijun Z, Broas R F J, Alexopolous N G and Yablonovitch E 1999 *IEEE Trans. Microw. Theory Tech.* **47** 2059
[19] Lockyear M J, Hibbins A P and Sambles J R 2009 *Phys. Rev. Lett.* **102** 073901
[20] Dockrey J A *et al* 2013 *Phys. Rev.* B **87** 125137
[21] Rozanov K N 2000 *IEEE Trans. Antennas Propag.* **48** 1230
[22] Foster R M 1924 *Bell Syst. Tech. J.* **3** 259
[23] Linvill J G 1953 *Proc. IRE* **41** 725
[24] Sussman-Fort S E and Rudish R M 2009 *IEEE Trans. Antennas Propag.* **57** 2230
[25] Zhu N and Ziolkowski R W 2011 *IEEE Antennas Wireless Propag. Lett.* **10** 1582
[26] Long J, Jacob M M and Sievenpiper D F 2014 *IEEE Trans. Microw. Theory Tech.* **62** 789
[27] Mirzaei H and Eleftheriades G V 2015 *IEEE Trans. Antennas Propag.* **63** 1997
[28] Weldon T, Miehle K, Adams R and Daneshvar K 2012 *Proc. IEEE* 1–5
[29] Hrabar S, Krois I, Bonic I and Kiricenko A 2013 *Appl. Phys. Lett.* **102** 054108
[30] Saadat S, Adnan M, Mosallaei H and Afshari E 2013 *IEEE Trans. Antennas. Propag.* **61** 1210
[31] Ugarte-Muñoz E, Hrabar S, Segovia-Vargas D and Kiricenko A 2012 *IEEE Trans. Antennas Propag.* **60** 3490
[32] Gregoire D J, White C R and Colburn J S 2011 *IEEE Antennas Wireless Propag. Lett.* **10** 1586
[33] Long J and Sievenpiper D 2016 *IEEE Trans. Antennas Propaga.* **64** 3003
[34] Fong B H, Colburn J S, Ottusch J J, Visher J L and Sievenpiper D 2010 *IEEE Trans. Antennas Propag.* **58** 3212
[35] Wan X, Shen X, Luo Y and Cui T J 2014 *Laser Photonics Rev.* **8** 757
[36] Wan X *et al* 2016 *Adv. Opt. Mater.* **4** 1567
[37] Chen P Y, Argyropoulos C and Alù A 2013 *Phys. Rev. Lett.* **111** 233001

Surface-Wave Coupling and Antenna Properties in Two Dimensions

Chao Wang, *Student Member, IEEE*, En Li, *Member, IEEE*, and Daniel F. Sievenpiper, *Fellow, IEEE*

***Abstract*— Antennas are characterized by their gain and effective aperture area, and the coupling between two antennas in 3-D free space is governed by the Friis transmission equation. In this paper, we derive the properties of antennas in 2-D space, and the equivalent coupling equation. This is useful for evaluating surface-wave coupling between antennas that share the same ground plane or substrate. We propose a quantity which is the effective width for surface-wave coupling, and derive its value for an isotropic surface-wave radiator in two dimensions. We also determine the surface-wave directivity for dipole-like modes, which is relevant to many small planar antennas. The total coupling between two coplanar antennas is a combination of surface waves and space waves, and these two components are distinguished in simulations by calculating antenna coupling as a function of distance. Several simple examples are illustrated including patch and monopole antennas on various substrates. Quantifying the effective surface wave width can serve as a useful tool for optimizing the coupling between coplanar antennas.**

***Index Terms*— Effective aperture, effective width, gain, mutual coupling, surface waves, transmission equation.**

I. Introduction

MUTUAL coupling often occurs between antennas that share the same substrate or ground [1]–[3], and it plays an important role in many applications such as arrays, multi-in multi-out systems, or other colocated communication systems that share the same ground plane. Mutual coupling may increase the signal correlation among antennas and reduce the efficiency of multiantenna systems [4]–[7]. The coupling between antennas can be attributed to three components: 1) near-field coupling, in which the fields decay with distance as ρ^{-2} or ρ^{-3}; 2) free-space coupling, which has ρ^{-1} dependence; and 3) surface-wave coupling where the fields decay as $\rho^{-1/2}$ [8]. In order to design antennas to have low mutual coupling, it is useful to distinguish between the different kinds of mutual coupling and to have a method to quantify their effects.

Near-field coupling occurs when one antenna is in the reactive near-field zone of another antenna, which extends to a radius of roughly $\lambda/2\pi$. This kind of coupling dominates when antennas are closely spaced [9], but is insignificant at greater distances due to the rapid decay of the near-field components. Free-space wave coupling is due to the standard antenna radiation in the horizontal direction, propagating parallel to the substrate. This kind of coupling can be efficiently reduced only if the antenna radiation in horizontal directions is suppressed, such as by designing the antenna to have low gain toward the horizon. Surface-wave coupling is due to surface waves which are guided by the substrate and the ground plane [10]. This kind of coupling dominates at longer distances, or when other coupling components have already been minimized. There have been several attempts to reduce mutual coupling, especially surface-wave coupling between antenna elements. For example defected ground structures have been implemented by etching slots of different shapes in the ground plane [11]–[14] and using electromagnetic bandgap structures to reduce the surface waves [15]–[17]. Other approaches to reduce the surface-wave coupling include high-impedance surfaces [18], [19] or soft surfaces [20], [21]. However, the free-space coupling and surface-wave coupling mechanisms and their contributions are not clearly distinguished in previous papers.

In this paper, we introduce the effective width of an antenna which characterizes how strongly it couples to surface waves, and calculate the effective width of an isotropic surface-wave radiator. We then determine the directivity of a surface-wave radiator with a dipole-like distribution, which is different from its directivity for free-space waves. We then use these results to determine the 2-D equivalent to the Friis transmission equation, which characterizes the surface-wave coupling component between two antennas. Finally, we provide simulations of several simple examples and evaluate them in terms of effective width and effective aperture. It is expected that the approach presented here will be useful for designing antennas with low mutual coupling because it will enable the designer to identify the relative strength of the different coupling components in order to optimize the design. For example, this approach can help to illustrate whether additional coupling reduction can be obtained by further reducing surface-wave effects, or to design the maximum allowable substrate thickness or permittivity for a given antenna configuration.

II. 2-D-Surface-Wave Transmission Equation

A. Antenna Effective Aperture From Blackbody Radiation

Our first goal is to calculate the 2-D effective width of an antenna for transmitting or receiving surface waves. This quantity $W_{\text{eff}} = G_2 W_i$ is the product of the effective width W_i of

Manuscript received September 23, 2016; revised April 22, 2017; accepted August 6, 2017. Date of publication August 11, 2017; date of current version October 5, 2017. This work was supported in part by the National Natural Science Foundation of China under Grant 61671123 and Grant 61001027, in part by AFOSR Contract FA9550-16-1-0093, and in part by the China Scholarship Council. *(Corresponding author: Chao Wang.)*

C. Wang is with the School of Electronic Engineering, University of Electronic Science and Technology, Chengdu 611731, China, and also with the University of California, San Diego, La Jolla, CA 92093 USA (e-mail: chaowang-alvin@outlook.com).

E. Li is with the School of Electronic Engineering, University of Electronic Science and Technology, Chengdu 611731, China (e-mail: lien@uestc.edu.cn)

D. F. Sievenpiper is with the University of California at San Diego, La Jolla, CA 92130 USA (e-mail: dsievenpiper@eng.ucsd.edu).

Color versions of one or more of the figures in this paper are available online at http://ieeexplore.ieee.org.

Digital Object Identifier 10.1109/TAP.2017.2738030

an ideal 2-D isotropic radiator, and a 2-D gain component G_2. In this paper, the subscript 2 is used to distinguish this term from the 3-D directivity associated with free-space waves. The term W_{eff} is analogous to the effective aperture in three dimensions. Thus, it would seem straightforward to simply follow the derivation of the effective aperture for an isotropic radiator, but with reduced dimensionality. Unfortunately, nearly all texts on this subject base the derivation on calculating the effective aperture of an infinitesimal dipole, and dividing by its directivity. Fortunately, an alternative method exists based on the power radiated and received by an ideal blackbody, and this approach is amenable to derivation with reduced dimensionality. The 3-D derivation is briefly summarized here to illustrate that it produces the intended result, and then repeated for the 2-D case.

We begin by outlining the Rayleigh–Jeans law for the spectral brightness of a blackbody radiator [22]. In a 3-D cubical cavity of length a, the allowable modes are defined by

$$n_x^2 + n_y^2 + n_z^2 = \left(\frac{2a}{\lambda}\right)^2. \tag{1}$$

Note that this is the standard starting point to calculate density of states in three dimensions, and is not related to the final size or shape of the antenna or radiating structure. The mode frequencies are

$$f = \frac{c}{\lambda} = \frac{cr}{2a} \tag{2}$$

where

$$r^2 = n_x^2 + n_y^2 + n_z^2. \tag{3}$$

The modes between f and $f + df$ are

$$N(f)df = \frac{4\pi r^2 dr}{8} \times 2 \tag{4}$$

where the factor of 2 is due to the two possible polarizations, and the factor of 1/8 is because we only need to consider positive indices for n, so we only integrate over 1/8 of the sphere in n-space.

Each mode has energy kT, so the spectral energy density assuming a cavity volume of a^3 is

$$u_f(T)df = \frac{N(f)df}{a^3} kT. \tag{5}$$

And

$$u_f(T) = \frac{8\pi a^3}{a^3}\frac{f^2}{c^3} kT = 8\pi kT \frac{f^2}{c^3}. \tag{6}$$

Because the radiation travels at velocity c, the spectral energy density is related to the spectral brightness B_3 as

$$u = \frac{1}{c}\int_{4\pi} B_3 d\Omega = \frac{4\pi}{c} B_3 \tag{7}$$

which has units of W/(sr m^3 Hz).

Thus

$$\frac{4\pi}{c} B_3 = u_f(T) = 8\pi kT \frac{f^2}{c^3}. \tag{8}$$

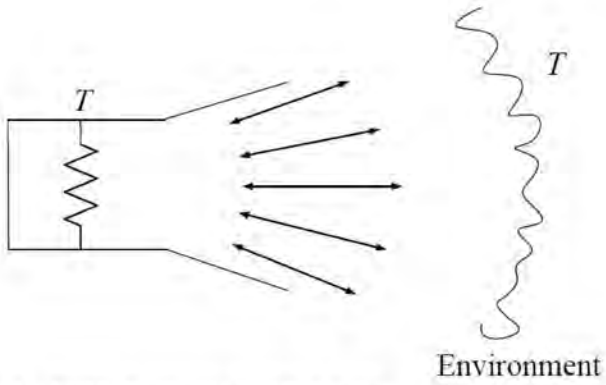

Fig. 1. Blackbody thermal equilibrium model.

And

$$B_3 = \frac{2kTf^2}{c^2} = \frac{2kT}{\lambda^2} \tag{9}$$

which is the Rayleigh–Jeans law [23], [24].

Now assume an isotropic antenna matched with a resistor at temperature T, which is in thermal equilibrium with its environment. It will radiate energy kT from the resistor, and it will receive an equal amount of energy from the environment, shown in Fig. 1. Using the spectral brightness calculated above, we can integrate over 4π steradians to determine the effective aperture A_e of an isotropic radiator. Because half of the power is radiated into one polarization, we divide B_3 by 2 to determine the effective aperture of an isotropic antenna for a single polarization

$$\frac{1}{2}\int B_3 d\Omega = \frac{1}{2}\int \frac{2kT}{\lambda^2} d\Omega = A_e 4\pi \frac{kT}{\lambda^2} = kT. \tag{10}$$

And

$$A_e = \frac{\lambda^2}{4\pi}. \tag{11}$$

This is consistent with the effective aperture calculated using other methods. The maximum effective aperture A_{eff} of any antenna is related to its gain G_3 by

$$A_{\text{eff}} = A_e \cdot G_3 = \frac{\lambda^2}{4\pi} G_3. \tag{12}$$

This density of states-based approach is also amenable to two dimensions, such as for surface-wave problems. We now apply this approach to determine the effective width of an isotropic radiator in two dimensions. This is also the effective width of an infinite line source in 3-D space.

B. Calculate the Effective Width for Surface Waves

In two dimensions, a square cavity has modes defined by

$$n_x^2 + n_y^2 = \left(\frac{2a}{\lambda}\right)^2 \tag{13}$$

and allowable frequencies

$$f = \frac{cr}{2a} \tag{14}$$

where

$$r^2 = n_x^2 + n_y^2. \tag{15}$$

The modes between f and $f+df$ are

$$N(f)df = \frac{2\pi r dr}{4} \times 2 \tag{16}$$

where we have integrated over 1/4 of the circle in n-space, and have included two polarizations.

The 2-D spectral energy density is

$$u_f(T)df = \frac{N(f)df}{a^2}kT. \tag{17}$$

And

$$u_f(T) = \frac{4\pi a^2}{a^2}\frac{f}{c^2}kT = 4\pi\frac{f}{c^2}kT. \tag{18}$$

The 2-D spectral brightness is

$$u = \frac{1}{c}\int_{2\pi} B_2 d\theta = \frac{2\pi}{c}B_2 \tag{19}$$

with units of W/(rad m^2 Hz).

Thus

$$\frac{2\pi}{c}B_2 = u_f(T) = 4\pi\frac{f}{c^2}kT. \tag{20}$$

And

$$B_2 = 2kT\frac{f}{c} = \frac{2kT}{\lambda}. \tag{21}$$

For an isotropic surface-wave radiator and one polarization, we multiply by the effective width W_i, and integrate over 2π to obtain the total radiated power, which is equal to kT

$$\frac{1}{2}\int B_2 d\theta = \frac{1}{2}\int \frac{2kT}{\lambda}d\theta = W_i 2\pi\frac{kT}{\lambda} = kT. \tag{22}$$

Thus, the effective width for an isotropic surface-wave radiator is found to be

$$W_i = \frac{\lambda}{2\pi}. \tag{23}$$

C. Calculate the Maximum Directivity and Maximum Effective Width of Antenna

As we know, the directivity of classic dipole antenna is 1.5 in free space

$$D_3 = \frac{4\pi}{\int_0^{2\pi}\int_0^{\pi}\sin^2\theta\sin\theta d\theta d\varphi} = 1.5. \tag{24}$$

For the 2-D case, we follow the 3-D case but only integrate over the azimuth. The surface-wave directivity of a dipole mode, that is, parallel to the surface is 2

$$D_2 = \frac{2\pi}{\int_0^{2\pi}\sin^2\varphi d\varphi} = 2. \tag{25}$$

For a vertical monopole antenna, the surface-wave directivity is $D_2 = 1$. Note that this is because the vertical null does not appear in the plane of the surface, so the antenna is isotropic with respect to surface waves.

In general, the maximum effective width W_{eff} of any antenna is related to its gain G_2 by

$$W_{\text{eff}} = W_i \cdot G_2 = \frac{\lambda}{2\pi}G_2. \tag{26}$$

Thus, when (26) is multiplied by the linear power density of the incident wave (in W/m), it leads to the maximum surface-wave power that can be delivered to the load. This assumes that there are no conductive or dielectric losses, the antenna is matched to the load, and the polarization of the impinging wave matches that of the antenna. For a transmitting antenna, this also assumes that all of the power couples into surface waves. Losses, polarization mismatch, and surface-wave coupling efficiency can be combined into a single-efficiency term, and gain is related to directivity D_2 and efficiency ζ_2 in the same way as in 3-D

$$G_2 = \zeta_2 D_2. \tag{27}$$

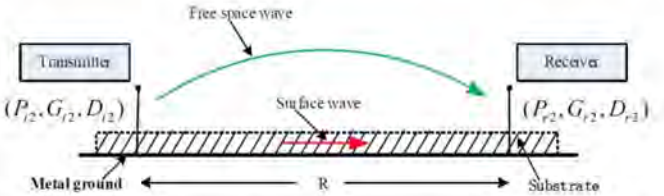

Fig. 2. Geometrical orientation of transmitting and receiving antennas for the transmission equation.

D. Calculate the 2-D-Surface-Wave Transmission Equation

The 2-D surface-wave transmission equation for mutual coupling between antennas relies on the transmitted and received power of the two array antennas placed in a distance. Referring to Fig. 2, let us assume that the transmitter is initially isotropic. If the input power at the terminals of the transmitting antenna is P_{t2}, then its maximum transmitted power density can be written as

$$S_{t2} = \frac{P_{t2}\zeta_{t2}D_{t2}}{2\pi R} = \frac{P_{t2}G_{t2}}{2\pi R} \tag{28}$$

where G_{t2} is the gain and D_{t2} is the directivity in the direction of the maximum of the surface wave. The maximum effective width W_{eff} of the receiving antenna is related to its efficiency ζ_{r2} and directivity D_{r2} by

$$W_{\text{eff}} = W_i \cdot \zeta_{r2}D_{r2} = \frac{\lambda}{2\pi}G_{r2}. \tag{29}$$

So the power P_{r2} collected by the receiving antenna can be written, using (28) and (29), as

$$P_{r2} = W_{\text{eff}}S_{t2} = G_{r2}\frac{\lambda}{2\pi}S_{t2} = G_{r2}\frac{\lambda}{2\pi}\frac{P_{t2}G_{t2}}{2\pi R} \tag{30}$$

or the ratio of the received to the input power as

$$\frac{P_{r2}}{P_{t2}} = \frac{G_{t2}G_{r2}}{4\pi^2}\frac{\lambda}{R}. \tag{31}$$

For impedance-matched and polarization-matched antennas aligned for maximum directional radiation and reception, (31) is the 2-D surface-wave transmission equation, and it relates the power P_{r2} (delivered to the receiver load) to the input power of the transmitting antenna P_{t2} in the same way as the Friis equation governs 3-D transmission. The term $\lambda/4\pi^2$R is the surface loss factor, and it takes into account the losses due to the spreading of the energy in two dimensions.

The total transmission including free-space wave coupling, surface-wave coupling, and mutual phase coupling between

the two antennas but neglecting near-field effects is

$$\frac{P_r}{P_t} = G_{t3}G_{r3}\left(\frac{\lambda}{4\pi R}\right)^2 + G_{t2}G_{r2}\frac{\lambda}{4\pi^2 R} + 2G_3G_2\frac{\lambda}{4\pi R}\sqrt{\frac{\lambda}{4\pi^2 R}}\cos\theta_R. \quad (32)$$

The first term is the standard Friis equation, the second term is the additional coupling due to surface-wave effects, and the third one is the mutual phase difference and resulting cross term in (32). The θ_R is the coupled phase difference between free space and surface wave, it can be obtained by

$$\theta_R = (k_{\mathrm{TM}} - k_0)\cdot R \quad (33)$$

where k_{TM} is the wavenumber of surface wave and k_0 is the wavenumber of free-space wave.

Consider a dielectric slab with permittivity ε_d and thickness h residing on a ground plane. For this configuration, we can have the equation is given by [25]

$$\frac{\varepsilon_d k_0^2 - k_{\mathrm{TM}}^2}{\varepsilon_d}\cdot h = \frac{\sqrt{k_{\mathrm{TM}}^2 - k_0^2}}{\varepsilon_0}. \quad (34)$$

From (34), we can see that if the thickness of the slab is very small, the wavenumber k_{TM} is almost equal to the wavenumber k_0. Thus, the total transmission equation is approximated by

$$\frac{P_r}{P_t} = G_{t3}G_{r3}\left(\frac{\lambda}{4\pi R}\right)^2 + G_{t2}G_{r2}\frac{\lambda}{4\pi^2 R} + 2G_3G_2\frac{\lambda}{4\pi R}\sqrt{\frac{\lambda}{4\pi^2 R}}. \quad (35)$$

By simulating the transmission between two identical antennas at various distances, we can determine the values of G_2 and G_3 separately, because they become fitting parameters in (35).

III. Comparison of Theoretical and Simulated Mutual Coupling

In this section, we will compare the mutual coupling theoretical results with numerical experiments using various lossless substrates. As described above, there are three kinds of mutual coupling between antennas, the near-field coupling, the free-space wave coupling, and the surface-wave coupling. Note that we are assuming lossless substrates, and we are focusing on the relative strength of the free space and surface-wave components. If the substrate is sufficiently loss, or the antennas are very close together, it is possible that the near-field term can be dominant [26], [27]. We will compare the results for the mutual coupling between a pair of rectangular patch antennas and a pair of monopole antennas. For all of the simulation results presented in this paper, the rectangular microstrip patch and monopole antennas are designed to operate at a frequency of 3 GHz ($\lambda = 100$ mm), with the same substrate and parameters shown in Figs. 3, 5, and 7. Ansys HFSS was used for the simulations, and the exterior surfaces of the simulation volume were all radiation boundaries.

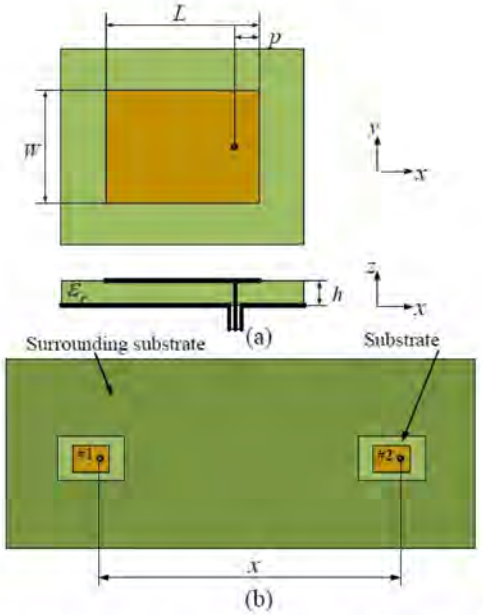

Fig. 3. (a) Top and view of classical microstrip antenna. (b) Coordinate system for coupled antennas.

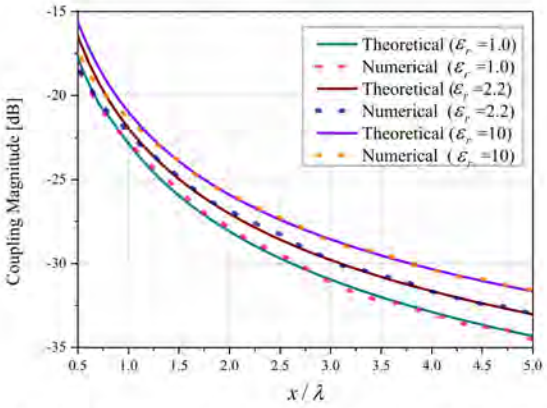

Fig. 4. Coupling comparison for the theoretical results and simulation results between microstrip antennas.

A. Rectangular Microstrip Patch Antenna

The geometry used in the calculation of the mutual coupling between two identical rectangular patch antennas is shown in Fig. 3(a). To exclude the influence of the substrate losses on the coupling, we only investigated antennas on lossless substrates. The substrate thickness is $h = 1.5$ mm and it has a relative dielectric constant ε_r of 5. Note that a small space is left around the patch with dielectric constant of 5, so that the same antenna design can be kept for surrounding substrates with different dielectric constants without having to retune the antenna design for each case. The patch length is $L = 21.3$ mm and the width is $W = 28.87$ mm. The patch is fed by a coaxial line, whose location is determined by matching conditions, and is set to $p = 3.2$ mm. In the computational models, we assume that the ground plane is infinite.

We evaluate the coupling between a pair of identical microstrip antennas which are printed on a lossless surrounding substrate with three different dielectric constants (1, 2.2, and 10). The dielectric constant below the patch was kept

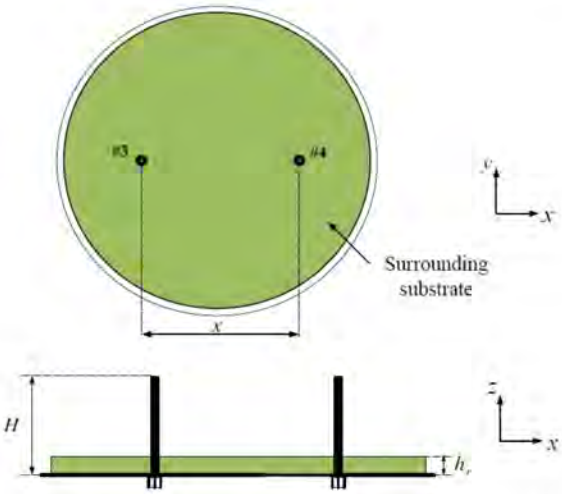

Fig. 5. Top and view of coupled monopole antennas.

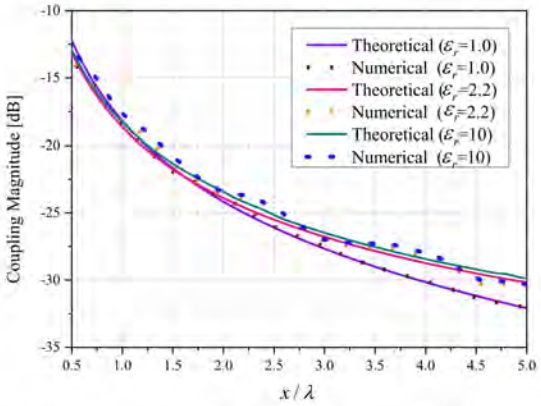

Fig. 6. Coupling comparison for the theoretical results and simulation results between monopole antennas.

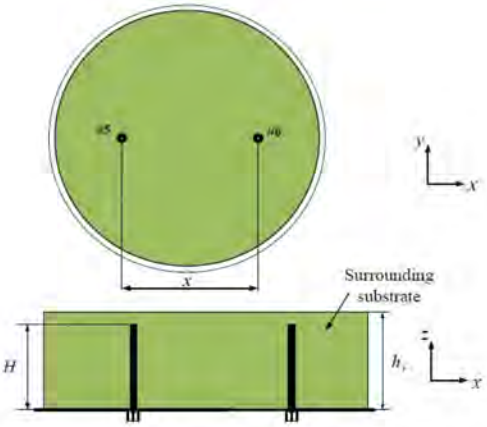

Fig. 7. Top and view of full dielectric coupled monopole antennas.

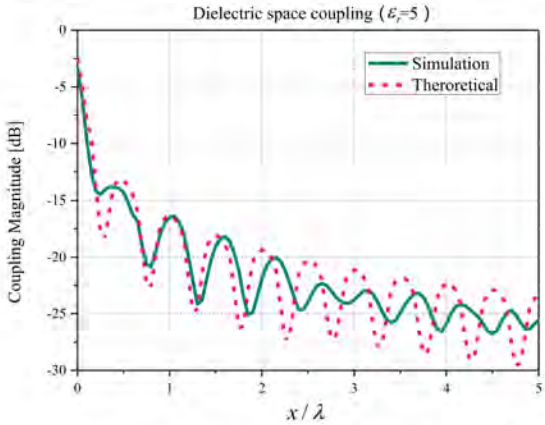

Fig. 8. Dielectric layer coupling comparison for the theoretical results and simulation results between monopole antennas.

constant in the three cases so that the same antenna design could be used, and would not have to be retuned for each substrate. The antennas are placed along the x-axis, as shown in Fig. 3(b). The space between the antennas varies from 0.5λ to 5λ. The simulation results for the mutual coupling versus distance are plotted in Fig. 4.

Note that the theoretical results match the numerical results much well with the least-squares technique once the gain parameters are determined, verifying the general form of (35). The slight difference between 0.5λ and 0.8λ is likely due to near-field effects, which are not included.

B. Monopole Antenna

As a second example, a monopole antenna surrounded by a thin dielectric substrate is shown in Fig. 5. The substrate has a thickness $h_r = 1.5$ mm, and relative dielectric constant ε_r of either 1 (the case of no substrate), 2.2, 4.4, or 10. The length of monopole is $H = 23.53$ mm, and it is fed by a coaxial line.

We evaluate the coupling between a pair of identical monopole antennas which are located on the infinite ground plane, the antennas are placed along the x-axis, as shown in Fig. 5. As with the patch antenna, we use a lossless surrounding substrate with the three different dielectric constants. For the three different surrounding substrates, the theoretical results and simulation results are in good agreement, as shown in Fig. 6. For the air substrate case, coupling is primarily due to free-space waves and the presence of oscillations is due to the small changes in phase between one or more surface waves and space waves for the relative dielectric constant ε_r of 10 case. Except for this, there is in good agreement between the calculated results and simulation results using (35) for various dielectric substrates.

Another example of the coupling between monopole antennas is shown in Fig. 7. All the parameters are the same as in Fig. 5, except that the substrate height h_r exceeds the height of the antennas. In this case, G3 is set to 0, the substrate has a relative dielectric constant ε_r of 5, and the length of monopoles has been tuned so that it is matched at 3 GHz. The purpose of this paper is to examine a case where surface-waves dominate. The simulated data from Fig. 8 shows sinusoidal variations that are likely due to interference between multiple surface modes which are present in the thick dielectric substrate. Based on the surface guided wave theory [28], we can obtain the cutoff frequencies as

$$f_c = \frac{n}{4h\sqrt{\varepsilon_d \mu_d - \varepsilon_0 \mu_0}} \quad n = 0, 2, 4 \ldots \tag{36}$$

From (36), we know there only two modes exist in this frequency range, so we may neglect higher order modes. Thus, neglecting differences in excitation strength between the

TABLE I
2-D AND 3-D GAIN VALUES FOR VARIOUS ANTENNAS AND VARIOUS DIELECTRIC SUBSTRATES

ε_r \ Type	Patch		Monopole		Slot		Monopole embedded	
	G_2	G_3	G_2	G_3	G_2	G_3	G_2	G_3
1	0.12	0.67	0.12	1.40	0.10	0.22	0.12	1.50
2.2	0.16	0.67	0.14	1.41	0.12	0.21	0.80	0.00
4.4	0.19	0.67	0.15	1.40	0.13	0.20	0.73	0.00
10	0.20	0.67	0.16	1.40	0.14	0.20	0.57	0.00

TABLE II
EFFECTIVE WIDTH AND EFFECTIVE APERTURE FOR VARIOUS ANTENNAS AND VARIOUS DIELECTRIC SUBSTRATES

ε_r \ Type	Patch		Monopole		Slot		Monopole embedded	
	W_{eff} (mm)	A_{eff} (cm^2)	W_{eff} (mm)	A_{eff} (cm^2)	W_{eff} (mm)	A_{eff} (cm^2)	W_{eff} (mm)	A_{eff} (cm^2)
1	1.9	5.3	1.9	11.1	1.6	1.7	1.9	11.9
2.2	2.5	5.3	2.2	11.2	1.9	1.7	12.7	0.0
4.4	3.0	5.3	2.4	11.1	2.1	1.6	11.6	0.0
10	3.2	5.3	2.5	11.1	2.2	1.6	9.1	0.0

two modes, (32) is changed to

$$\frac{P_r}{P_t} = G_{t2}G_{r2}\frac{\lambda}{4\pi^2 R}\cos[(k_{\mathrm{TM}_0} - k_{\mathrm{TM}_2})R] \tag{37}$$

where k_{TM0} and k_{TM2} correspond to the wavenumber of the first two surface-wave modes. There is a phase difference between the surface waves, so the simulation curve shows oscillations as a function of antenna separation. Because of neglecting the relative excitation strength of the two surface waves, the least-squares technique does not provide an exact match to the simulated data. Nonetheless, we can approximately fit (37) to the data.

IV. SUMMARY OF COUPLING COEFFICIENTS

We provide simulations of several simple examples and evaluate them in terms of 2-D gain G_2 and 3-D gain G_3, shown in Table I, as well as the effective width and effective aperture shown in Table II. For the first three examples, the operating frequency is 3 GHz ($\lambda = 100$ mm), the thickness of lossless surrounding substrate is 1.5 mm and dielectric constant is ε_r. In each case the antennas are well-matched ($S_{11} < -20$ dB). One case is the monopole embedded in a 20 mm thick dielectric, and retuned to match.

We also study the slot antenna, where the permittivity above the slot is kept fixed at 5 in order to avoid retuning the slot for each case, while the surrounding permittivity is varied. One way to reduce free-space coupling between antennas is to ensure that they do not have a direct line-of-sight path between them, such as by placing the antennas in cups or troughs. However, those features will also radiate, so free-space coupling cannot be entirely eliminated. The limiting case of a deep trough is simply a slot antenna, which is why it is included.

We can draw several conclusions from Tables I and II. First, the 3-D or space-wave gain of each antenna is roughly constant with substrate permittivity, as we expect. However, the 2-D or surface-wave gain increases with permittivity, which is also expected. The monopole has the highest G_3 toward the horizon, and the slot has the lowest. In terms of G_2, the patch has the highest value and the slot is the lowest. Thus, the patch and monopole are not ideal choices for minimizing coupling between antennas, and the slot appears to be the best choice regardless of the substrate. We know the least-squares technique only produces an estimate of the best fit. Thus, several possible answers for G_2 and G_3 could produce the same curves. So here an average sensitivity $\bar{\varphi}$ is introduced

$$\overline{\varphi} = \frac{\sum_1^N \varphi}{N} = \frac{\sum_1^N \Delta\mathrm{LSE}}{\Delta G_3 \cdot N} = \frac{\sum_1^N |D_{\mathrm{sim}} - D_{\mathrm{fitting}}|^2}{\Delta G_3 \cdot N} \tag{38}$$

where φ is the sensitivity for different points N in the distance of five wavelengths between antennas, Δ LSE is the least-square error, ΔG_3 is the difference of changed G_3, D_{sim}, and D_{fitting} are simulation data and fitting curve data, respectively. For embedded antennas (EA), the $\overline{\varphi}_{\mathrm{EA}} = 0$ can be obtained from (38) when the G_3 value varies from 0 to 2. Thus, the curve fitting has a high degree of uncertainty for G_3 and a unique solution for G_2 in this case. In other words, surface waves become much more significant whereas free space waves can be ignored. Compared with the EA case, we get an average sensitivity of $\overline{\varphi}_P = 20$ for the patch case when the G_3 value is changed from 0.60 to 0.72. So the curve fitting has a unique solution for both G_2 and G_3. Similarly, monopole antenna has an average sensitivity of $\overline{\varphi}_m = 5.7$ when the G_3 value varies from 1.43 to 1.56. Thus, the curve fitting has a unique solution for both G_2 and G_3. In the case of slot antennas, the average sensitivity is $\overline{\varphi}_s = 5.6$ when the G_3 value is changed from 0.16 to 0.25. Hence, the curve fitting also has a unique solution for both G_2 and G_3.

Note that the gain of the monopole is 1.5 rather than 3. As we know, the transmission between two dipoles in free space is the same as the transmission between two equivalent monopoles sharing the same ground plane, because the ground plane simply acts as a symmetry plane in an otherwise identical problem. Logan and Rockway [29] and Trainotti *et al.* [30] have explained this by showing that antennas on a ground plane have different values for transmit gain and receive gain, e.g., $G_t = 3$ and $G_r = 0.75$ for transmitting and receiving monopoles. Because we are interested in mutual coupling in both directions, we avoid any confusion in this regard by simply using the geometric mean of the transmitting and receiving gain values

$$G_3 = \sqrt{G_{t3}G_{r3}} \quad G_2 = \sqrt{G_{t2}G_{r2}}. \tag{39}$$

Our final transmission equation is as follows:

$$\frac{P_r}{P_t} = G_3^2\left(\frac{\lambda}{4\pi R}\right)^2 + G_2^2\frac{\lambda}{4\pi^2 R} + 2G_3G_2\frac{\lambda}{4\pi R}\sqrt{\frac{\lambda}{4\pi^2 R}}. \tag{40}$$

V. RELATIVE CONTRIBUTION OF SURFACE WAVES

A plot of the total mutual coupling between a pair of conventional rectangular microstrip patch antennas, a pair of

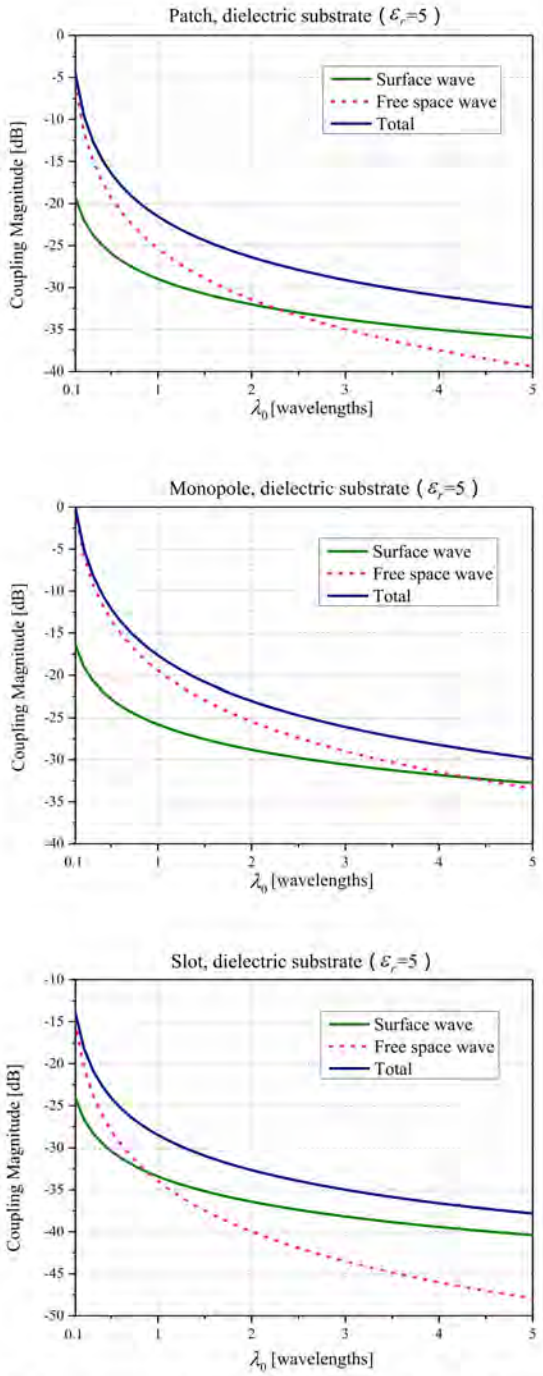

Fig. 9. Different components of the mutual coupling between different types of antennas.

monopole antennas, and a pair of slot antennas is shown in Fig. 9. Considering that the thickness of the slab is very small, the wavenumber k_{TM} is almost equal to the wavenumber k_0 [25], so the $\cos\theta_R$ term is negligible. After fitting to determine G_2 and G_3, the free-space and surface-wave contributions can be plotted separately. The navy curve is total coupling from simulated data between antennas, and it is divided into free-space coupling (pink) and surface-wave coupling (dark cyan). This plot closely matches previous analytical studies of the microstrip antenna coupling [1].

From Fig. 9, we can see that there is a crossing point between surface-wave coupling and free-space wave coupling.

TABLE III

FREE-SPACE WAVE/SURFACE-WAVE CROSSING POINT FOR VARIOUS SUBSTRATE DIELECTRIC CONSTANTS AND ANTENNA TYPES

ε_r \ Type	Patch	Monopole	Slot
	Crossing Point	Crossing Point	Crossing Point
1	-37.1 dB	-37.2 dB	-37.0 dB
2.2	-34.0 dB	-34.1 dB	-34.0 dB
4.4	-32.5 dB	-32.4 dB	-32.4 dB
10	-29.5 dB	-29.5 dB	-28.4 dB

Referring to formula (40), the distance of crossing point can be given by

$$G_3^2\left(\frac{\lambda}{4\pi R'}\right)^2 = G_2^2\frac{\lambda}{4\pi^2 R'}. \tag{41}$$

Because the two antennas are identical, the formula can be rewritten to determine the distance beyond which the surface-wave coupling dominates

$$R' = \frac{\lambda}{4}\left(\frac{G_3}{G_2}\right)^2 = \frac{1}{\lambda}\left(\frac{A_{\mathrm{eff}}}{W_{\mathrm{eff}}}\right)^2. \tag{42}$$

Free-space wave coupling is dominant for $R < R'$, and surface-wave coupling is dominant for $R > R'$. For this patch example, R' is approximately 2.5λ, as shown in Fig. 9. For the case of the monopole and the slot, R' is approximately 4.3λ and 0.8λ, respectively. At much shorter distances, (closer than $\lambda/2\pi$) coupling is dominated by the near fields.

Based on this analysis, the control of mutual coupling can be explained by the following steps in order of importance. Some of these may not be possible depending on the application.

1) Keep the separation distance much greater than the boundary of the near-field region ($R \gg \lambda/2\pi$).
2) Arrange the antennas such that they each have a null in their pattern toward the other antenna if possible.
3) Minimize free-space coupling by ensuring that the antennas do not have line-of-sight exposure to each other (i.e., slots are preferred over monopoles).
4) Minimize surface-wave coupling by choice of substrate or by other means (e.g., reactive surfaces).

Note that although control of the surface-wave coupling is often the focus of research, it is the last issue that should be addressed after dealing with the near-field and free-space coupling because it only dominates at greater distances. Based on the analysis above, the relevant distance where they become important is on the order of a few wavelengths, depending on antenna and substrate type. Nonetheless, in applications where coupling requirements are extremely low, i.e., less than -30 dB, control of surface waves becomes important.

Note that in Fig. 9, although each antenna type had a different value of R', the magnitude of the coupling at R' was the same for all antenna types. In Table III, we compare the magnitude of coupling at R' for various substrates and antenna types. We find that the magnitude of the crossing point is independent of the antenna type, and only depends on the substrate. Thus, for a given substrate, it is possible to determine the coupling magnitude below which surface waves

must be controlled. For example, on a bare ground plane with no dielectric, if coupling of higher than −37 dB, then surface waves are not significant.

VI. Conclusion

In this paper, we introduce the effective width of an antenna with respect to surface-wave radiation and derive the effective width of an isotropic surface-wave radiator. We determine the directivity of a surface-wave radiator for various radiation modes, including a planar dipole pattern and a vertical monopole pattern. We then add the 2-D surface-wave propagation component to the Friis transmission equation. By the comparison of the theoretical results and the numerical results on mutual coupling between pairs of antennas, the relative contributions of surface waves and free-space waves can be separated.

We also defined the distance beyond which surface waves dominate in terms of the 2-D and 3-D gain components, and found that this distance is on the order of a few wavelengths, depending on the antenna type. For the design that is most effective at minimizing free-space coupling (the slot antenna), the surface waves are the most important coupling mechanism, and they dominate the coupling at distances beyond one wavelength.

The ultimate purpose of this paper is for antenna designers to understand the relative contributions of surface waves, free-space waves, and antenna design considerations to the mutual coupling. At distances of a few wavelengths, coupling can be controlled primarily by using low-profile antenna elements, and if possible by controlling their orientation to minimize gain along the horizon. Only after these issues have been addressed should the designer be concerned with surface waves. Finally, we provide a way to quantify surface-wave coupling in terms of the 2-D gain G_2.

References

[1] M. A. Khayat, J. T. Williams, D. R. Jackson, and S. A. Long, "Mutual coupling between reduced surface-wave microstrip antennas," *IEEE Trans. Antennas Propag.*, vol. 48, no. 10, pp. 1581–1593, Oct. 2000.

[2] E. M. Koper, W. D. Wood, and S. W. Schneider, "Aircraft antenna coupling minimization using genetic algorithms and approximations," *IEEE Trans. Aerosp. Electron. Syst.*, vol. 40, no. 2, pp. 742–751, Apr. 2004.

[3] D. A. Tsyanenka, E. V. Sinkevich, and A. A. Matsveyeu, "Computationally-effective worst-case model of coupling between on-board antennas that takes into account diffraction by conducting hull," in *Proc. IEEE Int. Symp. Electromagn. Compat. (EMC EUROPE)*, Sep. 2016, pp. 602–607.

[4] P. N. Fletcher, M. Dean, and A. R. Nix, "Mutual coupling in multi-element array antennas and its influence on MIMO channel capacity," *Electron. Lett.*, vol. 39, no. 4, pp. 342–344, Feb. 2003.

[5] B. N. Getu and R. Janaswamy, "The effect of mutual coupling on the capacity of the MIMO cube," *IEEE Antennas Wireless Propag. Lett.*, vol. 4, pp. 240–244, 2005.

[6] I. J. Gupta and A. Ksienski, "Effect of mutual coupling on the performance of adaptive arrays," *IEEE Trans. Antennas Propag.*, vol. AP-31, no. 5, pp. 785–791, Sep. 1983.

[7] E. M. Friel and K. M. Pasala, "Effects of mutual coupling on the performance of STAP antenna arrays," *IEEE Trans. Aerosp. Electron. Syst.*, vol. 36, no. 2, pp. 518–527, Apr. 2000.

[8] J.-W. Yook and L. P. B. Katehi, "Micromachined microstrip patch antenna with controlled mutual coupling and surface waves," *IEEE Trans. Antennas Propag.*, vol. 49, no. 9, pp. 1282–1289, Sep. 2001.

[9] M. M. Nikolic, A. R. Djordjevic, and A. Nehorai, "Microstrip antennas with suppressed radiation in horizontal directions and reduced coupling," *IEEE Trans. Antennas Propag.*, vol. 53, no. 11, pp. 3469–3476, Nov. 2005.

[10] R. E. Collin, *Foundations for Microwave Engineering*. NewYork, NY, USA: McGraw-Hill, 1992.

[11] M. Salehi, A. Motevasselian, A. Tavakoli, and T. Heidari, "Mutual coupling reduction of microstrip antennas using defected ground structure," in *Proc. 10th IEEE Int. Conf. Commun. Syst.*, Oct./Nov. 2006, pp. 1–5.

[12] Y. Hajilou, H. R. Hassani, and B. Rahmati, "Mutual coupling reduction between microstrip patch antennas," in *Proc. 6th EUCAP*, Mar. 2012, pp. 1–4.

[13] J. Ouyang, F. Yang, and Z. M. Wang, "Reducing mutual coupling of closely spaced microstrip MIMO antennas for WLAN application," *IEEE Antennas Wireless Propag. Lett.*, vol. 10, pp. 310–313, 2011.

[14] A. Habashi, J. Nourinia, and C. Ghobadi, "Mutual coupling reduction between very closely spaced patch antennas using low-profile folded split-ring resonators (FSRRs)," *IEEE Antennas Wireless Propag. Lett.*, vol. 10, pp. 862–865, 2011.

[15] F. Yang and Y. Rahmat-Samii, "Microstrip antennas integrated with electromagnetic band-gap (EBG) structures: A low mutual coupling design for array applications," *IEEE Trans. Antennas Propag.*, vol. 51, no. 10, pp. 2936–2946, Oct. 2003.

[16] M. Niroo-Jazi, T. A. Denidni, M. R. Chaharmir, and A. R. Sebak, "A hybrid isolator to reduce electromagnetic interactions between Tx/Rx antennas," *IEEE Antennas Wireless Propag. Lett.*, vol. 13, pp. 75–78, 2014.

[17] H. S. Farahani, M. Veysi, M. Kamyab, and A. Tadjalli, "Mutual coupling reduction in patch antenna arrays using a UC-EBG superstrate," *IEEE Antennas Wireless Propag. Lett.*, vol. 9, pp. 57–59, 2010.

[18] D. Sievenpiper, L. Zhang, R. F. J. Broas, N. G. Alexopolous, and E. Yablonovitch, "High-impedance electromagnetic surfaces with a forbidden frequency band," *IEEE Trans. Microw. Theory Techn.*, vol. 47, no. 11, pp. 2059–2074, Nov. 1999.

[19] A. C. Durgun, C. A. Balanis, C. R. Birtcher, H. Huang, and H. Yu, "High-impedance surfaces with periodically perforated ground planes," *IEEE Trans. Antennas Propag.*, vol. 62, no. 9, pp. 4510–4517, Sep. 2014.

[20] E. Rajo-Iglesias, Q. Uevedo-Teruel, and L. Inclan-Sanchez, "Planar soft surfaces and their application to mutual coupling reduction," *IEEE Trans. Antennas Propag.*, vol. 57, no. 12, pp. 3852–3859, Dec. 2009.

[21] Ó. Quevedo-Teruel, L. Inclan-Sanchez and E. Rajo-Iglesias, "Soft surfaces for reducing mutual coupling between loaded PIFA antennas," *IEEE Antennas Wireless Propag. Lett.*, vol. 9, pp. 91–94, 2010.

[22] *National Radio Astronomy Observatory*. Univ. Virginia, Blackbody Radiation. Accessed on Sep. 2008. [Online]. Available: http://www.cv.nrao.edu/course/astr534/BlackBodyRad.htmls

[23] J. H. Jeans, "XI. On the partition of energy between matter and aether," *Philos. Mag.*, vol. 10, pp. 91–98, no. 55, 1905.

[24] J. W. S. Rayleigh, "The dynamical theory of gases and of radiation," *Nature*, vol. 72, no. 1855, pp. 54–55, 1905.

[25] J. Jian-Ming, *Theory and Computation of Electromagnetic Fields*. New York, NY, USA: Wiley, 2011.

[26] J. R. Wait, "The ancient and modern history of EM ground-wave propagation," *IEEE Antennas Propag. Mag.*, vol. 40, no. 5, pp. 7–24, Oct. 1998.

[27] N. Chahat, G. Valerio, M. Zhadobov, and R. Sauleau, "On-body propagation at 60 GHz," *IEEE Trans. Antennas Propag.*, vol. 61, no. 4, pp. 1876–1888, Apr. 2013.

[28] R. F. Harrington, *Time—Harmonic Electromagnetic Fields*. New York, NY, USA: Wiley, 2001.

[29] J. C. Logan and J. W. Rockway, "Dipole and monopole antenna gain and effective area for communication formulas," Naval Command, Control Ocean Surveill. Center, RDT&E Division, San Diego, CA, USA, Tech. Rep. 1756, Sep. 1997.

[30] V. Trainotti and G. Figueroa, "Vertically polarized dipoles and monopoles, directivity, effective height and antenna factor," *IEEE Trans. Broadcast.*, vol. 56, no. 3, pp. 379–409, Sep. 2010.

Chao Wang (S'14) received the B.Sc. degree in electrical engineering from the Xi'an University of Posts and Telecommunications, Xi'an, China, in 2010, and the Ph.D. degree in electromagnetic fields and microwave technology from the University of Electronic Science and Technology of China, Chengdu, China, in 2017.

He was a Visiting Graduate Student with the Applied Electromagnetics Research Group, University of California at San Diego, La Jolla, CA, USA, from 2015 to 2017. His current research interests include ultrawideband antenna, theoretical arithmetic for surface-wave attenuation, and impedance surfaces for reducing mutual coupling between antennas.

En Li (M'14) received the M.S. degree in physical electronics and the Ph.D. degree in electromagnetic field and microwave technology from the University of Electronic Science and Technology of China, Chengdu, China, in 2003 and 2009, respectively.

He is currently a Professor with the University of Electronic Science and Technology of China. He has authored or co-authored over 100 journal, conference papers, and 12 authorized national invention patents.

His current research interests include microwave plasma diagnosis, electromagnetic parameter measurement of dielectric material at high temperatures, nonlinear parameter measurement of high-power amplifier, and design of microwave devices.

Dr. Li was a receipient of the Second Prize of The National Science and Technology Progress Award, the First Prize, the Second Prize, and the Third Prize of the Provincial And Ministerial Level Scientific and Technological Progress Awards. In 2010, he was a winner of Education Ministry's New Century Excellent Talents Supporting Plan, a receipient of the title of excellent experts with outstanding contribution of Sichuan Province in 2013. He is a Guest Professor with the National Defense Science and Technology Key Laboratory of Advanced Function Composite Material.

Daniel F. Sievenpiper (M'94–SM'04–F'09) received the B.S. and Ph.D. degrees in electrical engineering from the University of California, Los Angeles, CA, USA, in 1994 and 1999, respectively.

He was the Director with the Applied Electromagnetics Laboratory, HRL Laboratories, Malibu, CA, USA, where he was invoved in artificial impedance surfaces, conformal antennas, tunable and wearable antennas, and beam steering methods. He is currently a Professor with the University of California, San Diego, CA, USA, where he is focused on antennas and electromagnetic structures. He has more than 70 issued patents and more than 120 technical publications.

Dr. Sievenpiper was awarded the URSI Issac Koga Gold Medal in 2008. Since 2010, he has been served as an Associate Editor of the IEEE ANTENNAS AND WIRELESS PROPAGATION LETTERS.

Guiding Waves Along an Infinitesimal Line between Impedance Surfaces

Dia'aaldin J. Bisharat[1,2,*] and Daniel F. Sievenpiper[2,†]
[1]Department of Electronic Engineering, City University of Hong Kong, Kowloon, Hong Kong, China
[2]Electrical and Computer Engineering Department, University of California, San Diego, California 92093, USA
(Received 19 January 2017; published 8 September 2017)

We present a new electromagnetic mode that forms at the interface between two planar surfaces laid side by side in free space, effectively guiding energy along an infinitesimal, one-dimensional line. It is shown that this mode occurs when the boundaries have complementary surface impedances, and it is possible to control the mode confinement by altering their values correspondingly. The mode exhibits singular field enhancement, broad bandwidth, direction-dependent polarization, and robustness to certain defects. As a proof of concept, experimental results in the microwave regime are provided using patterned conducting sheets. Our proposed effective-medium-based approach is general, however, thus allowing for potential implementation up to optical frequencies. Our system is promising for applications including integrated photonics, sensing, switching, chiral quantum coupling, and reconfigurable waveguides.

DOI: 10.1103/PhysRevLett.119.106802

Having a peak field bound to the interface of two media makes surface waves (SWs) [1] attractive for energy transmission with simple implementation for sensing and communication applications [2,3]. Exploiting the plasmon polariton's nature [4], SWs can exhibit strong light confinement, which is useful for realizing subwavelength guiding structures, and hence high-density integration of optical circuits and lower waveguide bending loss. Variations such as V-shaped grooves [5] and wedges [6], albeit with more complexity, reduce SWs to one dimension (1D) despite the absence of an enclosing structure, thus enabling greater guiding control. Similarly, guided modes at the edge of photonic crystals (PCs), within shared bulk and surface band gaps, have been proposed [7]. In addition, edge plasmons have been observed in graphene ribbons [8].

Recently, there has been special attention paid to structures with interface modes exhibiting robust directional propagation. Notably, this includes photonic topological insulators based on symmetry-protected topological (SPT) phases [9–12]. In these systems, where time-reversal (TR) symmetry is not broken [13–16], crystalline or intrinsic symmetries of the wave fields and differing topology of bulk bands give rise to wave-vector-locked states at the interface [12]. Analogously, opposite single-negative bulk materials [17] support bound states that exhibit a similar though limited robustness [18–20]. In addition, trivial structures such as nanofibers and glide-plane PC waveguides [21], where light is tightly confined with evanescent wave on their interface, can exhibit direction-dependent polarizations [22].

In this work, we introduce a new 1D mode, analogous yet different from SWs, that is confined to the interface line between two planes. The line wave (LW) possesses robust wave-vector-locked states, broad bandwidth, strong—ideally singular—field enhancement, and tunable mode confinement. We analyze how the LW can arise due to complementary surface impedances and demonstrate experimentally its feasibility using periodic surfaces with suitable effective-medium properties. Furthermore, we examine the characteristics of our system at different conditions and suggest possible applications. Our work opens a new door for planar, compact, and efficient routing and concentration of electromagnetic energy, and for unconventional devices.

SW modes can be guided on planar structures with subwavelength periodic inclusions, known as metasurfaces [23,24], whose response to impinging waves and their guiding properties can be conveniently characterized by surface impedance [25,26]. This methodology has been extensively used for a variety of applications including electromagnetic guiding, absorption, radiation, scattering alteration, cloaking, and self-focusing [27–32]. Consider a field with an exponential decay $e^{-\alpha y}$ away from the surface and a propagation function $e^{-j\beta z}$, such that $\alpha^2 = \beta^2 - k^2$, where k is the wave number in free space. The surface impedances for transverse-magnetic (TM) and transverse-electric (TE) polarized waves are [33]

$$Z_{\mathrm{TM}} = j\eta_0 \frac{\alpha}{k}, \qquad Z_{\mathrm{TE}} = -j\eta_0 \frac{k}{\alpha}, \tag{1}$$

where η_0 is the intrinsic impedance of free space. Meanwhile, the refractive index n seen by the SW is $n = c/v_p = \beta/k$, where c is the speed of light in free space and v_p is the phase velocity of the wave along the surface. Therefore, the relationship between the surface impedance and the refractive index is [34]

$$Z_{\mathrm{TM}} = \eta_0 \sqrt{1 - n^2}, \qquad Z_{\mathrm{TE}} = \eta_0 / \sqrt{1 - n^2}. \tag{2}$$

Accordingly, for TM- and TE-polarized SWs propagating at equal phase velocities, we can define a new

parameter ζ that relates the two respective surface impedances as

$$j\frac{Z_{\mathrm{TE}}}{\eta_0} = j\frac{\eta_0}{Z_{\mathrm{TM}}} = \zeta. \tag{3}$$

First, consider the case where ζ is infinite, so that the TM (TE) surface becomes a perfect electric (magnetic) conductor [PEC (PMC)]. Obviously, the PEC (PMC) boundary forces the tangential electric (magnetic) field to vanish, thus allowing only the TM (TE) SW mode to survive. When interfacing the two surface types, as shown in Fig. 1(a), a new localized mode, which is a product of interference between TM and TE modes, appears at the interface. Consequently, the associated E-field vectors point in the transverse direction adjacent to the Z_{TE} surface and vary gradually toward the normal direction as we trace a path at constant distance away from the interface towards the Z_{TM} surface. Hence, using cylindrical coordinates, the waveform of the mode is deduced as [35] (see Supplemental Material [36])

$$E_z = E_0 K_{\frac{1}{2}}(\alpha\rho)\sin\left(\frac{\phi}{2}\right)e^{-j\beta z},$$
$$H_z = \frac{E_0}{\eta_0}K_{\frac{1}{2}}(\alpha\rho)\cos\left(\frac{\phi}{2}\right)e^{-j\beta z}, \tag{4}$$

where K is the modified Bessel function of the second kind, and $\alpha^2 = k^2 - \beta^2$, with $\beta \geq k$.

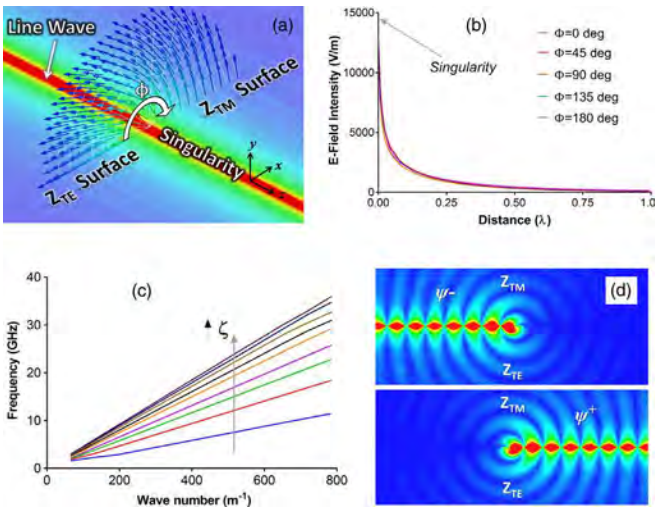

FIG. 1. Simulated field characteristics of the line wave: (a) Magnitude distribution and vector plot of the E field above the interfaced TE and TM surfaces (linear scale), (b) decay profile of the E field at different directions about the interface line, (c) dispersion of the line mode at different values of complementary impedances, and (d) pseudospin states excited by electric and magnetic Hertzian dipoles along the y axis in phase (above) or out of phase (below).

The waveform is verified with full wave simulation in ANSYS HFSS software, which clearly shows the singular nature of field intensity at the interface, as depicted in Fig. 1(b). Here, for a given ζ value, the field intensity decays away from the interface at different ϕ angles at the same rate. Note that although the field is infinite at the interface line, the field everywhere has a finite integral; thus the power carried by the LW is finite. Just as SWs on good conductors are only loosely bound to the surface, this is also the case for LWs, which have $\beta = k$ for the limit of a PEC-PMC interface. A more tightly bound mode is readily attainable by adopting a finite ζ value, hence $\beta > k$, as shown in Fig. 1(c). Note that regardless of the ζ value, the field remains infinite at the line in the absence of loss [36].

To realize the LW, two surfaces whose impedances take the form in Eq. (3) are required, i.e., an inductive (capacitive) surface to support a TM (TE). These criteria can be fulfilled by simple frequency-selective surfaces (FSS) such as these shown in Fig. 2(b). Here, the conducting grid (patches) exhibits a dominant inductive (capacitive) response at frequencies where the FSS cell is subwavelength. Figure 2(c) shows that the respective SW modes of the complementary surface have dispersion curves (phase velocities) that overlap over a wide bandwidth as desired

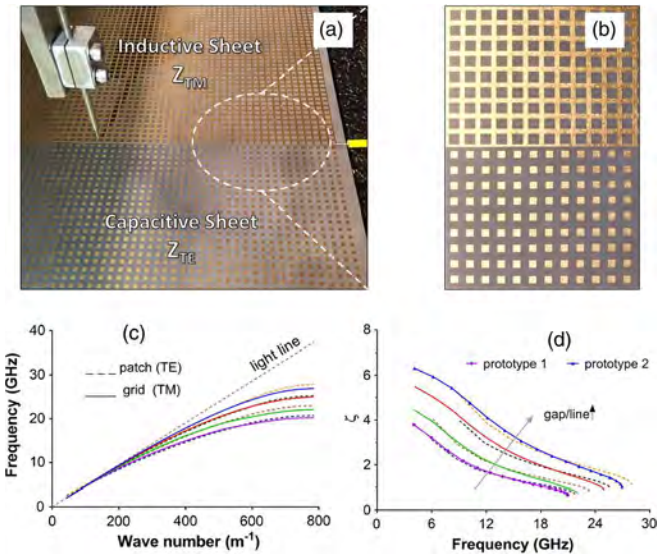

FIG. 2. Measurement setup and characteristics of the fabricated FSS sheets: (a) A probe antenna (right) oriented along the interface line is used as the excitation source while another probe (left) oriented vertically at a $1 \sim 2$ mm distance above the surface is used to scan the relative intensity of the normal E-field component; (b) enhanced complementary FSS sheets fabricated on a printed circuit board on Rogers 5880 ($\varepsilon r = 2.2$, $\delta t = 0.001$) substrate with a 0.8 mm thickness; (c) dispersion characteristics of TM and TE FSS cells of different sizes; and (d) ζ values versus frequency for different sizes of FSS cells. Prototypes 1 and 2 both have a unit cell period of 4 mm. Prototype 1 (2) has a grid-line width of 0.2 mm (1.2 mm) and gap width of 0.8 mm (2.2 mm) between patches.

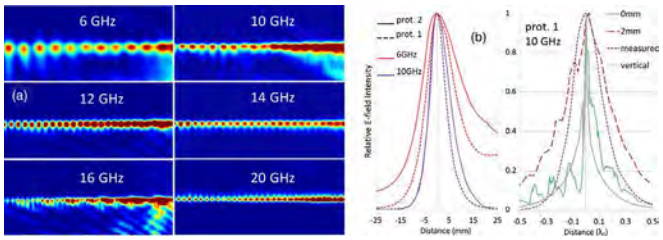

FIG. 3. Measured results of the line wave: (a) E-field magnitude distribution at different frequencies on top of prototype 1 (left) and prototype 2 (right), and (b) normalized decay curves of the normal E-field component along the transverse direction to the interface line (linear scale) at $1 \sim 2$ mm above the two prototypes (left) and comparison with simulated results at 2 and 0 mm above the surface as well as through the origin along the normal (vertical) direction to the surface (right).

[38]. Figure 2(d) shows the associated ζ values, including for the two fabricated prototypes, at different frequencies.

Figure 3(a), which maps the relative intensity of the normal E-field component measured at a fixed distance above the impedance surfaces, shows successful excitation and transmission of the LW along the interface for a distance of several wavelengths. As shown in Fig. 3(b), the normal E-field component is evident on both sides of the interface, as expected, albeit with slightly larger amplitude on the TM side (positive x axis). Moreover, due to lower ζ values, prototype 1 exhibits greater field concentration than prototype 2, as expected. The simulated and measured results across the interface at roughly $1 \sim 2$ mm above the surface are in good agreement. On the other hand, the simulated field intensity at the center of the interface shows higher enhancement level [36] with an effective mode width of less than $\lambda_0/15$.

The measured operation range, which spans roughly two octaves of bandwidth, could be extended by adopting other artificial surfaces with lesser dispersion and broader overlap between the complementary dispersion curves. In addition, the fields at the singularity are limited in physical implementations by the thickness of the surface, dissipation losses, and periodicity of the FSS structures [36]. Thus, at higher frequencies up to the optical domain, it is more suitable to use two-dimensional (2D) materials such as graphene at the terahertz regime, which features highly confined long-lifetime plasmons [39]. Importantly, graphene can be modeled as an impedance sheet and support TM and TE SWs depending on its doping level [40], hence allowing straightforward implementation and tunabilty thanks to the universality of the proposed effective surface-impedance approach.

Another important aspect is that the LW exhibits wave-vector-locked states. Joined PEC ($\varepsilon = -\infty$, $\mu = 1$) and PMC ($\varepsilon = 1$, $\mu = -\infty$) boundaries may preserve an otherwise broken electromagnetic duality by forming mirror images about the yz plane satisfying the $\varepsilon(x) = \mu(-x)$ inversion-symmetry [41,42]. Note that a single PEC-PMC interface is sufficient to partially bound energy due to ε-negative and μ-negative materials possessing different topological orders when considering a fixed wave polarization [18–20]. As the new decoupled interface modes form a hybrid of magnetic and electric modes with a specific phase relationship, they possess conserved pseudospin values [43,36]. Also, since the pseudospin configuration is uniquely defined by the direction of the propagation wave vector (β), the interface constitutes a spin-filtered channel [10,41]. This makes our system somewhat reminiscent of TR-invariant SPT states formed between two claddings of opposite bianisotropy [12], where intrinsic symmetries of the fields and differing topology of bulk bands give rise to counterpropagating pseudospin states, ψ^+ and ψ^- [36].

The approach above can be generalized to interfacing inductive-capacitive surfaces with identical ζ value. Notably, this solves the issue of the weak cross coupling between TM and TE modes in the PEC-PMC case, which otherwise necessities using a closed waveguide configuration for practical applications. The paradigm of effective surface impedance has been exploited in relation with band geometric (Zak) phases to explain the appearance of interface states in 1D and 2D systems of PCs [44,45]. In comparison, our system is free of the bandwidth limitation associated with band gaps in PCs, and supports direction-dependent polarizations as evident from the full-wave simulation shown in Fig. 1(d). Note that although the spin-momentum locking property is universal in evanescent waves [22], it is more prominent in the case of the LW due to the strict confinement in the transverse plane to the wave vector leading to 1D propagation only.

The spin-momentum locking feature enforced by the boundary-inversion symmetry endows our line guide with robustness against reflection from certain structural defects. To qualify this symmetry protection, we introduce a discrete discontinuity in surface impedance over a finite distance along the interface [36]. As shown in Fig. 4(a), for a large impedance variation ($6 \leq \zeta \leq 20$) in either one or both impedance surfaces, reflection coefficient (S_{11}) lower than -30 dB and isolation (S_{21}) of about -0.1 dB are achieved. This is expected given that such a defect does not violate spin degeneracy or cause reversal of boundary conditions. The larger reflection in case of one-sided impedance discontinuity is because of the degraded boundary symmetry, which leads to mismatch in phase velocity across the interface. This result, though it does not show complete immunity to backscattering, somewhat emulates topological protection [36].

This symmetry protection allows for variations in the field enhancement and propagation constant of the LW at arbitrary sections of the waveguide, as shown in Fig. 4(b). For example, this enables the design of compact and lossless delay lines without the need for any bends. However, switching the impedance surfaces' orientation

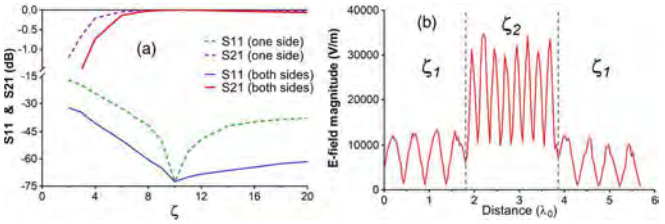

FIG. 4. Influence of a finite discontinuity in surface impedance on the line wave: (a) Transmission and reflection coefficients of the mode due to a defect ($\zeta \neq 10$) at one or both sides of the interface over a distance of $0.6\lambda_0$, and (b) snapshot of a field magnitude depicting an increased enhancement and a shorter wavelength over a finite distance due to change in surface impedances across the interface.

across the interface forbids the LW propagation [36]. This is useful for building network devices, with simple implementation, such as magic T structure as shown in Fig. 5(a). Here, the LW fed at port 1 is guided to ports 2 and 4 with no energy coupling to port 3 as desired.

On the other hand, guiding the LW along a bent path causes scattering similarly to conventional SWs along a curved surface [36]. Although the LW mode must be localized near the interface, energy can couple to the SW modes that are supported at the same frequency (i.e., no surface band gap). As shown in Fig. 5(b), this leakage can be prevented by adjusting the relative ζ values across the interface so that the mismatch between the respective phase velocities is amended. Alternatively, this feature can be exploited, for instance, to form a coupler

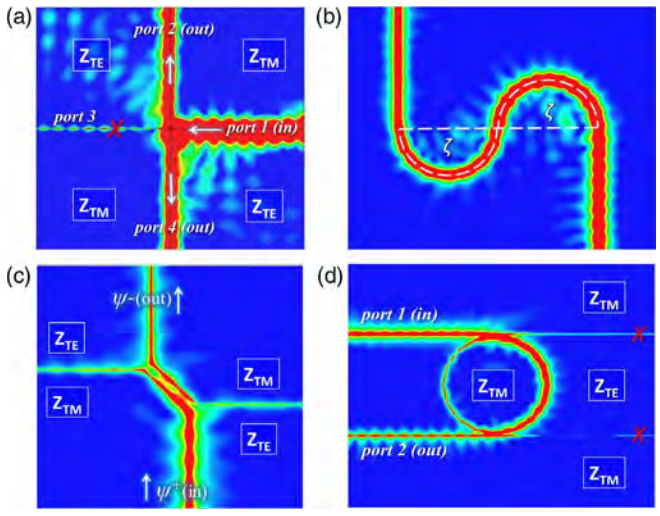

FIG. 5. Full-wave simulations for potential applications of the line wave: (a) Wave transmission in four-port network (magic-T) of a junction due to surface-impedance reversal; (b) wave transport along a curved interface line with a proper change in TM and TE surface impedances; (c) coupler structure showing excitation of a reversed pseudospin mode; and (d) an implementation of a ring resonator showing frequency selection.

device that could transfer energy between eigenfields of the opposite pseudospin polarizations, as shown in Fig. 5(c). Also, this allows the formation of a ring resonator device, as shown in Fig. 5(d), for filtering applications.

The above findings make the LW appealing for energy confinement, transport, and integrated photonics applications, as the 1D object is the smallest waveguide possible. Also, due to its planar configuration, strong mode confinement [46], and pseudospin polarization [43], LW is attractive for light-matter interaction and chiral quantum processes [21,36]). Moreover, the significant field enhancement and the available air channel at the interface line can potentially offer simple implementation for microplasma and vacuum-based electronic devices [47]. Furthermore, the adopted effective-medium approach allows for forming LWs with reconfigurable pathways [48,40]. The associated tuning capability and the field singularity may also pave the way to nonlinear photonic structures for switching and modulation applications [49].

This work has been supported in part by AFOSR Grant No. FA9550-16-1-0093.

*dbisharat2-c@my.cityu.edu.hk
†dsievenpiper@eng.ucsd.edu

[1] J. A. Jr. Polo, T. G. Mackay, and A. Lakhtakia, *Electromagnetic Surface Waves: A Modern Perspective*, 1st ed. (Elsevier Inc., London, 2013).
[2] J. Homola, *Surface Plasmon Resonance Based Sensors* (Springer, New York, 2006).
[3] M. Dragoman and D. Dragoman, Prog. Quantum Electron. **32**, 1 (2008).
[4] A. V. Zayats, I. I. Smolyaninov, and A. A. Maradudin, Phys. Rep. **408**, 131 (2005).
[5] S. I. Bozhevolnyi, V. S. Volkov, E. Devaux, J. Y. Laluet, and T. W. Ebbesen, Nature (London) **440**, 508 (2006).
[6] E. Moreno, S. G. Rodrigo, S. I. Bozhevolnyi, L. Martín-Moreno, and F. J. García-Vidal, Phys. Rev. Lett. **100**, 023901 (2008).
[7] L. Lu, J. D. Joannopoulos, and M. Soljačić, Phys. Rev. Lett. **108**, 243901 (2012).
[8] A. Y. Nikitin, F. Guinea, F. J. Garcia-Vidal, and L. Martín-Moreno, Phys. Rev. B **84**, 161407(R) (2011).
[9] A. B. Khanikaev, S. H. Mousavi, W.-K. Tse, M. Kargarian, A. H. MacDonald, and G. Shvets, Nat. Mater. **12**, 233 (2013).
[10] T. Ma, A. B. Khanikaev, S. H. Mousavi, and G. Shvets, Phys. Rev. Lett. **114**, 127401 (2015).
[11] L.-H. Wu and X. Hu, Phys. Rev. Lett. **114**, 223901 (2015).
[12] A. Slobozhanyuk, S. H. Mousavi, X. Ni, D. Smirnova, Y. S. Kivshar, and A. B. Khanikaev Nat. Photonics **11**, 130 (2017).
[13] L. Lu, J. D. Joannopoulos, and M. Soljačić, Nat. Photonics **8**, 821 (2014).
[14] M. Hafezi, E. A. Demler, M. D. Lukin, and J. M. Taylor, Nat. Phys. **7**, 907 (2011).

[15] W. Gao, M. Lawrence, B. Yang, F. Liu, F. Fang, B. Beri, J. Li, and S. Zhang, Phys. Rev. Lett. **114**, 037402 (2015).
[16] M. C. Rechtsman, J. M. Zeuner, Y. Plotnik, Y. Lumer, D. Podolsky, F. Dreisow, S. Nolte, M. Segev, and A. Szameit, Nature (London) **496**, 196 (2013).
[17] A. Alù and N. Engheta, IEEE Trans. Antennas Propag. **51**, 2558 (2003).
[18] W. Tan, Y. Sun, H. Chen, and S.-Q. Shen, Sci. Rep. **4**, 3842 (2014).
[19] X. Shi, C. Xue, H. Jiang, and H. Chen, Opt. Express **24**, 18580 (2016).
[20] M. G. Silveirinha, Phys. Rev. B **93**, 075110 (2016).
[21] P. Lodahl, S. Mahmoodian, S. Stobbe, A. Rauschenbeutel, P. Schneeweiss, J. Volz, H. Pichler, and P. Zoller Nature (London) **541**, 473 (2017).
[22] T. Van Mechelen and Z. Jacob, Optica **3**, 118 (2016).
[23] F. J. Garcia-Vidal, L. Martín-Moreno, and J. B. Pendry, J. Opt. A **7**, S97 (2005).
[24] S. Maci, G. Minatti, M. Casaletti, and M. Bosiljevac, IEEE Antennas Wireless Propag. Lett. **10**, 1499 (2011).
[25] B. H. Fong, J. S. Colburn, J. J. Ottusch, J. L. Visher, and D. F. Sievenpiper, IEEE Trans. Antennas Propag. **58**, 3212 (2010).
[26] H. J. Bilow, IEEE Trans. Antennas Propag. **51**, 2788 (2003).
[27] F. Elek, B. B. Tierney, and A. Grbic, IEEE Trans. Antennas Propag. **63**, 3956 (2015).
[28] R. Quarfoth and D. Sievenpiper, IEEE Trans. Antennas Propag. **63**, 4593 (2015).
[29] A. M. Patel and A. Grbic, IEEE Trans. Antennas Propag. **59**, 2087 (2011).
[30] H. Wakatsuchi, S. Kim, J. J. Rushton, and D. F. Sievenpiper, Phys. Rev. Lett. **111**, 245501 (2013).
[31] P.-Y. Chen and A. Alú, Phys. Rev. B **84**, 205110 (2011).
[32] Z. Lou, X. Chen, J. Long, R. Quarfoth, and D. Sievenpiper, Appl. Phys. Lett. **106**, 211102 (2015).
[33] S. Ramo, J. Whinnery, and T. Van Duzer, *Fields and Waves in Communication Electronics*, 2nd ed. (John Wiley and Sons, New York, 1984).
[34] D. F. Sievenpiper, PhD thesis, UCLA, 1999.
[35] J.-M. Jin, *Theory and Computation of Electromagnetic Fields*, 1st ed. (Wiley, New Jersey, 2010).
[36] See Supplemental Material at http://link.aps.org/supplemental/10.1103/PhysRevLett.119.106802, which includes Ref. [37], for additional details, discussions, and results.
[37] J. D. Kraus and R. J. Marhefka, *Antenna: For All Applications*, 3rd Ed. (Mc Graw Hill, New York, 2002).
[38] M. Lei, S. Xiao, J. Long, and D. F. Sievenpiper, IEEE Trans. Antennas Propag. **64**, 3811 (2016).
[39] F. J. García de Abajo, ACS Photonics **1**, 135 (2014).
[40] A. Vakil and N. Engheta, Science **332**, 1291 (2011).
[41] W.-J. Chen, Z.-Q. Zhang, J.-W. Dong, and C. T. Chan, Nat. Commun. **6**, 8183 (2015).
[42] M. G. Silveirinha, Phys. Rev. B **95**, 035153 (2017).
[43] L. Marrucci, Nat. Phys. **11**, 9 (2015).
[44] M. Xiao, Z. Q. Zhang, and C. T. Chan, Phys. Rev. X **4**, 021017 (2014).
[45] M. Xiao, X. Huang, A. Fang, and C. T. Chan, Phys. Rev. B **93**, 125118 (2016).
[46] A. F. Koenderink, A. Alù, and A. Polman, Science **348**, 516 (2015).
[47] E. Forati, T. J. Dill, A. R. Tao, and D. Sievenpiper, Nat. Commun. **7**, 13399 (2016).
[48] X. Cheng, C. Jouvaud, X. Ni, S. H. Mousavi, A. Z. Genack, and A. B. Khanikaev, Nat. Mater. **15**, 542 (2016).
[49] M. Kauranen and A. V. Zayats, Nat. Photonics **6**, 737 (2012).

SUPPLEMENTARY MATERIAL

Guiding waves along an infinitesimal line between impedance surfaces

Dia'aaldin J. Bisharat[1,2*] and Daniel F. Sievenpiper[2†]

[1]*Department of Electronic Engineering, City University of Hong Kong, Kowloon, Hong Kong, China*
[2]*Electrical and Computer Engineering Department, University of California, San Diego, California, 92093, USA*
**dbisharat2-c@my.cityu.edu.hk; †dsievenpiper@eng.ucsd.edu*

I. Waveform of the line mode

We have presented a new type of one-dimensional electromagnetic mode that forms at the interface between two co-planar boundaries of complementary surface impedances. The mode has hybrid transverse-magnetic (TM) and transverse-electric (TE) modal field distributions as a result of the two boundary conditions and is necessarily localized at the interface due to the open boundary nature of the system. Since the wave is confined in both transverse directions to the wavevector along the infinitesimal line, where maximum -ideally singular- field enhancement exist, we term it as line wave. The mode's field variations are best described in cylindrical coordinates as evident from Fig.1a and b in the text. Looking at the cross sectional view, we can see that the electric field (E) vectors, for instance, lying in the transverse plane follow a sinusoidal variation along the angular (ϕ) direction. In addition, the fields' decay away from the interface line as a Bessel function in the radial (ρ) direction.

The general solution of the mode's waveform is given in terms of the longitudinal fields' components as:

$$E_z = E_0 K_{1/2}(\alpha\rho)\mathrm{Sin}\left(\frac{\phi}{2}\right)e^{-j\beta z} \quad , \quad H_z = \frac{E_0}{\eta_0} K_{1/2}(\alpha\rho)\mathrm{Cos}\left(\frac{\phi}{2}\right)e^{-j\beta z}$$

The remaining fields' components can then be derived in terms of the above using Maxwell's equations as follows:

$$E_\rho = \frac{j}{\alpha^2}\left(\frac{\omega\mu}{\rho}\frac{\partial H_z}{\partial\varphi} + \beta\frac{\partial E_z}{\partial\rho}\right) \quad \Rightarrow \quad E_\rho = -j\left(\frac{\beta+k_0}{2\alpha^2\rho} + \frac{\beta}{\alpha}\right)E_z$$

$$H_\rho = \frac{j}{\alpha^2}\left(\frac{-\omega\varepsilon}{\rho}\frac{\partial E_z}{\partial\varphi} + \beta\frac{\partial H_z}{\partial\rho}\right) \quad \Rightarrow \quad H_\rho = -j\left(\frac{\beta+k_0}{2\alpha^2\rho} + \frac{\beta}{\alpha}\right)H_z$$

$$E_\phi = \frac{j}{\alpha^2}\left(\frac{\beta}{\rho}\frac{\partial E_z}{\partial\varphi} - \omega\mu\frac{\partial H_z}{\partial\rho}\right) \quad \Rightarrow \quad E_\phi = j\eta_0\left(\frac{\beta+k_0}{2\alpha^2\rho} + \frac{k_0}{\alpha}\right)H_z$$

$$H_\phi = \frac{j}{\alpha^2}\left(\frac{-\beta}{\rho}\frac{\partial H_z}{\partial\varphi} - \omega\varepsilon\frac{\partial E_z}{\partial\rho}\right) \quad \Rightarrow \quad H_\phi = \frac{-j}{\eta_0}\left(\frac{\beta+k_0}{2\alpha^2\rho} + \frac{k_0}{\alpha}\right)E_z$$

II. Pseudo-Spin States and Spin-Momentum Locking

The spatial-inversion symmetry in our system due to the arrangement of the complementary boundaries across the propagation axis leads to forming a spin-filtered waveguide, in a similar fashion to that revealed in Ref. S1.

Firstly, this symmetry ensures that EM duality is ensured in a system with, for instance, PEC ($\varepsilon=-\infty,\mu=1$) and PMC ($\varepsilon=1,\mu=-\infty$) boundaries, which are ε -negative and μ -negative, respectively. In our proposed configuration, following the coordinate systems defined in Fig.1a, the system has a spatial inversion-symmetry of the form $\varepsilon(x)=\mu(-x)$. Thus, the Maxwell's equations for fields due to electric (*J*) and magnetic (*M*) current sources reduce to two decoupled equations:

$$\begin{pmatrix} J_x(x)\pm M_x(-x) \\ J_y(x)\mp M_y(-x) \\ J_z(x)\mp M_z(-x) \end{pmatrix} = i\omega\varepsilon(x)\psi^{\pm}(x)\pm\begin{pmatrix} 0 & \partial_z & -\partial_y \\ \partial_z & 0 & \partial_x \\ -\partial_y & -\partial_x & 0 \end{pmatrix}\psi^{\pm}(-x)\ , \qquad \psi^{\pm}(x)=\begin{pmatrix} E_x(x)\pm H_x(-x) \\ E_y(x)\mp H_y(-x) \\ E_z(x)\mp H_z(-x) \end{pmatrix}$$

Here, variables y and z are omitted while $E(M)$, $H(J)$ and ω are normalized by $1/\sqrt{\varepsilon_0}$, $1/\sqrt{\mu_0}$ and $1/\sqrt{\varepsilon_0\mu_0}$, respectively.

The states ψ^+ and ψ^- , which we refer to as pseudospin-up and pseudospin-down, respectively, are compatible with time-reversal (TR) symmetry requirement and are orthogonal to each other. Clearly, as dictated by the phase relation between the fields' components, the *E* and *H* field distributions of ψ^+ and ψ^- form anti-mirror and mirror reflection about the yz plane.

Secondly, the spatial inversion of PEC and PMC boundary conditions, and more generally *complementary* boundaries supporting only TM and TE (i.e., Z_{TM} and Z_{TE} surfaces, see equation 3), about the yz plane only allow ψ^+ and ψ^- to exists in forward ($+z$) and backward ($-z$) directions, respectively. As illustrated in Fig. S1, waves moving in the two opposite directions see different orientations of surface boundary conditions: a wave moving forward (backward) sees Z_{TE} (Z_{TM}) boundary to the right and Z_{TM} (Z_{TE}) to the left. Here, the simulated vector fields plots for line waves of opposite wavevectors show distinct (orthogonal) fields distributions (polarization patterns), which agree with the states ψ^+ and ψ^- definition. As a result, spin-momentum locking (i.e. direction-dependent polarizations) is enforced and the line interface constitutes a spin-filtered channel.

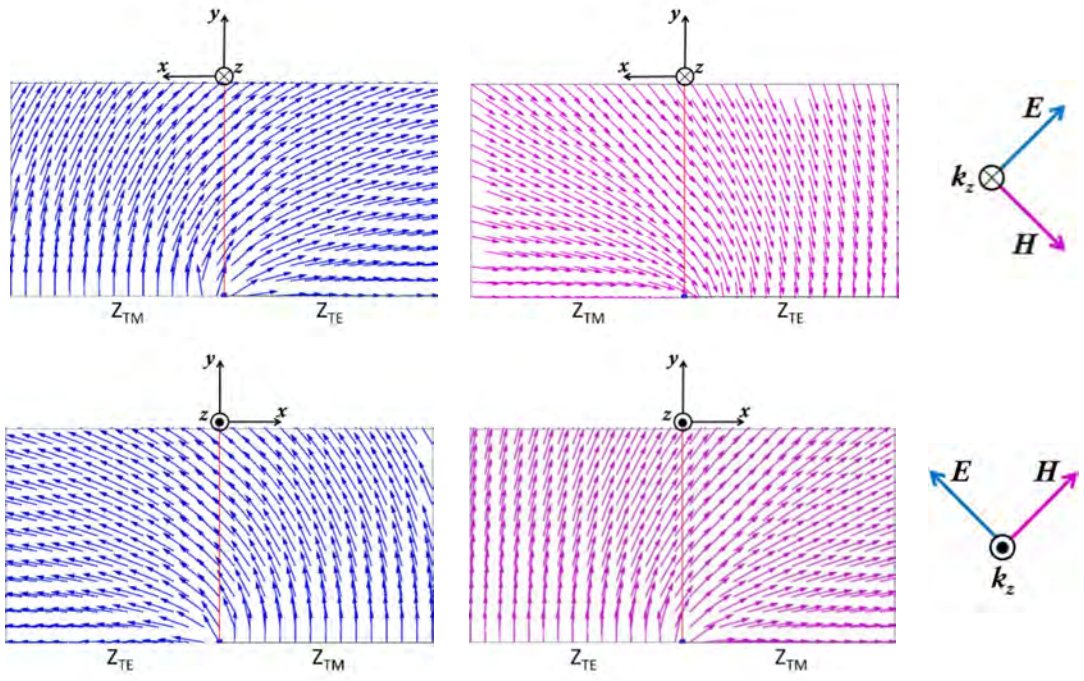

FIG. S1. Simulated vector fields distributions of the line wave. (Above) the eigen electric (blue arrows) and magnetic (magenta arrows) fields of the corresponding forward (into-page) mode, showing only ψ^+ state is supported, and (below) the eigen electric (blue arrows) and magnetic (magenta arrows) fields of the corresponding backward (out-of-page) mode, showing only ψ^- state is supported. The interface forms spin-filtered channel due to the boundaries' reversal, as the illustrated right-handed triad (above) and left-handed triad (below) show.

III. Symmetry-protection and Robustness

Consistently with the aforementioned definition of ψ^+ and ψ^-, the full-wave simulation shown in Fig.1d use electric and magnetic Hertzian dipoles along y-axis out-of-phase (in-phase) to excite ψ^+ (ψ^-) mode, which evidently turns out to be supported along the interface line in the forward (backward) direction only. Therefore, once one of the two orthogonal modes is excited, the wave cannot be reflected, as long as the boundary inversion-symmetry is not broken. As expected, one the other hand, the reversal of surface boundaries as shown Fig.5a prohibits the line wave from being transmitted further onward since the direction along which the excited mode is allowed becomes opposite across the junction.

This symmetry-protection grants our line-wave guide with topological-like robustness against certain defects (structural imperfections). These defects must not violate pseudospin-degeneracy or cause reversal of boundary conditions. For example, in Fig.4a we demonstrate reflection coefficient (S_{11}) levels lower than -30dB for large variations in impedance discontinuity compared to the original state at minimum of about -70dB. The situation we investigate is illustrated in Fig. S2 (left). In addition, we have examined scattering due to curvature in the line interface path, which

causes coupling of the mode's energy to the surrounding bulk's surface modes, as shown in Fig. S2 (middle), as well as to free space. We also analyze the sensitivity of line wave's transmission characteristics to the size of the defect region, where $\zeta_0 = 10$ and $\zeta_1 = \zeta_2 = 5$, as shown in Fig. S2 (right). As expected, the larger the defect, the larger its influence on the line modes. Here, S_{11} levels lower than -30dB are observed for defect size as large as $1.25\,\lambda_0$.

Note that, like in our work, topologically-protected modes in reciprocal photonic topological insulators (PTIs) systems could couple to backscattering channels along opposite directions compatible with time-reversal symmetry, could scatter into free space upon any encounter of a defect (even a topology-preserving defect) in the case of open-boundary structure, and are subject to intrinsic material dissipation losses. Also, while it is usual to interface PTIs that are based on TR-symmetry broken by magnetization with arbitrary trivial boundaries such as PEC or air, this is not always a suitable choice for SPT systems as it can break the EM duality, which in turn results in a breakdown of the pseudo-spin degree of freedom and prevents the formation of the topological surface state at the interface [Ref. S2].

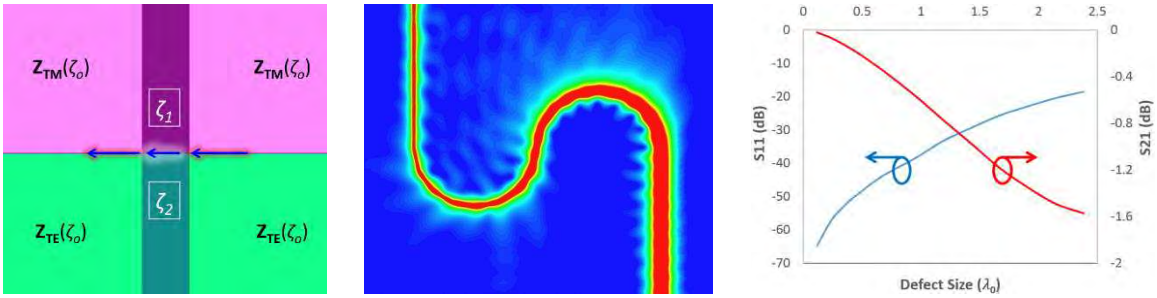

FIG. S2. Simulated transmission characteristics of the line wave in presence of a defect. (Left) schematic of the investigated impedance discontinuity across the line interface, (middle) leakage of line wave into surrounding bulk's surface modes due to bent interface line (curvature diameter = $2.5\,\lambda_0$), and (right) transmission and reflection coefficients of the line mode due to a defect ($\zeta_0 = 10$ and $\zeta_1 = \zeta_2 = 5$) of different sizes.

IV. Analogy to Topological Systems

Truly topologically-protected states require the existence of a bandgap, which is absent in our system. Thus, the notions of bulk-edge correspondence and Chern number that are usually associated with topological insulators are not applicable here. Nonetheless, our system shares some similarities with PTIs, particularly time-reversal (TR) invariant symmetry-protected topological (SPT) states formed between two claddings of opposite bianisotropy [Ref. 2].

Firstly, SPT system' interface must too preserve EM duality. A 2D domain wall with the flip of bianisotropy can be described as an interface across which the effective mass reverses its sign in a

corresponding manner to the emergence of edge states in 2D electronic systems that are described by a 2D Dirac equation [Ref. S2]. Likewise, by mapping between Maxwell's and the Dirac equation, ε-negative and μ-negative materials, which may effectively describe gaps of 1D symmetric photonic crystals (PCs), was shown to correspond to effective masses with opposite signs [Ref. S3, Ref. S4]. Hence, it is worth noting that our structure is comparable to an interface between these opposite single negative materials, both of which support evanescent waves but have opposite signs of imaginary impedance. Although interfacing ε-negative and μ-negative claddings gives rise to a bound state within the common bandgap, this is not as robust as SPT nontrivial states [Ref. 4]. This is because the topological order identified in this case considers either TM or TE polarization, whereas an overall topological number for a bulk isotropic dielectric, when there are no polarization restrictions, in any frequency interval, turns out to be always zero, i.e. trivial [Ref. S5].

Secondly, in PTIs with SPT states, the topologically nontrivial phase is created by engineering spin-orbit coupling of light with its polarization state playing the role of a spin degree of freedom in electronic systems [Ref. 2]. Similarly, our design supports wavevector-locked states of opposite polarizations. Evidently, our demonstrated transmission characteristics are to large extent robust against structural defects and discontinuities that preserve the material boundary properties, i.e. a capacitive (inductive) surface that supports TE (TM) mode does not become inductive (capacitive). This result, though does not show complete immunity to backscattering, is in a way reminiscent of topological protection in Ref. 2 which exists as long as a bandgap, which separates two inverted bands, does not close.

Clearly, the existence of the proposed line mode is not simply due to a mismatch in refractive index but necessarily due to interfacing two boundaries that have complementary effects on electric and magnetic fields. While drawing parallel between our design and ε-negative and μ-negative interface helps shed light on the origin of our proposed mode, it is important to differentiate between the two. Importantly, the associated band structure calculations inferring band inversion, hence topological protection, in these PC systems are not applicable in our effective-medium (continuum) approach. Also, while previous systems concern bulk media forming two semi-infinite spaces, across which a 2D surface wave resides, our system concerns two semi-infinite sheets that are laid side by side in free space, across which a 1D line wave resides. Furthermore, our design does not have a photonic bulk bandgap, i.e. susceptible to leakage into the bulk; as its two constituent surfaces support TM and TE modes at the frequency of interest. Notably, the presence of symmetry-protection (robustness against defects) in the absence of a bandgap would allow extra control over the mode properties and opens the door for more functionalities.

V. Singular Field Enhancement Prospect

We have experimentally demonstrated the feasibility of using artificial surfaces of properly tailored effective medium properties for implementing a line wave. Since the respective electromagnetic response of the two surfaces across the interface is complementary over a wide frequency band, a line wave is supported at these frequencies showing successful energy transmission and confinement. In particular, the theoretical field singularity of the line mode, which distinguishes it from other electromagnetic modes, is attractive for many applications. This singular field enhancement only exists for truly homogeneous surfaces with no losses. The line wave features are thus limited in our proof-of-concept demonstration by the thickness, dissipation loss, and the finite periodicity of the metasurface.

Here, we show additional results from full-wave simulations performed in ANSYS HFSS software of the fabricated prototype to quantify the achievable levels of field enhancement with realistic geometry and material properties. Figs.S3a and b show the simulation setup and surface plots of the electric field magnitude distribution (linear scale) over prototype 1 at 10 GHz. The setup and results are similar to those used and obtained in the ideal case shown in Fig.1a. This shows confinement of the wave in both transverse directions to the interface line albeit with some spurious surface modes excited on the horizontal plane across the interface line. Note also, as shown in Fig.3b in the text, the fields in both transverse direction, though have comparable decay profiles as expected from the ideal case in Fig.1b, seem more confined in the vertical direction with no apparent distortion (ripples) from surface modes.

As noted in the main text, the measured results are in good agreement with simulations but do not show the full extension of field concentration due to the finite distance of the scanning probe from the surface. Fig.S3c shows the electric field magnitude at different frequencies and distances above the simulated prototype's surface. Clearly, the field is highly concentrated within small area around the interface line. Though finite, the origin of the interface exhibits substantial increase in field intensity that is about 5 times larger than at merely 1mm ($\lambda_0/30$ at 10 GHz) distance away. In addition, increased field intensities are observed at higher frequencies. This is in agreement with the dispersion characteristics of the metasurface shown in Fig.2c and d, where ζ decreases with frequency. This correlation is also observed in the ideal case shown in Fig.4b, where an impedance discontinuity is introduced over a finite distance to tune the phase velocity of the wave.

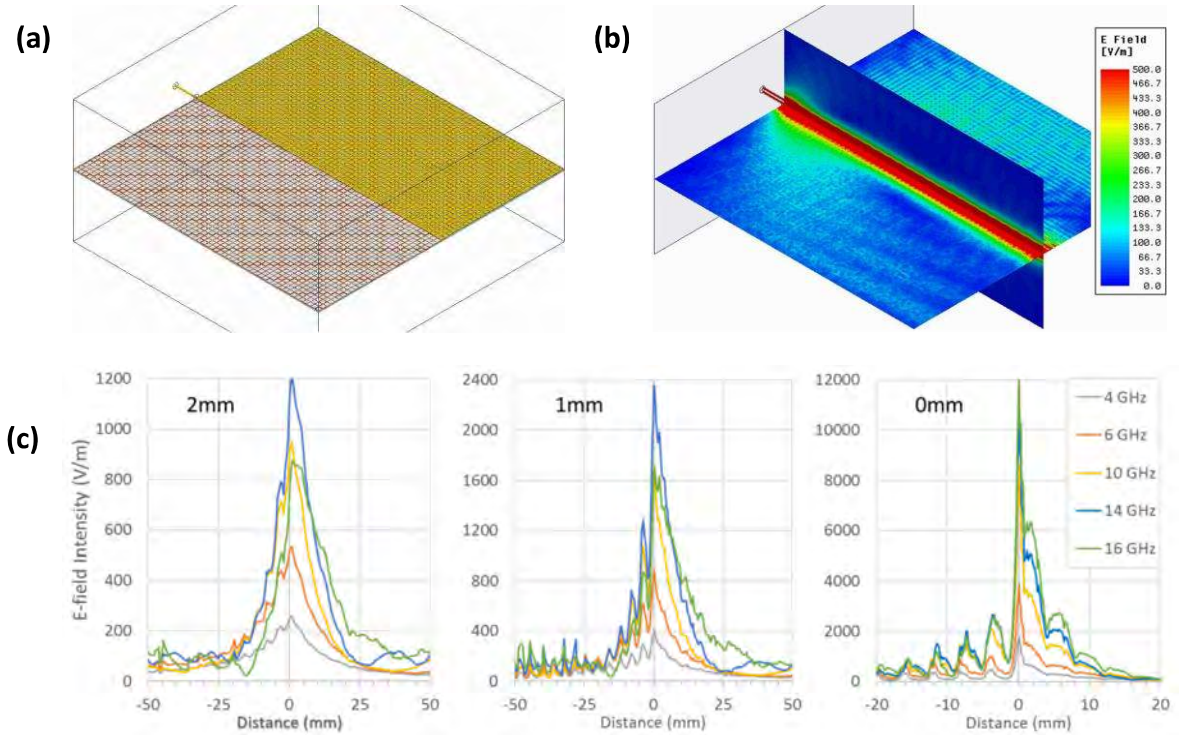

FIG. S3. Full-wave simulation of the fabricated metasurface prototype with identical geometric and material parameters. (a) Schematic of the fabricated metasurface and simulation setup, (b) surface plot of the electric field magnitude distribution (linear scale) over prototype 1 at 10 GHz, showing the confinement of the wave in both transverse directions to the interface line, (c) electric field enhancement within the vicinity of the line interface at different frequencies, obtained along the horizontal transverse direction at different distances above the metasurface.

As pointed out in the text, since the surface impedance methodology is general, one could potentially use new 2D materials that satisfy the required operation criteria at specific frequency range, such as graphene in the terahertz regime, which is known for its highly-confined long-lifetime plasmons. This approach would evade the drawbacks of finite periodicity and thickness of artificial surfaces. To quantify the effect of intrinsic material losses, the boundaries across the line interface could be modeled with complex surface impedances instead of purely imaginary ones. Fig. S4a shows the wave attenuation with propagation distance along the interface line for different complementary impedance values, where $\zeta = \zeta_0(1 + j\delta)$. Besides the expected shortening of the propagation distance due to higher losses, there is a trade-off between mode confinement and propagation distance. Here, the attenuation length of the line wave decreases with the decrease of phase velocity similarly to conventional surface modes. This is a result of slowing down the wave (i.e., shorting the effective wavelength), which leads to stronger localization of the mode at the surface; hence stronger interaction with the surface material. On the other hand, increasing ζ_0 will cause energy to be less bounded to the surface and hence allow longer propagation distance.

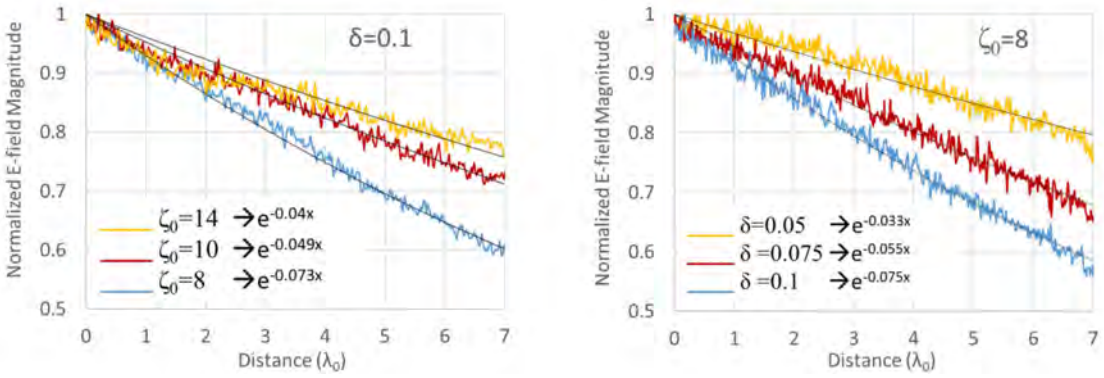

FIG. S4. Simulated attenuation results of the line mode on complementary impedance surfaces with losses. (Left) normalized decay curves of the electric fields and attenuation lengths of the line mode along the propagation direction (interface) at different levels of mode confinement (ζ_0 , phase velocity) with a fixed dissipation ratio (δ , resistance), and (right) decay curves and attenuation lengths of the line mode along the interface at different dissipation ratio (δ) with fixed mode confinement (ζ_0).

VI. Chiral Coupling Application

It has been shown in Ref. S6 that every fast decaying evanescent wave is inherently circularly polarized (CP) with its handedness tied to the direction of propagation. It is thus expected that the proposed line wave has this feature as well. This characteristic of direction-dependent polarization is key to chiral quantum processes, where the interaction depends on the light's propagation direction and the quantum emitter's transition dipole moment polarization. Commonly studied structures include nanofibers and photonic-crystal glide-plane waveguides, where chiral coupling occurs due to tight confinement of light in the transverse direction to propagation, which leads to a longitudinal component of the electric field. The phase of the longitudinal and transverse field components differs by ±π/2, with the sign depending on the propagation direction—forwards or backwards [Ref. S7]. As such, the electric field is elliptically polarized and has a transverse spin component that flips sign with the reversal of propagation direction.

In the investigation and implementation of chiral coupling application, the source is usually a pure electric dipole, unlike that in the simulations in Fig. 1d. The simulations in Fig.1d use both electric and magnetic Hertzian dipoles as a point source in accordance with the mathematical formulation of the states ψ^+ and ψ^- given above. That is, by specifying the phase relations between E and H fields (in our simulations *Ey* and *Hy*) we are able to selectively excite ψ^+ or ψ^-. Here, we directly relate our spin-locking feature to chiral coupling by showing that the interface line can equivalently restrict the radiation from electric dipole sources of opposite CP senses to opposite directions.

As well known, a magnetic dipole is equivalent to electric loop (concentric around the axis of the magnetic dipole). When excited by the same current, the radiated fields of the electric loop

(magnetic dipole) and electric dipole of the same origin position and axis, are orthogonal in orientation to each other and have π/2 phase difference [Ref. S8]. Thus, by combining the two, it is possible to realize a CP radiation pattern in the azimuth plane.

Based on the above discussion, it is clearly possible to excite ψ^+ or ψ^- and show direction-dependent polarization using CP source similar to that in Ref. 7. The CP source is formed by two electric dipoles pointing in the transverse (normal to surface) and longitudinal (along the interface line) directions, respectively. The field's distributions in Fig. S5 demonstrate a spin-filtered channel along the line interface similarly to that observed in Fig.1d. When the longitudinal dipole advances (lags) the transverse dipole by π/2 in phase, the line wave propagates only to the left (right) hand side. In both these cases the CP source is placed at $\lambda_0/10$ distance directly above the interface line. When the right-hand side source is placed at equal distance above the surface but with an offset of $\lambda_0/10$ in the horizontal direction, the line wave remains supported to the right side but with some wave also propagating to the left.

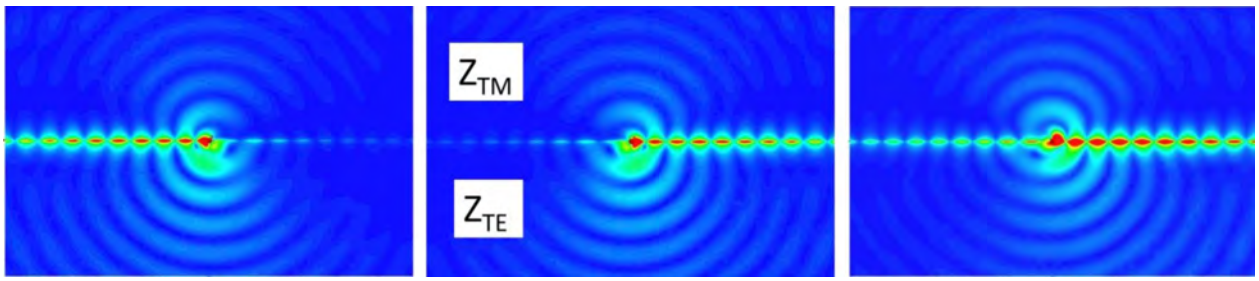

FIG. S5. Simulated direction-dependent circular polarization radiated by electric dipole source. Electric field surface distribution when LHCP source is above and at the center of the interface line (left), when RHCP source is above and at the center of the interface line (middle), and when RHCP source is above and to the side of the interface line.

References:

S1. Chen, W.-J., Zhang, Z.-Q., Dong, J.-W. & Chan, C. T. Symmetry-protected transport in a pseudospin-polarized waveguide. Nat. Commun. 6, 8183 (2015)

S2. Slobozhanyuk, A. et al. Three-dimensional all-dielectric photonic topological insulator. Nat. Photonics 11, 130 (2017)

S3. Tan, W., Sun, Y., Chen, H. & Shen, S.-Q. Photonic simulation of topological excitations in metamaterials. Sci. Rep. 4, 3842 (2014)

S4. Shi, X. et al. Topological description for gaps of one- dimensional symmetric all-dielectric

photonic crystals. Opt. Exp. 24(16), 18580 (2016)

S5. Silveirinha, M. G. Z2 topological index for continuous photonic materials. Phys. Rev. B 93, 075110 (2016)

S6. Mechelen, T. Van & Jacob, Z. Universal spin-momentum locking of evanescent waves. Optica 3, 118–126 (2016)

S7. Lodahl, P. et al. Chiral quantum optics. Nature 541, 473 (2017)

S8. Kraus, J. D. & Marhefka, R. J., Antenna: For All Applications 3rd Ed. New York: Mc Graw Hill (2002)

Method for Extracting the Effective Tensor Surface Impedance Function From Nonuniform, Anisotropic, Conductive Patterns

Jiyeon Lee, *Student Member, IEEE*, and Daniel F. Sievenpiper, *Fellow, IEEE*

***Abstract*— A patterning technique known as the point shifting method has enabled the generation of smoothly varying and highly anisotropic impedance surfaces with a wide range of patch sizes and shapes. Previously, the surface impedances of different shapes of unit cells were assumed by the impedance of similar size rectangle cells. In this paper, we study an approach to calculate the surface impedances for anisotropic polygon unit cells more accurately, based on the area moment of inertia equations. We define an alternative unit cell called the equivalent rectangle, which has the same tensor impedance properties of a general polygon unit cell in the surface impedance pattern. The size of the equivalent rectangle cell is calculated by using the moment of inertia equations between the polygon and the rectangle. The extracted surface impedance from the equivalent rectangle is compared to the surface impedance of polygon in the unit cell simulation, validating our method. We also verify the method by comparing the results between PEC patterns and impedance boundary sheets to which the extracted impedances are applied. Simulations of the patterns are verified by measurements as well.**

***Index Terms*— Anisotropic surface, artificial surface, metasurface, moment of inertia, patterning, surface impedance, surface waves.**

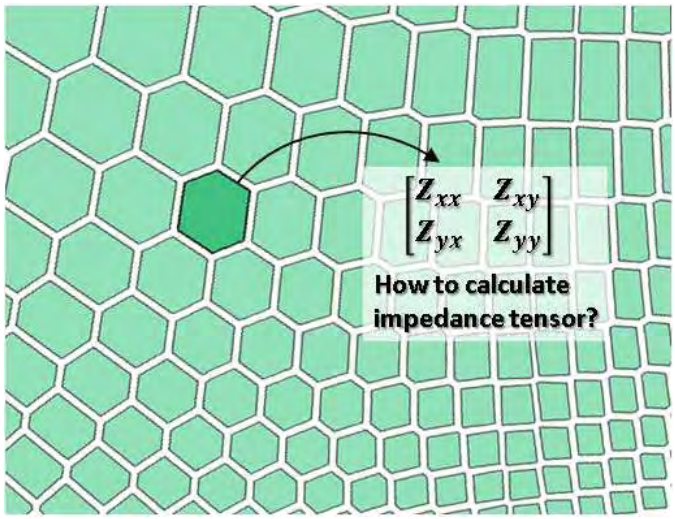

Fig. 1. Arbitrary anisotropic impedance surfaces generated by the point shifting method. The unit cells of the pattern have all different shapes and sizes.

I. Introduction

ARTIFICIAL impedance surfaces are engineered metasurfaces which enable surface waves to be controlled as changing electromagnetic properties of surfaces [1]. Those electromagnetic characteristics are determined by the capacitance between metal patches, the thickness and material of the substrate, and so on. Vertical conducting vias are also used when very high impedance values are needed or to block or absorb surface waves [2]–[5]. Among various conditions, varying the shape and size of the unit cells allows the designer to change the surface impedance properties. As the unit cells have nonsymmetric shapes, the impedance surface can have anisotropic properties, which are important for surface wave guiding [6]–[9], scattering [10]–[12], cloaking [13], [14], controlling polarization [15]–[17], and so on. Anisotropic surfaces can be described using the tensor impedance boundary condition [18] and various types of unit cell geometries for tensor impedance surfaces have been studied previously [19]. Most of the conventional impedance surfaces control their properties by changing the direction or size of gaps in periodic unit cells. This approach has limitations in the range of achievable anisotropy, limited freedom to change propagating direction of waves, and minimal diversity of the types of patterns that can be produced.

To address the limitation of conventional artificial impedance surfaces, a patterning technique that is called the point shifting method [20] has been developed. Fig. 1 shows that impedance surfaces produced by the point shifting method have smoothly varying anisotropic patterns with various shapes of unit cells which vary over the surface along with the impedance values. Previously, we assumed that the impedances of polygon patches produced by the point shifting method can be represented by the tensor impedance of rectangular or square unit cells as an approximation. However, as the unit cells created by the point shifting method are highly asymmetric and polygonal, their shapes are sufficiently different from rectangles that we cannot accurately determine

Manuscript received October 26, 2017; revised October 17, 2018; accepted November 28, 2018. Date of publication January 31, 2019; date of current version May 3, 2019. This work was supported by the Air Force Office of Scientific Research under Grant FA9550-16-1-0093. *(Corresponding author: Jiyeon Lee.)*

The authors are with the Electrical and Computer Engineering Department, University of California at San Diego, San Diego, CA 92093-0407 USA (e-mail: y0l001@ucsd.edu).

Color versions of one or more of the figures in this paper are available online at http://ieeexplore.ieee.org.

Digital Object Identifier 10.1109/TAP.2019.2896714

their surface impedance using this assumption. In addition, as the unit cells smoothly vary their orientations, the tensor impedance of each cell changes according to the tilt angle. For these reasons, we have developed a technique to accurately calculate tensor impedances for various shapes and directions of polygon cells.

In this paper, we introduce a new method to extract surface impedances from arbitrarily shaped patch cells using the moment of inertia equations. We discuss the details of the extraction process and provide an example of a calculation for a polygon unit cell. We verified that the extracted surface impedances of polygon unit cells are in the reasonable range by comparing the simulation results between a PEC pattern and an impedance boundary sheet. Measurements show that the field profile matches the simulations, verifying that this method produces the intended impedance profile.

II. Extracting Tensor Surface Impedance

Surface impedance is related with the geometry of a unit cell and specifically depends on the length in the propagation dimension when the unit cell is a rectangle [21]. Our goal is to find an equivalent rectangle that has the same tensor impedance properties of a general polygon unit cell in the surface impedance patterns to extract accurate surface impedances in a convenient way. We take this approach because the impedance properties of rectangular cells can be calculated easily using periodic boundary conditions, while more complex or less symmetrical cells cannot be arranged into periodic boundaries.

In calculating the impedance of the equivalent rectangular cell, we assume that it is in an infinite homogeneous surface consisting of identical cells. Thus, assigning this equivalent surface impedance to a general polygon unit cell corresponds to the local impedance at that cell, which is actually part of a spatially varying impedance function. The use of an impedance function based on the local impedance values corresponding to individual unit cells has been established previously in this paper on holographic impedance surfaces [18], [22].

In attempting to define a function that relates the impedance tensor to the unit cell shape, we found that the impedance of a rectangular lattice is higher in the direction in which the cells are longer, and we observe that this is similar to the mechanical moment of inertia of a flat rectangular plate, which is higher when it is rotated around the short axis. In this paper, we define the equivalent rectangle of the polygon unit cell as the rectangle having the same second moment of inertia [23] with the polygon unit cell. We note that this technique has been applied to limited patch style cells since other types of unit cells, such as active unit cells or patches with vias, have additional factors that determine their surface impedances besides the geometrical dimensions of the patches or the gaps between cells.

The concept of the moment of inertia was borrowed to calculate the equivalent rectangular cell because it can explain the geometrical property of an area regarding directions and weight of the cell. Fig. 2 shows a polygon and a rectangle in Cartesian coordinates, of which the second moment of inertia

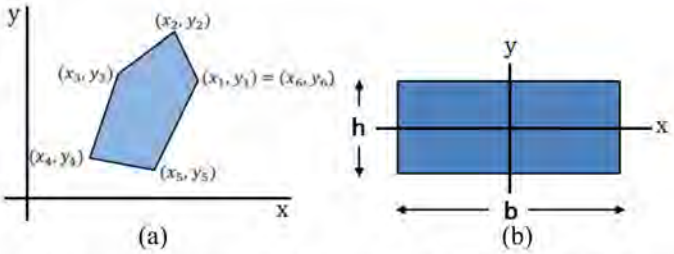

Fig. 2. Polygon and a rectangle for the moment of inertia equations are placed in Cartesian coordinates. (a) Numbering of vertices is counterclockwise. (b) Rectangle is located at the center of the coordinate system, where h is the length and b is the width.

for the polygon is obtained from the locations of the vertices, given by

$$I_x = \frac{1}{12}\sum_{i=1}^{i=N}\left(y_i^2 + y_i y_{i+1} + y_{i+1}^2\right)\left(x_i y_{i+1} - x_{i+1} y_i\right) \quad (1)$$

$$I_y = \frac{1}{12}\sum_{i=1}^{i=N}\left(x_i^2 + x_i x_{i+1} + x_{i+1}^2\right)\left(x_i y_{i+1} - x_{i+1} y_i\right) \quad (2)$$

$$I_{xy} = \frac{1}{24}\sum_{i=1}^{i=N}\left(x_i y_{i+1} + 2x_i y_i + 2x_{i+1} y_{i+1} + x_{i+1} y_i\right) \times \left(x_i y_{i+1} - x_{i+1} y_i\right) \quad (3)$$

and for the rectangle is given by

$$I_x = \int_A y^2 dA = \int_{-b/2}^{h/2}\int_{-h/2}^{h/2} y^2 dy dx = \int_{-b/2}^{b/2} \frac{1}{3}\frac{h^3}{4} dx = \frac{bh^3}{12} \quad (4)$$

$$I_y = \int_A x^2 dA = \int_{-b/2}^{b/2}\int_{-h/2}^{h/2} x^2 dy dx = \int_{-b/2}^{b/2} hx^2 dx = \frac{b^3 h}{12}. \quad (5)$$

The variable "N" in (1)–(3) is a number of vertices of the polygon.

Fig. 3 shows the procedure of calculating an equivalent rectangle that has the same impedance tensor as that of the polygon. A diamond-shaped unit cell is used as an example polygon in Fig. 3, because the impedance tensor of both of these shapes can be solved using periodic boundaries, thus we can verify the approach. As shown in (1)–(3) and Fig. 2(a), not only the shape (position of vertices) and size of polygon but also its location on the xy plane affects on the moment of inertia. Therefore, we set a centroid of the polygon as the zero point of the x- and y-axes first, shown as a red dot in Fig. 3(a) before calculating the moment of inertia. Once the moment of inertia matrix I is calculated from (1)–(3), we find the eigenvalues and eigenvectors of the matrix I. Since the eigenvalues of matrix I mean Ixx and Iyy of the diamond cell when the cell is perpendicular to axes, we apply these two values to (4) and (5) by definition of the equivalent rectangle. From (4) and (5), we can find a length and a width of the equivalent rectangle as shown in Fig. 3(b). Fig. 3(c) shows the tilted equivalent rectangle by θ, which is the angle of the polygon from the x-axis. The angle is calculated from

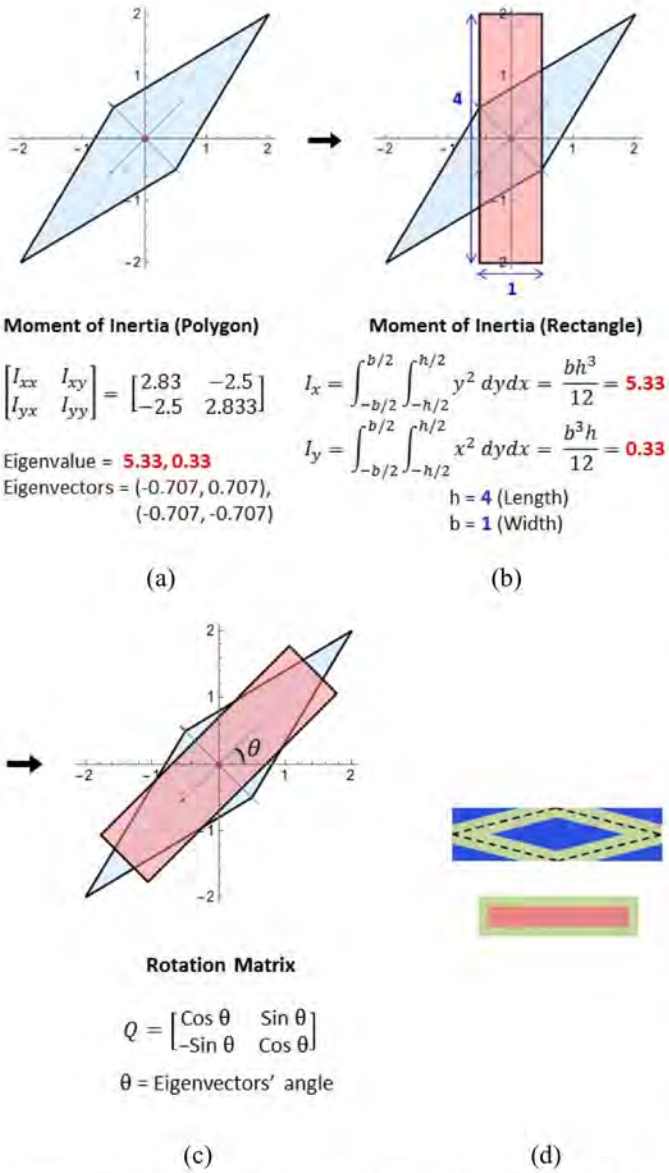

Fig. 3. (a) Polygon unit cell and centroid (a red dot) at the zero point. (b) Equivalent rectangle is calculated by the relationship between eigenvalues of the moment of inertia matrix for the polygon and the second moment of inertia of the rectangle. (c) Equivalent rectangle is tilted by the angle θ. θ is the angle that is calculated from eigenvectors of the moment of inertia matrix for the polygon. (d) Top view of polygon and rectangle cells for eigenmode simulations in HFSS. Polygon cell dimension is $4\sqrt{2}$ mm $\times\sqrt{2}$ mm and the equivalent rectangle is 4 mm $\times$ 1 mm with 0.25 mm gaps (0.5 mm gap width between patches). Structures are surrounded by two pairs of periodic boundaries.

eigenvectors of the polygon which is $-45°$ in the example. Fig. 3(d) shows the top view of polygon and rectangle cells for eigenmode simulations in Ansys HFSS version 18.2 (a full-wave, commercial software package). We assign 0.25 mm gaps on the cell so that the gap width between patches is 0.5 mm as shown in the diamond cell. Dashed lines in the diamond cell present the original size, as shown in Fig. 3(a).

Fig. 4 shows the plot of the surface impedance for rectangular cells which are analyzed as a function of cell geometry for a given substrate, thickness, frequency, and gap between patches. The rectangular unit cell structure was simulated by changing both its longitudinal and transverse length in the

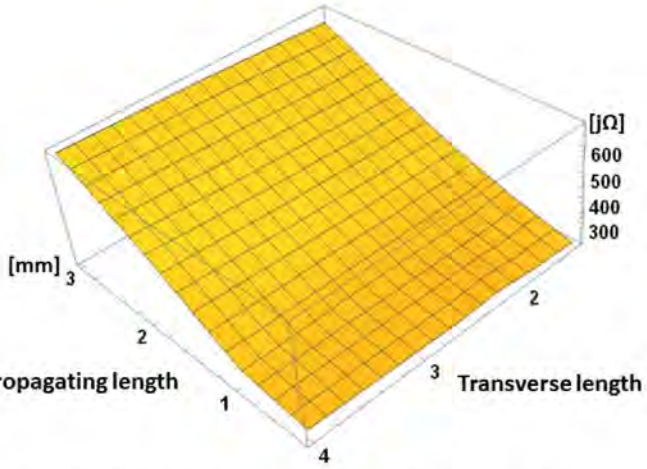

Fig. 4. Simulated impedance versus propagating lengths and transverse lengths at 7 GHz for rectangle unit cells on 2.5 mm Rogers 6010 with 0.25 mm gaps.

eigenmode solver in HFSS. The surface impedance for TM waves was calculated as

$$Z_{TM} = Z_0\sqrt{1-\left(\frac{k_{TM}c}{\omega}\right)^2}. \tag{6}$$

Although the surface impedances of a rectangular unit cell are mainly affected by the length in the propagation direction [21], there is still some dependence on the transverse dimension. This can be ignored in periodic rectangular cell patterns; however, here we consider the impedance variation due to the transverse length as well for the accuracy of the tensor impedance of a smoothly varying impedance pattern [11]. According to the graph in Fig. 4 which is for rectangular cells on a grounded 2.5 mm thick Rogers 6010 substrate ($\varepsilon_r = 10.2$) with 0.25 mm gap, a tensor impedance matrix of the equivalent rectangle, Z_{ER}, for 4 mm $\times$ 1 mm size [from Fig. 3(b)] at 7 GHz is

$$Z_{ER} = \begin{bmatrix} Z_{xx} & Z_{xy} \\ Z_{yx} & Z_{yy} \end{bmatrix} = \begin{bmatrix} 292.64 & 0 \\ 0 & 790.64 \end{bmatrix} j\Omega. \tag{7}$$

Once Z_{ER} is obtained from the surface impedance graph, we need to rotate the impedance tensor to fully represent the polygon in its coordinate system. In order to keep the properties of equivalent rectangle in the matrix, we use Jacobi rotation where the rotation matrix Q [24] is

$$Q = \begin{bmatrix} \mathrm{Cos}\theta & \mathrm{Sin}\theta \\ -\mathrm{Sin}\theta & \mathrm{Cos}\theta \end{bmatrix}. \tag{8}$$

Therefore, a tensor impedance matrix of polygon, Z_p, at 7 GHz from Z_{ER} is

$$Z_P = Q^T Z_{ER} Q = \begin{bmatrix} Z_{P\_xx} & Z_{P\_xy} \\ Z_{P\_yx} & Z_{P\_yy} \end{bmatrix} = \begin{bmatrix} 541.64 & -249 \\ -249 & 541.64 \end{bmatrix} j\Omega. \tag{9}$$

III. Tensor Impedance Simulation

To prove the validity of the equivalent rectangle, we simulated each polygon and equivalent rectangle unit cell in

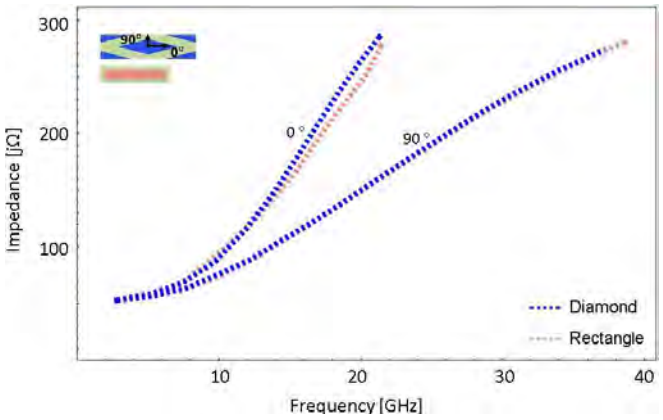

(a)

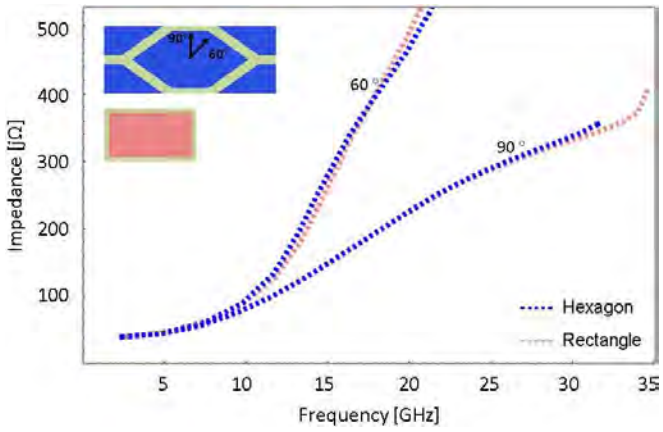

(b)

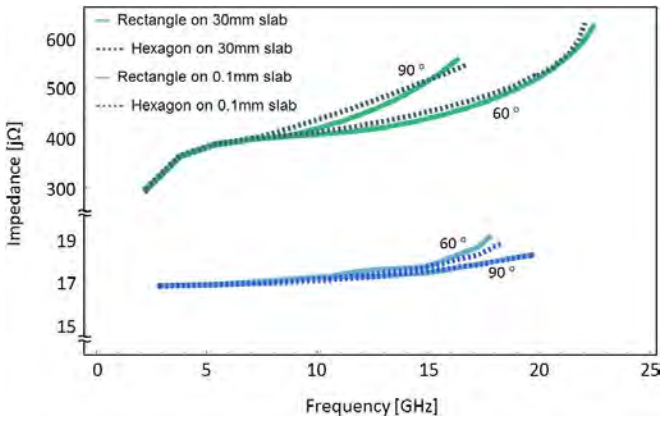

(c)

Fig. 5. Simulated surface impedance versus frequency for polygon and equivalent rectangle cells. (a) Diamond cell and its equivalent rectangle from Fig. 3. The size of diamond cell is $4\sqrt{2}$ mm $\times\sqrt{2}$ mm and the equivalent rectangle is 4 mm $\times$ 1 mm on 1.575 mm thick Rogers 5880. (b) Hexagon cell and its equivalent rectangle from the calculation. Transverse and longitudinal dimensions of hexagon are 6.9 and 3.46 mm, respectively, and the equivalent rectangle size is 5.1 mm $\times$ 2.97 mm with 0.25 mm gaps on 1.575 mm thick Rogers 5880. (c) Same hexagon and its equivalent rectangle cells from Fig. 5(b) with different thicknesses of the substrate. The impedances of equivalent rectangle and hexagon are matched in both electrically thick (30 mm) and thin (0.1 mm) cases as well.

the eigenmode solver. Fig. 5 shows frequency-dependent surface impedance plots of polygons and equivalent rectangles. Various propagation directions—0°, 60°, and 90° from the

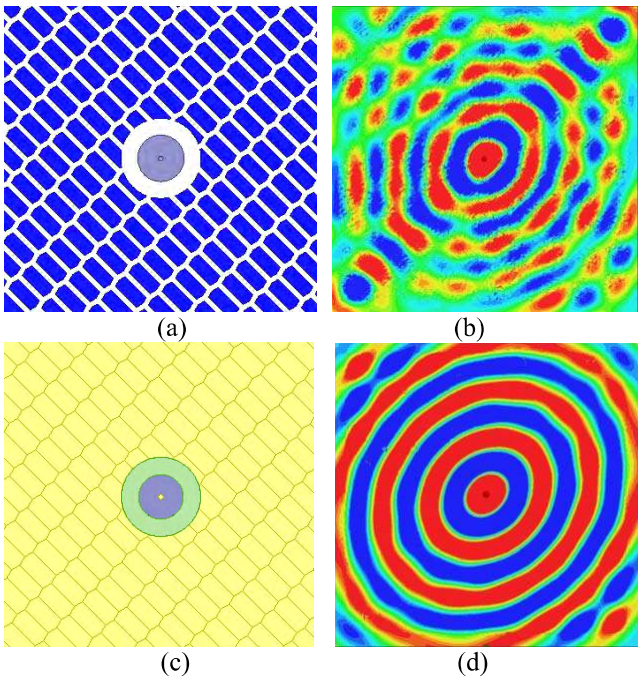

Fig. 6. (a) Enlarged section of the PEC pattern with hexagon unit cells and a coaxial feed. (b) Normalized electric field at 5.3 GHz. (c) Impedance boundaries for extracted tensor impedances of hexagon cells with a coaxial feed. Surface impedance of the substrate, 50 jΩ, is applied to the green region. (d) Normalized electric field at 5.3 GHz shows the same field trend with the PEC pattern.

x-axis—are simulated (the x-axis is defined as 0°) and they show the impedances of the polygon and the equivalent rectangle are matched well. We note that symmetric polygon cells are taken as examples here to prove this concept since nonsymmetric unit cell cannot be analyzed in the eigenmode solver [25]. In Fig. 5(a) and (b), we use Rogers 5880 grounded slabs with a thickness of 1.575 mm which is in the typical subwavelength region. In Fig. 5(c), we change the slab thickness of the hexagon and its equivalent rectangle cells to 30 and 0.1 mm thicknesses to verify the technique for the electrically thick and thin slabs. As shown in Fig. 5(c), the fair agreement of surface impedances between the hexagon and equivalent rectangle cells is plotted for both cases of 30 and 0.1 mm thicknesses. The plot of 30 mm thickness slab covers from $(\lambda/4)$ to 2λ frequency range and the plot of 0.1 mm thickness slab also show the agreement in $(\lambda/1000) \sim (\lambda/166)$ frequncy range.

We also extend this method from a single unit cell to a whole impedance pattern for the purpose of validating our impedance extraction technique. The impedance values extracted from individual unit cells are simulated using tensor impedance boundaries in HFSS and compared to a simulation of the conducting patches. We start with a simple anisotropic impedance pattern with hexagonal unit cells, which is generated by the point shifting method [20]. As shown in Fig. 6(a), unit cells are symmetric hexagon shapes and form an angle of 45° with the x- and y-axes. The size of the hexagonal unit cell is 3.58 mm in the long dimension and 1.47 mm in the short dimension with 0.6 mm gaps between the cells, and all cells have same sizes on the pattern. The overall pattern dimensions are 220 mm $\times$ 220 mm, with

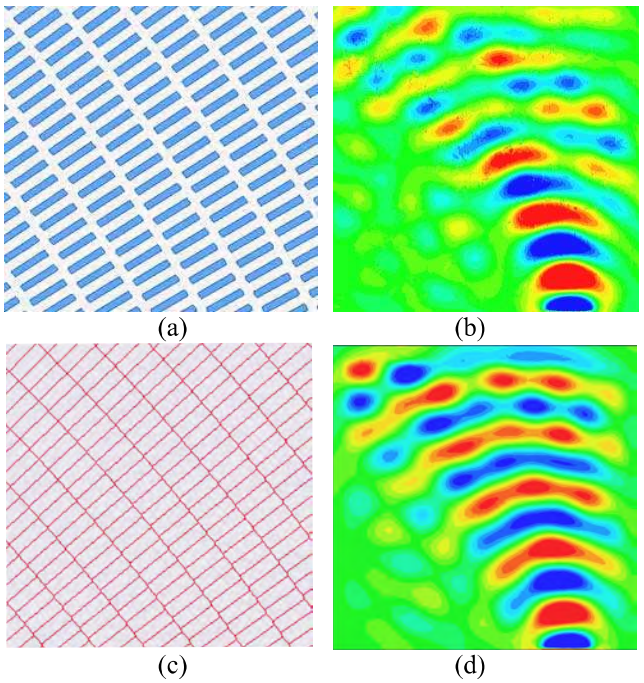

Fig. 7. (a) Part of the PEC pattern with anisotropic polygon cells. (b) Normalized electric field at 7 GHz. (c) Impedance boundaries for extracted tensor impedances of polygon cells. (d) Normalized electric field at 7 GHz shows the same field trend with the PEC pattern.

5952 perfectly conducting patches on a grounded 2.5-mm-thick Rogers 6010 substrate. A coaxial feed is located in the middle of the panel and its diameter is 5 mm. Fig. 6(b) shows the field plot at 2 mm above the board at 5.3 GHz from the driven modal solver in ANSYS HFSS. The wave propagates faster in the low impedance region and more slowly in the high impedance direction, so that the anisotropy produces ellipse-shaped patterns of constant phase as expected. The additional variations shown in PEC simulation are indicative of a standing-wave pattern which is caused by edge scattering.

We calculate the equivalent rectangle and the surface impedance matrix of the hexagonal unit cell using the impedance extraction procedure. The equivalent rectangle of the hexagonal unit cell is 3.4 mm $\times$ 1.45 mm, and the impedance Z_p based on the extracted impedance function is $\begin{bmatrix} 245 & -78 \\ -78 & 245 \end{bmatrix}$ jΩ at 5.3 GHz. For verifying the calculated impedance value Z_p, we have simulated an impedance boundary sheet with the extracted impedance profile. Fig. 6(c) shows a part of the impedance boundary sheet which is divided into individual cells that are assigned the effective impedance boundary extracted from the hexagonal unit cells. The impedance Z_p has been applied on each region of the impedance boundary sheet and the size of the whole sheet is the same as the panel that is patterned with conductive cells. In Fig. 6(d), we have obtained the field plot that matches with the result of the PEC pattern, under the same simulation setup. Except for reflections due to the edges in Fig. 6(b), the regions where reflections are not significant still show the same shape of oval with the same aspect ratio.

We generated an additional surface impedance pattern using the point shifting method, which is highly anisotropic and smoothly varies the direction of high impedance over a 90° rotation. A part of the pattern is shown in Fig. 7(a). Each elongated polygon unit cell that is close to a rectangular cell has a slightly different shape and size as the pattern has a gradual change with the rotation angle. It has different orientations of the maximum and minimum values of impedance so that every cell has a different surface impedance Z_p tensor. The overall pattern dimensions are 150 mm $\times$ 150 mm, with 7750 conductive patches on a grounded 2.5-mm-thick Rogers 6010 substrate, and there are 0.6 mm gaps between the cells. A thin, wide rectangular source is placed at the right bottom edge of the panel for excitation. Fig. 7(b) shows the field plot of the whole panel at 2 mm above the board at 7 GHz analyzed in the driven modal solver in HFSS. The sets of Z_P from the impedance extraction method are applied to each impedance boundary region correspondingly which is shown in Fig. 7(c). As elongated unit cells have a smooth transition toward 90°, the range of Z_{P-xx} is 468.23 jΩ to 236.65 jΩ and Z_{P-yy} is 231.86 jΩ to 464.28 jΩ at 7 GHz. Fig. 7(d) shows the field plot from the impedance boundary simulation which has the same trend as the panel consisting of conducting patches, verifying that the impedances extracted from the metallic patches are accurate.

Fig. 8 shows another inhomogeneous pattern including smoothly varying impedance transition with various shapes of unit cells. As shown in Fig. 8(a), the pattern consists of both isotropic and anisotropic cells that have different shapes and sizes. Fig. 8(b) shows a whole PEC pattern on 1.5 mm thick Rogers 6010, and the same coaxial feed in Fig. 6 is located in the middle of the plane. The board dimensions are 110 mm $\times$ 110 mm with the pattern consisting of 2580 perfectly conducting patches. Fig. 8(c) shows a normalized field plot at 2 mm above the PEC pattern at 9 GHz. The range of Z_{P-xx} is 480.128 jΩ to 98.58 jΩ and Z_{P-yy} is 480.13 jΩ to 98.58 jΩ at 9 GHz. In Fig. 8(c), the field at the four corners propagates faster since the impedances in diagonal directions are lower than neighboring impedances as the transition of unit cells shows the pattern. These stretched fields in the diagonal directions make planar wavefronts in the four directions which could be useful, for example, to feed a planewave in multiple directions. Fig. 8(e) shows the normalized field plot at 9 GHz from the impedance boundary simulation with the extracted tensor impedance set. The overall agreement between two simulations proves that this technique extracts tensor impedances within a reliable margin of error. A mismatch of field distributions in the center regions of Fig. 8(c) and (e) is likely due to a limitation of the patterning technique as shown in Fig. 9. We note that phase difference could be seen in the field distribution comparison between PEC pattern simulations and impedance boundary simulations due to different dispersion characteristics. The impedance boundary simulation in the driven modal solver is an approximation for the wave behavior only based on assigned impedances, so it is possible that there are some differences between PEC and impedance boundary simulation results. However, we can check the trend of the wave propagation in the comparison and it allows us to prove the validity of the extracted impedance set.

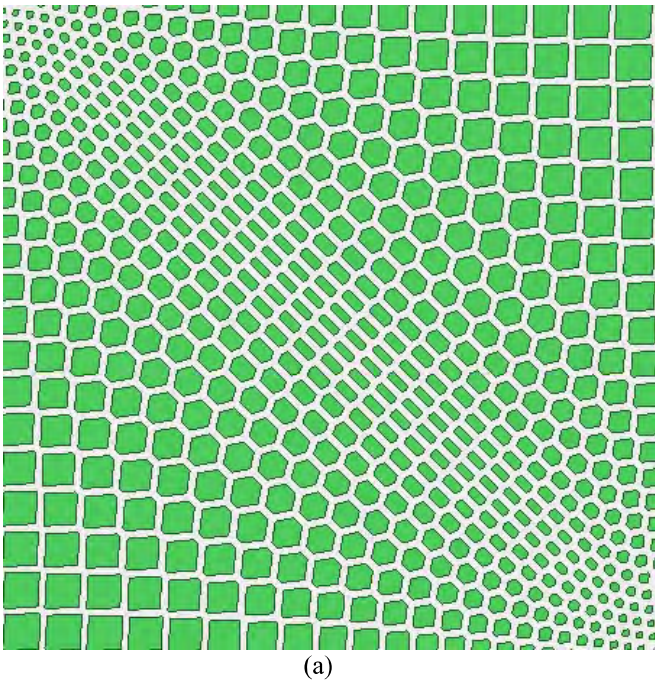

Fig. 8. (a) Enlarged section of the PEC pattern. The largest cell size is 3 mm × 3 mm and the smallest one is 0.5 mm × 0.5 mm. The gaps between patches are 0.6 mm. (b) Pattern on the board with a coaxial feed. (c) Normalized electric field at 9 GHz at 2 mm above the PEC pattern. Circular fields from the coaxial feed turn into square fields as it follows the impedance surface. (d) Impedance boundaries corresponding to polygon unit cells and the board. (e) Normalized electric field at 9 GHz at 2 mm above the impedance boundary plane.

IV. Experiments

The hexagonal cell pattern was fabricated using printed circuit fabrication technology and is shown in Fig. 10(a). The panel is 230 mm × 230 mm with 5952 copper patches on the top of the board, and the bottom of the board is a ground plane. There is a 5 mm diameter hole in the middle of the pattern

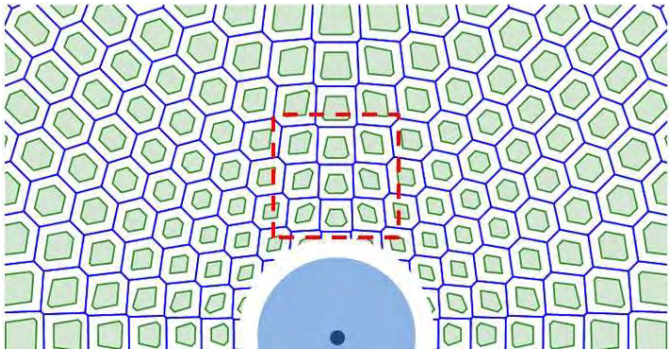

Fig. 9. Part of the impedance boundary pattern (blue) and the PEC pattern (green). The shapes of some of the small-size unit cells around the coaxial feed differ from their impedance boundary unit cells due to a limitation of the point shifting method. This brings a mismatch around the feed in the field plot as shown in Fig. 8(c) and (e), although impedance boundary cells have same surface impedances as the PEC cells.

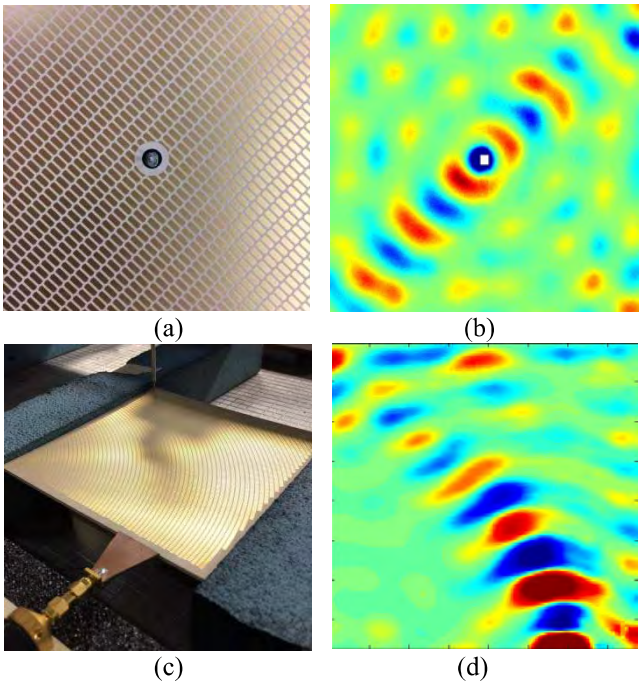

Fig. 10. (a) Closeup photograph of the fabricated hexagon cells pattern. (b) Normalized near-field plot of the surface waves scanned over a 230 mm × 230 mm area. (c) Details of the feed and the measurement technique for the fabricated 90° curved pattern. (d) Normalized near-field plot of the surface waves scanned over a 150 mm × 150 mm area.

for a coaxial feed which is the excitation source. A vertical probe was swept 2 mm above the surface along a 1 mm grid and an Agilent E5071C vector network analyzer recorded the magnitude and the phase of the surface wave. Normalized field results are shown in Fig. 10(b). The circular wavefronts generated by the feed are transformed into elliptical wavefronts as they follow the anisotropic impedance profile, as expected. The result is matched with that shown in Fig. 6(b) including the effect shown by edge scattering.

The 90° curve pattern and its measurement setup are shown in Fig. 10(c). The feed is a trapezoidal sheet of Rogers 5880 and an end-launch SMA adapter is attached to the back

of the feed, which functions as a small H-plane sectoral horn. A field map was produced in the same way as with the hexagonal cell pattern described earlier and is plotted in Fig. 10(d). The 35 mm wide flat wavefronts excited by the feed smoothly move from the bottom edge to the left side edge of the panel along the anisotropic impedance pattern of the structure.

V. Conclusion

We have introduced an approach to extract surface impedances of polygon unit cells using the second moment of inertia equations. This method has the ability to calculate the impedance for nonsymmetric patch cells, which cannot be obtained directly from eigenmode simulations. We have demonstrated that the extracted impedances obtained from the equivalent rectangle are matched with the impedances of the original polygon unit cells. We have chosen a simple and practical example to validate our method experimentally, in the form of a hexagonal anisotropic pattern as well as an anisotropic 90° curved pattern and a square field pattern.

Acknowledgment

The author would like to thank J. Rushton, A. Li, and Y. Li for helpful suggestions and contributions during the work.

References

[1] T. B. A. Senior, "Approximate boundary conditions," *IEEE Trans. Antennas Propag.*, vol. AP-29, no. 5, pp. 826–829, Sep. 1981.
[2] S. Kim, H. Wakatsuchi, J. J. Rushton, and D. F. Sievenpiper, "Switchable nonlinear metasurfaces for absorbing high power surface waves," *Appl. Phys. Lett.*, vol. 108, no. 4, 2016, Art. no. 041903.
[3] H. Wakatsuchi, S. Kim, J. J. Rushton, and D. F. Sievenpiper, "Circuit-based nonlinear metasurface absorbers for high power surface currents," *Appl. Phys. Lett.*, vol. 102, no. 21, May 2013, Art. no. 214103.
[4] A. Li, S. Kim, Y. Luo, Y. Li, J. Long, and D. F. Sievenpiper, "High-power transistor-based tunable and switchable metasurface absorber," *IEEE Trans. Microw. Theory Techn.*, vol. 65, no. 8, pp. 2810–2818, Aug. 2017.
[5] D. Sievenpiper, L. Zhang, R. F. J. Broas, N. G. Alexopolous, and E. Yablonovitch, "High-impedance electromagnetic surfaces with a forbidden frequency band," *IEEE Trans. Microw. Theory Techn.*, vol. 47, no. 11, pp. 2059–2074, Nov. 1999.
[6] R. Quarfoth and D. Sievenpiper, "Artificial tensor impedance surface waveguides," *IEEE Trans. Antennas Propag.*, vol. 61, no. 7, pp. 3597–3606, Jul. 2013.
[7] M. Li, S. Xiao, J. Long, and D. F. Sievenpiper, "Surface waveguides supporting both TM mode and TE mode with the same phase velocity," *IEEE Trans. Antennas Propag.*, vol. 64, no. 9, pp. 3811–3819, Sep. 2016.
[8] R. G. Quarfoth and D. F. Sievenpiper, "Nonscattering waveguides based on tensor impedance surfaces," *IEEE Trans. Antennas Propag.*, vol. 63, no. 4, pp. 1746–1755, Apr. 2015.
[9] A. M. Patel and A. Grbic, "Transformation electromagnetics devices based on printed-circuit tensor impedance surfaces," *IEEE Trans. Microw. Theory Techn.*, vol. 62, no. 5, pp. 1102–1111, May 2014.
[10] R. Quarfoth and D. Sievenpiper, "Surface wave scattering reduction using beam shifters," *IEEE Antenna Wireless Propag. Lett.*, vol. 13, pp. 963–966, 2014.
[11] G. Minatti, S. Maci, P. De Vita, A. Freni, and M. Sabbadini, "A circularly-polarized isoflux antenna based on anisotropic metasurface," *IEEE Trans. Antennas Propag.*, vol. 60, no. 11, pp. 4998–5009, Nov. 2012.
[12] A. M. Patel and A. Grbic, "A printed leaky-wave antenna based on a sinusoidally-modulated reactance surface," *IEEE Trans. Antennas Propag.*, vol. 59, no. 6, pp. 2087–2096, Jun. 2011.
[13] R. Quarfoth and D. Sievenpiper, "Anisotropic surface impedance cloak," in *Proc. IEEE Antennas Propag. Soc. Int. Symp. (APSURSI)*, Jul. 2012, pp. 1–2.
[14] P.-Y. Chen and A. Alù, "Mantle cloaking using thin patterned metasurfaces," *Phys. Rev. B, Condens. Matter*, vol. 84, no. 20, Nov. 2011, Art. no. 205110.
[15] G. Minatti, F. Caminita, E. Martini, M. Sabbadini, and S. Maci, "Synthesis of modulated-metasurface antennas with amplitude, phase, and polarization control," *IEEE Trans. Antennas Propag.*, vol. 64, no. 9, pp. 3907–3919, Sep. 2016.
[16] X. Wan *et al.*, "Manipulations of dual beams with dual polarizations by full-tensor metasurfaces," *Adv. Opt. Mater.*, vol. 4, no. 10, pp. 1567–1572, Oct. 2016.
[17] S. Liu *et al.*, "Full-state controls of terahertz waves using tensor coding metasurfaces," *ACS Appl. Mater. Interfaces*, vol. 9, no. 25, pp. 21503–21514, Jun. 2017.
[18] B. H. Fong, J. S. Colburn, J. J. Ottusch, J. L. Visher, and D. F. Sievenpiper, "Scalar and tensor holographic artificial impedance surfaces," *IEEE Trans. Antennas Propag.*, vol. 58, no. 10, pp. 3212–3221, Oct. 2010.
[19] R. Quarfoth and D. Sievenpiper, "Broadband unit-cell design for highly anisotropic impedance surfaces," *IEEE Trans. Antennas Propag.*, vol. 62, no. 8, pp. 4143–4152, Aug. 2014.
[20] J. Lee and D. Sievenpiper, "Patterning technique for generating arbitrary anisotropic impedance surfaces," *IEEE Trans. Antennas Propag.*, vol. 64, no. 11, pp. 4725–4732, Nov. 2016.
[21] R. Quarfoth and D. Sievenpiper, "Simulation of anisotropic artificial impedance surface with rectangular and diamond lattices," in *Proc. IEEE Int. Symp. Antennas Propag. (APSURSI)*, Jul. 2011, pp. 1498–1501.
[22] Y. B. Li, X. Wan, B. G. Cai, Q. Cheng, and T. J. Cui, "Frequency-controls of electromagnetic multi-beam scanning by metasurfaces," *Sci. Rep.*, vol. 4, Nov. 2014, Art. no. 6921.
[23] F. P. Beer, E. R. Johnston, and P. J. Cornwell, *Vector Mechanics for Engineers*, 10th ed. New York, NY, USA: McGraw-Hill, 2013, p. 495.
[24] G. H. Golub and C. F. Van Loan, *Matrix Computations*, 3rd ed. Baltimore, MD, USA: Johns Hopkins University Press, 1996.
[25] L. Brillouin, *Wave Propagation in Periodic Structures: Electric Filters and Crystal Lattices*. Chelmsford, U.K.: Courier Corporation, 2003.

Jiyeon Lee (S'14) received the B.S. degree from Hongik University, Seoul, South Korea, in 2007, and the M.S. and Ph.D. degrees from the University of California at San Diego, San Diego, CA, USA, in 2013 and 2018, respectively.

From 2008 to 2011, she was a Software Engineer of management information systems with SK C&C, Seoul. She is currently with Qualcomm Technologies, Inc., San Diego. Her current research interests include artificial impedance surfaces, metamaterials, antenna, and communication circuits.

Daniel F. Sievenpiper (M'94–SM'04–F'09) received the B.S. and Ph.D. degrees in electrical engineering from the University of California at Los Angeles, Los Angeles, CA, USA, in 1994 and 1999, respectively.

He was the Director of the Applied Electromagnetics Laboratory, HRL Laboratories, Malibu, CA, USA. He is currently a Professor with the University of California at San Diego, San Diego, CA, USA, where he is involved in antennas and electromagnetic structures. He has authored or co-authored more than 100 technical publications. He holds more than 70 issued patents. His current research interests include artificial impedance surfaces, conformal antennas, tunable and wearable antennas, and beam steering methods.

Dr. Sievenpiper was a recipient of the URSI Issac Koga Gold Medal in 2008. He has been an Associate Editor for IEEE Antennas and Wireless Propagation Letters since 2010.

Simulation Analysis of Electromagnetic Surface Wave Suppression by Soft Surfaces, Including Effects of Resistive and Active Elements

Chao Wang, *Member, IEEE*, Dia'aaldin Bisharat, *Student Member, IEEE*, Sanghoon Kim, *Member, IEEE*, En Li, *Member, IEEE*, and Daniel F. Sievenpiper, *Fellow, IEEE*

***Abstract*—The soft surface is defined by its anisotropic surface impedance, and it has the property of suppressing surface wave propagation for any polarization of the electric field. It can be used as a general design element for reducing scattering or controlling coupling between nearby antennas. In this letter, the suppression capabilities and bandwidth limitations of soft surfaces are analyzed using simulations to draw the following conclusions: First, a soft surface is as good as an ideal perfect magnetic conductor for suppressing vertically polarized surface currents; second, adding loss to the soft surface actually increases coupling between nearby antennas; third, the bandwidth of soft surfaces can be extended using active loading; and fourth, a soft surface boundary condition can suppress coupling below even the expected free-space wave coupling. Several simple examples are illustrated using simulations, including the effect of lossy substrates, designs for active loading, and the effects of soft surfaces on the contributions to coupling between nearby planar antennas.**

***Index Terms*—Active loading, free-space wave, minimum coupling, mutual coupling, surface impedance, surface waves.**

I. Introduction

THE electromagnetic soft surface was first described by Kildal [1], [2] as a periodic structure, which suppresses both transverse magnetic (TM) and transverse electric (TE) surface waves within a given frequency band. It can also be characterized as an electromagnetic band gap surface. For TM waves (the primary source of coupling between antennas on thin grounded substrates), it has the same surface wave suppression characteristics as an artificial magnetic conductor or high-impedance surface [3], [4], with the added benefit of simplicity as it only requires a one-dimensional (1-D) array of periodic grounded metal strips. These structures can be used to decrease mutual coupling between antenna elements that share the same ground plane [5], improve the efficiency of antennas [6], and cut down the backward radiation of antennas on finite ground planes [7]. In addition, many other applications of soft surfaces are introduced in the literature [8]–[11]. An electromagnetic soft surface may be made up of a dielectric slab containing a linear array of metal strips connected to the ground plane by vertical conducting vias [10]. This structure approximates a corrugated surface, but it is more practical because it is amenable to printed circuit board fabrication. However, soft surfaces have often narrow bandwidth, and the ideal design parameters and fundamental limitations of soft surfaces have not been fully explored. Several articles have been published to improve bandwidth [11]–[13] by changing the shape of the patches or strips. However, the bandwidth increase is typically still limited by the thickness of the substrate. To our knowledge, no publications to date have analyzed the fundamental limits of soft surfaces for suppressing surface waves, the effects of adding loss, the potential to improve bandwidth with active elements, or the performance metrics relative to other kinds of surface treatments or ideal impedance boundaries.

We have recently studied surface-wave coupling between antennas that share the same ground plane or substrate focusing on the properties of antennas in 2-D space and the equivalent coupling equation [14]. In this letter, we focus on the design of soft surfaces for suppressing surface-wave coupling and present an analysis, which provides four important results: 1) we find that the lossless soft surface is as good as an ideal perfect magnetic conductor (PMC) for suppressing TM surface waves, which are the most significant mode for antennas on thin substrates; 2) we show the counterintuitive result that adding any loss to the surface actually increases surface wave propagation and coupling relative to the lossless case; 3) we demonstrate that the bandwidth of soft surfaces can potentially be enhanced for a given thickness by using a non-Foster circuit loading, indicating the potential for active broadband surface wave suppression; and 4) we show that the coupling between two antennas can actually be suppressed below the level of free-space coupling, indicating that a soft surface boundary not only eliminates surface waves, but also has an effect on the nearby propagating free-space waves.

II. Effect of Loss on Soft Surface Performance

Our first goal is to analyze the effect of a soft surface on suppression of surface currents. The conventional soft surface structure is as shown in Fig. 1 [15]–[18]. The unit cell is 16.6 mm

Manuscript received September 15, 2018; revised October 4, 2018 and October 10, 2018; accepted October 12, 2018. Date of publication October 16, 2018; date of current version November 29, 2018. This work was supported in part by Air Force Office of Scientific Research (AFOSR) under Contract FA9550-16-1-0093; and in part by the China Scholarship Council. *(Corresponding author: Chao Wang.)*

C. Wang is with the Huawei Technologies Co., Ltd., Shenzhen 518129, China, with the University of Electronic Science and Technology of China, Chengdu 611731, China, and also with the University of California, San Diego, CA 92093 USA (e-mail: chaowang-alvin@outlook.com).

D. Bisharat is with the Department of Electronic Engineering, City University of Hong Kong, Hong Kong (e-mail: dbisharat2-c@my.cityu.edu.hk).

E. Li is with the University of Electronic Science and Technology of China, Chengdu 611731, China (e-mail: lien@uestc.edu.cn).

S. Kim and D. F. Sievenpiper are with the University of California, San Diego, CA 92130 USA (e-mail: sak041@ucsd.edu; dsievenpiper@eng.ucsd.edu).

Digital Object Identifier 10.1109/LAWP.2018.2876332

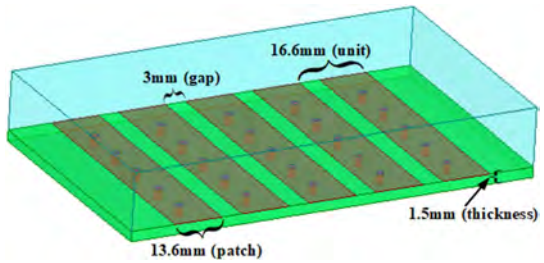

Fig. 1. Conventional soft surface structure consists of metallic strips that are connected to a ground plane by vertical conducting vias.

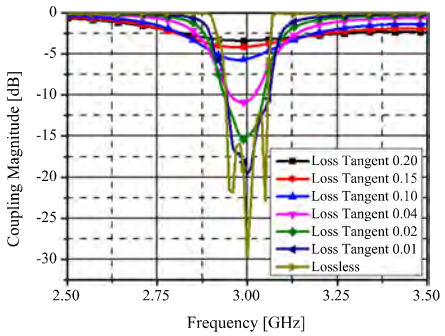

Fig. 2. Comparison of the perfectly reactive surface and lossy substrate.

wide and is composed of a 13.6 mm conductive strip on the top surface of a substrate, with 3 mm gaps between the strips. The substrate is 1.5 mm thick, with a relative permittivity of 5. Vertical metal vias connect the strips to the ground plane.

We simulated the conventional soft surface structure shown in Fig. 1. The simulation model consisted of a thin section of soft surface separating two wave ports, and the vertical walls of the simulation volume were set as magnetic conductors. This represents an infinite strip of soft surface for TM surface waves. We are primarily concerned with TM surface waves because they are supported on metallic structures such as grounded dielectric slabs or printed circuit boards. As for the case of TE surface waves, they can be easily eliminated by ensuring that the substrate is sufficiently thin.

We first analyze the effect of adding loss. The incentive for this study is that many engineers, who attempt to design electromagnetic isolation structures, assume that adding resistive elements or lossy materials will improve the performance. The intuitive assumption is that increasing absorption should reduce coupling due to surface waves. However, we find here that the opposite is true. We varied the substrate from perfectly lossless up to a loss tangent of 0.2. The simulation results shown in Fig. 2 indicate that adding loss actually increases transmission, diminishing the performance of the soft surface for reducing surface wave coupling. This can be understood by considering an effective circuit model for the soft surface. The gaps between the metal strips appear as a sheet capacitance, and the conductive path through the vias and the ground plane provides sheet inductance. The parallel resonant *LC* circuit results high surface impedance near resonance, which effectively creates an open-circuit condition for the TM surface waves. This is the same boundary provided by a PMC, which is very effective at suppressing TM surface waves. In fact, a simulated PMC boundary with the same length as the soft surface provides the same level of coupling suppression, at –20 dB.

The ideal PMC boundary is not bandwidth-limited as the soft surface is, but such a boundary only exists in simulations. Note that the bandwidth of the soft surface appears to increase slightly with added loss, depending on our definition of bandwidth. For example, if we consider the frequency range over which the transmission suppression is half its maximum value, the high-loss cases appear to have broader bandwidth. However, this is at the expense of significantly diminishing the surface wave suppression capabilities, so the improved bandwidth is not worth the cost.

When loss is added to the substrate, this is equivalent to adding a resistive component to the equivalent circuit model of the surface. The lossless surface is modeled as a parallel *LC* circuit, which has infinite impednace at its resonance frequency. Thus, it is similar to an artificial magnetic conducting boundary, and provides significant suppression of TM surface waves. Added resistance appears in parallel to the equivalent *LC* circuit of the lossless surface, and only serves to reduce the surface impedance from this ideal infinite value, thus diminishing the surface wave suppresion capabilities.

We also studied the effect of the vias in the soft surface. Two example structures are shown in Fig. 3, both with and without vias. Aside from the presence of the vias, the two structures are otherwise identical. Note that the version with the vias effectively suppresses surface waves, while the version wtihout the vias does not. For TM waves, the soft surface is similar the high-impedance surface. The only difference is that the individual patches of the high impedance surface are connected to form continuous transverse strips in the soft surface case. Since the electric field across these gaps is zero for TM waves, the difference only affects the TE surface wave behavior. Thus, we may expect that the soft surface is subject to the same bandwidht limit as the high-impednace surface, $B = 2\pi t\mu_r/\lambda$, where t is the substrate thickness and λ is the wavelength at resonance. The example shown here has a bandwidth of about 4%, which is just under half the theoretical bandwidth of 9% for this thickness and resonance frequency. Wider bandwidth may be possible with an improved geometrical design.

III. Active Loading for Wideband Soft Surface

In order to achieve a wideband soft surface, a non-Foster circuit can be added to the conventional soft surface structure. This can suppress the propagation of surface waves in a much wider frequency range. As in the passive version, a thin rectangular strip is used for the electromagnetic soft surface structure, as shown in Fig. 4 [16]. The dimensions and materials are the same as the passive version discussed above.

When a periodic array of capacitors is added to the strips, the resonant frequency of the soft surface is reduced [19]. To simulate this effect in an high frequency structure simulator (HFSS), a series of lumped capacitors are added to gap between patches and swept from 1 fF to 2 pF using lump resistance inductance capacitance (RLC) boundaries. Fig. 5 shows two examples of the coupling magnitude for two values of capacitance, and the stop band is clearly reduced by capacitive loading. Intermediate capacitance values produced stop bands between these extremes.

We choose the points in the middle of each stop band for each value of capacitance. For example, in Fig. 5, frequency A corresponds to the resonance for 1 fF, and frequency B corresponds to the resonance for 2 pF. Using a series of such points, we can derive a table of required reactance versus frequency over the bandwidth of 2.7–3.1 GHz.

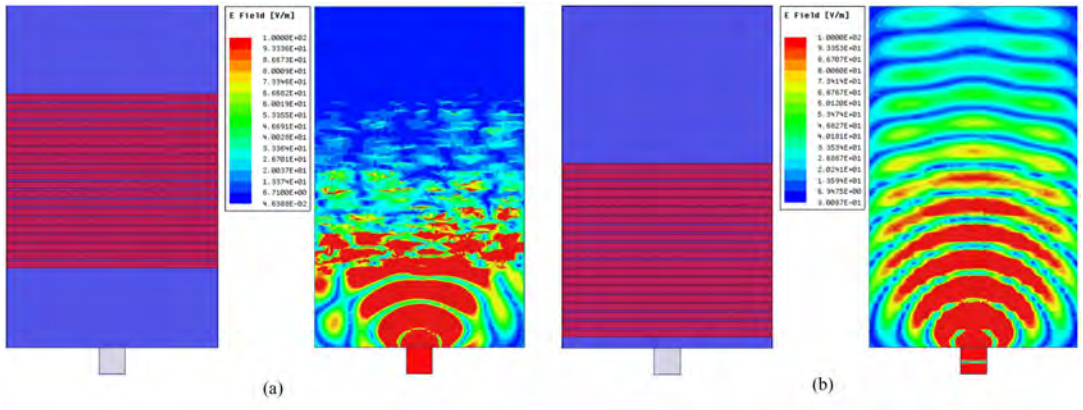

Fig. 3. Comparison of the electric-field distribution. (a) Electric-field distribution of soft surface with vias. (b) Electric-field distribution of soft surface without vias.

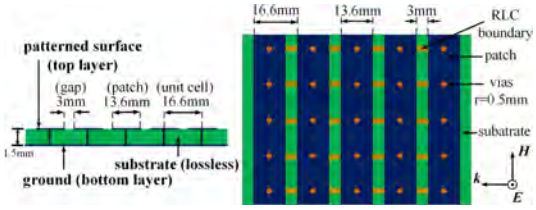

Fig. 4. Impedance surface dimension and its structure with loads.

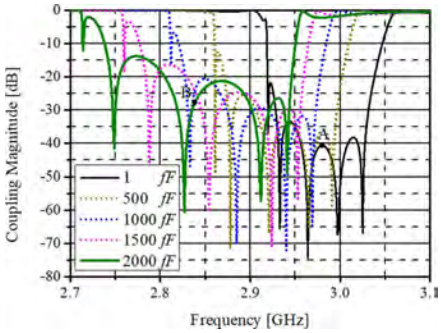

Fig. 5. Simulated coupling magnitude results of the sweep with the driven mode.

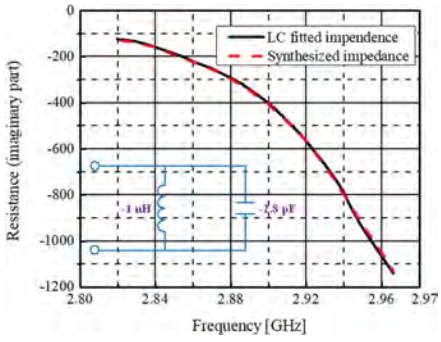

Fig. 6. Synthesized loading impedance (red dashed curve) and its equivalent non-Foster element combination (black solid curve).

The frequency-dependent impedance of the simulated soft surface structure is shown as the red dashed curve in Fig. 6. Here, we note that it has a negative slope, indicating that a non-Foster impedance is required [20]. This curve can be fitted to a parallel resonant circuit consisting of a -1 nH inductor and -2.8 pF capacitor. The actual implementation of non-Foster circuits is beyond the scope of this letter, and is described in many other works. In practice, proper design of stable non-Foster circuits requires carefully controlling for parasitics, and a choice of circuit topology which is appropriate for the impedances attached to it [21]–[25]. Nonetheless such circuits have been successfully applied to microwave structures including metasurfaces throughout the UHF range [19]. Here, we will demonstrate the utility of these circuits for increasing the bandwidth of soft surfaces.

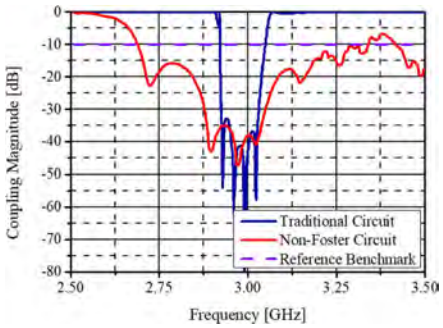

Fig. 7. Comparison between the band gap of soft surfaces based on the proposed method with loads and conventional strips.

Fig. 7 shows the transmission across the non-Foster loaded soft surface compared to the passive reference. If we consider –10 dB to be a reference benchmark, the results in Fig. 7 show that a passive soft surface has a 0.15 GHz stop band, corresponding to a 5% bandwidth. The non-Foster loaded soft surface has a 0.6 GHz stop band, which is about 20% bandwidth, or four times the bandwidth of the passive version. This indicates that although resistive elements only tend to reduce performance, active circuit elements can actually increase performance, and may be useful for providing broadband coupling suppression in future applications.

IV. Mutual Coupling Suppression by Soft Surface

In this section, we compare the suppression of mutual coupling due to surface-wave propagation and free-space wave propagation. Low profile antennas, such as patches sharing the same substrate, experience three types of mutual coupling: near-field coupling, surface-wave coupling, and free-space coupling [14]. Mutual coupling is undesired as it may increase the signal correlation among antennas and reduce the efficiency of

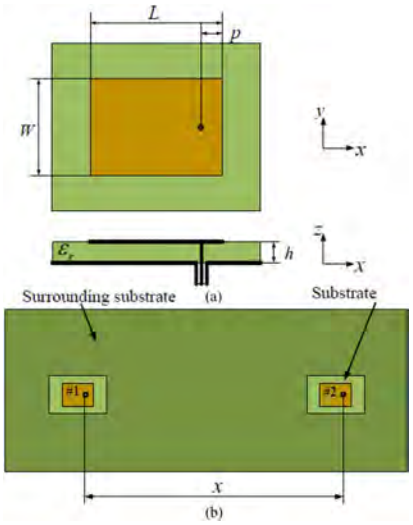

Fig. 8. (a) Top and side views of typical microstrip antenna. (b) Coordinate system for coupled antennas.

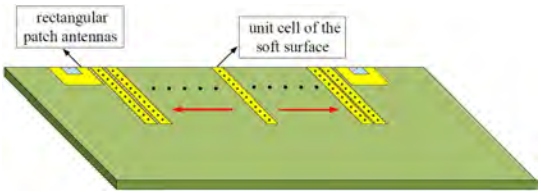

Fig. 9. Model of soft surface units between patch antennas.

multi-antenna systems [26]–[29]. Since the soft surface is as good as an ideal PMC for suppressing surface currents, it can be used for suppressing the surface wave component. In addition, however, we have found that the coupling between antennas can be reduced even below the level which would be expected for the free-space alone, due to the effect of the soft boundary on nearby propagating plane waves. We will demonstrate these effects using a pair of rectangular patch antennas.

The simulations were performed using ANSYS HFSS software. The antenna parameters, shown in Fig. 8(a), have substrate thickness $h = 1.5$ mm, relative dielectric constant $\varepsilon_r = 5$, patch length $L = 21.3$ mm, patch width $W = 28.87$ mm, and coaxial line feed position $p = 3.2$ mm. The operating frequency is 3 GHz and input impedance is 50 Ω. For accuracy, we use a lossless substrate and infinite ground plane, and we set the exterior surfaces of the simulation volume to be radiation boundaries. As shown in Fig. (9), a soft surface consisting of several unit cells is placed between the two identical antenna elements. Note the number of unit cells increases as the distance between the antennas increases. The patches are arranged such that coupling is measured in the E-plane of each patch, thus focusing the study on TM surface waves which are typically the dominant surface wave coupling mechanism for thin dielectric substrates.

The simulation results for the mutual coupling versus the separation distance between the patch antenna elements are plotted in Fig. 10. The space between the antennas was varied from $0.1\lambda_0$ to $5\lambda_0$. The blue curve is the total coupling between the antennas from simulated data, and it is divided into free-space coupling (red) and surface wave coupling (black). The individual free-space and surface wave coupling components can be extracted by fitting the overall coupling curve to two functions, [14] representing a free-space term with ρ^{-1} dependence and

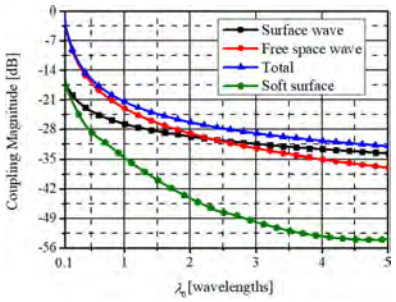

Fig. 10. Couplings suppressing for the surface wave and free-space wave with soft surface units between the patch antenna elements.

a surface-wave term with $\rho^{-1/2}$ dependence [22]. As expected, the free-space term dominates at shorter distances, while the surface wave term dominates at longer distances. In the case of the given example, the distance beyond which the surface wave coupling dominates is found to be approximately $2.5\lambda_0$. The green curve is the total coupling with a soft surface between the antennas. We may expect that when a soft surface is added, the coupling should be reduced to only the level of the free-space wave coupling. However, we find that the coupling is actually reduced to even lower than the free-space component. Thus, we can conclude that the soft surface suppresses not only surface waves, but also a part of the free-space wave near the surface.

This somewhat surprising result that a soft surface suppresses coupling through not only surface waves but also through free-space waves near the surface may be understood as follows. A perfect electric conducting boundary not only suppresses TE surface waves, but also suppresses the propagation of TE-polarized plane waves parallel to the surface. This can be verified by considering a wave front propagating parallel to the surface, then, applying the Huygens' principle to represent that wave front as a set of sources, and then, considering the image sources in the perfect electric conductor. Clearly, the TE-polarized plane wave is not permitted to propagate near an electric conductor. Indeed, it is observed that such waves are strongly diffracted when impinging at a grazing angle on the edge of a conducting sheet, such as an aircraft wing. The same can be said of TM waves propagating near a PMC. Furthermore, the waves of both polarizations are forbidden to propagate near a soft surface, which behaves as a PEC for TE waves and a PMC for TM waves. Thus, the soft surface reduces the coupling between nearby antennas beyond suppressing the surface waves, to even lower than what would be expected due to a free-space coupling alone.

V. Conclusion

We have analyzed the limitations of soft surfaces using simulations, from which we draw four important conclusions: 1) we have found that adding loss actually reduces the soft surface's ability to suppress surface wave coupling; 2) a lossless soft surface is as good at suppressing TM surface waves as an ideal PMC; 3) we have also demonstrated the potential for increasing bandwidth using active non-Foster circuit loading; and 4) finally, by separating the surface wave and free-space wave components of coupling, we have found that a soft surface can actually reduce the coupling between antennas to lower than the level expected for only free-space coupling. This will provide a useful guide for the design of future structures for mutual coupling reduction among antennas.

REFERENCES

[1] P. Kildal, "Definition of artificially soft and hard surfaces for electromagnetic waves," *Electron. Lett.*, vol. 24, no. 3, pp. 168–170, Feb. 1988.

[2] P. Kildal, "Artificially soft and hard surfaces in electromagnetics," *IEEE Trans. Antennas Propag.*, vol. 38, no. 10, pp. 1537–1544, Oct. 1990.

[3] D. F. Sievenpiper, "High-impedance electromagnetic surfaces," Ph.D. dissertation, Dept. Elect. Eng., UCLA, Los Angeles, CA, USA, 1999.

[4] D. F. Sievenpiper, L. Zhang, R. F. J. Broas, N. G. Alexópolous, and E. Yablonovitch, "High-impedance electromagnetic surfaces with a forbidden frequency band," *IEEE Trans. Microw. Theory Techn.*, vol. 47, no. 11, pp. 2059–2074, Nov. 1999.

[5] H. Mosallaei and K. Sarabandi, "Antenna miniaturization and bandwidth enhancement using a reactive impedance substrate," *IEEE Trans. Antennas Propag.*, vol. 52, no. 9, pp. 2403–2414, Sep. 2004.

[6] A. P. Feresidis, G. Goussetis, S. Wang, and J. C. Vardaxoglou, "Artificial magnetic conductor surfaces and their application to low profile high-gain planar antennas," *IEEE Trans. Antennas Propag.*, vol. 53, no. 1, pp. 209–215, Jan. 2005.

[7] Y. Huang, A. De, Y. Zhang, T. K. Sarkar, and J. Carlo, "Enhancement of radiation along the ground plane from a horizontal dipole located close to it," *IEEE Antennas Wireless Propag. Lett.*, vol. 7, pp. 294–297, 2008.

[8] E. Rajo-Iglesias, Ó. Quevedo-Teruel, and L. Inclán-Sánchez, "Planar soft surfaces and their application to mutual coupling reduction," *IEEE Trans. Antennas Propag.*, vol. 57, no. 12, pp. 3852–3859, Dec. 2009.

[9] S. Abushamleh, H. Al-Rizzo, H. Khaleel, and A. Kishk, "Enhancement of the strips electromagnetic soft surfaces using ledge edges," in *Proc. Int. Symp. IEEE Antennas Propag.*, Chicago, IL, USA, Jul. 2012, pp. 1–2.

[10] E. Rajo-Iglesias, L. Inclán-Sánchez, and Ó. Quevedo-Teruel, "Back radiation reduction in patch antennas using planar soft surfaces," *Prog. Electromagn. Res. Lett.*, vol. 6, pp. 123–130, 2009.

[11] P. S. Kildal and A. A. Kishk, "EM modeling of surfaces with STOP or GO Characteristics artificial magnetic conductors and soft and hard surfaces," *Appl. Comput. Electromagn. Soc. J.*, vol. 18, no. 1, pp. 32–40, Mar. 2003.

[12] S. A. Abushamleh, H. M. Al-Rizzo, A. A. Kishk, A. I. Abbosh, and H. Khaleel, "Miniaturized thin soft surface structure using metallic strips with ledge edges for antenna applications," *Prog. Electromagn. Res. B*, vol. 57, pp. 221–232, Jan. 2014.

[13] H. S. Farahani, M. Veysi, M. Kamyab, and A. Tadjalli, "Mutual coupling reduction in patch antenna arrays using a UC-EBG superstrate," *IEEE Antennas Wireless Propag. Lett.*, vol. 9, pp. 57–59, 2010.

[14] C. Wang, E. Li, and D. F. Sievenpiper, "Surface wave coupling and antenna properties in two dimensions," *IEEE Trans. Antennas Propag.*, vol. 65, no. 10, pp. 5052–5060, Oct. 2017.

[15] T. T. Thai, G. R. DeJean, and M. M. Tentzeris, "Design and development of a novel compact soft-surface structure for the front-to-back ratio improvement and size reduction of a microstrip Yagi array antenna," *IEEE Antennas Wireless Propag. Lett.*, vol. 7, pp. 369–373, 2008.

[16] C. Wang, E. Li, and D. F. Sievenpiper, "Wideband electromagnetic soft surfaces with non-foster circuit loading" in *Proc. Int. Symp. IEEE Antennas Propag. Soc.*, San Diego, CA, USA, Jul. 2017, pp. 2217–2272.

[17] E. Rajo-Iglesias, M. Caiazzo, L. Inclan-Sanchez, and P. S. Kildal, "Comparison of bandgaps of mushroom-type EBG surface and corrugated and strip-type soft surfaces," *IET Proc. Microw, Antennas Propag.*, vol. 1, no. 1, pp. 184–189. Feb. 2007.

[18] E. Rajo-Iglesias, J. L. Vazquez-Roy, O. Quevedo-Teruel, and L. Inclan-Sanchez, "Dual band planar soft surfaces," *IET Proc. Microw., Antennas Propag.*, vol. 3, no. 5, pp. 742–748, Aug. 2009.

[19] J. Long and D. F. Sievenpiper, "Low-profile and low-dispersion artificial impedance surface in the UHF band based on non-foster circuit loading," *IEEE Trans. Antennas Propag.*, vol. 64, no. 7, pp. 3003–3010, Jul. 2016.

[20] J. Long and D. F. Sievenpiper, "Dispersion-reduced high impedance surface loaded with non-foster impedances," in *Proc. Int. Symp. IEEE Antennas Propag. Soc.*, Vacouver, BC, Canada, Jul. 2015, pp. 69–70.

[21] R. M. Foster, "A reactance theorem," *Bell Syst. Tech. J.*, vol. 3, no. 2, pp. 259–267, Apr. 1924.

[22] J. G. Yook and L. P. B. Katehi, "Micromachined microstrip patch antenna with controlled mutual coupling and surface waves," *IEEE Trans. Antennas Propag.*, vol. 49, no. 9, pp. 1282–1289, Sep. 2001.

[23] N. Zhu and R. W. Ziolkowski, "Active metamaterial-inspired broad bandwidth, efficient, electrically small antennas," *IEEE Antennas Wireless Propag. Lett.*, vol. 10, pp. 1582–1585, 2011.

[24] H. Mirzaei and G. V. Eleftheriades, "A wideband metamaterial-inspired compact antenna using embedded non-Foster matching," in *Proc. Int. Symp. IEEE Antennas Propag.*, Jul. 2011, pp. 1950–1953.

[25] J. Long, M. M. Jacob, and D. F. Sievenpiper, "Broadband fast-wave propagation in a non-Foster circuit loaded waveguide," *IEEE Trans. Microw. Theory Techn.*, vol. 62, no. 4, pp. 789–798, Apr. 2014.

[26] B. N. Getu and R. Janaswamy, "The effect of mutual coupling on the capacity of the MIMO cube," *IEEE Antennas Wireless Propag. Lett.*, vol. 4, pp. 240–244, 2005.

[27] I. J. Gupta and A. A. Ksienski, "Effect of mutual coupling on the performance of adaptive arrays," *IEEE Trans. Antennas Propag.*, vol. AP-31, no. 5, pp. 785–791, Sep. 1983.

[28] Ó. Quevedo-Teruel, L. Inclan-Sanchez, and E. Rajo-Iglesias, "Soft surfaces for reducing mutual coupling between loaded PIFA antennas," *IEEE Antennas Wireless Propag. Lett.*, vol. 9, pp. 91–94, 2010.

[29] E. Rajo-Iglesias, L. Inclán-Sánchez, and Ó. Quevedo-Teruel, "Textile soft surface for back radiation reduction in bent wearable antennas," *IEEE Trans. Antennas Propag.*, vol. 62, no. 7, pp. 3873–3878, Jul. 2014.

Research article

Dia'aaldin J. Bisharat* and Daniel F. Sievenpiper*

Manipulating line waves in flat graphene for agile terahertz applications

https://doi.org/10.1515/nanoph-2017-0133
Received December 27, 2017; revised March 4, 2018; accepted March 21, 2018

Abstract: Reducing open waveguides enabled by surface waves, such as surface plasmon polaritons, to a one-dimensional line is attractive due to the potentially enhanced control over light confinement and transport. This was recently shown to be possible by simply interfacing two co-planar surfaces with complementary surface impedances, which support transverse-magnetic and transverse-electric modes, respectively. Attractively, the resultant "line wave" at the interface line features singular field enhancement and robust direction-dependent polarizations. Current implementations, however, are limited to microwave frequencies and have fixed functionality due to the lack of dynamic control. In this article, we examine the potential of using gate-tunable graphene sheets for supporting line waves in the terahertz regime and propose an adequate graphene-metasurface configuration for operation at room temperature and low voltage conditions. In addition, we show the occurrence of quasi-line wave under certain conditions of non-complementary boundaries and qualify the degradation in line wave confinement due to dissipation losses. Furthermore, we show the possibility to alter the orientation of the line wave's spin angular momentum on demand unlike conventional surface waves. Our results on active manipulation of electromagnetic line waves in graphene could be useful for various applications including reconfigurable integrated circuits, modulation, sensing and signal processes.

Keywords: graphene metasurface; one-dimensional wave; spin-momentum locking; surface impedance; terahertz photonics.

1 Introduction

The ability to focus and guide electromagnetic (EM) energy, such as light, is of great scientific interest and key to modern communications, sensing, and quantum processing technologies. In particular, extensive research has been done on localization and transmission of EM waves, known as surface waves (SWs), at the interface between two media due to their easily accessible, planar, and open boundary configuration [1]. For example, surface plasmon polaritons (SPP) [2] featuring subwavelength confinement may exist at air-metal interface, and Block SWs [3] featuring low attenuation loss may exist at the interface between air and periodic dielectric stacks. The properties of SWs can be tailored through interfacing different materials [4] or by altering the structure of the interface surface, for instance, via metasurfaces [5, 6]. Since these design approaches are scalable, they have been widely used for applications across the entire EM spectrum [7–9]. Notably, metasurfaces have paved the way for implementing transformation optics [10, 11]. However, once fabricated, the EM response of the structures is fixed, allowing only for limited functionality. By contrast, the prospect of dynamically altering the photonic properties of the constituent materials provides full active control over the overall desired device operation [12, 13].

Especially attractive is the use of graphene as a platform for active nanophotonic structures in the terahertz (THz) to mid-infrared regime [14, 15]. Excess of electrons or holes in this atomically thin material can produce collective plasmon oscillations with relatively long lifetime, hence lower dissipation losses than conventional metals [16, 17]. In addition, the doping level in graphene can be varied via electrostatic gating, hence allowing easy tuning of its photonic response [18, 19]. As a result, graphene properties have been exploited for numerous photonic applications [20–22], including the use of graphene metasurface as

***Corresponding authors: Dia'aaldin J. Bisharat,** Department of Electronic Engineering, City University of Hong Kong, Kowloon, Hong Kong SAR, China; and Electrical and Computer Engineering Department, University of California San Diego, La Jolla, California, 92093, USA, e-mail: dbisharat2-c@my.cityu.edu.hk. http://orcid.org/0000-0003-2229-2123; and **Daniel F. Sievenpiper,** Electrical and Computer Engineering Department, University of California San Diego, La Jolla, California, 92093, USA, e-mail: dsievenpiper@eng.ucsd.edu

a screen for modulating phase, polarization, steering, and absorption profiles of free-space beams [23–26]. However, for most functionalities involving in-plane routing of EM signals, the plasmonic modes must ideally be confined also laterally in the graphene sheet. This is known to occur in graphene nanoribbons, which support strongly localized edge modes besides the traditional surface modes [27–29]. Also recently, other one-dimensional (1D) guided modes in graphene were proposed by depositing a graphene layer onto a sculpted substrate with V-shaped wedge or groove channels [30–33]. However, these modes require specific geometries different from the usual flat sheet, and hence hinder the ability to route signals over reconfigurable arbitrary pathways over the graphene surface.

In this work, we propose a more versatile, agile graphene platform based on line waves (LW) [34]. This 1D EM mode forms as an interference product between transverse-magnetic (TM) and transverse-electric (TE) types of SWs, at the line interface between co-planar, complementary boundaries, which support the two decoupled modes, respectively. Given the open boundary nature of the structure, it decays away in both transverse directions from the infinitesimal line, where ideally a singular field concentration exists, hence the name "line wave". Meanwhile, the mode confinement (phase velocity) of LW is dependent on the parameters of the interfaced boundaries. In addition, due to the spatial symmetry-inversion of the boundaries about the propagation direction, the LW exhibits pseudospin-polarizations locked to the wavevector, making it immune to backscattering due to certain structural defects [35–37]. Here, we discuss the required conductivity profiles of a freestanding graphene sheet necessary for LW operation and present an adequate graphene-metasurface configuration. In addition, we examine the general characteristics of LW in case of non-complementary conditions and dissipation loss. Moreover, we analyze the spin angular momentum of LW and how that differs from other types of EM waves. Then, we illustrate some examples of the possible circuit functionalities using a tunable LW-based graphene platform. Our contribution to combining the unique properties of LW and graphene could advance emerging THz applications such as robust integrated photonics, strong light-matter interaction, quantum information processes, and reconfigurable systems.

2 Results and discussion

2.1 Principle analysis

To establish a criterion for the LW existence, we characterize the interfaced boundaries simply by isotropic surface impedances (Z_s). In general, using Z_s conditions, which relate the tangential electric (E) and magnetic (H) field components on the surface, allows for the analysis and control of SW modes on a certain surface boundary [38–41]. Distinctly, TM (TE) mode (also known as E (H) mode or p (s) polarization) may form on an inductive (capacitive) surface with positive (negative) sign of Z_s, specified as follows [42]:

$$Z_{TM} = \eta_0 \sqrt{1-n^2} = j\eta_0 / \zeta, \quad Z_{TE} = \eta_0 / \sqrt{1-n^2} = -j\eta_0 \times \zeta \qquad (1)$$

where η_0 (≈377Ω) is the intrinsic wave impedance in free space, n is the refractive index, and ζ is an arbitrary positive real number. When interfacing boundaries of Z_{TM} and

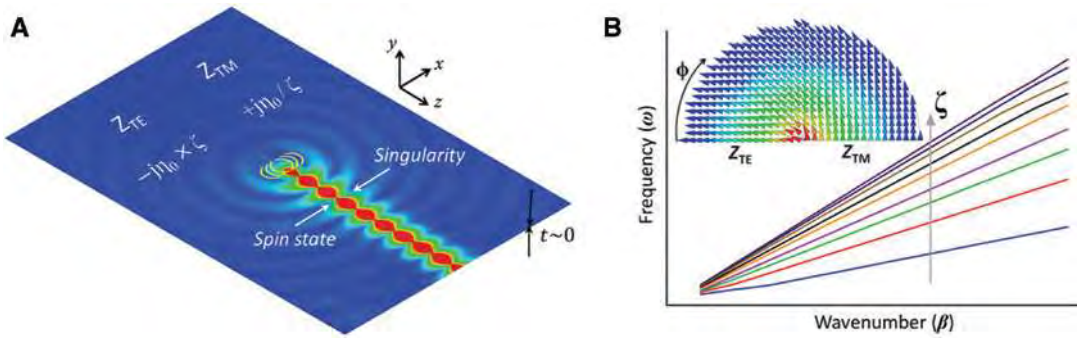

Figure 1: Formation and ideal characteristics of line wave.
(A) Magnitude distribution of the E-field across the interface between complementary TE and TM impedance surfaces showing the line wave formation with a direction-dependent polarization (pseudo-spin state) and maximum – ideally singular – field concentration along the interface line, and (B) the associated ideal dispersion relation at variable impedance values, hence confinement rates, as well as a vector plot of the E-field – in inset – showing the field's intensity decay in the radial direction away from the interface line, and the change in the field's vector orientation at different directions in the transverse plane to the interface line.

Z_{TE}, an effective cross coupling between the TM and TE modes occurs when there is no mismatch in wave momentum ($\beta = nk_0$, k_0 being the wavenumber in free space) across the interface. This corresponds to the two surfaces having identical ζ value, in which case they are considered complementary as they have equal but opposite effect on the E and H field components of the EM wave. As a result, the line interface preserves EM duality and a LW emerges, as shown in Figure 1, as desired.

Since doped graphene sheets may support both TM and TE plasmons [43–45], they may also be used to support LWs. The dispersion relations for TM and TE SWs along a freestanding graphene sheet in free space can be solved for β yielding [46]

$$\beta_{TM} = k_0\sqrt{1-(2/\sigma_g\eta_0)^2},\quad \beta_{TE} = k_0\sqrt{1-(\sigma_g\eta_0/2)^2} \tag{2}$$

where σ_g is the optical surface conductivity of graphene (see Section 4). Here, the factor of 2 takes into account the two-faced layout of the graphene sheet, i.e. $Z_{s(g)} = 2/\sigma_g$. Clearly, no SW propagation is possible for a real-valued σ_g, whereas for a pure-imaginary σ_g, a real solution with $\beta \geq k_0$ exists for TM (TE) mode at $\mathrm{Im}[\sigma_g] < 0$ ($\mathrm{Im}[\sigma_g] > 0$), as also directly inferred from Eq. (1). Figure 2A plots both real and imaginary parts of the actual σ_g as a function of frequency, with carrier relaxation lifetime $\tau = 0.5ps$. Here, $\mathrm{Re}[\sigma_g]$ spikes in a step-like fashion at $\omega\hbar = 2E_F$, where $\omega\hbar$ is the photon (plasmon) energy and E_F is the Fermi energy (i.e. chemical potential) of graphene. This is associated with the interband absorption of radiation, thus inhibiting SW formation [47]. In contrast, at zero temperature, both TM and TE exist without decay in the frequency ranges $\omega\hbar < 1.667E_F$ and $1.667E_F < \hbar\omega < 2E_F$, respectively. However, as temperature increases, $\mathrm{Re}[\sigma_g]$ becomes finite at all frequencies; hence, the modes acquire finite damping, and $\mathrm{Im}[\sigma_g]$ value within the TE range becomes limited.

As Figure 2B shows, the TM mode is generally tightly confined ($\mathrm{Re}[\beta] \gg k_0$) and is highly attenuated ($\mathrm{Im}[\beta] \gg k_0$) in the vicinity of the transition point, corresponding to $E_F = 0.15$ eV at frequency $\omega/2\pi = 60$ THz. In contrast, the TE mode extends significantly above the surface as its dispersion relation closely follows the free-space wave and is lightly damped. Due to the discrepancy between the confinement factors of the two modes, it is not plausible to use a freestanding graphene sheet to support LW operation at room temperature. The mismatch in wavenumbers may be alleviated by adding a dielectric cladding to the graphene layer hosting the TE mode in order to increase the associated mode confinement. In such case, it is necessary, however, to evaluate the effect of the possible difference in dielectric constant between a substrate and superstrate on the TE mode formation. Assuming a vacuum superstrate and a dielectric substrate are used, we find that the TE mode exists only when $\varepsilon_r - 1 < (4\alpha\mathrm{Im}[\sigma_g]/\sigma_0)^2$, where ε_r is the dielectric constant, $\alpha \approx 1/137$ is the fine-structure constant, and $\sigma_0 = e^2/\pi\hbar$ is the characteristic conductivity [48]. Evidently, the allowable deviation ($<10^{-3}$ for $\hbar\omega < 2E_F$) in dielectric values is trivial, thus practically excluding the potential use of any substrate.

2.2 Proposed structure

Alternatively, we propose the use of a graphene-metasurface configuration such as shown in the schematic in Figure 3A. The parallel stack structure is made of a layer consisting of periodic subwavelength arrangement of

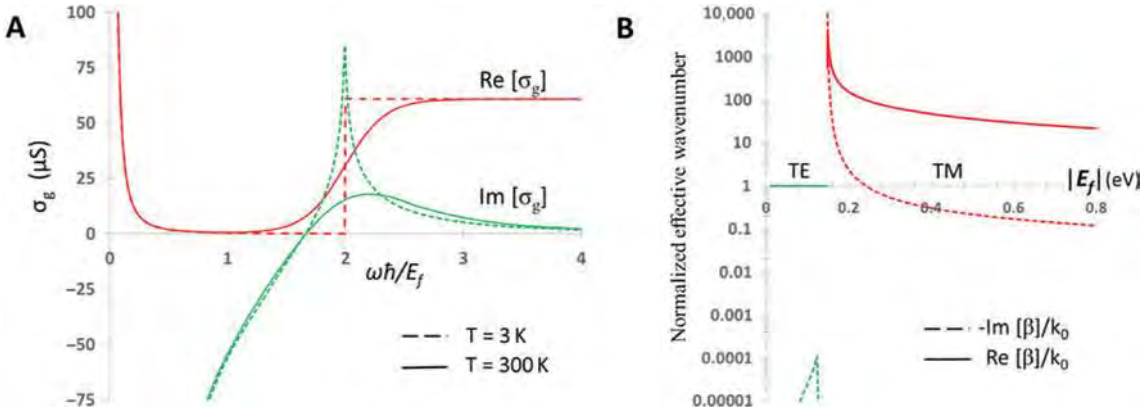

Figure 2: Surface conductivity of graphene and associated surface waves.
(A) Surface conductivity of graphene as a function of frequency (normalized by chemical potential) at different temperatures (T), and (B) surface wave propagation constant (normalized by free-space wavenumber) as a function of chemical potential at $\omega_h = 0.26$ eV ($\omega/2\pi = 60$ THz).

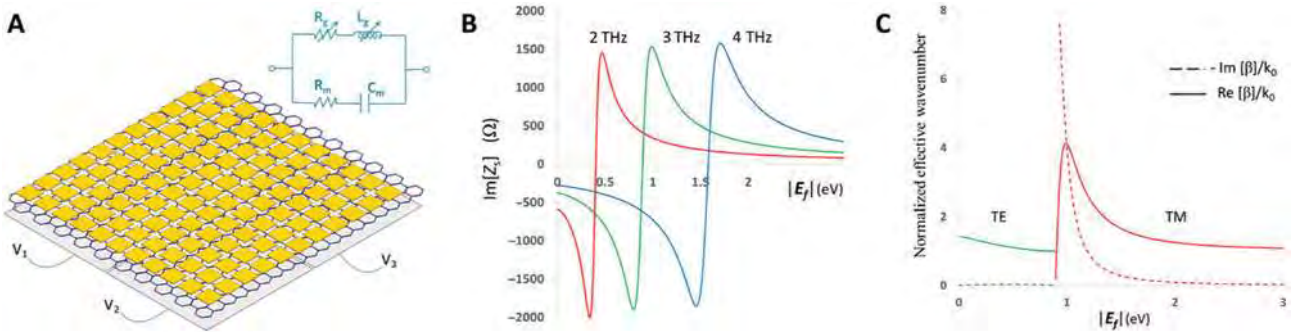

Figure 3: Details of the proposed structure and associated properties.
(A) Schematic of the proposed LW platform based on graphene-metasurface and the corresponding circuit model of a parallel transmission line in the inset, (B) the surface reactance of the structure as a function of chemical potential at different frequencies, and (C) the associated SW propagation constants as a function of chemical potential at $\omega/2\pi = 3$ THz.

metallic patches, which has an effective capacitive EM response, and a graphene layer, which has an inductive EM response. Here, it becomes possible to make better use of the graphene properties by operating in the low THz regime, where graphene's conductivity (hence, $Z_{s(g)}$) can be significantly tuned and dissipation losses are minimum [49]. For in-plane wave propagation, the structure response can be modeled as parallel transmission lines (i.e. $1/Z_s = 1/Z_{s(g)} + 1/Z_{s(m)}$), where the surface impedance of the metasurface, assuming it has zero resistance, is [50, 51]

$$Z_{s(m)} = \frac{-j\eta_0}{2a\frac{k_0}{\pi}\ln\left[\csc\left(\frac{\pi g}{2a}\right)\right]} / \varepsilon_{eff} \tag{3}$$

where $a = 10$ μm is the unit cell size, $g = 1$ μm is the gap spacing between adjacent patches, and $\varepsilon_{\text{eff}} = 1.4$ is the effective dielectric constant. Note that since depositing metal directly on a graphene sheet changes its conductivity significantly, here we consider an isolation layer of SiO_2 with a thickness of 0.2 μm (see Section 4). Accordingly, by altering the impedance of the graphene sheet, while that of the metasurface layer remains fixed at a given frequency, the effective net response of the overall structure can be varied from capacitive to inductive, as shown in Figure 3B. In the meanwhile, at any given chemical potential the structure's EM response switches from inductive at the lower frequency end to capacitive towards higher frequencies.

As Figure 3C shows, at low values of E_F, TE mode is supported with relatively greater confinement than that of the previously studied case of isolated graphene sheet. Specifically, for the given structure parameters, the confinement factor at 3THz spans $1 < \text{Re}[\beta_{TE}]/k_0 < 1.42$ and decreases with the increase of E_F, as expected. As E_F is increased further, a TM mode appears instead with a maximum confinement close to the transition point. For the range $0.9 < E_F < 3$, a confinement factor of $1 < \text{Re}[\beta_{TM}/k_0] < 4.1$ is obtained. Since similar momenta of the two modes are attainable in the range $1 < \text{Re}[\beta/k_0] < 1.42$ with little attenuation ($\text{Im}[\beta]/k_0 < 0.2$), the proposed structure proves capable of supporting LW at room temperature. The possible LW's operation range is determined by the practical limitations incurred by both modes. Particularly, the TE momentum has an upper limit that is set by the fixed capacitive response of the metasurface, whereas the TM momentum has a lower limit that is set by the highest achievable inductive response of the graphene sheet (i.e. E_F). Note that while the upper limit incurred by TE mode can be improved by increasing the capacitance of the metasurface, for instance, by shrinking its gaps, this necessitates a higher chemical potential of graphene to maintain the lower limit incurred by the TM mode, and vice versa.

In general, since the energy dispersion (i.e. electronic density of states) in graphene is linear and gapless around its charge neutrality (Dirac) point, σ_g can be varied significantly with carrier concentration (N) compared to other materials, as $E_F = \hbar v_F \sqrt{\pi N}$, where v_F ($\approx 10^8$ cm s^{-1}) is the Fermi velocity [52]. However, as its energy states are filled, it becomes predictably harder to raise E_F. Here, N can be increased via chemical doping or by applying electrostatic bias to the graphene sheet, as illustrated in Figure 3A, via gate voltage. The first approach, which entails adding dopant atoms to graphene, would increase the carrier scattering rate, τ^{-1}, thus increasing the dissipation loss, whereas in the latter approach, an applied voltage exceeding the breakdown threshold of the supporting dielectric layer would render the devise obsolete. In contrast,

the use of top-gated ionic gel has been experimentally shown to be capable of providing doping levels up to $N=1.0\times10^{14}\text{cm}^{-2}$, hence $E_F\approx1.6\text{eV}$, with a low gate voltage $V_g\approx4$ V [53, 54]. This is as a result of its high gate capacitance ($C_{\text{EDL}}\approx2\mu\text{F cm}^{-2}$) due to the formation of a thin electric double layer (thickness ≈1 nm) close to the graphene surface. Acting as one of the formed capacitor plates, the graphene sheet would thus have a charge carrier concentration of $N=C_{\text{EDL}}V_g/e$.

Here, we propose the use of ion-based solid electrolyte, which exhibits similar performance to ion-gel designs but can be used as both a back gate and a substrate to support graphene, hence allowing easier implementation and more device functionalities [55, 56]. In addition, we propose the use of multilayer graphene sheets in order to achieve higher Fermi energy, given a fixed bias voltage. Being electrically connected and having negligible separation, the injected carriers due to a bias voltage are distributed among the different graphene layers [57]. As the extra carriers add up to the total charge in the gate capacitor, the equivalent Femi level corresponds to the sum of the individual levels, leading to an increase in total conductivity proportionally to the number of layers (n), as follows [58]:

$$\sigma_g^{\text{total}}=\sigma_g^1+\ldots+\sigma_g^n=\frac{-je^2\sum_{i=1}^{n}|E_F^{(i)}|}{\pi\hbar^2(\omega-j\tau^{-1})} \tag{4}$$

The above Drude conductivity model is valid since the intraband contribution is dominant at the operating range under consideration. Furthermore, note that the carrier scattering rate and mobility in multilayer graphene remain conveniently similar to that in a single layer [58]. Therefore, a good performance is attainable using only three layers of graphene, where $E_F=3$ eV merely requires $V_g=1.56$ V.

2.3 Line mode characteristics

Figure 4A shows the propagation characteristics at 3THz of the LW with different ζ values, at which the complementary surfaces have the relation $\text{Im}[Z_{TM}]\times\text{Im}[Z_{TE}]=\eta_0^2$. The attainable modes, with $1.05<\zeta<2.47$, have a normalized propagation constant of $1.6<\text{Re}[\beta/k_0]<5.9$ with the maximum occurring at $\zeta=1.13$. On the other hand, the figure-of-merit $\text{Re}[\beta]/\text{Im}[\beta]$ dictating the relative propagation length of the mode increases proportionally with the increase of ζ due to diminishing attenuation. Figure 4B plots the propagation results at $\zeta=1.94$ as a function of distance between the interfaced regions, over which a linear rather than abrupt transition (see inset) is assumed in the conductivity profile of the graphene sheet. While the propagation length decreases with larger transition distances (d), as expected, the LW characteristics are roughly unchanged at $d\leq1$ μm. Therefore, the proposed configuration proves adequate for supporting operational LW modes within the limited range of Z_s values of the proposed structure under realistic conditions.

To probe the LW properties more systematically, Figure 4C shows the effect of dissipation loss on the confinement and propagation factors of LW as a function ζ. Here, we use the actual complex conductivities of graphene on both TE and TM sides of the LW and multiply the real part of the overall surface impedance by a factor of $0\leq\delta\leq1$, where 0 corresponds to the lossless case. While the LW tends to maximum confinement at the lower limit $\zeta=1$, the effective propagation length increases proportionally with ζ, indicating a trade of between the two factors. In addition, the LW confinement is deteriorated due to loss, predominantly at lower ζ values, indicating a dependence of the LW propagation constant on $\text{Re}[Z_s]$ rather than solely on $\text{Im}[Z_s]$. Meanwhile, Figure 4D compares the normalized intensity profile of E-field distribution of the LW in the transverse direction across the line interface at different ζ values. Favorably, the LW features a comparable, albeit slightly less lateral energy concentration at higher ζ values, making such values equally fit for 1D waveguide operation. Moreover, the associated moderate mode confinement makes it easy to couple external waves, for instance in air, to the LWs due to the little momentum mismatch.

We note that an interface between inductive and capacitive impedance surfaces of non-complimentary values can support a quasi-line mode. As shown in Figure 5A, this mode exhibits similar field profiles to traditional edge modes, indicating that LW and edge mode share similar characteristics [59]. An implementation of the quasi-line mode has been recently studied based on a graphene/graphene platform at low temperature [60]. Figure 5B plots the normalized propagation constants of the quasi-line modes in the lossless case along with that of the conventional 2D SW. These 1D modes show two notable properties: they exhibit sharp increase in confinement reciprocally with ζ, at either side of the interface; and they cease to exist when $Z_{TM}>-Z_{TE}$. The later property is in agreement with the observation that no LW is supported at $\zeta<1$, while the former property is akin to the asymptotic behavior of LW (see Figure 4C) presumably towards infinite confinement (i.e. zero wave speed) at $\zeta=1$. For the

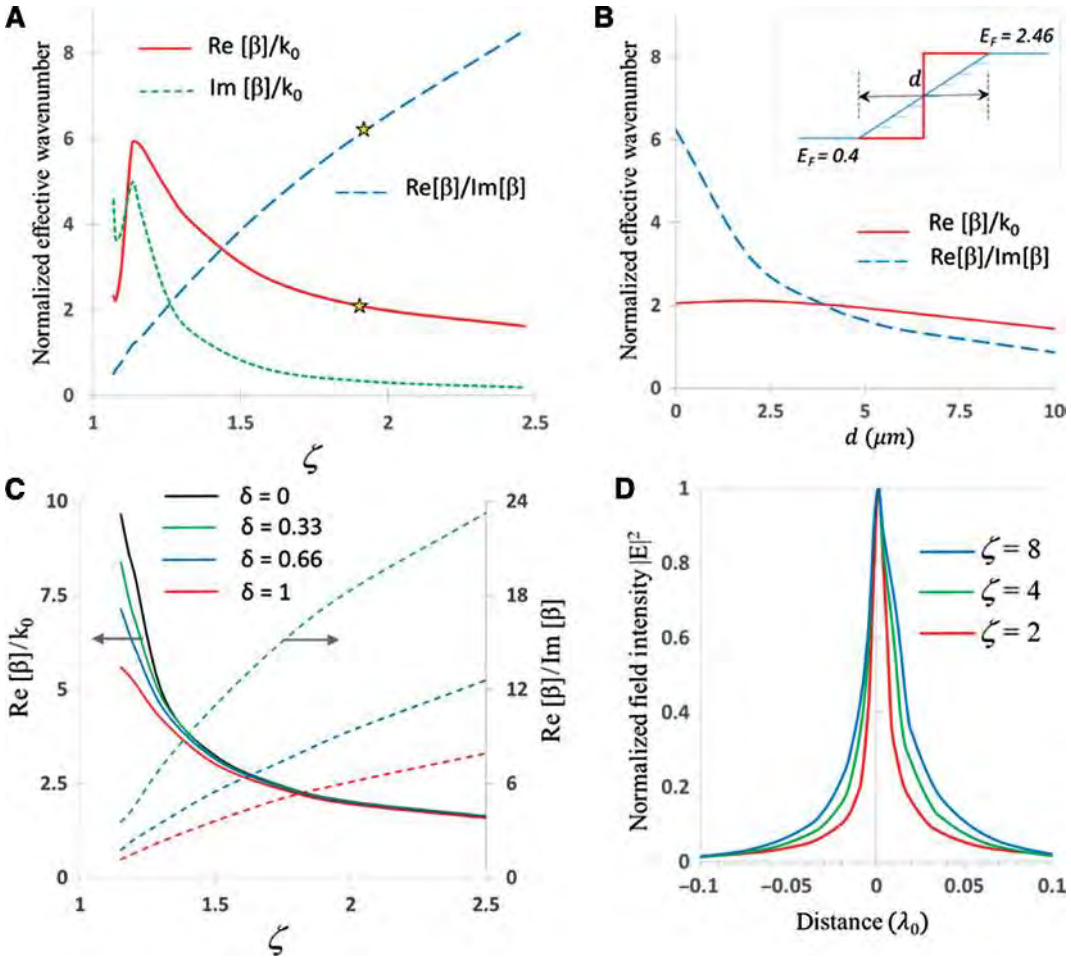

Figure 4: Numerical simulation of the line wave's mode properties under different conditions.
(A) Propagation characteristics of LWs with different ζ values supported by the graphene metasurface at 3 THz, (B) associated propagation characteristic of the structure at $\zeta = 1.94$ in the case of non-abrupt, linear change in Femi energy of graphene – as illustrated in the inset – over different distances across the line interface, (C) general relation of confinement and propagation factors of LWs versus ζ with prescribed values of loss factor ($\mathrm{Re}[Z_s]_{new} = \delta\ \mathrm{Re}[Z_s]_{actual}$), and (D) general field intensity profile distribution in the transverse direction to the line interface, over the surface, for LWs of different ζ values.

sake of clarity, unsteady results from our full-wave simulations near $Z_{TM} = -Z_{TE}$ and $\zeta = 1$ have been excluded from the presented figures. Nonetheless, the asymptotic limit of the wavenumbers for LW and quasi-line mode is evident from the increase in mode confinement, which diverges relative to that of SW [2] on similar Z_s surface towards lower ζ values.

2.4 Optical spin-orbit interaction

Recently, it has been shown that evanescent waves universally possess spin angular momentum tied to the propagation direction [61]. This coupling occurs in TM (TE) SWs due to the wave confinement in the perpendicular direction to propagation axis, leading to a longitudinal component of the E (H) field with a $\pm\pi/2$ phase difference relative to the field component normal to the surface [62]. As such, the E (H) field vector rotates in the plane normal to the surface (i.e. is elliptically polarized) resulting in a purely transverse spin component that flips sign with the reversal of propagation direction. In contrast, circularly polarized (CP) plane waves in free space have purely longitudinal spin that is in the range [–1, 1] (i.e. parallel or anti-parallel to the wavevector) depending on the helicity of the mode. The decay of EM fields in the two directions orthogonal to propagation axis in the case of LW, which leads to the presence of all six EM field components, makes LW different from the aforementioned cases. This mode is essentially a hybrid of TE and TM modes yet exhibits a different spin orientation from that of either mode.

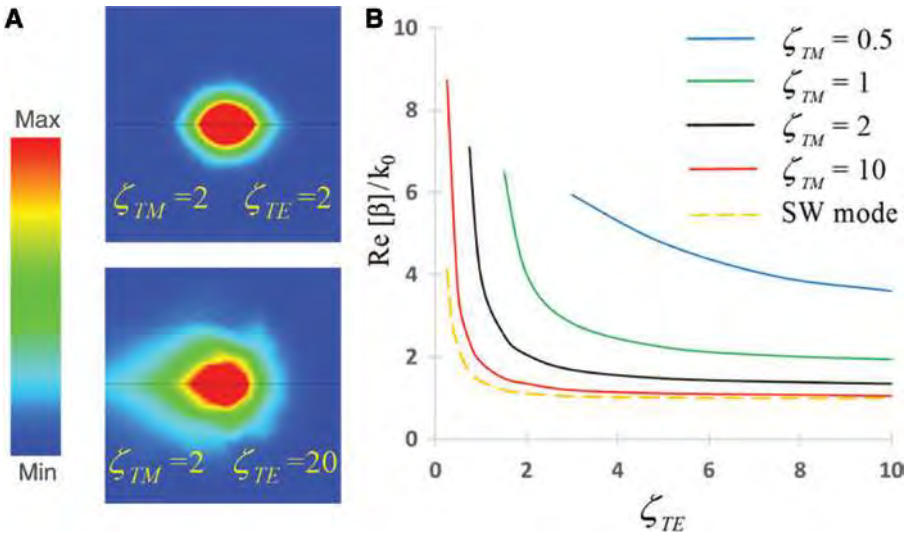

Figure 5: Numerical simulation of the quasi-line mode confinement properties.
(A) Distribution of the E-field magnitude over a cross-sectional area within the transverse plane to the propagation direction of the line mode (top) and a quasi-line mode (bottom), and (B) normalized propagation constant (confinement factor) of the quasi-line mode at different surface impedance values in case of non-complementary and lossless impedance surfaces across the line interface and comparison with conventional surface wave (SW) mode.

The spin orientation can be understood from Figure 6A, which depicts the rotation of both E and H field vectors at an angle with respect to the surface. The value of the local spin density (in units of $\hbar$ per photon) is determined by the relation [63]

$$\mathbf{S}=\frac{\mathrm{Im}[\mathbf{E}^{*}\times\mathbf{E}+\mathbf{H}^{*}\times\mathbf{H}]}{W} \tag{5}$$

where $W=|\mathbf{E}|^{2}+|\mathbf{H}|^{2}$ is the local energy density of the fields. Figure 6B plots the spin magnitude and the relative contribution of the individual spin components (e.g. $S_{x}'=\mathbf{S}\cdot\hat{x}/|\mathbf{S}|$) in the vicinity of the line interface above the surface. Clearly, the orientation angle of the spin in the transverse *xy* plane is variable depending on the relative Z_s values across the line interface. In addition, a longitudinal spin emerges upon the introduction of loss to the supporting surface. As such, unlike conventional SWs, the spin orientation relative to the propagation direction of LW could be flexibly tuned. This observation also applies to the case of quasi-line modes, making such tunability easily attainable.

The spin-momentum locking property allows for robust unidirectional flow of evanescent waves in general via an excitation beam carrying similar spin angular

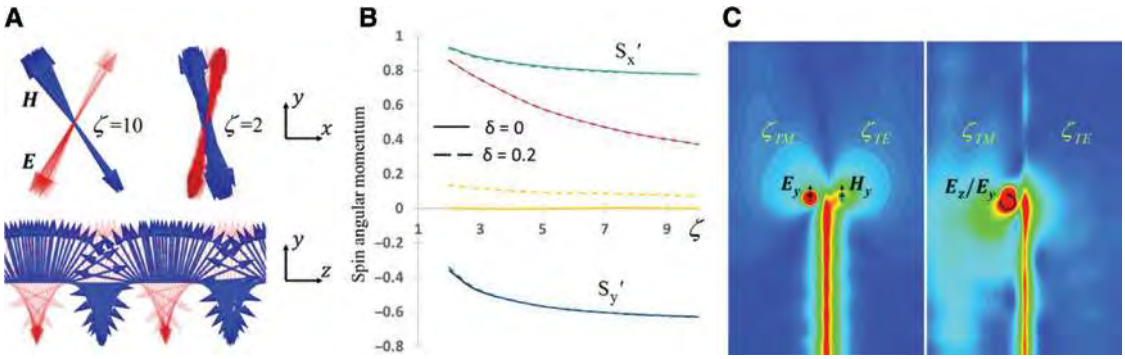

Figure 6: Spin angular momentum properties of line wave.
(A) Snapshot in time of electric and magnetic field vectors of LW along the propagation axes with a cross-section view (top) and longitudinal section view (bottom), (B) magnitude of spin angular momentum (red) and normalized contributions of the spin components along different directions of the LW as a function of ζ with and without loss, and (C) E-field magnitude distribution over the surface showing directional excitation of LW via a CP electric dipole (left) and a pair of linearly polarized, in-phase electric and magnetic dipoles (right) on opposite sides of the line interface.

momentum [64]. This is usually tested through the near field of a point source CP electric dipole placed in the vicinity of a TM-supportive surface [65]. Likewise, a CP magnetic dipole may excite a directional SW mode over a TE-supportive surface. The LW may be excited with either source since its spin relies on the dual contribution of the E and H fields as shown in Eq. (5). As shown in Figure 6C, it can also be excited using a dipole pair of different types that are placed within half-wavelength distance apart across the line interface. Here, the linearly polarized parallel dipoles excite SWs respectively omni-directionally, proving that the unidirectional excitation of the LW is not simply due to that of the surrounding SWs. Instead, it is due to the phase relation between E and H fields, given that the two components have a phase combination that is unique to a particular spin orientation. This property along with the tunability of the spin orientation of LW offers a new degree of freedom for manipulating wave-matter interactions, such as routing the flow of photoluminescence depending on the polarization of the emitter transition [66], which has attracted focused interest lately for use in quantum signal processes.

2.5 Reconfigurable circuits

Many recent research works have been done on transmission line structures with high field concentration [67–69] including based on spoof SPP at the THz regime [70, 71]. However, the majority of the associated applications lack reconfigurability, enabling only limited circuit functionality. Figure 7A shows a schematic of an agile, versatile platform based on graphene-LW combination. By using a large array of bias control pads beneath the structure, we could guide signals along arbitrary pathways between selectively different inputs/outputs. Since the orientation of the impedance surfaces across the line interface is reversed in the backward/forward propagation directions, the associated spin orientations are opposite, allowing the corresponding orthogonal polarization states of LW to be used for transmitting and receiving of signals without interference. In addition, the associated robustness could be exploited to alter the surface impedances across the line interface to control the mode confinement at specific sections along the waveguide for use as compact delay lines with tunable phase shift [34]. Moreover, since switching the impedance surface type across the interface at a particular section would forbid further propagation of a given LW polarization, this can be used as a switching functionality or for implementing network devices such as the magic-T structure shown in Figure 7C.

3 Conclusion

In summary, we have discussed the properties of LWs and proposed a practical implementation in flat graphene, which allows for their dynamic manipulation. Specifically, a stack of multilayer graphene and a metallic patch metasurface over a back-gated electrolyte substrate was shown to emulate the necessary impedance surfaces using low bias voltage variation at room temperature. Unlike other 1D modes, our approach based on LWs allows for readily reconfigurable wave pathways, mode confinement, and polarization states. In addition, LWs are attractive for sensing and potentially nonlinear applications due to the higher mode confinement compared to conventional SWs. Furthermore, we have shown that LWs exhibit unique flexible optical spin-momentum relation, which could

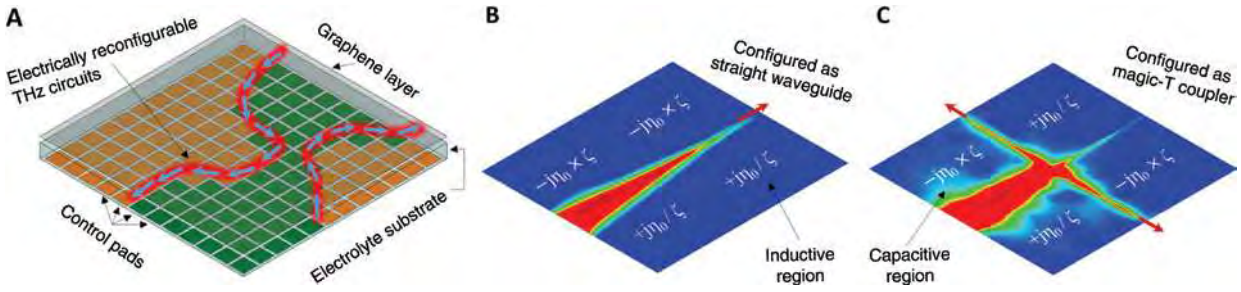

Figure 7: Illustration of an electrically programmable platform of line waves for (A) guiding signals along arbitrary-shaped pathways, (B) robust straight delay lines with tunable phase shift capability, and (C) network circuits such as a magic-T coupler based on spin-filtered channels.
The arrows indicate one sense of polarization that is specific to the shown propagation direction due to spin-momentum locking. Figures B and C show the full-wave simulation results of the electric field intensity distribution above the surface of the proposed graphene metasurface structure with the actual complex conductivities corresponding to $\zeta = 2.4$.

be beneficial for circuits based on spintronic processes. Moreover, we have pointed out the occurrence of quasi-LWs under certain conditions of non-complementary boundaries, which exhibit similar characteristics to LW albeit with asymmetric field profile and lower field concentration. Finally, although our study concerns graphene at the low THz regime, our results may be extended to similar 2D materials at other frequencies [49, 72, 73], allowing for potentially more applications and improved performance.

4 Methods

4.1 Graphene conductivity

In our classical approach, the EM response of the graphene sheet is derived from its optical surface conductivity (σ_g). In the absence of external magnetic field, this is given in the local limit of the random-phase approximation at a finite temperature by [15, 17]

$$\sigma_g(\omega, E_F, \tau, T) = \sigma^{\text{intra}}(\omega, E_F, \tau, T) + \sigma^{\text{inter}}(\omega, E_F, \tau, T)$$

$$\sigma^{\text{intra}} = \frac{-je^2}{\pi\hbar^2(\omega - j\tau^{-1})}\left\{E_F + 2k_BT\ln\left[\exp\left(\frac{-E_F}{k_BT}\right)+1\right]\right\}$$

$$\sigma^{\text{inter}} = \frac{e^2}{4\hbar}\left(\frac{1}{2} + \frac{1}{\pi}\arctan\left[\frac{\omega\hbar - 2E_F}{2k_BT}\right] + \frac{j}{2\pi}\ln\left[\frac{(\omega\hbar + 2E_F)^2}{(\omega\hbar - 2E_F)^2 + (2k_BT)^2}\right]\right) \quad (6)$$

where ω is the angular frequency, e is the electron charge, k_B is the Boltzmann constant, T is the temperature, $\hbar$ is the reduced Planck constant, τ is the carrier relaxation lifetime, and E_F is the Fermi energy. The first (second) term is attributed to intraband (interband) transition (i.e. electron-photon scattering process), which is dominant for $\omega\hbar \ll 2E_F$ ($\omega\hbar \geq 2E_F$), in which case the sheet's response is inductive (capacitive).

In our study, where high doping at room temperature and frequencies are well below $2E_F$, we can safely neglect temperature and interband effects, which reduces the expression above for σ_g to the Drude conductivity model given in Eq. (4).

4.2 Numeral analysis

Full-wave simulations were performed using the Eigenmode setup (for dispersion relations) and Driven-mode setup (for transmission data) in ANSYS HFSS, which is a finite element method-based commercial software. The graphene was modeled as a sheet of zero thickness with an assigned isotropic impedance value (i.e. surface impedance boundary). The metallic patch metasurface was modeled as perfect electric conductor of finite size. Unit cell incorporating the stacked two layers with an isolation dielectric was solved for using periodic boundaries, and the extracted effective net impedance was found to be in agreement with the theoretical calculations of the parallel transmission line model in Figure 3B. Here, $\varepsilon_{\text{eff}} = (t\varepsilon_r + 1)/2$, where $(1/\varepsilon_r) < t < 1$ is a constant dependent on the dielectric layer thickness. Subsequently, the overall structure was modeled as two adjacent semi-infinite surface impedance boundaries, with values corresponding to Z_{TM} and Z_{TE} across the interface of LW.

Acknowledgments: This work has been supported in part by AFOSR grant FA9550-16-1-0093.

References

[1] Polo JA Jr., Lakhtakia A. Surface electromagnetic waves: a review. Laser Photon Rev 2011;5:234–46.
[2] Maier SA. Plasmonics: fundamentals and applications. New York, USA, Springer-Verlag, 2007.
[3] Meade RD, Brommer KD, Rappe AM, Joannopoulos JD. Electromagnetic Bloch waves at the surface of a photonic crystal. Phys Rev B 1991;44:10961–4.
[4] Ramos-Mendieta F, Halevi P. Electromagnetic surface modes of a dielectric superlattice: the supercell method. J Opt Soc Am B 1997;14:370–81.
[5] Holloway CL, Kuester EF, Gordon JA, O'Hara J, Booth J, Smith DR. An overview of the theory and applications of metasurfaces: the two-dimensional equivalents of metamaterials. IEEE Antennas Propag Mag 2012;54:10–35.
[6] Garcia-Vidal FJ, Martín-Moreno L, Pendry JB. Surfaces with holes in them: new plasmonic metamaterials. J Opt A: Pure Appl Opt 2005;7:S97–101.
[7] Kildishev AV, Boltasseva A, Shalaev VM. Planar photonics with metasurfaces. Science 2013;339:1232009.
[8] Williams CR, Andrews SR, Maier SA, Fernández-Domínguez AI, Martín-Moreno L, García-Vidal FJ. Highly confined guiding of terahertz surface plasmon polaritons on structured metal surfaces. Nat Photon 2008;2:175–9.
[9] Yu L, Barakat E, Sfez T, Hvozdara L, Francesco JD, Herzig HP. Manipulating Bloch surface waves in 2D: a platform concept-based flat lens. Light Sci Appl 2014;3:e124.
[10] Werner DH, Kwon DH. Transformation electromagnetics and metamaterials. London, UK, Springer-Verlag, 2014.
[11] Xu L, Chen H. Conformal transformation optics. Nat Photon 2015;9:15–23.
[12] Shaltout AM, Kildishev AV, Shalaev VM. Evolution of photonic metasurfaces: from static to dynamic. J Opt Soc Am B 2016;33:501–10.

[13] Zheludev NI, Kivshar YS. From metamaterials to metadevices. Nat Mater 2012;11:917–24.
[14] Tassin P, Koschny T, Soukoulis CM. Graphene for terahertz applications. Science 2013;341:620–1.
[15] Low T, Avouris P. Graphene plasmonics for terahertz to mid-infrared applications. ACS Nano 2014;8:1086–101.
[16] He X, Gao P, Shi W. A further comparison of graphene and thin metal layers for plasmonics. Nanoscale 2016;8:10388–97.
[17] Xiao S, Zhu X, Li B-H, Mortensen NA. Graphene-plasmon polaritons: from fundamental properties to potential applications. Front Phys 2016;11:117801.
[18] Gao W, Shi G, Jin Z, et al. Excitation and active control of propagating surface plasmon polaritons in graphene. Nano Lett 2013;13:3698–702.
[19] He X, Lin F, Liu F, Shi W. Terahertz tunable graphene Fano resonance. Nanotechnology 2016;27:485202.
[20] Bao Q, Loh KP. Graphene photonics, plasmonics, and broadband optoelectronic devices. ACS Nano 2012;6:3677–94.
[21] Wong LJ, Kaminer I, Ilic O, Joannopoulos JD, Soljačić M. Towards graphene plasmon-based free-electron infrared to X-ray sources. Nat Photon 2016;10:46–52.
[22] Rodrigo D, Limaj O, Janner D, et al. Mid-infrared plasmonic biosensing with graphene. Science 2015;349:165–8.
[23] Yao Y, Shankar R, Kats MA, et al. Electrically tunable metasurface perfect absorbers for ultrathin mid-infrared optical modulators. Nano Lett 2014;14:6526–32.
[24] He X. Tunable terahertz graphene metamaterials. Carbon 2015;82:229–37.
[25] Sherrott MC, Hon PWC, Fountaine KT, et al. Experimental demonstration of >230° phase modulation in gate-tunable graphene – gold reconfigurable mid-infrared metasurfaces. Nano Lett 2017;17:3027–34.
[26] Dutta-Gupta S, Dabidian N, Kholmanov I, Belkin MA, Shvets G. Electrical tuning of the polarization state of light using graphene-integrated anisotropic metasurfaces. Phil Trans R Soc A 2017;375:20160061.
[27] Nikitin AY, Guinea F, Garcia-Vidal FJ, Martín-Moreno L. Edge and waveguide terahertz surface plasmonmodes in graphene microribbons. Phys Rev B 2011;84:161407.
[28] Christensen J, Manjavacas A, Thongrattanasiri S, Koppens FHL, García de Abajo FJ. Graphene plasmon waveguiding and hybridization in individual and paired nanoribbons. ACS Nano 2012;6:431–40.
[29] Fei Z, Goldflam MD, Wu J-S, et al. Edge and surface plasmons in graphene nanoribbons. Nano Lett 2015;15:8271–6.
[30] Liu P, Zhang X, Ma Z, Cai W, Wang L, Xu J. Surface plasmon modes in graphene wedge and groove waveguides. Opt Express 2013;21:32432–40.
[31] Cui J, Sun Y, Wang L, Ma P. Graphene plasmonic waveguide based on a high-index dielectric wedge for compact photonic integration. Optik 2016;127:152–5.
[32] Gonçalves PAD, Dias EJC, Xiao S, Vasilevskiy MI, Mortensen NA, Peres NMR. Graphene plasmons in triangular wedges and grooves. ACS Photonics 2016;3:2176–83.
[33] Ansell D, Radko IP, Han Z, Rodriguez FJ, Bozhevolnyi SI, Grigorenko AN. Hybrid graphene plasmonic waveguide modulators. Nat Commun 2015;6:8846.
[34] Bisharat DJ, Sievenpiper DF. Guiding waves along an infinitesimal line between impedance surfaces. Phys Rev Lett 2017;119:106802.
[35] Chen W-J, Zhang ZQ, Dong J-W, Chan CT. Symmetry-protected transport in a pseudospin-polarized waveguide. Nat Commun 2015;6:8183.
[36] Xu X, Li Y, Miao X. Robust waveguide against surface perturbations due to band inversion in two kinds of single-negative metamaterials. EPL 2016;116:44001.
[37] Slobozhanyuk A, Mousavi SH, Ni X, Smirnova D, Kivshar YS, Khanikaev AB. Three-dimensional all-dielectric photonic topological insulator. Nat Photon 2017;11:130–6.
[38] Gok G, Grbic A. Tailoring the phase and power flow of electromagnetic fields. Phys Rev Lett 2013;111:233904.
[39] Quarfoth R, Sievenpiper D. Artificial tensor impedance surface waveguides. IEEE Trans Antennas Propag 2013;61:3597–606.
[40] Patel AM, Grbic A. Transformation electromagnetics devices based on printed-circuit tensor impedance surfaces. IEEE Trans Microw Theory Techn 2014;62:1102–11.
[41] Lee J, Sievenpiper DF. Patterning technique for generating arbitrary anisotropic impedance surfaces. IEEE Trans Antennas Propag. 2016;64:4725–32.
[42] Sievenpiper D, Zhang L, Broas RFJ, Alexopolous NG, Yablonovitch E. High-impedance electromagnetic surfaces with a forbidden frequency band. IEEE Trans Microw Theory Techn 1999;47:2059–74.
[43] Mikhailov SA, Ziegler K. New electromagnetic mode in graphene. Phys Rev Lett 2007;99:016803.
[44] Vakil A, Engheta N. Transformation optics using graphene. Science 2011;332:1291–4.
[45] He XY, Tao J, Meng B. Analysis of graphene TE surface plasmons in the terahertz regime. Nanotechnology 2013;24:345203.
[46] Hanson GW. Dyadic Green's functions and guided surface waves for a surface conductivity model of graphene. J App Phys 2008;103:064302.
[47] Jablan M, Buljan H, Soljačić M. Plasmonics in graphene at infrared frequencies. Phys Rev B 2009;80:245435.
[48] Christensen T. Classical graphene plasmonics. In: Christensen T., ed. Classical to quantum plasmonics in three and two dimensions. Cham, Switzerland, Springer Theses Series; Springer, 2017, 97–129.
[49] Chen P-Y, Argyropoulos C, Farhat M, Gomez-Diaz JS. Flatland plasmonics and nanophotonics based on graphene and beyond. Nanophotonics 2017;6:1239–62.
[50] Luukkonen O, Simovski C, Granet G, et al. Simple and accurate analytical model of planar grids and high-impedance surfaces comprising metal strips or patches, IEEE Trans Antennas Propag 2008;56:1624–32.
[51] Padooru YR, Yakovlev AB, Kaipa CSR, Hanson GW, Medina F, Mesa F. Dual capacitive-inductive nature of periodic graphene patches: transmission characteristics at low-terahertz frequencies. Phys Rev B 2013;87:115401.
[52] Novoselov KS, Geim AK, Morozov SV, et al. Two-dimensional gas of massless Dirac fermions in graphene. Nature 2005;438:197–200.
[53] Aygar AM, Balci O, Cakmakyapan S, Kocabas C, Caglayan H, Ozbay E. Comparison of back and top gating schemes with tunable graphene fractal metasurfaces. ACS Photonics 2016;3:2303–7.
[54] Hu H, Zhai F, Hu D, et al. Broadly tunable graphene plasmons using an ion-gel top gate with low control voltage. Nanoscale 2015;7:19493–500.

[55] Zhao J, Wang M, Li H, et al. Lithium-ion-based solid electrolyte tuning of the carrier density in graphene. Sci Rep 2016;6:34816.
[56] Kakenov N, Balci O, Takan T, Ozkan VA, Altan H, Kocabas C. Observation of gate-tunable coherent perfect absorption of terahertz radiation in graphene. ACS Photonics 2016;3:1531–5.
[57] Yan X, Li X, Chandra B, et al. Tunable infrared plasmonic devices using graphene/insulator stacks. Nat Nanotechnol 2012;7:330–4.
[58] Rodrigo D, Tittl A, Limaj O, García de Abajo FJ, Pruneri V, Altug H. Double-layer graphene for enhanced tunable infrared plasmonics. Light Sci Appl 2017;6:e16277.
[59] Chamanara N, Caloz C. Fundamentals of graphene magnetoplasmons: principles, structures and devices. Forum Electromag Res Methods Appl Tech (FERMAT) 2015;10:1–15.
[60] Forati E, Hanson GW. Surface plasmon polaritons on soft-boundary graphene nanoribbons and their application in switching/demultiplexing. Appl Phys Lett 2013;103:133104.
[61] Mechelen TV, Jacob Z. Universal spin-momentum locking of evanescent waves. Optica 2016;3:118–26.
[62] Aiello A, Banzer P, Neugebauer M, Leuchs G. From transverse angular momentum to photonic wheels. Nat Photon 2015;9:789–95.
[63] Berry MV. Optical currents. J Opt A: Pure Appl Opt 2009;11:094001.
[64] Bliokh KY, Rodríguez-Fortuño FJ, Nori F, Zayats AV. Spin-orbit interactions of light. Nat Photon 2015;9:796–808.
[65] Rodríguez-Fortuño FJ, Marino G, Ginzburg P, et al. Near-field interference for the unidirectional excitation of electromagnetic guided modes. Science 2013;340:328–30.
[66] Lodahl P, Mahmoodian S, Stobbe S, et al. Chiral quantum optics. Nature 2017;541:473–80.
[67] Wang R, Xia H, Zhang D, et al. Bloch surface waves confined in one dimension with a single polymeric nanofiber. Nat Commun 2017;8:14330.
[68] Bakker RM, Yu YF, Paniagua-Domínguez R, Luk'yanchuk B, Kuznetsov AI. Resonant light guiding along a chain of silicon nanoparticles. Nano Lett 2017;17:3458–64.
[69] Bian Y, Ren Q, Kang L, Yue T, Werner PL, Werner DH. Deep-subwavelength light transmission in hybrid nanowire-loaded silicon nano-rib waveguides. Photon Res 2018;6:37–45.
[70] Zhang Y, Xu Y, Tian C, et al. Terahertz spoof surface-plasmon-polariton subwavelength waveguide. Photon Res 2018;6:18–23.
[71] Liang Y, Yu H, Zhang HC, Yang C, Cui TJ. On-chip sub-terahertz surface plasmon polariton transmission lines in CMOS. Sci Rep 2015;5:14853.
[72] Ukhtary MS, Nugraha ART, Hasdeo EH, Saito R. Broadband transverse electric surface wave in silicene. Appl Phys Lett 2016;109:063103.
[73] Musa MY, Renuka M, Lin X, et al. Confined transverse electric phonon polaritons in hexagonal boron nitrides. 2D Mater 2018;5:015018.

Topological valley transport under long-range deformations

Zhixia Xu,[1,2,*] Xianghong Kong,[2,3] Robert J. Davis,[2] Dia'aaldin Bisharat,[2] Yun Zhou,[4] Xiaoxing Yin,[1,†] and Daniel F. Sievenpiper[2,‡]

[1]*State Key Laboratory of Millimeter Waves, Southeast University, Nanjing 210096, China*

[2]*Electrical and Computer Engineering Department, University of California San Diego, San Diego, California 92093, USA*

[3]*Department of Electronic Engineering, Shanghai Jiao Tong University, Shanghai 200240, China*

[4]*Department of Mechanical and Aerospace Engineering, University of California San Diego, San Diego, California 92093, USA*

(Received 23 July 2019; revised manuscript received 14 January 2020; accepted 7 February 2020; published 26 February 2020)

Edge states protected by bulk topology of photonic crystals show robustness against short-range disorder, making robust information transfer possible. Here, topological photonic crystals under long-range deformations are investigated. The vertices of each regular hexagon in a honeycomb crystalline structure are shifted randomly to establish a deformed system. By increasing the degree of random deformations, a transition from an ordered system to an amorphous system are investigated, where the close of the topological band gap is clearly shown. We further present comprehensive investigations into excitation methods of the proposed deformed system. Due to the lack of strict periodicity, excitation of topological edge modes becomes difficult. We discuss chiral and linearly polarized sources as two different methods respectively. It is found that chiral sources are sensitive and rely on the ordered lattice. Even a weak long-range deformation can bring fluctuations to transmission. We further designed and fabricated metal-dielectric-metal sandwichlike samples working in the microwave band. Using a linearly polarized source, we detected the existence of topological transport in the deformed system. This work investigates excitation and robustness of bulk topology against long-range deformations and may open the way for exploiting topological properties of materials with a deformed lattice.

DOI: 10.1103/PhysRevResearch.2.013209

I. INTRODUCTION

Systems with spatial order are the predominate topic in physical science where every individual unit cell behaves the same. Much of this is motivated by the simplicity of the analysis, as the behavior of waves interacting in a system can be deduced elegantly from rigorous formulas once properties of the unit cell are known. Imperfections are usually undesirable because random scattering is usually unpredictable and may deteriorate the performance of an ordered system. However, scattering in systems can be regarded as an elastic process in that information is not lost and random scattering is reversible [1]. As an example, photonic band gaps, which widely exist in long-range ordered crystalline structures [2,3], can also be found in quasicrystals and amorphous structures without any translational symmetry [4–6]. To some extent, disorder opens an extra degree of statistical freedom to analyze the performance of systems, leading to potential applications based on artificial structures [7–10].

In particular, topology links order and disorder, attracting intense research interest recently [11–14]. Topological invariants defined within the Brillion zone of ordered structures divides photonic band gaps into trivial and nontrivial band gaps. When some symmetry of a system is broken, corresponding degeneracies vanish and nontrivial band gaps will appear, while edge states under topological protection are immune to disorder. Gyroscopes and gyromagnetic materials have been used to break time-reversal symmetry to realize spin Hall effects from mechanical to photonic systems [15–19]. Breaking the geometric symmetry also helps establish nontrivial band gaps. For example, reducing crystalline symmetry can generate pseudospin modes [20]. Photonic crystals with C3 symmetry featuring inversion asymmetry can support topological valley transport [21–25]. Using chiral waveguides or perturbations in the cylindrical structures breaks z symmetry and opens a nontrivial band gap [26,27]. Within most of these structures, a long-range ordered lattice is required to be preserved with translational symmetry where the unit cell is repeated periodically over the entire space.

Robustness against defects is an interesting property of topological materials. Most studies add a short-range disorder to observe robust topological edge modes, but when the disorder of the whole structure increases, topological states will vanish [28]. Thus, it is important to investigate how much spatial order is necessary to hold topological states. The Bott index has been proposed as a substitute for the Chern number [29–31]. According to the Bott index,

*Corresponding author: zxxucn@seu.edu.cn
†xxyin@seu.edu.cn
‡dsievenpiper@eng.ucsd.edu

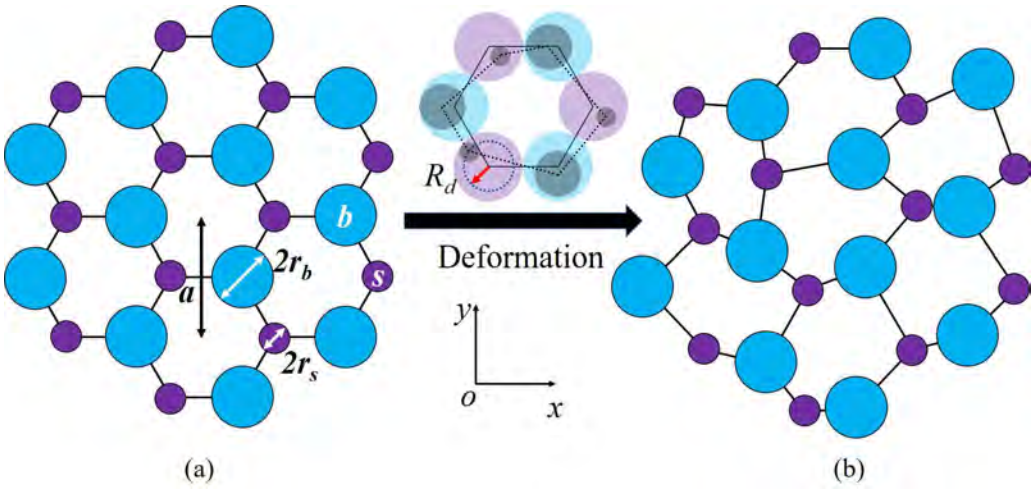

FIG. 1. (a) Honeycomb lattice with C3 symmetry whose geometric parameters are listed as side length of hexagon lattice $L = 10$ mm; radius of rods $r_b = 0.4L$, $r_s = 0.2L$; lattice length is a; and the refractive index of all dielectric rods is set around 1.7. (b) Randomly deformed lattice. The center of every rod is random, located in a circle centered in the original position whose radius R_d can be regarded as the degree of deformation. The inset shows a situation where $R_d = L/2 - r_i$, with $i = b$ or s standing for rods with two different size.

topological surface states at interfaces between the free space and bulk of quasicrystals or amorphous systems have been studied [32–34]. Another emerging topic is that of topological edge modes existing at the interface of two different amorphous materials. Recently, amorphous systems with broken time-reversal symmetry have been reported with unidirectional edge modes along the interface between two different amorphous bulks [35,36]. It is natural, therefore, to further investigate topological transport between different deformed structures without breaking time-reversal symmetry. In this work, we randomly deform a honeycomb lattice. Robust valley transport is investigated. Photonic density of states (PDOS), as a statistical parameter, is calculated to evaluate the existence of a photonic band gap. With increasing degree of deformation, the valley band gap becomes narrower until it eventually disappears. We further designed and fabricated two samples with straight and triangular interfaces, respectively, based on the three-dimensional (3D) printing technique and measured topological transport within the band gap.

II. DEFORMATION SCHEME

The original structure is a periodic honeycomb lattice, as shown in Fig. 1(a). Dielectric rods with two different radii are placed on vertices with C3 symmetry, opening a Dirac point at K/K′ with the valley topological property [21–24,37–40]. We assume the height of the dielectric rods is infinite to simplify the model to a two-dimensional (2D) structure in the x-y plane. We further deform the whole lattice to investigate topological transport with long-range disorder. Inspired by the nature of foam that every node is shared by three bubbles, we propose the deformed systems as shown in Fig. 1(b), where vertices are shifted randomly. The region of deformation marked in the inset ensures each node still connects three convex hexagons, which is the most common and stable topology of a bubble cluster statistically [41].

III. RESULTS AND ANALYSIS

A. Original periodic structure

Here, we consider TM modes with electric field perpendicular to the structure plane (x-y plane). We first present simulations of the original ordered structure without any deformation. Figure 2(a) shows the simulated band diagram of a hexagonal unit cell with periodic boundary conditions. The dotted lines correspond to the honeycomb lattice with C6 symmetry where all rods are exactly the same size ($r_b = r_s = 0.4L$). Initially, there exists a degeneracy at K/K′. We then arrange two different rods in turn ($r_b = 0.4L$, $r_s = 0.2L$) to reduce the C6 symmetry to the C3 symmetry, thereby realizing a topological valley band gap. Figure 2(b) shows the phase distribution at valley states carrying intrinsic orbital angular momentum (OAM), counterclockwise or clockwise. Using a 1×12-size superlattice with periodic boundary conditions along the y axis and electric boundary conditions along the x axis, we can obtain the dispersion diagram of the edge mode supported by the small-rod interface shown in Fig. 2(c) and corresponding electric field distribution shown in Fig. 2(d), where energy is bound at the interface, propagating along the y axis and decaying along the x axis.

B. Photonic density of states

When random deformations are added, translational symmetry of crystalline structures is no longer valid. As shown in the inset of Fig. 3, we set periodic boundary conditions around the perimeter as an approximation to suppose that the structure is infinite and further obtain eigenvalues. Figure 3(a) shows eigenvalues of the superlattice under investigation; the horizontal axis shows the index of eigenmodes and the vertical axis represents the dimensionless frequency. We can observe a band gap at around 0.5 with several sparse points marked as red in the band gap. A typical eigenstate within the band gap

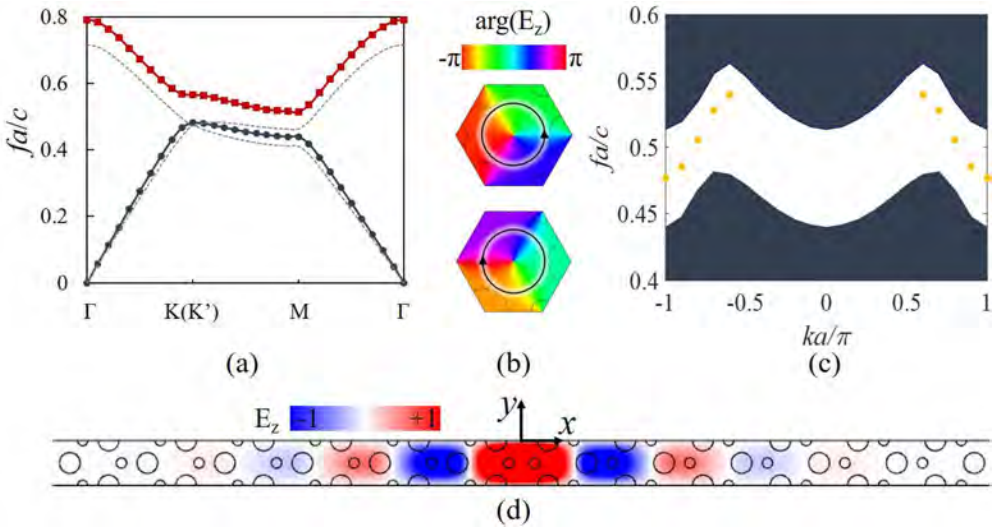

FIG. 2. (a) The opening of a valley band gap. (b) Intrinsic OAM modes and phase distributions of E_z at valley points. (c) Valley-dependent edge mode. (d) Edge mode supported by the interface.

is shown in Fig. 3(b), where most of the energy is distributed around boundaries of the superlattice. These eigenstates can be regarded as errors brought on by the periodic boundary approximation. Figure 3(c) shows a bulk state out of the band gap in which energy permeates into the whole superlattice.

Based on distributions of eigenvalues, PDOS of these superlattices can be further calculated, as shown in Fig. 4. We investigate the PDOS of four different superlattices undergoing different degrees of deformation defined by R_d. We coded the deformed pattern using MATLAB and then transferred it into COMSOL Multiphysics to establish the models. Thus, there may exist some geometrical error during this process but it would not influence the conclusion. With the increasing degree of deformation to almost an amorphous distribution, the valley band gap becomes narrower and it eventually disappears. The PDOS approach is a valid method to find band gaps of nonperiodic structures such as quasicrystals [31,32,34] and amorphous structures [10,33,35], where thousands of eigenvalues of a superlattice need to be calculated to detect band gaps with enough accuracy. Thus, PDOS is a statistical parameter to analyze the deformed structure. We also calculate the corresponding Fourier spectra of the superlattices. As the degree of deformation increases, the number of energy peaks in the reciprocal space decreases. The number of hexagonally distributed points in the Fourier spectra show the level of similarity between a deformed structure and the undeformed periodic lattice in real space. The greater the deformation, the fewer maximum points that can be found in the Fourier spectra. If hexagonally distributed points disappear in the Fourier spectra, the structure can be regarded as an amorphous material whose band gap disappears as well. In the presented examples, photonic band gaps that are clearly recognizable in Figs. 4(a) and 4(b) become weak in Fig. 4(c) and finally disappear in Fig. 4(d). These identifiable points in the reciprocal space contain the average symmetry information of the lattice and could be regarded as a limitation to judge the

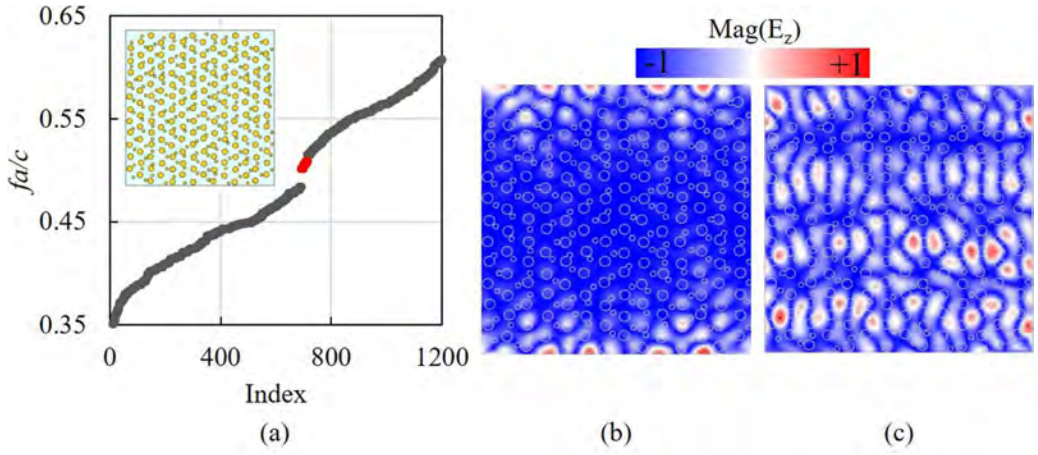

FIG. 3. (a) Distribution of eigenstates where the inset shows the superlattice with periodic boundary conditions. The degree of deformation is defined as $R_d = L/2 - r_i$. (b) An eigenstate within the band gap. (c) An eigenstate out of the band gap.

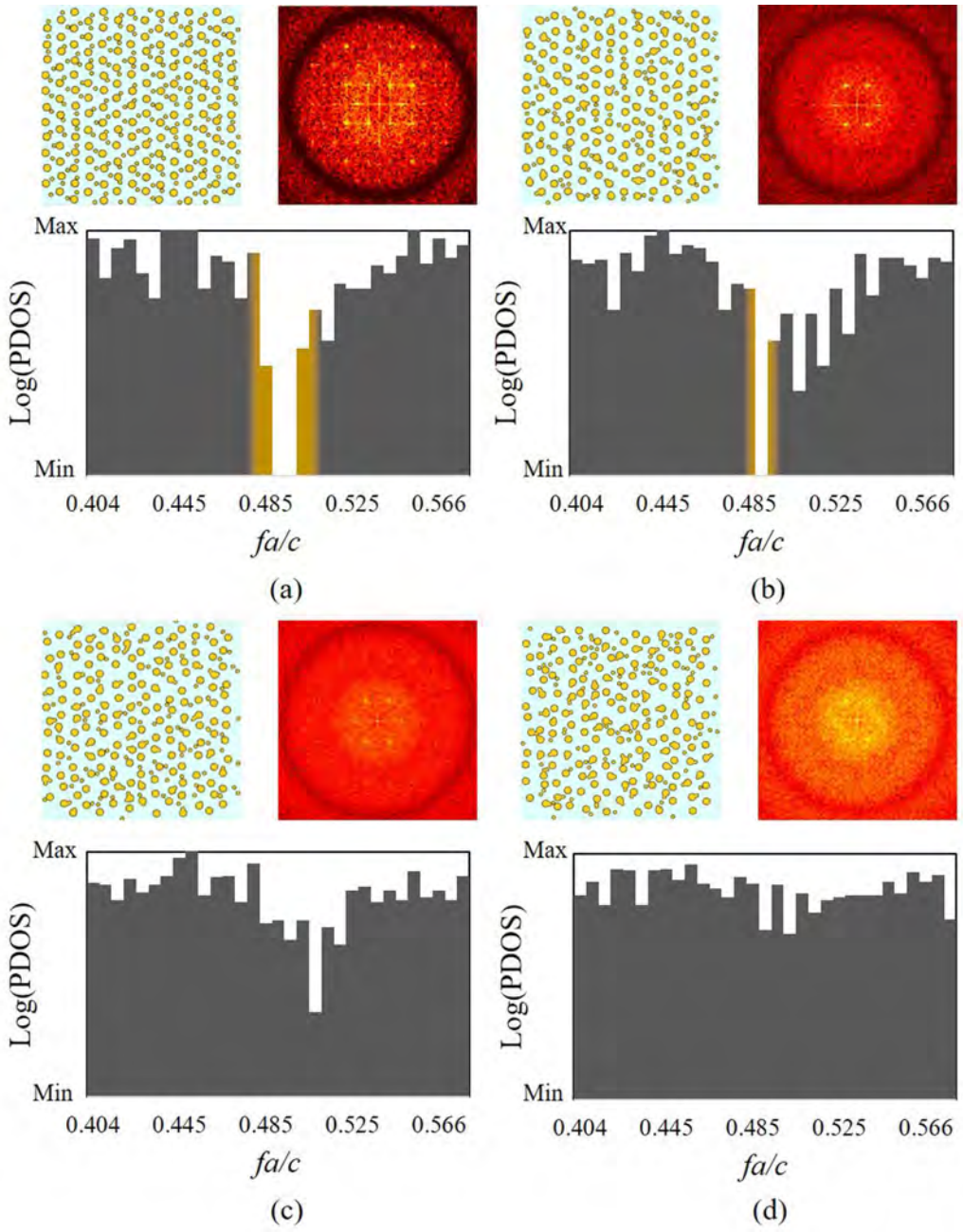

FIG. 4. Superlattices (upper left), Fourier transformations (upper right), and PDOS (bottom) under different degrees of deformation: (a) $R_d = 1\times(L/2 - r_i)$, (b) $R_d = 2\times(L/2 - r_i)$, (c) $R_d = 3\times(L/2 - r_i)$, and (d) $R_d = 4\times(L/2 - r_i)$.

reservation of topological properties when materials undergo deformation.

C. Topological edge transport

We further verify valley transport along the interface of photonic crystals under the deformation ($R_d = L/2 - r_i$). The topological index difference at the K/K′ points lead to unidirectional edge modes. Figure 5 shows two different interfaces: straight and triangular interfaces. Unidirectional propagation can be observed in periodic structures and deformed structures, as shown in Figs. 5(a)–5(d). The circularly polarized excitation is set at one side of the interface waveguide, and OAM modes are excited at valley points, as shown in Fig. 5(e). Probes at the output side are set to obtain the transmission spectra in Fig. 5(f). Maximum and minimum transmission points in deformed structures are marked as circles and squares, where corresponding field distributions are shown in Figs. 5(b), 5(d), and 6, respectively. Transmission bandwidths of straight interfaces are wider than bandwidths of triangular interfaces because straight interfaces support propagation along the y axis while triangular interfaces support propagation towards both the y axis and at an angle of 60 degrees. That means waves in more directions need to be forbidden in the case of a triangular interface than waves in the case of a straight interface. Thus, it is natural to observe

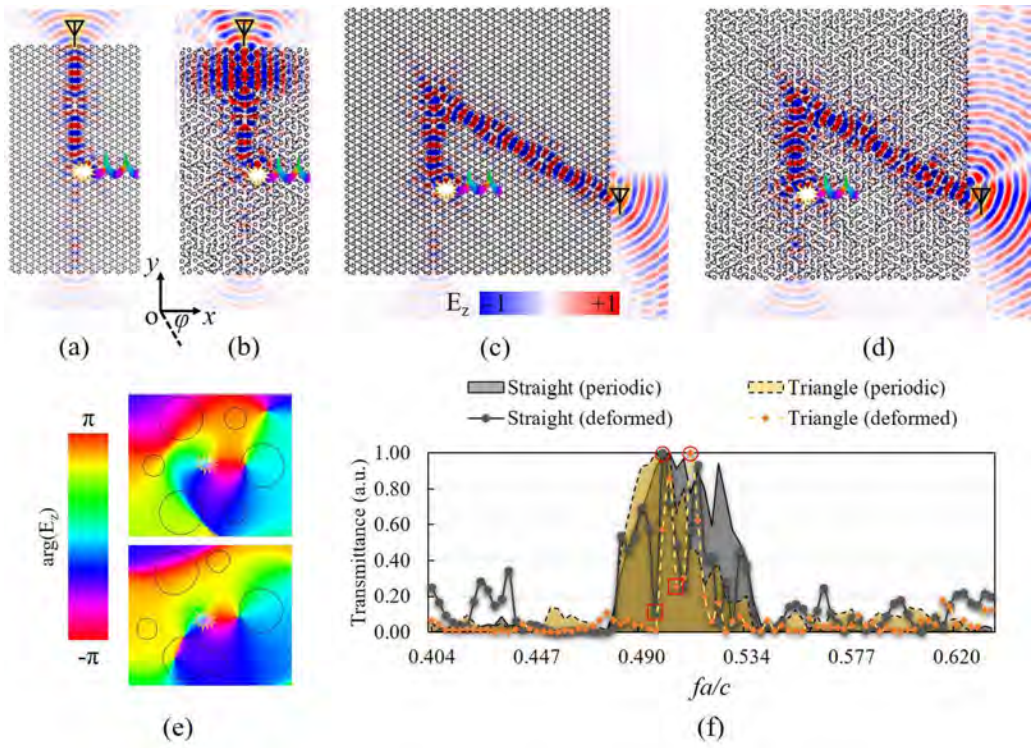

FIG. 5. Topological transports excited by chiral sources ($M_{//} = M_x + jM_y$). Straight interface: (a) periodic structure, (b) deformed structure. Triangular interface: (c) periodic structure, (d) deformed structure. (e) The chiral point source is utilized to excite OAM modes at valley points in a hexagonal unit cell. (f) Normalized transmission spectra where maximum and minimum transmission points in deformed structures are marked as circles and squares, respectively.

a narrower bandwidth when we bend a straight interface into a triangular interface. When deformations happen, the bandwidth becomes narrower, as shown in Fig. 4. Besides the change of bandwidth, transmission along interfaces of deformed structures varies because the excitation sources are no longer at the strict center of the deformed hexagonal unit cell, which causes inevitable mismatch between the source and the intended spin mode. Thus, the transmission efficiency is almost perfect at some frequencies where ideal unidirectional transport can be observed clearly, as shown in Figs. 5(b) and 5(d). However, at some frequencies within the band gap, transmission efficiency is low, as marked in Fig. 5(f).

Electric field distributions at these minimum transmission points are shown in Fig. 6. The point source is set at the same position, and we can observe the edge modes along the interface instead of the unidirectional propagation shown in Figs. 5(b) and 5(d), the maximum transmission points. Radiation happens at both ends of the interfaces clearly, which is a typical property of valley transport [24]. This means that in a random deformed structure, it is difficult to excite pure unidirectional transport within the whole band gap due to the mismatch between the circularly polarized source and eigenmodes of a random deformed hexagon at valley points. Although the deformed bulk still reserves the statistical topological band gap, eigenmodes of any particular deformed hexagon are unpredictable. The excitation can be divided into two orthogonal spin modes propagating towards two opposite directions along the interface, and at the end of the interface, radiation occurs.

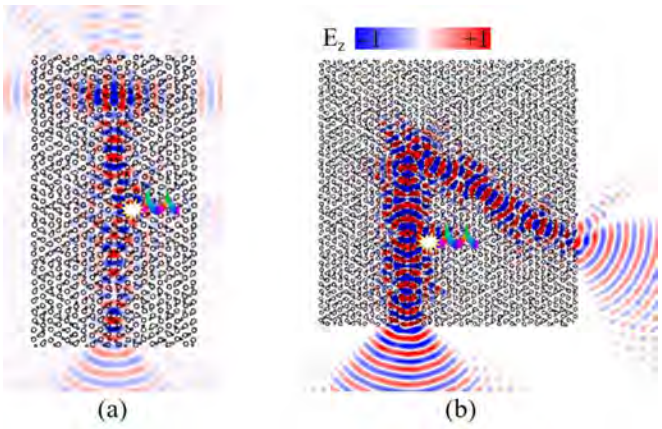

FIG. 6. Electric field distribution of edge modes at minimum transmission points within the photonic band gap: (a) straight interface and (b) triangular interface.

D. Experiments

We further utilized a 3D printing technique to design and fabricate a sandwichlike sample to prove the existence of a topological edge mode in a system with random deformations. Figure 7(a) shows eigenmodes at valley points of an original sandwichlike unit cell with periodic boundary conditions. Figure 7(b) shows the structure undergoing random

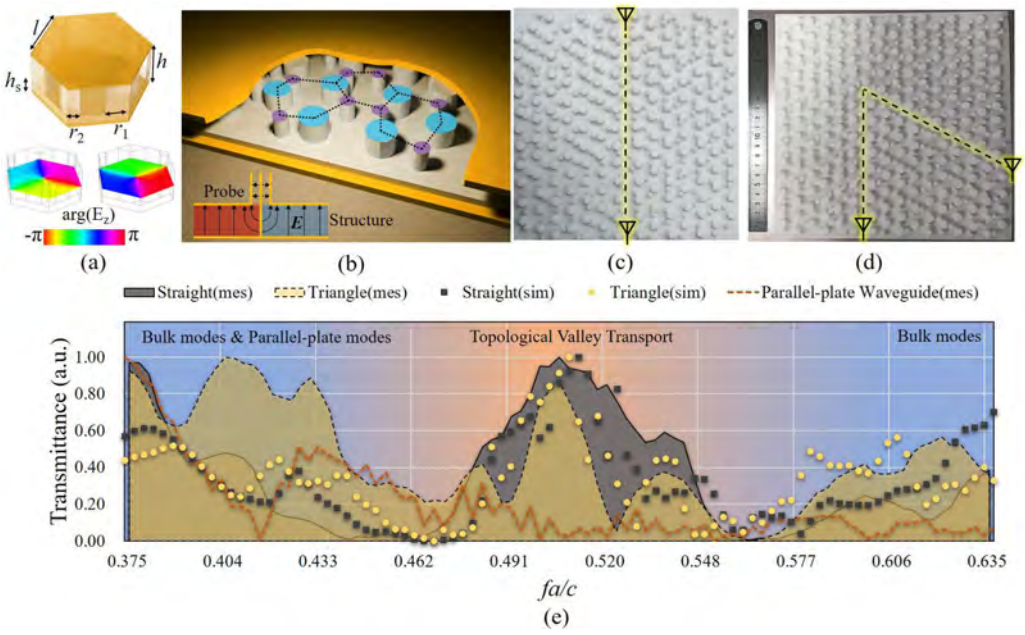

FIG. 7. (a) The ordered metal-dielectric-metal unit cell with periodic boundary conditions working in the microwave band and corresponding phase distributions E_z of two OAM modes at valley points. Geometric parameters: the total thickness of dielectric structure is $h = 8$ mm, and the thickness of the dielectric plate is $h_s = 2$ mm, radii of the rods are $r_1 = 4$ mm and $r_2 = 2$ mm, the side length $l = 10$ mm. (b) The sandwichlike structure under random deformation $R_d = L/2 - r_i$; the inset shows the setup of probes at the interface of two topological structures. Fabricated samples with (c) straight and (d) triangular interface. (e) Simulated and measured transmission where the results of two samples are normalized. The measured transmission property of a parallel-plate waveguide with an 8-mm gap, exactly the same as the structure height, is also shown as a benchmark.

deformations, and the inset shows the excitation setup. Two fabricated samples with straight and triangular interfaces are shown in Figs. 7(c) and 7(d), respectively, where positions of two probes connected to a vector network analyzer (Keysight PNA N5224A) are marked. In Fig. 7(e), simulated and measured transmissions are compared. The simulation setup is exactly the same as in the experiments, where linearly polarized probes are set at the center of the interface to measure the transmissions. We also removed the dielectric structure in the middle layer and measured background transmission of the parallel-plate waveguide as a benchmark. The background transmission is mainly brought by parallel-plate modes, which are difficult to eliminate [42]. The background transmission is much higher in the low-frequency band and becomes almost neglectable within the topological band gap. After assembling the sandwichlike waveguides, the transmission within the topological band gap increases dramatically, and due to the existence of bulk modes out of the topological band gap, transmission out of the band gap is also enhanced to some extent, making it difficult to observe the topological transport. Similar to previous works [22,26,40,43–45], we can further distinguish topological transmission from bulk transmission by minimum transmission points on both sides of the topological band gap.

Note that we set probes perpendicular to the metal plates to excite and detect the TM polarized mode. The ideal method to excite topological edge modes is to use chiral waves at the center of a hexagonal unit cell [20,37,46], but a localized source at the interface can also excite the topological edge mode as well [22,47–49]. As mentioned before, the eigenmode at valley points of any deformed hexagonal cell cannot be a pure OAM mode. Even if we keep a hexagonal lattice undeformed, the structure still lacks strict periodic boundary conditions to ensure an ideal OAM mode. Therefore, we have no choice but to place a linearly polarized probe at the center of the interface to excite the edge transport along the interface. We could not obtain the exact transmission efficiency of the deformed structure due to the lack of transition designs between probe and the interface. However, by comparing transmission spectra of the straight interface and the triangular interface as shown in Fig. 7(e), we found that transmission peaks of straight and triangular interfaces are almost the same, demonstrating that the topological edge mode is immune to the sharp defect of the interface. The bandwidth of the straight interface is wider than the bandwidth of the triangular interface, similar to the discussion about Fig. 5(f).

IV. DISCUSSION

We investigate photonic topological insulators under long-range deformations, where the transition from the ordered to the amorphous structure is discussed. As long as statistical features, such as the band gap shown in the PDOS, and the peaks of the Fourier spectra are recognizable, the bulk can maintain its topological properties. We further designed and conducted experiments based on a 3D printing technique. Excitation of the deformed system is a challenging task. Traditional chiral wave-coupling methods are no longer valid due the lack of strict periodicity. Even in a slightly

deformed lattice, mismatch between a chiral source and the intrinsic modes of a particular unit cell is obvious. Thus, a linearly polarized source at the center of the interface acts as a more robust method. Transmissions of straight and triangular interfaces were simulated and measured to prove the robustness of topological transport in the deformed structure. This study extends investigations of topological transport from local disorder to long-range deformations of the whole lattice.

ACKNOWLEDGMENTS

This work was supported by the National Natural Science Foundation of China (No. 61771127 and No. 61427801), Scientific Research Foundation of Graduate School of Southeast University (No. YBJJ1814), and Postgraduate Research & Practice Innovation Program of Jiangsu Province (No. KYCX18_0098), as well as AFOSR Contract No. FA9550-16-1-0093.

[1] D. S. Wiersma, Nat. Photon. **7**, 188 (2013).

[2] E. Yablonovitch, T. J. Gmitter, R. D. Meade, A. M. Rappe, K. D. Brommer, and J. D. Joannopoulos, Phys. Rev. Lett. **67**, 3380 (1991).

[3] J. D. Joannopoulos, P. R. Villeneuve, and S. Fan, Nature (London) **386**, 143 (1997).

[4] P. W. Anderson, Phys. Rev. **109**, 1492 (1958).

[5] K. Edagawa, S. Kanoko, and M. Notomi, Phys. Rev. Lett. **100**, 013901 (2008).

[6] M. E. Zoorob, M. D. B. Charlton, G. J. Parker, J. J. Baumberg, and M. C. Netti, Nature (London) **404**, 740 (2000).

[7] K. Nagao, T. Inuzuka, K. Nishimoto, and K. Edagawa, Phys. Rev. Lett. **115**, 075501 (2015).

[8] K. Viebahn, M. Sbroscia, E. Carter, J.-C. Yu, and U. Schneider, Phys. Rev. Lett. **122**, 110404 (2019).

[9] C. López, Adv. Opt. Mater. **6**, 1800439 (2018).

[10] J. Ricouvier, P. Tabeling, and P. Yazhgur, Proc. Natl. Acad. Sci. USA **116**, 9202 (2019).

[11] T. Fukui, Y. Hatsugai, and H. Suzuki, J. Phys. Soc. Jpn. **74**, 1674 (2005).

[12] J. E. Moore, Nature (London) **464**, 194 (2010).

[13] L. Lu, J. D. Joannopoulos, and M. Soljačić, Nat. Photon. **8**, 821 (2014).

[14] T. Ozawa, H. M. Price, A. Amo, N. Goldman, M. Hafezi, L. Lu, M. C. Rechtsman, D. Schuster, J. Simon, O. Zilberberg, and I. Carusotto, Rev. Mod. Phys. **91**, 015006 (2019).

[15] L. M. Nash, D. Kleckner, A. Read, V. Vitelli, A. M. Turner, and W. T. M. Irvine, Proc. Natl. Acad. Sci. USA **112**, 14495 (2015).

[16] F. D. M. Haldane and S. Raghu, Phys. Rev. Lett. **100**, 013904 (2008).

[17] S. Raghu and F. D. M. Haldane, Phys. Rev. A **78**, 033834 (2008).

[18] Z. Wang, Y. D. Chong, J. D. Joannopoulos, and M. Soljačić, Phys. Rev. Lett. **100**, 013905 (2008).

[19] Z. Wang, Y. Chong, J. D. Joannopoulos, and M. Soljacic, Nature (London) **461**, 772 (2009).

[20] L.-H. Wu and X. Hu, Phys. Rev. Lett. **114**, 223901 (2015).

[21] K. F. Mak, K. L. McGill, J. Park, and P. L. McEuen, Science **344**, 1489 (2014).

[22] M. I. Shalaev, W. Walasik, A. Tsukernik, Y. Xu, and N. M. Litchinitser, Nat. Nanotechnol. **14**, 31 (2019).

[23] X.-D. Chen, F.-L. Zhao, M. Chen, and J.-W. Dong, Phys. Rev. B **96**, 020202(R) (2017).

[24] T. Ma and G. Shvets, New J. Phys. **18**, 025012 (2016).

[25] X. Ni, D. Purtseladze, D. A. Smirnova, A. Slobozhanyuk, A. Alù, and A. B. Khanikaev, Sci. Adv. **4**, eaap8802 (2018).

[26] X. Cheng, C. Jouvaud, X. Ni, S. H. Mousavi, A. Z. Genack, and A. B. Khanikaev, Nat. Mater. **15**, 542 (2016).

[27] M. C. Rechtsman, J. M. Zeuner, Y. Plotnik, Y. Lumer, D. Podolsky, F. Dreisow, S. Nolte, M. Segev, and A. Szameit, Nature (London) **496**, 196 (2013).

[28] K. Kobayashi, T. Ohtsuki, and K.-I. Imura, Phys. Rev. Lett. **110**, 236803 (2013).

[29] T. A. Loring and M. B. Hastings, Europhys. Lett. **92**, 67004 (2010).

[30] I. C. Fulga, D. I. Pikulin, and T. A. Loring, Phys. Rev. Lett. **116**, 257002 (2016).

[31] H. Huang and F. Liu, Phys. Rev. B **98**, 125130 (2018).

[32] M. A. Bandres, M. C. Rechtsman, and M. Segev, Phys. Rev. X **6**, 011016 (2016).

[33] A. Agarwala and V. B. Shenoy, Phys. Rev. Lett. **118**, 236402 (2017).

[34] H. Huang and F. Liu, Phys. Rev. Lett. **121**, 126401 (2018).

[35] N. P. Mitchell, L. M. Nash, D. Hexner, A. M. Turner, and W. T. M. Irvine, Nat. Phys. **14**, 380 (2018).

[36] B. Yang, H. Zhang, T. Wu, R. Dong, X. Yan, and X. Zhang, Phys. Rev. B **99**, 045307 (2019).

[37] J.-W. Dong, X.-D. Chen, H. Zhu, Y. Wang, and X. Zhang, Nat. Mater. **16**, 298 (2017).

[38] F. Gao, H. Xue, Z. Yang, K. Lai, Y. Yu, X. Lin, Y. Chong, G. Shvets, and B. Zhang, Nat. Phys. **14**, 140 (2017).

[39] Z. Gao, Z. Yang, F. Gao, H. Xue, Y. Yang, J. Dong, and B. Zhang, Phys. Rev. B **96**, 201402(R) (2017).

[40] M. Yan, J. Lu, F. Li, W. Deng, X. Huang, J. Ma, and Z. Liu, Nat. Mater. **17**, 993 (2018).

[41] D. L. Weaire and S. Hutzler, *The Physics of Foams* (Clarendon Press, Oxford, 2001).

[42] J. D. Shumpert, W. J. Chappell, and L. P. B. Katehi, IEEE Trans. Microw. Theory Technol. **47**, 2099 (1999).

[43] Z. Zhang, Y. Tian, Y. Cheng, Q. Wei, X. Liu, and J. Christensen, Phys. Rev. Appl. **9**, 034032 (2018).

[44] P. Gao, Z. Zhang, and J. Christensen, Phys. Rev. B **101**, 020301(R) (2020).

[45] B.-Z. Xia, S.-J. Zheng, T.-T. Liu, J.-R. Jiao, N. Chen, H.-Q. Dai, D.-J. Yu, and J. Liu, Phys. Rev. B **97**, 155124 (2018).

[46] Y. Yang, Y. F. Xu, T. Xu, H.-X. Wang, J.-H. Jiang, X. Hu, and Z. H. Hang, Phys. Rev. Lett. **120**, 217401 (2018).

[47] W. J. Chen, S. J. Jiang, X. D. Chen, B. Zhu, L. Zhou, J. W. Dong, and C. T. Chan, Nat. Commun. **5**, 5782 (2014).

[48] A. B. Khanikaev, S. Hossein Mousavi, W.-K. Tse, M. Kargarian, A. H. MacDonald, and G. Shvets, Nat. Mater. **12**, 233 (2013).

[49] S. Peng, N. J. Schilder, X. Ni, J. van de Groep, M. L. Brongersma, A. Alù, A. B. Khanikaev, H. A. Atwater, and A. Polman, Phys. Rev. Lett. **122**, 117401 (2019).

Research Article | Vol. 28, No. 2 / 20 January 2020 / Optics Express 2070
Optics EXPRESS

Spin-momentum locked modes on anti-phase boundaries in photonic crystals

XIANGHONG KONG,[1,2,4] YUN ZHOU,[3,5] GAOBIAO XIAO,[1,6] AND DANIEL F. SIEVENPIPER[2,7]

[1]Department of Electronic Engineering, Shanghai Jiao Tong University, Shanghai 200240, China
[2]Department of Electrical and Computer Engineering, University of California, San Diego, California 92093, USA
[3]Department of Mechanical and Aerospace Engineering, University of California, San Diego, California 92093, USA
[4]klovek@sjtu.edu.cn
[5]yuz421@eng.ucsd.edu
[6]gaobiaoxiao@sjtu.edu.cn
[7]dsievenpiper@eng.ucsd.edu

Abstract: An anti-phase boundary is formed by shifting a portion of photonic crystal lattice along the direction of periodicity. A spinning magnetic dipole is applied to excite edge modes on the anti-phase boundary. We show the unidirectional propagation of the edge modes which is also known as spin-momentum locking. Band inversion of the edge modes is discovered when we sweep the geometrical parameters, which leads to a change in the propagation direction. Also, an optimized source is applied to excite the unidirectional edge mode with high directivity.

1. Introduction

The quantum spin-Hall effect indicates that the spin of the electron is locked to the direction of propagation [1]. The Z_2 index, or the spin Chern number which is a topological invariant of the given quantum system is defined to verify if the spin Hall conductance exists on the edge of the bulk material [2,3]. After introducing the Z_2 topological index to analyze the system, a variety of unidirectional edge modes in quantum systems were discovered [4–6]. By analogy with the quantum spin-Hall effect of electrons, spin-momentum locking phenomena can also be found in photonic topological insulators [7–11]. The direction of propagation is still used to define 'momentum' of the light while the concept of 'spin' is not as clear as the spin of the electron. It may refer to the bonding (antibonding) states of electric and magnetic fields [7], left-hand (right-hand) circular polarizations of electric fields [8], and clockwise (anticlockwise) circulations of coupled resonator optical waveguides [11].

Spin-momentum locked edge modes can also be discovered in trivial optical systems without topological properties, such as photonic crystal waveguides [12–14], surface plasmon polaritons [15,16], and even dielectric waveguides [16]. A pair of orthogonal dipoles with $\pm\pi/2$ phase differences which represent opposite spin directions are applied to excite the unidirectional edge modes in these systems. The spin of dipole sources couples to the spin of evanescent waves near the edges, giving rise to the spin-momentum locked edge modes.

An anti-phase boundary is created by shifting the crystal by one-half period along the propagation direction. It can be observed in electronic systems and can be treated as a defect in the crystal that breaks the translation symmetry [17,18]. Accurate atomic manipulation is required in order to design the anti-phase boundaries in electronic systems [19,20]. It is easier to design the anti-phase boundary in photonic system, which may help us have a deeper understanding of how the energy is distributed near the anti-phase boundary.

#379672 https://doi.org/10.1364/OE.379672
Journal © 2020 Received 10 Oct 2019; revised 20 Nov 2019; accepted 7 Jan 2020; published 15 Jan 2020

Optics EXPRESS

In this paper, we create an anti-phase boundary in a photonic crystal structure by shifting the structure along the direction of periodicity. Unidirectional propagation of the edge modes is discovered. To the authors' best knowledge, spin-momentum locked edge modes have not been found on anti-phase boundaries in quantum or optical systems. It will not only make the existence of the propagating edge modes along anti-phase boundaries in quantum systems possible, but also provide a new way to design chiral waveguides in photonic crystal structures.

2. Spin-momentum locked modes

As shown in Fig. 1, an anti-phase boundary is created by shifting the photonic crystal along the direction $\vec{a}_2$ by $-a_0/2$, which is one-half period. The geometry and material parameters are given in Fig. 1. Here we only investigate the transverse magnetic (TM) modes of the electromagnetic waves, where only E_z, H_x, and H_y are nonzero. According to [8], tuning the distance between

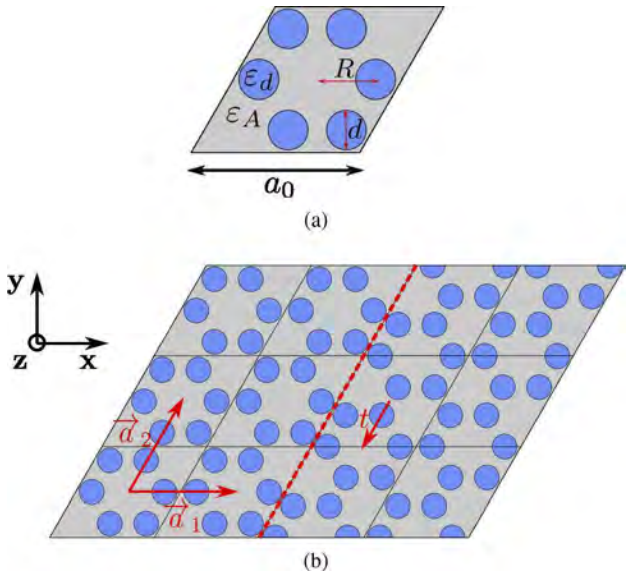

Fig. 1. (a) Unit cell of photonic crystal with d the diameter of cylinders, a_0 the length of diamond edge, and R the distance between the center of the diamond and the center of the cylinders. ε_d and ε_A are the relative permittivities of the cylinders and surrounding environment respectively. (b) Anti-phase boundary (red dashed line) formed by shifting the photonic crystal along $\vec{a}_2$ by one-half period $t = -a_0/2$ where $\vec{a}_1$ and $\vec{a}_2$ are lattice vectors of the crystal. The angle between $\vec{a}_1$ and $\vec{a}_2$ is $\pi/3$.

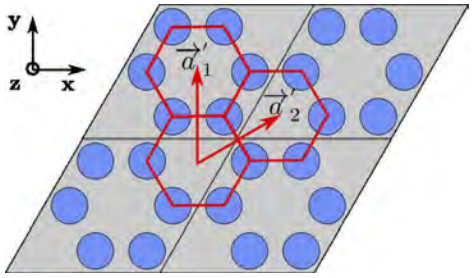

Fig. 2. The red hexagons are unit cells of the crystal for $R = a_0/3$ while $\vec{a}'_1$ and $\vec{a}'_2$ are lattice vectors.

Optics EXPRESS

the center of the diamond and the center of cylinders R will change the topological properties of the crystal. When $R < a_0/3$, the structure behaves as a topologically trivial material with Z_2 index equal to zero. Band folding occurs when $R = a_0/3$ since the lattice vectors of the unit cell change into $\vec{a}'_1 = -\vec{a}_1/3 + 2\vec{a}_2/3$ and $\vec{a}'_2 = \vec{a}_1/3 + \vec{a}_2/3$ as shown in Fig. 2. The size of the unit cell shrinks while the Brillouin zone expands. If the original Brillouin zone ($R \neq a_0/3$) is chosen, the bands on expanded Brillouin zone ($R = a_0/3$) must be folded to fit in the original one, which leads to the creation of a Dirac cone at the Γ point. Further increasing R opens the band gap at Γ point and turns the trivial crystal into a topological insulator with nonzero Z_2 index. Band inversion happens at the Γ point when $R > a_0/3$ with dipole modes in the higher band and quadrupole modes in the lower band. Unidirectional edge modes can be found at the boundary between the topological insulator ($R > a_0/3$) and trivial crystal ($R < a_0/3$). Here we place the topological insulator with $R > a_0/3$ on both sides of the boundary as shown in Fig. 1(b). However, the topological properties of the photonic crystal cannot explain the edge modes discovered on the anti-phase boundary since shifting will not change the band diagram and Z_2 index of the

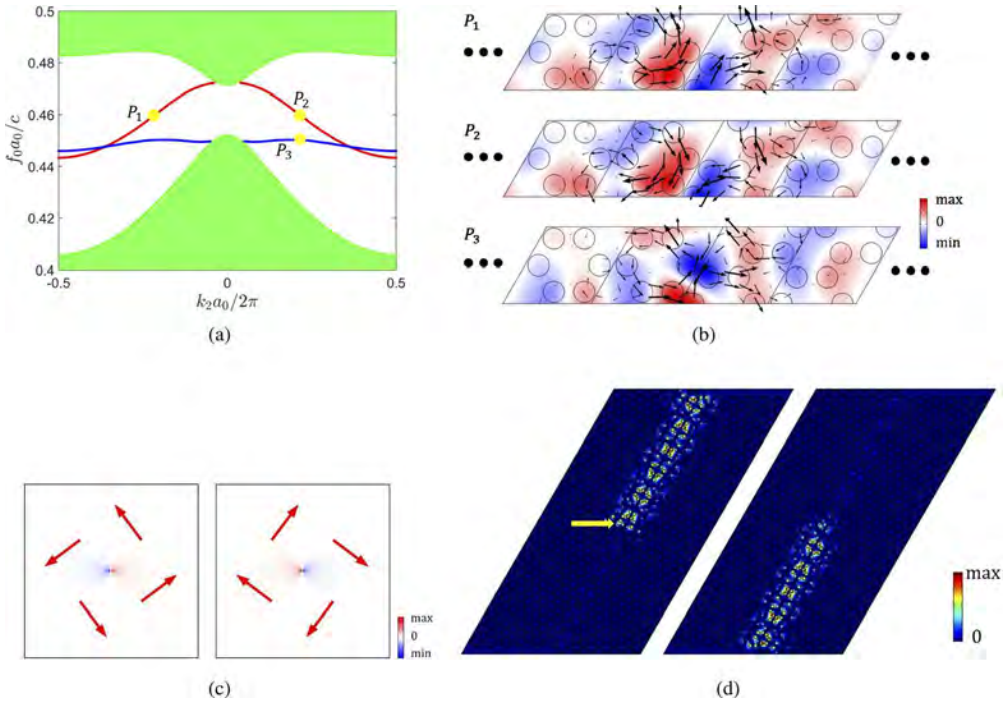

Fig. 3. (a) Dispersion relation of the super-cell which is periodic in $\vec{a}_2$ direction and of 8 unit cells on each side of anti-phase boundary in $\vec{a}_1$ direction. Label k_2 means the projection of k vector onto $\vec{a}_2/|\vec{a}_2|$. The green-shaded region is the projected band diagram of the bulk modes. Red and blue lines represent the odd modes and even modes respectively. The diameter of cylinder and distance between cylinder center and diamond center are $d = 0.24a_0$ and $R = 0.345a_0$. The relative permittivities are $\varepsilon_d = 11.7$ and $\varepsilon_A = 1$. (b) Real part of E_z distributions at points P_1, P_2 and P_3 as shown in (a). The black arrows indicate the time-averaged Poynting vectors over a period. (c) Real part distributions of E_z of magnetic dipoles $(\hat{x} - i\hat{y})/\sqrt{2}$ (left) and $(\hat{x} + i\hat{y})/\sqrt{2}$ (right) are plotted. The red arrows represent the time-averaged Poynting vectors. (d) $|E_z|$ are plotted for the driven modes excited by magnetic dipoles $(\hat{x} - i\hat{y})/\sqrt{2}$ (left) and $(\hat{x} + i\hat{y})/\sqrt{2}$ (right) respectively. The yellow arrow indicates the location of the source, which is at the center of the unit cell. The normalized frequency of the source is chosen to be $f_0a_0/c = 0.46$.

Optics EXPRESS

crystal. As shown in Fig. 3(a), the odd edge modes (anti-symmetric distributions) and the even edge modes (symmetric distributions) are caused by the mirror symmetry of the super-cell. The field distributions of the edge modes calculated by COMSOL are given in Fig. 3(b). The E_z distributions at point P_1 and P_2 defined in Fig. 3(a) are the same while the Poynting vectors are in opposite directions. Here we define the counter clockwise rotation of the Poynting vectors on the left side of the anti-phase boundary as spin-up and the clockwise rotation as spin-down. By comparing P_1 and P_2 we know that the edge modes with the same frequency but opposite k vectors have different spin directions. Also, we show that the edge modes with the same k vector have opposite spin directions by comparing the fields at P_2 and P_3. In order to excite the edge modes, a circularly polarized magnetic dipole is chosen as the source in our driven mode simulation. By observing the Poynting vectors in Fig. 3(c), we conclude that magnetic dipole $(\hat{x} - i\hat{y})/\sqrt{2}$ behaves like the spin-up source while $(\hat{x} + i\hat{y})/\sqrt{2}$ like the spin-down source. The frequency of excitation is chosen to be inside the band gap of the bulk modes, which only excite the odd edge modes as we can conclude from Fig. 3(a). We apply the spin-up source to the shifted structure to excite the spin-up edge mode at P_1. Since the group velocity at P_1 is positive, the wave will propagate along the direction $\overrightarrow{a}_2$. The simulation result shown on the left side of Fig. 3(d) matches this theoretical prediction. Similarly, a spin-down source will excite the edge mode propagates along $-\overrightarrow{a}_2$, which is also shown on the right side of Fig. 3(d).

Tuning the parameter R to $R < a_0/3$ will dramatically change the properties of the edge modes. According to [8], the band diagram has been closed and reopened at the Γ point when tuning

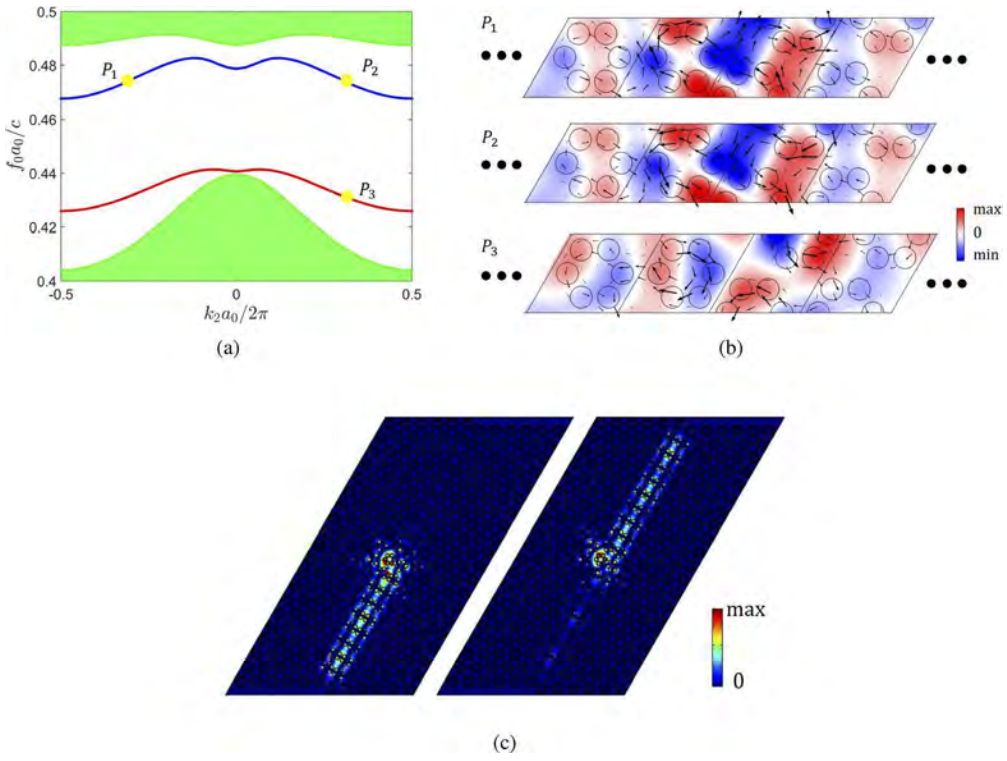

Fig. 4. (a) Dispersion relation of the super-cell when $R = 0.3a_0$. Red and blue lines represent the odd modes and even modes respectively. (b) Real part of E_z distributions at points P_1, P_2 and P_3 as shown in (a). (c) $|E_z|$ are plotted for the driven modes excited by magnetic dipoles $(\hat{x} - i\hat{y})/\sqrt{2}$ (left) and $(\hat{x} + i\hat{y})/\sqrt{2}$ (right) respectively. The normalized frequency of the source is chosen to be $f_0a_0/c = 0.473$.

Optics EXPRESS

the R from $R > a_0/3$ to $R < a_0/3$. The even edge mode rises while the odd mode declines. As shown in Fig. 4(a), the even mode is above the odd mode inside the band gap when $R = 0.3a_0$, which is opposite to the result shown in Fig. 3(a). If we apply the spin-up source $(\hat{x} - i\hat{y})/\sqrt{2}$ with normalized frequency inside the band gap, it will excite the spin-up edge mode at P_2 as shown in Fig. 4(b). Since the group velocity at P_2 is negative, the wave will propagate along the $-\vec{a}_2$ direction, which is verified by the left part of Fig. 4(c). This indicates both topological and trivial photonic system can form anti-phase boundary and support spin-momentum locked edge modes on the boundary. The source of the same spin can excite wave with opposite propagation directions in these two photonic crystal systems.

3. Band inversion of edge modes when tuning the offset

By tuning the offset t which is defined in Fig. 1(b), we can get a series of dispersion relations as shown in Fig. 5(a) and Fig. 5(b). Since the mirror symmetry is broken for $t \neq -0.5a_0$, we can't define the odd mode or even mode according to the mirror plane. For the trivial unit cell, varying from the anti-phase boundary with $t = -0.5a_0$ to the two dimensional photonic crystal with $t = 0$ will make the dispersion curve get closer to the projected bulk band diagram. The variation of dispersion curves for the structure consisting of topological unit cell is more complicated. As shown in Fig. 5(a), the two dispersion curves converge at the Γ point and form a degenerate point

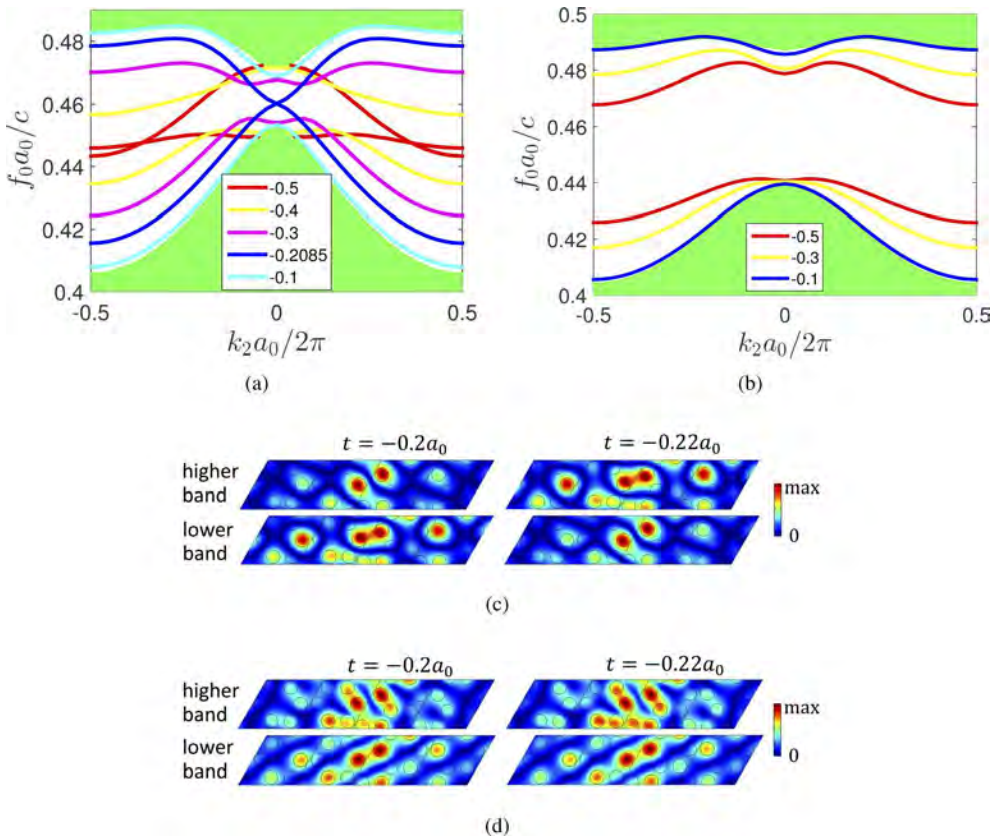

Fig. 5. Dispersion relations of the super-cells with (a) $R = 0.345a_0$ and (b) $R = 0.3a_0$ when tuning the offset t in units of a_0. $|E_z|$ distributions are plotted for the edge modes with $R = 0.345a_0$ when (c) $k_2a_0/2\pi = 0$ and (d) $k_2a_0/2\pi = 0.1$.

Optics EXPRESS

at Γ when the offset $t = -0.2085a_0$. If we continue changing t from $-0.2085a_0$ to 0, the gap between two edge modes reopens and increases until the two curves vanish into the bulk bands.

The band inversion occurs at the Γ point when the offset crosses over the degenerate case $t = -0.2085a_0$. As shown in Fig. 5(c), the E_z distributions in the higher band of the case $t = -0.2a_0$ are the same as the lower band when $t = -0.22a_0$. When k_2 is sufficiently far away from the Γ point, the field distributions look similar in the higher band or lower band for different offsets. We can conclude that only the edge modes that are close to Γ point will be inverted when $-0.5a_0 < t < -0.2085a_0$, which is similar to the band inversion of the bulk modes in [8].

4. Edge modes in gradual shift structure

We can also create an anti-phase boundary by gradually shifting the unit cells on the two sides of the boundary as shown in Fig. 6(a). Here the unit cell with $R = 0.345a_0$ is studied. We can conclude from the dispersion relations shown in Fig. 5(a) that the edge modes which decay rapidly into the bulk can only be found when the offset between the adjacent unit cells is large enough. For the offset with $|t| < 0.1a_0$, the dispersion curves are so close to the bulk band diagram that their energy is not well confined to the boundary. Hence the offset of $t = 0.05a_0$ is chosen between the adjacent unit cells on the two sides of the anti-phase boundary to prevent the appearance of redundant edge modes. The unit cells will look the same if they are far enough from the boundary, which is different from the radical shift structure where the offset difference always exists on the two sides. In this structure, there is no long-range offset between the two sides, only a local shift in the unit cells near the boundary. The dispersion relation and field distribution are shown in Fig. 6(b) and Fig. 6(c) respectively, which is similar to the radical shift case as shown in Fig. 3(a) and Fig. 3(b). The unidirectional propagation of the edge modes can also be found when we excite with sources of different spin directions as shown in Fig. 6(d). The similarity between gradual shift structure and radical shift structure is still valid for the topologically trivial case.

5. Optimization of the source

By optimizing the combination of two orthogonal magnetic dipoles, we can achieve edge modes with better directionality. The magnetic dipole can be defined as:

$$\overrightarrow{m} = \cos\theta\hat{x} + \sin\theta\exp(-i\phi)\hat{y} \tag{1}$$

where $0 < \theta < \pi/2$ and $-\pi < \phi < \pi$. The spin-up $((\hat{x} - i\hat{y})/\sqrt{2})$ and spin-down $((\hat{x} + i\hat{y})/\sqrt{2})$ source mentioned above are the particular cases when θ and ϕ in Eq. (1) are set to $\pi/4, \pi/2$ and $\pi/4, -\pi/2$ respectively.

According to [21], we can also define the directionality of the edge mode by

$$D = \frac{c_+ - c_-}{c_+ + c_-} \tag{2}$$

where $c_+(c_-)$ is the line integration of the Poynting vector measured on the top(bottom) of the structure as shown in Fig. 4(c). If $|D|$ is close to 1, we can conclude that the system has good directionality while no directionality can be observed when $D = 0$. As shown in Fig. 7, the signs of D at the locations of spin-up and spin-down source are opposite for $R > a_0/3$ and $R < a_0/3$, which verifies the conclusion that wave propagates in opposite directions for the same source when we tune the R of the system.

Optics EXPRESS

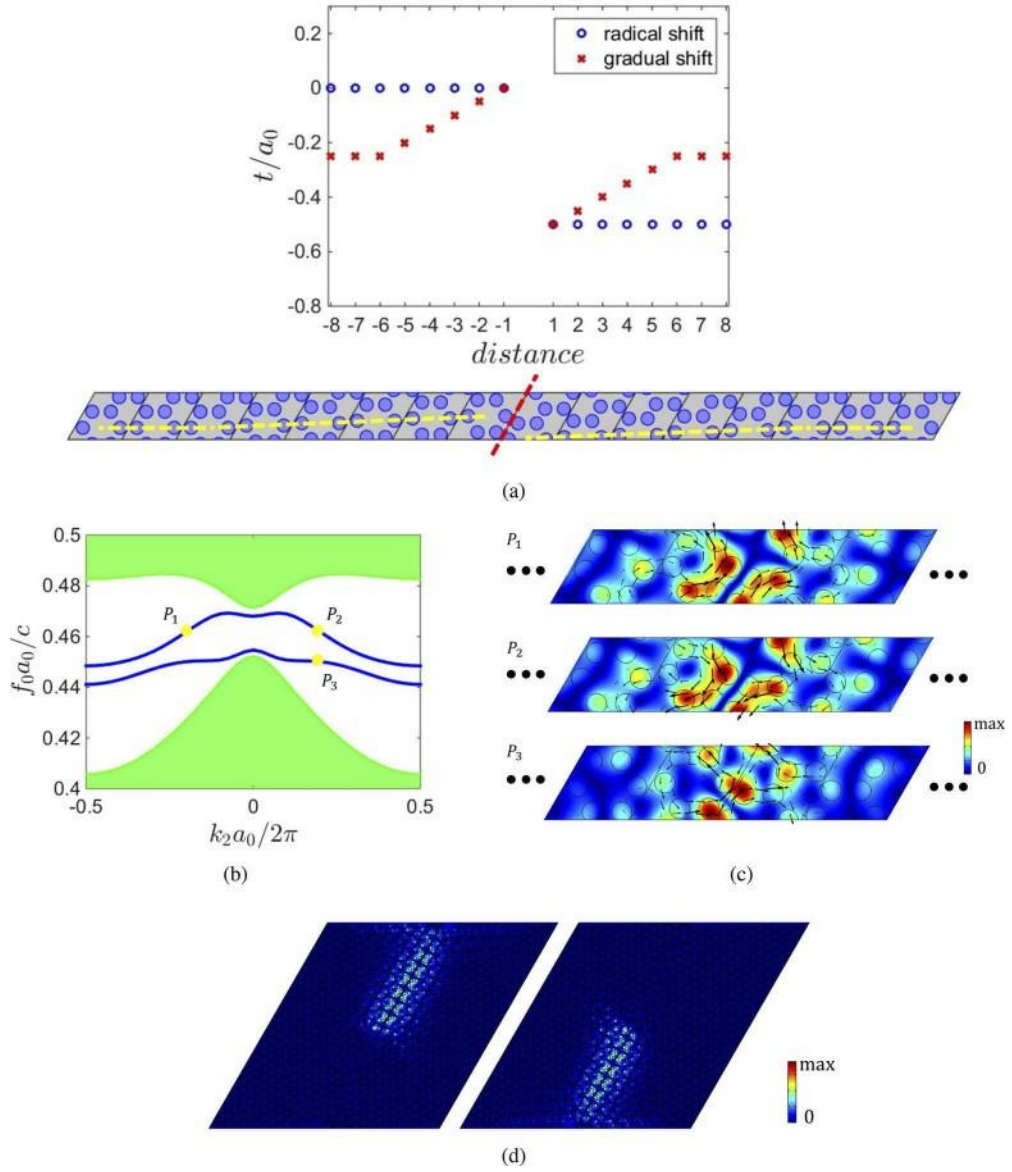

Fig. 6. (a) Comparison between radical and gradual shift super-cell. A shift *oft* = *0.0Sao* is set between adjacent unit cells on the two sides of the boundary marked by red dashed line . The far left with *t* = - *0.25ao* has the same pattern as the far right. (b) Dispersion relation of the gradual shift super-cell when *R* = *0.345ao.* (c) IEzI distributions at points P1 , P2 and *P3* as shown in (b). (d) IEzI are plotted for the driven modes exci ted by magnetic dipole s *(x* - *iy)/Y2* (left) and *(x* + *iy)/Y2* (right) respectively. The norm ali zed frequency of the source is chosen to *be foao/ c* = 0 .462. The source is located at the center of the unit cell with *t* = 0.

Optics EXPRESS

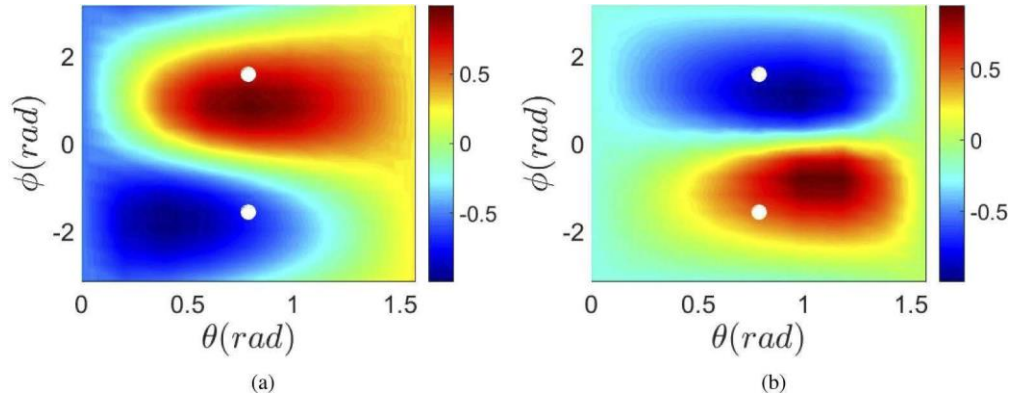

Fig. 7. Directionality *D* defined i n Eq. (2) is plotted as a function of *0* and ¢ for (a) *R = 0.345aoJoao/c* = 0.46 and (b) *R = 0.30ao, fo ao/c* = 0.473. The white dots indicate the locations of the sources *(.x* - iy)/Y2 (upper) and (.x + iy)/Y2 (lower).

6. Conclusion

Spin-momentum locked edge modes are discovered on the anti-phase boundaries which are formed by shifting two halves of a photonic crystal along the direction of periodicity. By applying magnetic dipole sources with different spin directions, we can excite the edge modes propagating in opposite directions. The inversion of the edge modes is revealed when we adjust the distance between the center of the unit cell and the cylinders, which leads to opposite propagation directions with the same source. Also, tuning the offset of the unit cells on two sides can cause band inversion of the edge modes for th e topologically non-trivial photonic crystal system. Optimization of the source gives the edge modes better directionality and helps us to further understand the system, making it more practical for the unidirectional wave propagation applications.

Funding

Air Force Office of Scientific Research (FA9550-16-l-0093); China Scholarship Council (201706230113).

Acknowledgments

The authors acknowledge discussions with D. Bisharat.

Disclosures

The authors declare no conflicts of interest.

References

l. C. L. Kane and E. J. Mele, "Quantum spin hall effec t in graphene," Phys. Rev. Lett. 95(22), 226801 (2005).
2. C. L. Kane and E. J. Mele, "Z 2 topologic al order and the quantum spi n hall effect," Phys. Rev. Lett. 95(14), 146802 (2005).
3. D. Sheng , Z. Weng, L. Sheng , and F. Haldane, "Quantum spi n-h all effect and topologically invariant chem num bers," Phys. Rev. Lett. 97(3), 036808 (2006).
4. M. Konig , H. Buh mann , L. W. Molenkamp, T. Hughe s, C.-X. Liu, X.-L. Qi, and S.-C. Zhang, "The quantum spin hall effec t: theory and experiment," J. Phys. Soc. Jpn. 77(3), 031007 (2008).
5. F. Kuemmeth, S. Ilani, D. Ralph, and P. McEuen, "Co up ling of spin and orbital motion of elect rons in carbon nanotubes," Natur e 452(7186), 448-452 (2008).

Optics EXPRESS

6. A. Soumyanarayanan, N. Reyren, A. Fert, and C. Panagopoulos, "E mergent phenomena induced by spin-orbit coupling at surfaces and in terfaces," Nature 539(7630) , 509-517 (2016).
7. A. B. Khanikaev, S. H. Mousavi, W.-K. Tse, M. Kargarian, A.H. MacDonald, and G. Shvets, "Photonic topological insulators," Nat. Mater. 12(3), 233-239 (2013).
8. L.-H. Wu and X. Hu, "Sch eme for achieving a topological photonic crystal by using dielectric material," Phys. Rev. Lett. 114(22), 223901 (2015).
9. T. Ma and G. Shvets, "Scattering-free edge states between hete rogeneous photonic topological ins ulator s," Phys. Rev. B **95(16)**, 165102 (2017).
10. T. Ozawa, **H. M.** Price, A. Amo, N. Goldman, M. Hafezi, L. Lu, M. C. Rechtsma n, D. Schuster, J. Simon, 0. Zilberberg, and I. Carusotto, "Topologi cal photoni cs," Rev. Mod. Phys. **91(1)**, 015006 (2019).
11. M. Hafezi, E. A. Demler, M. D. Lukin , and J.M. Taylor, "Robust optical delay lines with topological protection ," Nat. Phys. 7(11), 907- 912 (201l).
12. I. Sollner, S. Mahmoodian, S. L. Hansen, L. Midolo, A. Javadi, G. Kirsanske, T. Preg nolato, H. El-E lla , E.H. Lee, J. D. Song, S. Stobbe, and P. Lodah l, " De term inistic photon-emitter coup l in g in chiral photonic circuits," Nat. Nanotechnol. 10(9), 775- 778 (2015).
13. R. Coles, D. Price , J . Dixon , B. Royall, E. Clarke, P. Kok , M. Skolnic k, A. Fox, and M. Makhonin, "Chirality of nanophotonic waveguide with embedded quantum emitter for unidirectional spin transfer," Nat. Commun. 7(1), 11183 (2016).
14. A. B. Young, A. Thijssen , D. M. Beggs, P. Androvitsaneas, L. Kuipers, J. G. Rarity, S. Hughes, and R. Oul ton, "Polarization engineering in photonic crystal waveguides for spin-photon entanglers," Phys. Rev. Lett. **115(** 15), 1 5390 I (2015).
15. T. Van Meche le n and Z. Jacob, "Universal s pin-momentum locking of evanescent waves," Optica 3(2), 118-126 (2016).
16. F. J. Rodrfguez-Fortuiio, G. Mari no , P. Ginzburg, D. O' Connor, A. Martinez, G. A. Wurtz, and A. V. Zayats, "Near-field interference for the unidirectional excitation of electromagnetic guided mode s," Science 340(6130), 328-330 (2013).
17. D. Cohen and C. Carter, "Structure of the (llO) antiph ase boundary in gallium phosphide," J. Microsc. **208(2),** 84-99 (2002).
18. K. Ahn, T. Lockman, A. Saxena, and A. Bishop, "Electronic properties of structural twin and antiphase boundaries in materials with strong electron-lattice couplings," Phys. Rev. B 71(21), 212102 (2005).
19. Z. Wang, H. Guo, S. Shao, M. Saghayezhian, J. Li, R. Fittipaldi, A. Vecchione, P. Siwakoti, Y. Zhu, J. Zhang, and E. W. Plummer, "Designing antiphase boundaries by atomic control of hete roin terfaces," Proc. Natl. Acad. Sci. 115(38), 9485-9490 (2018).
20. X.-K. Wei, A. K. Tagantsev, A. Kvaso v, K. Roleder, C.-L. Jia, and N. Setter, "Ferroelec tric translational antiphase boundaries in nonpolar materials ," Nat. Commun. 5(1), 303l (2014).
21. J. Petersen, J. Volz, and A. Rausch enbeute l, " Chiral nanophotonic waveguide interface based on spin-orbit interaction of light ," Science 346(6205), 67-71 (2014).

A Simulation Technique for Radiation Properties of Time-Varying Media Based on Frequency-Domain Solvers

Zhi-Xia Du, *Student Member, IEEE,* Aobo Li, *Student Member, IEEE,* Xiu Yin Zhang, *Senior Member, IEEE,* and Daniel F. Sievenpiper, *Fellow, IEEE*

Abstract **- *A* novel simulation technique is proposed for the radiation properties of time-varying media. This method divides the time-variation process into finite discrete time steps. The radiation field of the media at each instant in time is simulated by using commercially available frequency-domain solvers, and then these results are processed and synthesized to obtain the radiation field of the time-varying media. In other words, by using this technique, the radiation field of the time-varying media can be obtained based on the frequency-domain simulation results. The proposed technique is introduced with a time-varying grating, and the scattered wave and radiation pattern are illustrated. Moreover, an analytical model of the time-varying grating is also introduced to further explore the proposed technique. This simulation technique can be used to analyze many applications such as the radiation properties of time-modulated media, especially space-time-modulated metamaterials.** It **fills the gap of existing simulation methods and provides a new way for direct EM simulation of time-varying structures.**

Index Terms **- Simulation technique, time-varying media, radiation property, time-domain analysis.**

I. INTRODUCTION

Time modulation has gathered a lot of attention recently since it provides one more dimension to the design of circuits and antennas. Especially, it may greatly extend capabilities for wave manipulation, such as the transmitted and reflected waves by metamaterials and other media. Metamaterials are artificial materials based on suitably designed arrays of complex inclusions with a strong wave-matter interaction in a range of frequencies [l]-[3]. Introducing time variance into metamaterials opens up new capabilities for novel properties [4], [5]. The emerging field of space-time modulated metamaterials is of interest due to their potential for nonreciprocity [6]-[9]. This characteristic can be used in many applications, such as nonreciprocal antennas [10]-[12], circulators [13]-[15], isolators [16], and time-varying transmission-lines [17], [18].

Time-varying media can be analyzed by the methods borrowed and extended from special and general relativity, such as Minkowski spacetime and Lorentz transformations [4]. For example, the sub/super-luminal space-time slabs are described in the Minkowski diagram [19]-[21]. However, these methods are typically only used to theoretically analyze ideal models.

In [22], a relativistic finite-difference time-domain (FDTD) method is proposed to analyze uniformly moving object, which transforms the size of the object and the incident wave between the laboratory frame and the new frame moving with the object by using Lorentz transformation. However, it is not applicable to time-modulated med ia. By introducing the generalized sheet transition conditions (GSTCs), FDTD technique is able to analyze space-time modulated metasurfaces [23]-[25] . In [23], exploiting the periodicity of the surface susceptibilities in both time and space, the Floquet mode expansion method has been used to rigorously compute the scattered fields from the metasurface, by solving generalized sheet transition conditions in combination with Lorentzian surface susceptibilities. In [24], a finite-difference time-domain modeling of finite size zero thickness space-time-modulated Huygens' metasurfaces based on generalized sheet transition conditions is proposed and numerically demonstrated. The metasurface is modeled by the Lorentzian susceptibilities. These analytical methods analyze the ideal simplified periodically-modulated metasurface model with varying material permi ttivity.

In this paper, a novel simulation technique is proposed to analyze time-varying media without simplifying the media to ideal parameters. Usually, due to the time-vanation characteristic of the media, commercially available solvers are hard to directly simulate the radiation properties of the media. Thus in the proposed method, the time-variation process of the media is divided into finite discrete time steps. The radiation field of the time-varying media at each instant in time is simulated by using simulation tools, such as HFSS and CST. Subsequently, the simulation results are appropriately processed and combined to obtain the radiation field of the time-varying media. In other words, this work proposes a new way to simulate time-varying media placed in arbitrary scattering environments based on frequency-domain solutions.

Manuscript received July 24, 2019 , accepted by August 4, 2019.

This work was supported by AFOSR under Grant FA9550-16- l-0093 , and in part by the China Scholarship Council.

Z.-X. Du was with the School of Electronic and Information Engineering, South China University of Technology, Guangzhou 510641, Chin a, and also with the Department of Electrical and Computer Engineering , University of California, San Diego, La Jolla , CA 92093 USA.

A. Li and D. Sievenpiper are with the Electrical and Computer Engineering Department, University of California at San Diego, La Jolla, CA 92130USA.

X. Y. Zhang is with the School of Electronic and Information Enginee ring , South China University of Technology, Guangzhou 5 I 0641, China.

Corresponding author: D. Sievenpiper (dsievenpiper@eng.u csd.edu)

By using this method, we can take advantage of the well-developed and widely-available commercial frequency-domain simulation tools to solve the time-varying problem of actual models . It fills the gap of existing simulation methods and provides a new way for direct EM simulation of time-varying structures. Session II introduces the proposed numerical method with a time-varying grating, including the analysis of the scattered wave and radiation pattern. Session TIT proposes an analytical method for the time-varying grating, and compares the analytical result with the numerical one. Finally, Section IV summarizes the conclusion of the paper.

II. SIMULATION T ECHNIQUE FOR T IME-V ARYING M EDIA

A. Numerical method

A time-varying grating, as shown in Fig. **1,** is analyzed as an example to concisely introduce the proposed method, which is a simplified model of space-time modulated metasur faces. The grating consists of periodic strips in the XY plane with gap *g.* Each strip is constructed by placing the perfect conductor with the width wand length *I* on the substrate of Rogers 4350 with the thickness of 3 mm, dielectric constant of 3.66 and loss tangent of 0.004. The strips are arranged along the *x* direction at *z* = 0. They moves along *x* direction with the velocity *v* within the periodic boundary, which constructs the time-varying grating. In the example, the gap *g*, width *w* and length *I* are 20 mm, 10 mm and 100 mm, respectively. The grating is illuminated by an incident plane wave with an incident angle 0in at 10 GHz.

Firstly, when *v* = 0, the scattered wave of the time-invariant grating can be simulated by using HFSS. The frequency-domain result under the incident wave with initial phase 0° can be considered as the scattered wave at *t* = 0. In this case, the change of initial phase *rp* is equivalent to time variation with the relationship

$$t = \frac{\ldots !£ \_ XT}{360^\circ} \qquad (1)$$

where Tis a time period of the incident wave. In this case, the increasing initial phase *rp* corresponds to the incident wave varying with time *t.* Moreover, the incident wave impinges on the grating, and creates currents, which then radiate . In other words, the grating keeps radiating electromagnetic waves as time *t* goes by. Thus the time-domain wave can be obtained by recording the £-field varying with *t.*

Secondly, when the strips of the grating moves with the velocity *v,* simulating the time modulation, the scattered wave cannot be directly simulated by the existing frequency-domain simulation tools. It should be noted that the "movement" of the strips within the periodic boundary emulates the media with time-varying conductivity. It is a simplified model to clearly show the proposed method. In order to analyze the time-modulated grating, the time-varying process of the grating is divided into finite discrete time steps. The schematic diagram of the time-varying process of the grating is depicted in Fig. 2. At each time step, the strips of the grating move to a new position within the periodic boundary .

The exact procedure of the proposed method to analyze time-modulated media is presented as follows:

1. Divide the time modulation process (at least one modulation period) into discrete time steps with finite instants *(to, t, ...* tn .. . *tm),*
2. Identify the state of the media at each **instantltn-** In the example of the time-varying grating, the strips of which move within the periodic boundary, the displacement dn

$$dn = v \times tn = v \times \frac{\ldots}{3} \times T;n, \qquad (2)$$

where Tin is a time period of the incident wave, and the varying (f)n is the initial phase of the incident wave which simulates the change in time **tn, l v** is the velocity of the strips in the grating which simulates the time modulation. The modulation frequency *fp = 11 Tp = vi(w+g),* where (w+g) is the length of one unit of the time-varying grating.
3. Simulate the scattered field of the time-varying media at each instant tn by using frequency-domain solvers.
4. Set an observation circle around the grating in the scattered field region to extract the electric field strength varying with time tn for different scattering angles 0_5.
5. For each scattering angle 0_5, combine the electric field strength varying with time tn, which relate to the states of the time-varying medium at the corresponding time instants. Numerical computing tools, such as Matlab, can be used to construct the discrete time-domain waveform
6. Calculate the radiation pattern by

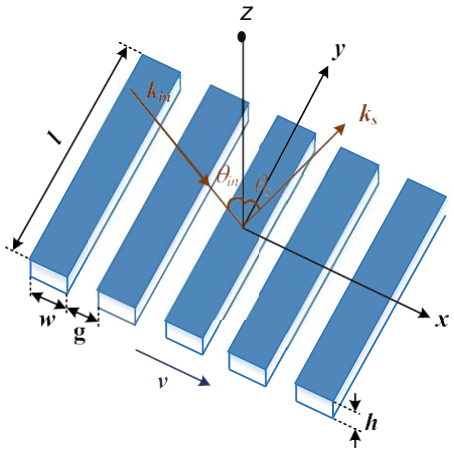

Fig. I. A time-varying grating as an examp le of the proposed method.

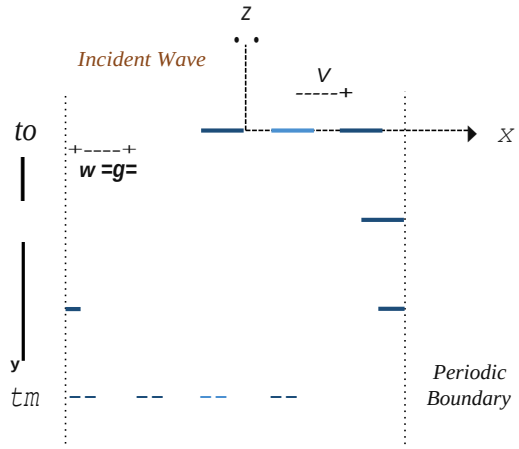

Fig. 2. Schematic diagram of the time-varying process of the grating.

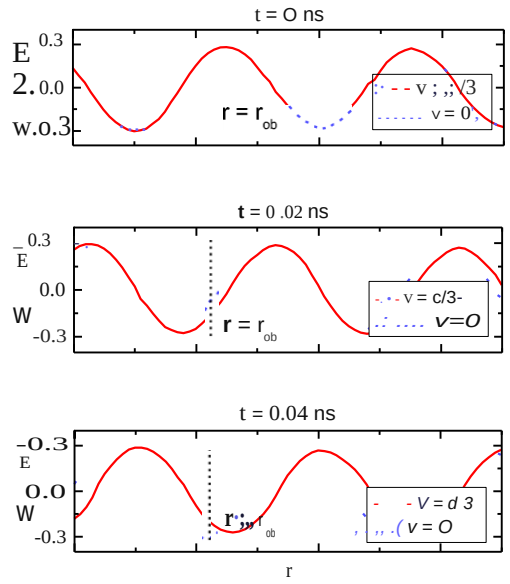

Fig. 3. Scattered wave of the grating along the scattering angle 0s = 70 °with the velocity of v = 0 (blue dash curve) and v = c/3 (red solid curve) at different instants t.

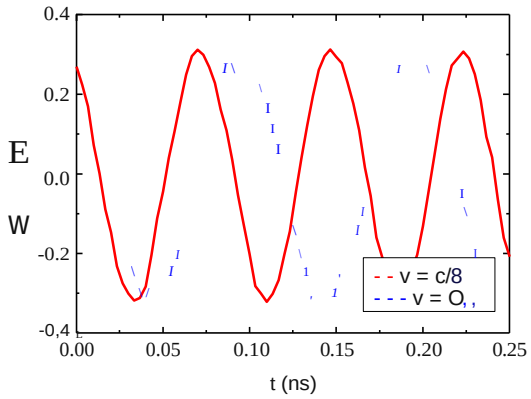

Fig. 4. Time-domain scattered wave of the grating at the observation position fob•

$$|E_{0s}| = \frac{L_{t=to}^{tm} |E0s,tl}{m+1} \quad (3)$$

where Es_0 ,t is the time-domain scattered electric field strength along the scattering angle es. $I\,E_0 5'$ is the average electric field strength along the scattering angle es• It is calculated by adding up the magnitude of the electric fields $IEse,tl$ at different instants tn and then being divided by (m+ l) to calculate the average electric field for each scattering angle es.

For example, when 0in = 0 the scattered waves of the grating along the scattering angle es of7O °at different instants t_{11} is shown in Fig. 3. As seen, the scattered wave of the grating with v = c/3 travels faster than that with v = 0, which means that the electric field varies faster. c is the speed of light. Subsequently, following step 4, the electric field strength varying with time t_{11} is extracted at the observation position rob (e.g. 5),.,). Then the time-domain wave can be constructed by using Matlab according to step 5, as shown in Fig. 4. The red solid curve represents the scattered wave of the grating with v

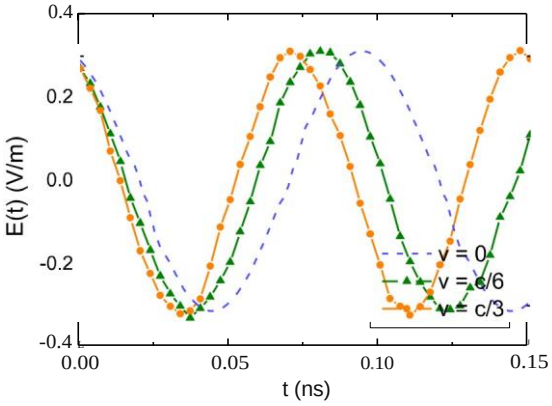

Fig. 5. Time-domain scattered wave of the grating along the scattering angle 0_5 = 70 °with different velocities v.

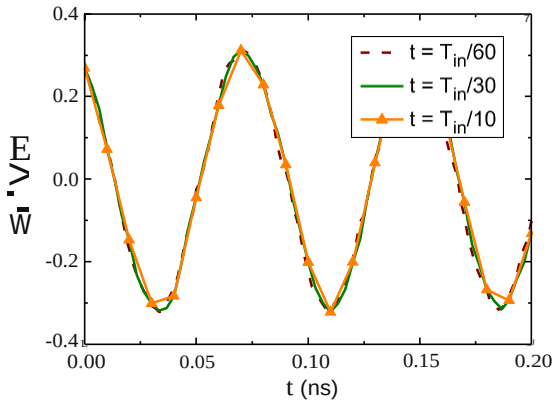

Fig. 6. Time-domain scattered wave of the grating with different time step sizes.

= c/3 while the blue dash curve shows that with v = 0. As observed, the frequency of the scattered wave of the time-varying grating is increased, which is consistent with the Doppler Effect.

When the velocity increases, the compression of the electric field is enhanced. Fig. 5 (a) shows the scattered wave of the grating with different velocities. As the velocity increases, the frequency of the scattered wave becomes higher.

Moreover, the scattered waves obtained by the proposed method with different time step sizes is also depicted in Fig. 6. As seen, the scattered wave with the time step of Tin/ 3O is similar to that with Tin / 6O. Since the smaller the time step size, the greater the computational cost, Tin / 3O is chosen in this example. It is worth noting that the time step size has less effect on the accuracy of the proposed method than that of the FDTD method which uses the iterative algorithm resulting in accumulating errors.

By following step 6, the radiation pattern of the time-varying grating under illumination by a normally incident wave is obtained, as shown in Fig. 7. Its main time-domain scattered waves in the transmission region are depicted in Fig. 8. As seen, the radiation pattern remains unchanged although the grating moves. However, the Doppler Effect occurs in the scattered wave except for components corresponding to the transmitted wave and the specular reflection (zeroth order component). To be specific, in the positive direction of the grating movement, the frequency of the grating becomes

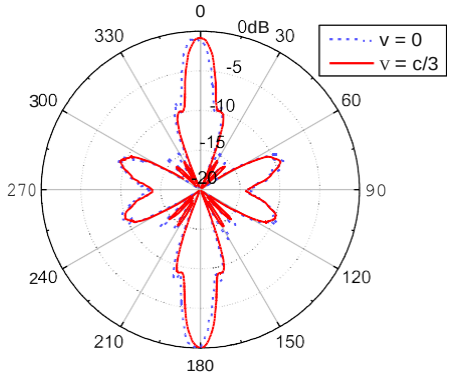

Fig. 7. Normalized radiation pattern of the grating with *w = ')J3* and *g* = 2x')J3 under illumination by a normally incident wave.

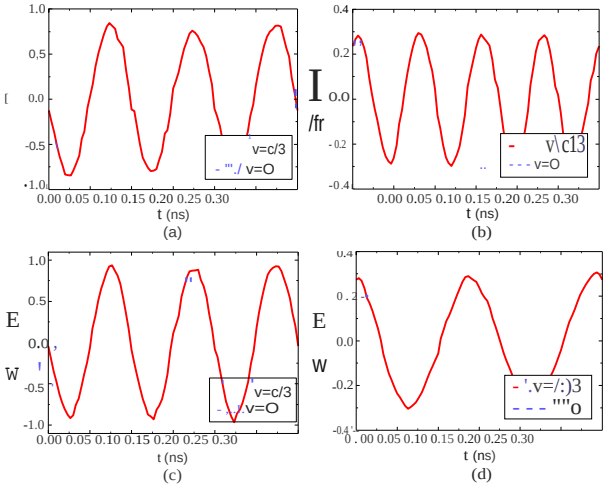

Fig. 8. Scattered wave of the grating with *w = ')J3, g* = 2x')J3 at the radiated angle of (a) 0° (Reflected wave), (b) 110 °, (c) 1 8 0° (Transmitted wave), and (d) 250°.

higher as the velocity *v* increases, as shown in Fig. 8 (b). Meanwhile, the frequency becomes lower in the opposite direction of the grating movement, as shown in Fig. 8 (d).

Besides, the radiation field of the time-varying grating under incident plane wave with an oblique angle can also be easily obtained by using this simulation technique. Fig. *9* shows the normalized radiation pattern of the stationary grating with *w = tJ3, g = 2 x)J3* under the incident plane wave with an angle of 45°. In addition to the reflected and transmitted waves, there are two large scattered waves. Note that they can be suppressed by decreasing the gap *g* from 2xw to *w/2*, which is *tJ6.* Fig. 10 shows the normalized radiation pattern of the grating (g = *2 xtJ 3)* with the velocity ofv = 0 and *v* = c/3. As observed, the radiation pattern remains unchanged although the grating moves. Fig. 11 illustrates the four main scattered waves of the grating. In comparison to the stationary grating, the time-varying grating has the same reflected and transmitted waves, but its scattered waves in other directions exhibit the Doppler shift. Fig. 12 shows the Doppler shift of the time-varying grating as the strips move towards different directions. When the strips in the grating move towards the *+x* direction, the frequency of the scattered waves between the transmitted and reflected waves increases. Meanwhile, the frequency of the scattered waves in the other directions

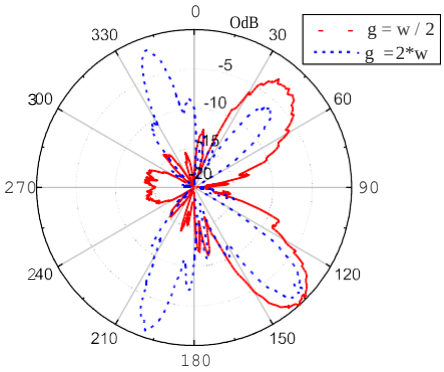

Fig. 9. Normalized radia tio n pattern of two gratings (w = ')J3) with *g* = 2xw and *g* = w/2 under the incident plane wave at the angle of 45 °.

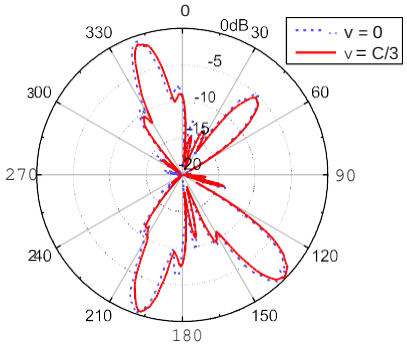

Fig. I 0. Normalized radiation pattern of the grating (g = 2x ')J3) with th e velocity of *v* = 0 and *v* = c/3 under the incident plane wave at the angle of 45

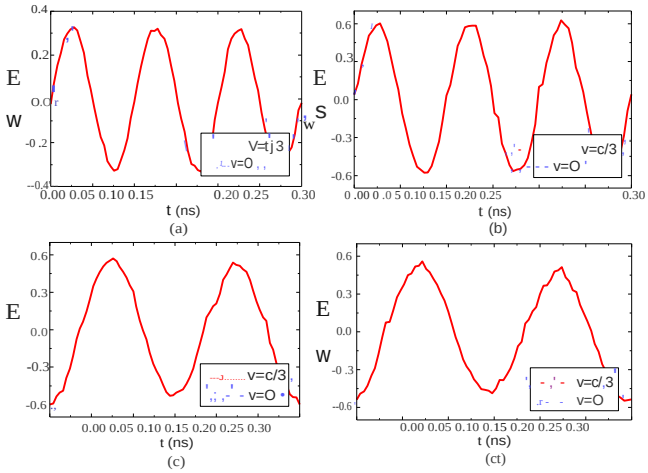

Fig. 11. Scattered wave of the grating with *w = ')J3, g* = 2x')J3 at the radiation angle of(a) 45° (Reflected wave), (b) 135° (Transmitted wave), (c) 200°, and (d) 340°.

decreases. On the contrary, as the strips in the grating move towards the *-x* direction, the Doppler shift performance is reversed. The transmission and reflection directions, rather than the $\pm x$ directions, are the boundary of the Doppler shift.

As analyzed above, the proposed method can be used to perform time-domain analysis based on the results simulated with frequency-domain solvers. It is worth noting that the proposed method focuses on synthesizing the radiation field of the time-varying media at discrete time steps. Thus no matter what the structure of the investigated medium is, as long as it

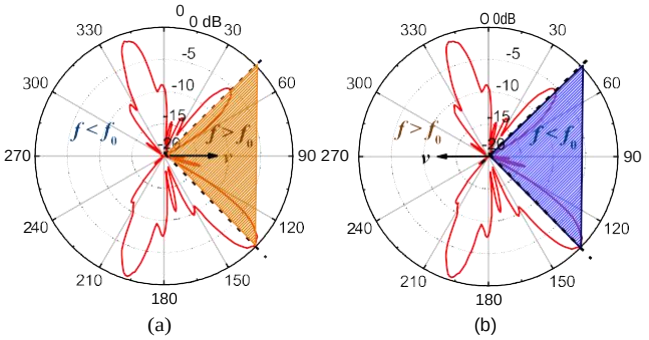

Fig. 12. Doppler shift of the time-varying grating as the strips move towards (a) the +*x* direction and (b) the -*x* direction.

can be modeled in the common simulation tools and its state at each time steps can be identified, the radiation fields at discrete time steps can be obtained and the time-varying problem can be solved by the proposed method . Therefore, the proposed method can be applied to many applications that are impossible or difficult to be directly simulated by the existing sim ulation tools, such as the radiation properties of a time-modulated medium.

B. Comparison

In order to verify the proposed method , a comparison between the numerical result and the scattered field in [24] is made in Table I. Since both methods are proposed to analyze the scattered waves resulting from wave-matter interaction between the input wave and the time-varying medium, the variation from incident wave to scattered wave of the time-varying medium in this work is compared with that in [24]. In [24], a space-time-modulated metasurface is under normally incident pulsed plane wave, resulting in generation of several frequency harmonics (CUJ+ %, CUJ, CUJ-0,\:,, etc.), refracted along different angles. Wp is the pumping frequency. In this work, the main time-domain scattered waves in the transmission region of the time-varying grating has been shown in Fig. 8. As seen, the frequencies of the main scattered waves in the transmission region are about 13.33 GHz (40/3 ;:;; 13.33 GHz, up-converted component), 10 GHz and 6.67 GHz (20/3 ;:;; 6.67 GHz, down-converted component), respectively, while that of the incident wave is 10 GHz. Since the modulation period of the time-varying grating $Ti, = (w+g)/v =$,V(c/3) = 3/fo, where Jo is the frequency of the incident plane wave, the modulation/pumping frequency $J;, = fo/3$ = 10/3GHz ;:;; 3.33 GHz. Therefore, the main spectral components generated by the complex interaction between the incident wave and time-varying grating areJ;,+ $Jo,Jo,J;,-Jo,$ respectively, which agree well with the results in [24]. Note that since the proposed method is based on a frequency-domain solver, like other frequency-domain algorithms, it is less efficient than the time-domain method for multiple frequency input.

Ill. ANALYTICAL MODEL FOR TIME-V ARYTNG GRATING

An analytical method is introduced to further explore the proposed method by using closed-form equations. The time-varying grating is uniform along the *y* direction and

Table T
COMPARISON OF THE MAI N S CATTERED W AVES IN THE T RANSMISSION REGION B ETWEE N REF. [24] AND T HIS WORK

	Up-conversion	Transmission	Down-conversion
Ref. [24] Frequency of the incident wave: [redacted] Modulation frequency [redacted]	-	[redacted]	[redacted]
This work Frequency of the in cident wave: - Modulation frequency: 3.33 GHz	13.33 GHz	10GHz	6.67 GHz

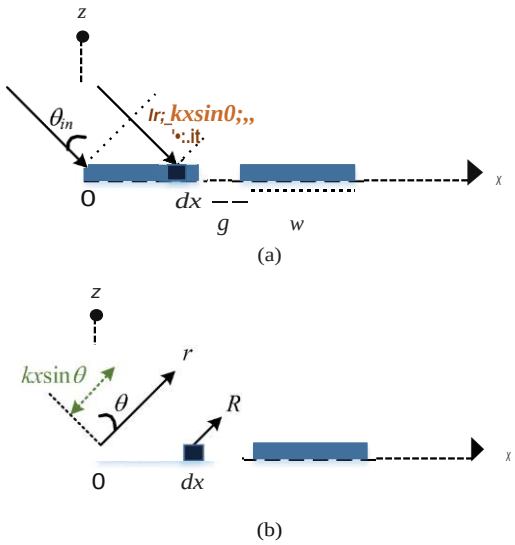

Fig. 13. (a) Incident and (b) scattering phase difference of the electric short dipoles in the stationary grating.

periodic along the *x* direction. Therefore, for simplification, only the plane y = 0 is considered in the following analysis.

A. Analysis of the stationary grating

The simplified model of the stationary grating is shown in Fig. 13. When the linearly polarized plane wave is incident on the conductive strips, electric current is induced which generates the scattered electric field. Thus, each strip can be considered as the combination of electric short dipoles with phase difference. Let1_0 be the amplitude of the electric current induced on a conducting strip for a given incident wave. The scattered £-field of the electric short dipole *dx* in the far field can be expressed as [26]

$$E_{0,dx} \cdot \frac{7/fodx}{r} \cos\theta \; e^{0} \; i(wt-kr) \qquad (4)$$

where *0* is the scattering angle. *ry* is the characteri stic impedance of free space. *A,* oJ and *k* are the wavelength, angular frequency and wave number of the incident plane wave . *r* is the propagation distance of the scattered wave. Moreover, considering the electric short dipole at *x* = 0 as reference, the phase difference of the one at position *x* is

$$\varphi_{in} = e^{-ikx\sin\theta_{in}} \quad (5)$$

as shown in Fig. 13(a). *0;n* is the incident angle. Therefore, by adding up the scattered £-fields of all the electric short dipoles in one conductive strip, the corresponding scattering £-field is

$$E_{\theta,S,O} = i\frac{\eta I_0}{2\lambda r}\cos\theta\int_0^w e^{-ikxsin\theta_{in}}e^{i\omega t}e^{-ik(r-x\sin\theta)}\,dx, \quad (6)$$

as depicted in Fig. 13 (b). Consequently, the scattering £-field of the whole grating at $t = to$ can be calculated as

$$E_{e,s} = \sum E_{e,s,o} = i\frac{\eta TJI}{2..1}\cos 0^{(lw}\int_0^{} f(x)\,dx + \int_{w+g}^{2w+g} f_0(x)\,dx + \ldots)$$

where

$$f_O(x) = e^{-ikx\sin\theta_{in}}e^{i\omega t}e^{-ik(r-x\sin\theta)} \quad (7b)$$

So far, the scattered field of the stationary grating at the instant tis calculated . The radiation pattern can be obtained by normalizing *Eo.s* with time variation at each radiated angle, which is

$$\overline{|E_{\theta,S}|} = \frac{\int_0^T |E_{\theta,S}|dt}{T}. \quad (8)$$

B. Scattered E-jield of the time-varying grating

In the time-varying grating, the conducting strips move along *x* direction. Thus the spatial phase of the electric short dipoles changes with time *t*. To be specific, as time goes by, both the time and space components of the phase of the electric short dipoles vary. As shown in Fig. 14, the phase difference of the electric short dipole at the relative position x' in a conductive strip now becomes

$$\varphi_{M,in} = e^{-ik(x'+v*t_m)\sin\theta_{in}} \quad (9)$$

In this case, the scattered £-field of the moving electric short dipoles in one conductive strip at the instant *tm* is expressed as (10), where [r - (x' + *v* x *tm)* sin 0) is the propagation

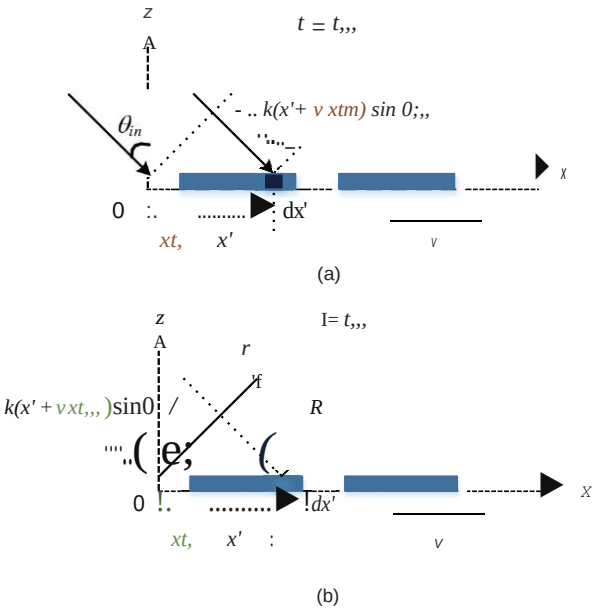

Fig. 14. (a) Incident and (b) scattering phase difference of the electric short dipoles in the ideal analytical model of time-varying grating.

distance *R* of the scattered wave of the electric short dipole at the position x' and scattering angle *0* as depicted in Fig. 14 (b). Likewise, the scattered £-field of the whole time-varying grating can be calculated and the radiation pattern is obtained by following (11). Fig. 15 shows the radiation patterns of the time-varying grating, which are respectively obtained by the proposed numerical technique and analytical model. Since the analytical model is an ideal model of current distribution without considering the substrate below the perfect conductor and the loss of the model, its radiation field is symmetric with respect to X-axis which has slight difference with the numerical result. The four main scattered wave of the analytical model with and without time modulation are illustrated in Fig. 16. The analytical solution of the variation of the scattered waves with or without time modulation is tabulated and compared with the numerical results in Table II. As observed, in both the numerical and analytical methods, the transmitted and reflected waves remain unchanged whether the grating is modulated or not. Meanwhile, for the other two

$$E_{eM} = i\frac{\eta I_0}{2.a.r}\cos 0\int_0^{W_e} \cdot ik(x'+v\ xt\,m)\,sin0\,ineiwt\,e\text{-}ik(r\text{-}(xr+vxtm)sin0)\,dx' \quad (10)$$

$$\left|\overline{Y_{0,M}}\right| = \frac{\int_T^{} |aEe,M,o|dt}{T}$$

$$= i\frac{TJI}{2..1r;'}\cos 0\int_0^{} Jr,\int_0^{w} f_{M,o}(x',t)\,dx' + \int_{w+g}^{2w+g} f_{M,o}(x',t)\,dx' + \ldots\,dt \quad (11a)$$

where

$$f_{M,O}(x',t) = e^{-ik(x'+v\times t_m)\sin\theta}e^{i\omega t}e^{-ik(r-(x'+v\times t_m)\sin\theta)} \quad (11b)$$

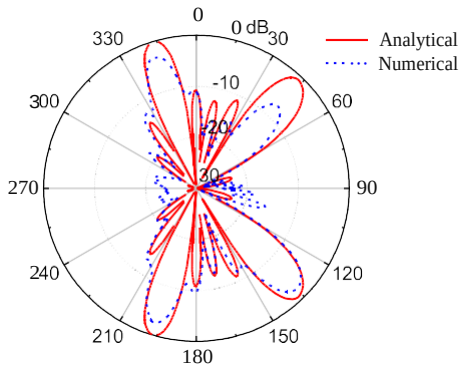

Fig. 15. Radiation patterns of the time-varying grating in Fig. I (numerical technique) and its ideal analytical model in Fig . 14, norm ali zed by the maximum scattered £ -field of the analytical solution (v = c/3, 0.n = 45°, w = *')J3*, g = 2x')J3).

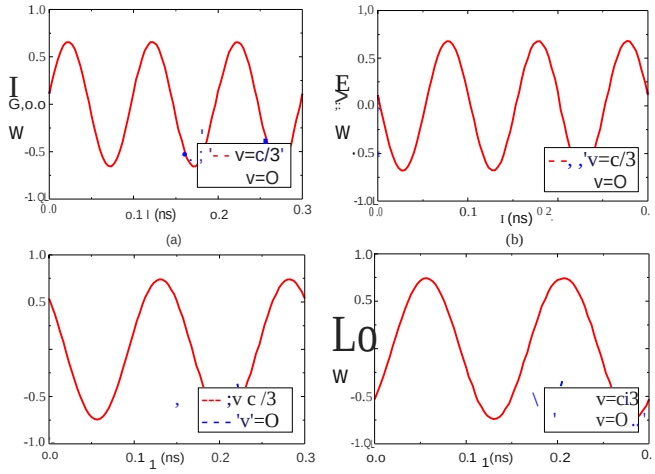

Fig. 16. Scattered wave of the analytical model with w = *')J3,* g = 2x')J3 at the radiation angle of(a) 45° (Reflected wave), (b) 135° (Transmitted wave), (c) 200°, and (d) 340°.

T able II
COMPARISON OF THE VARIATION OF THE S CATTERED W AVES WITH TH E M ODULATION FREQUENCY CHANGING FROM 0 (TIME-INVARIANT) TO 3.33 GHz (TIME MODULATION) BETWEE N THE NUMERICAL AND AN ALYTICAL R ESULTS

Scattering angle 0s	45 ° (Reflected wave)	135 ° (Transmitted wave)	200 °	340 °
Frequency/Sof the scattered wave by using the **Numerical method** (From/ = 0 to/ = 3.33 GHz)	Unchanged (10 GHz)	Unchanged (10 GHz)	From 10 GHz to 6.67 GHz	From 10 GHz to 6.67 GHz
Frequency/Sof the scattered wave by using the **Analytical method** (Fromfr = 0 tofr = 3.33 GHz)	Unchang ed (10 GHz)	Unchanged (IO GHz)	From 10 GHz to 6.67 GHz	From 10 GHz to 6.67 GHz

* Velocity $v = c/3$ corresponds to the modulation frequency of 3.33 GHz.

main scattering directions (*0,* = 200 ° and *0,* = 340 , the frequency ratios of the scattered waves of the time-modulated gratings and time-invariant grating are both 2/3. These methods are proposed to analyze the scattered waves resulting from wave-matter interaction between the input wave and the time-varying medium. The comparison of the variations of the scattered wave changing with the time-varying medium is significant. In this case, the analytical solution and the numerical result agree well with each other.

IV. CONCLUSION

This paper has presented a novel simulation technique to analyze the radiation properties of time-varying media. Since the analysis is based on frequency-domain results from the commercial simulation tools, it can be used to deal with time-varying media with complex structure rather than ideal models. In addition, an analytical model of a time-varying grating has been introduced to further explore the proposed method . Comparison with the existing publication has been made to verify the proposed simulation technique .

Interestingly, the proposed simulation technique allows one to easily study finite-size space-time metamaterials, and hence to design active metamaterials with well-controlled scattering property.

REFERENCES

[I] H.-F. Zhang, X.-L. Tia n, G.-8. Liu and X.-R. Kong, "A gravity tailored broadband metamaterial absorber containing liquid dielect rics," *IEEE Access* , vol. 7, pp. 25827-25835 , Feb. 20 I 9.

[2] 8. Feng, L. Li, Q. Zeng and C.-Y.-O. Sim , "A low-profile metamaterial loaded antenna array with anti-interference and polarization reconfigurable cha racterist ics ," *I EEE Acce ss,* vol. 6, pp. 35578-35589, Jun. 2018.

[3] R. Singha and D. Vakula, " Directive beam of the monopole antenna using broadband gradient refractive in dex metamaterial for ultra-wideband applicat ion ," *IEEE Access* , vol. 5, pp. 9757-9763, May 2017.

[4] A. Alii, "Enhancing metas urfaces and metamaterials with time-modulation and nonlinear responses", in *int. Congress Advanced Electromagnetic Mat. Mierow. Opt.,* Chania, Greece, Sept. 2016, pp. 16-18.

[5] C. Caloz, Z.-L. Deck-L t'ger, and N. Cham anara, "Towards space-time metamaterials", in *int. Congress Engin. Mat. Plat/ Novel Wave Phenom. Cong.*, Marseille, France, Aug. 2017, pp. 40-42.

[6] S. Taravati, "Aperiodic space-time modulation for pure frequency mixing," *Phys. Rev. B,* vol. 97 , p. 115131, Mar. 2018.

[7] N. Chamanara, Z.-L. Deck-Leger, and C. Caloz, "New electromagnetic modes in space-time modulated dispersion-engineered media", *Phys. Rev. A,* vol 97, p. 063829, Jun. 2018.

[8] S. Taravati, B. A. Khan, S. Gupta, K. Achouri, and C. Caloz, "Nonreciprocal nongyrotropic magnetless metasurface," *IEEE Trans. Antennas Propag.*, vol. 65, no. 7, pp. 3589- 3597 , Jul. 2017.

[9] Y. Hadad, D. L. Saunas, and A. Alu, "Space -time gradient metasurfaces," *Phys. Rev. B,* vol. 92, no. 10, p. 100304, Sep. 2015.

[10] S. Taravati and C. Caloz, "Mixer-duplexer-antenna leaky-wave system based on periodic space-time modulation," *IEEE Trans. Antennas Propag.*, vol. 65, no. 2, pp. 442-4 52, Feb. 2017.

[1 I] D. Ramaccia , D. L. Sa un as, A. Alu, F. Bilo tti, and A. Toscano , " Nonreciprocal horn antennas using angular momen tum-b ias e d metamaterial inclusions," *IEEE Trans. Antennas Propag.,* vol. 63, no. 12, pp. 5593- 5600, Dec. 2015.

[12] Y. Hadad, J.C. Saric, and A. Alu, " Breaking temporal symmetries for emission and absorption," *Proc. Nat. Acad. Sci. USA,* vol. 113 , no. 13 , pp. 3471- 3475, Mar. 2016.

[13] R. Fleury, D. L. Saunas, C. F. Sieck, M. R. Haberman, and A. Alu, "Sound isolation and giant linear nonreciprocity in a compact acoustic circulator," *Science,* vol. 343, no. 6170, pp. 516- 519, Jan. 2014.

[14] N. A. Estep, D. L. Sa un as, J. Saric, and A. Alu, "Magneticfree non-reciprocity and iso lation based on parametr ic ally modulated coupled-resonator loop s," *Natu re Phys* ., vol. 10, pp. 923- 927, Nov. 2014.

[15] D. L. Sounas, C. Caloz, and A. Alu, "Giant non-reciprocity at the subwavelength scale using angular momentum-biased metamat erials ," *Nature Commun.* , vol. 4, no. 2407, pp. 1- 7, Sep. 2013.

[16] S. Taravati, N. Chamanara, and C. Caloz, "Nonreciprocal electromagnetic scattering from a periodically space-time modulated slab and application to a quasisonic iso lator," *Physical Review B,* vol. 96, no. 16, p. 165144 , Oct. 2017.

[17] J. R. Reyes-Ayona and P. Halevi , "E lec tromagnetic wave propagation in an externally modulated low-pass transmission line ," *IEEE Trans. Mierow. Theory Techn.*, vol. 64, no. 11, pp. 3449- 3459, Nov. 2016.

[18] S. Qin , Q. Xu, and Y. E. Wang, "Nonreciprocal components with distributedly modulated capacitors," *IEEE Trans. Mierow. Theory Techn.*, vol. 62, no. 10, pp. 2260--2272, Oct. 2014.

[19] Z.-L. Deck-Leger, A. Akbarzadeh and C. Calo z, "Wave deflection and shifted refocusing in a medium modulated by a superluminal rectangular pulse," *Physical Review B,* vol. 97, no. 10, p. 104305, Jan. 2018.

[20] Z.-L. Deck-Leger and C. Caloz, "Sub/Super-lumina l space-time slab: fundamental scattering symmetries ," in *Proc. IEEE int. Antennas Propag. Symp. (APS)* , San Diego, CA, USA, Jul. 201 7, pp. 813-814.

[21] Z.-L. Deck-Leger and C. Caloz , " Sca ttering in superluminal space-time (ST) modulated electromagnetic crystals, " in *Proc. IEE E int. Antennas Propag. Symp. (APS)*, San Diego, CA, USA, Jul. 201 7, pp. 63-64.

[22] F. Harfoush, A. Taflove, and G. A. Kriegsm ann, "A numerical technique for analyzing electromagnetic wave scattering from moving surfaces in one and two dim ensions ," *IEEE Trans. Antennas Propag.*, vol. 37, no. I , pp. 55-63, 1989.

[23] S. Gupta, S. Stewart, and T. Smy, "Space-time modulation induced non-reciprocity in electromagnetic metasur faces," arXiv:1703.10823, Mar. 2017

[24] S. A. Stewart, T. J. Smy, and S. Gupta, "Finite-difference time-domain modelling of space-time modulated metasurfaces," *IEEE Trans. Antennas Propag.*, vol. 66, no. I, pp. 281- 292, Jan. 2018.

[25] Y. Vahabzadeh, N. Chamanara, and C. Caloz, "Generalized sheet transition condition FDTD simulation of metasu rface," *IEEE Trans. Antennas Propag.*, vol. 66, no. 1, pp. 271- 280, Jan. 2018.

[26] C. A. Balanis, *Antenna Theory: Analysis and Design*,, 3 ct ed., John Wiley & Sons, New Jersey , 2005.

Electromagnetic-Dual Metasurfaces for Topological States along a 1D Interface

Dia'aaldinj. Bisharat •: and Daniel F. Sievenpiper

The discovery of topological insulators was rapidly followed by the advent of their photonic analogues, motivated by the prospect of backscattering-immune light propagation. So far, however, implementations have mainly relied on engineering bulk modes in photonic crystals and waveguide arrays in two-dimensional (2D) systems, which closely mimic their electronic counterparts. In addition, metamaterials-based implementations subject to electromagnetic duality and bianisotropy conditions suffer from intricate designs and narrow operating bandwidths. Here, it is shown that symmetry-protected topological states akin to the quantum spin-Hall effect can be realized in a straightforward manner by coupling surface modes over metasurfaces of complementary electromagnetic responses. Specifically, stacking unit cells of such metasurfaces directly results in double Dirac cones of degenerate transverse-electric (TE) and transverse-magnetic (TM) modes, which break into a wide nontrivial bandgap at small interlayer separation. Consequently, the ultrathin structure supports robust gapless edge states, which are confined along a one-dimensional (1D) line rather than a surface interface, as demonstrated at microwave frequencies by near-field imaging. The simplicity and versatility of the proposed approach proves attractive as a tabletop platform for the study of classical topological phases, as well as for applications benefiting the compactness ofmetasurfaces and the potential of topological insulators.

1. Introduction

The discovery of topological insulators [1,2] in condensed-matter systems has promoted extensive research on analogous systems of classical waves including acoustics[3–7] and photonics.[8–10] Uniquely, these systems have insulating **bulk** but conducting interfaces that host chiral one-way[11–15] or helical spin-polarized[16–31] edge states. As a result, wave propagation is immune to backscattering unlike in ordinary photonic circuitry, where realistic fabrication imperfections, disorder, or arbitrary bends could severely reduce signal transmission, hence device performance. The key to this topological protection is interfacing two claddings of different Chern numbers,[32] which characterize the geometrical phase accumulation[33] of the wavefunctions in the reciprocal space. Such an extra phase results in a distinct evolution of the field profiles and it is invariant by any gauge transformation in both broken and conserved time-reversal symmetry-based systems.

Successful photonic implementations based on breaking time-reversal symmetry include using an external magnetic field and gyromagnetic materials in the microwave regime,[11,12] An alternative approach that relies on time modulation for generating a synthetic gauge field[13] with an arbitrary spatial distribution was also demonstrated at near-infrared frequencies using coupled waveguides.[14] However, these systems, which are analogues of quantum Hall topological **insulators**, are notably **bulky** and hard to implement in an integrated platform.[15] In the case of time-reversal-invariant systems, a nonperiodic array of coupled ring resonators was originally proposed, in which the spin degree of freedom is emulated by the rotation of the wave in the rings in clockwise or counter-clockwise directions.[11–&S-11] However, the conservation of pseudospins, which relies on the directional coupling between the rings, necessitates a large ring diameter, hence an extensive footprint of the system. Alternatively, crystalline symmetry could be exploited in photonic crystal structures to give rise to modal degeneracies that play the role of pseudospin states.[19,23] Commonly, the lattice valleys are folded onto the center of the Brillouin zone of a new lattice, thus creating photonic "molecules" supporting hybridized dipolar and quadrupolar circularly polarized eigenmodes. Meanwhile, the expansion (shrinking) of constituent elements in the unit cell causes bandgap opening with nontrivial (trivial) bulk bands. However, the interface of such systems may break the symmetry responsible for the topological order, thus causing the associated topological edge states to become gapped.

A more attractive approach for realizing photonic analogues of the quantum spin-Hall effect (QSHE) is based on the internal symmetry of electromagnetic fields (i.e., EM duality).[24–31] Here,

Dr. D. J. Bisharat, Prof. D. F. Sievenpiper
Electrical and Computer Engineering Department
University of California San Diego
La Jolla, CA 92093, USA
E-mail: dbisharat@eng.ucsd.edu

The ORCID identification number(s) for the author(s) of this article can be found under https://doi.org/10.1002/lpor.201900126

DOI: 10.1002/lpor.201900126

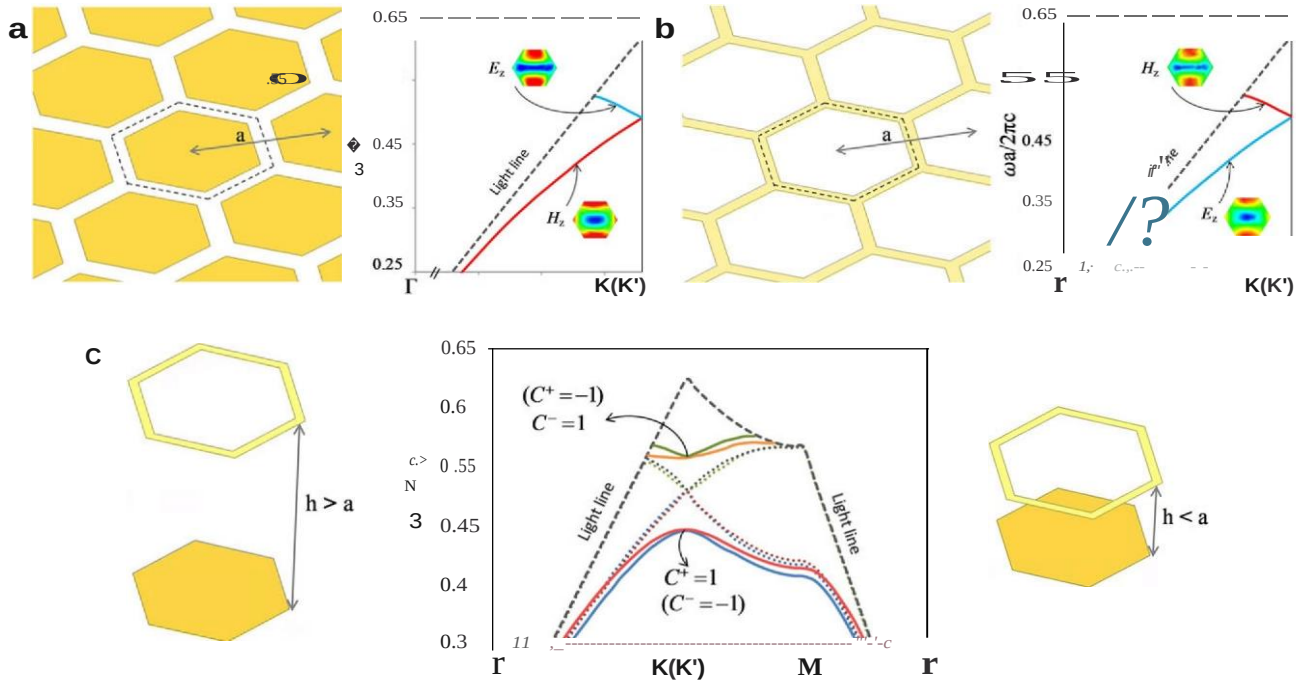

Figure 1. Unit cell design of the dual-metasurface and corresponding band structure. a) Schematic of the patch-type metasurface and the associated band structure. The unit cell is outlined by dashed black line. b) Schematic of the aperture-type metasurface and the associated band structure. c) Schematic of the EM dual-metasurface's unit cell and the corresponding band structure. Bands in the case of large inter-layer separation are marked with dotted lines whereas the bands in the case of small inter-layer separation are marked with solid lines. C+ and C- refer to spin-Chern number for 1/1+ and 1/1- states, respectively. The shown values without (within) parentheses indicate the nontrivial topological invarient is due to Berry phase accumulation around K (K') point.

metamaterials-based unit cells with equal permittivity (ε) and permeability (μ) tensors are used as building blocks for a 2D superlattice. The ε/μ matching condition enables constructing degenerate spin states out of linear combinations of transverse magnetic (TM) and transverse electric (TE) waves, while a bianisotropic coupling between the TE and TM modes plays a role analogous to that of spin-orbit interaction in electronic topological systems and produces a synthetic gauge field that acts separately on the decoupled spin states. However, due to the intrinsic dispersion of bianisotropic metamaterials, demonstrations in both metallic[25–27] and dielectric[28,29] structures at microwave frequencies satisfy the operation conditions only in a narrow frequency range. Furthermore, engineering such topological systems is not straightforward[29,30] and may require cumbersome designs that may be hard to realize in practice[31].

In this work, we demonstrate an ultrathin photonic topological insulator (PTI) based on EM duality, wherein stacking open-boundary metallic metasurfaces (also called designer/spoof surface plasmon crystals) of complementary EM properties naturally cross couples between TM and TE modes. Straightforwardly, the essential modal degeneracies are formed at the high-symmetry K/K' points of the band structure due to the use of hexagonal unit cells, while the strong effective magneto-electric coupling inherent to the overlapped metasurfaces opens a topological nontrivial bandgap over wide frequency range. Importantly, unlike the majority of existing PTIs, including those with finite thickness,[22,26,27,29] the topological phases here arise due to engineering surface waves rather than bulk waves. Consequently, the ensued topological edge modes, which occur at the boundary of such system, are confined along a 1D line[32–34] rather than a 2D surface interface, despite the lack of enclosing structures. In addition, we present a proof-of-concept in the microwave regime and experimentally show backscattering-immune propagation of the gapless edge modes around sharp corners by direct imaging of the near field. Owing to the simplicity, compactness, tunability, and open-boundary nature of the proposed system, it constitutes an attractive platform for photonic topological applications.

2. Results

2.1. EM-Dual Metasurface and Topological Bandgap Opening

Under EM duality symmetry, whereby electric and magnetic fields are treated on equal footing, it is possible to construct pseudo-spin states in the form of orthogonal polarizations.[39] Indeed, under duality transformation of Maxwell's equations, swapping electric and magnetic terms is equivalent to changing one wave polarization for its orthogonal counterpart, indicating that both polarizations propagate similarly.[40] However, except for a vacuum medium, this is not normally the case since unequal ε and μ tensors results in unequal propagation constants for TM and TE polarizations. Nonetheless, it may be feasible to counterbalance this unequal EM response in natural materials if we consider a combination of two media, which act separately on the EM modes in a dual manner, that is, exhibit equal but

opposite effects on the EM fields. Specifically, we employ a patch-type and an aperture-type metallic metasurfaces, as shown in **Figure 1,** which have complementary capacitive and inductive responses, hence support low-order TE and TM propagating surface modes, respectively, with identical wavenumbers qTE = qTM = /q/.[13,41] The thin complementary structures are constructed according to Babinet's principle simply by interchanging the holes and the metal.[14 1 4 2] TM/TE waves here are characterized as having nonvanishing electric/magnetic field components along the z (normal) direction, respectively. Additionally , the metasurfaces are arranged in free-space such that they satisfy a mirror reflection symmetry of the form e(x, y, z) = μ.,(x, y, - z).[13,9, 43 1]

To attain an intuitive understanding of the proposed system, we first consider the two metasurface layers separately. As the band structures shown in Figure 1 indicate, the respective triangular lattices comprising each of the two metasurfaces exhibit identical mode dispersion. Moreover, due to the C_{6v} symmetry of the employed hexagonal unit cells, the two sets of ind ependent TE and TM modes exhibit Dirac cones at the K/K ' points of the first Brillouin zone. Note that the degeneracy of each pair of bands is warranted (i.e., does not require fine-tuning), and the Dirac cones necessarily appear in pairs at each valley of the momentum space. Since the dispersion curves of these modes are below the light line (represented by the grey dashed line), the EM fields are tightly confin ed near the metallic surface in the z-direction. Accordingly, we can stack the two metasurface layers with a finite separation distance (larger than the lattice's period constant), at which the respective EM fields are noninteracting, to constitute one system, which has a fourfold TE/TM degeneracy at the Dirac point. This degeneracy effectively restores the dual symmetry responsible for the topological properties in our system.

Next, we consider the compound metasurface in the case of small inter-layer separation, where the surface modes of each layer interact with each other. This is naturally accompanied by the cross-coupling between the TM and TE modes which introduces an effective bianisotropy to the system. Then, the Maxwell's equations have the form ofv' x E = iw(μ ofiH + xE) and y' x H = - iw(t:o /i E + xH), whereμ =eisassumedandx is an effective magneto-electric coefficient tensor with nonzero elements $x_{xy} = -x_{yx}$. Considering the in-phase and out-of-phase combinations of the TE and TM modes **(1/±1** = Fa**E** ± #O **H)** gives v' x [(μ =F x r [1] V x 1/±] = (w/c)2 (μ ± x)i/1± .[13,1] This set of eigenmodes forms our two decoupled spin states (1/1;;, 1/J ; , t :) (spin-up) and W'1/Ji , 1/1;) (spin-down), which are doubly degenerate in the case of X = 0. On the other hand, finite X value lifts the spin degeneracy at the **K/K'** points and opens a complete bandgap throughout the Brillouin zone, while conserving the spin values for lower and upper bands (marked with solid lines **in** Figure le).

To verify the topological character of the new states, we numerically calculate the spin Chern number of the bands. This is done by evaluating the Berry curvature using the expression **r_i** ± **(k)** = v'k x (1/l; li v'k l1/l;) -z,fromwhichthespinChernnumber is computed as C± = (1/2n) $\int_{BZ}$ r_i±(**k**)**d²k.** Note that it is sufficient to carry out the integration about the points of broken degeneracy (i.e. , K/ K') since the topological properties of the band structure arise from the hybridization of modes near these points. As indicated in Figure le, the lower (upper) modes are characterized by C+ = 1(-1) and C- = -1(1). This implies that the formed bandgap is topologically nontrivial, thus qualifying the metasurface as a PTI. In addition, it is found that the sign of the spin Chern number becomes opposite when the orientation of the two constituent layers of the metasurface is flipped along the z-direction. This could be understood as a result of opposite signs of magneto-electric coupling of the two inverted metasurfaces, causing band inversion mechanism to the respective band structures.

2.2. Spin-Polarized Topological Edge States

The key property of topological structures that distinguishes them from their topologically trivial counterparts is their ability to support propagating modes along the boundary while being exclud ed from the bulk. In particular, edge states emerge between topologically distinct structures in which the (spin-) Chern number changes across the interface. First, we consider an interface between two metasurfaces with inverted structures (i.e., reversed bianisotropy) as shown schematically in **Figure 2.** Conveniently, the two adjacent topological domains share a common bandgap of the bulk. According to the bulk-boundary correspondence, the difference in the magnitude of the spin-Chern numbers across the domain wall (i.e., |Ct - C't.| = 2, |CZ - CR| = 2, where the subscripts *L* and *R* denote left and right PT!s) specifies the existence of a total of four gapless edge states, two with spin-up and two with spin-down, respectively.[12,5] Since the two decoupled spin states are linked by time-reversal symmetry requirement, the state 1/1 (1/1-) with wavevector **+q** has a counterpart **1/1- (1/1 +)** with wavevector **-q** at the same frequency. Hence, the pair 1/1+/-1/1 span the bandgap near the K valley as well as near K' valley of the Brillouin zone.

The counter propagating edge states for Kand K' valleys manifest the spin-momentum locking feature of QSHE, in other words spin-chirality in the absence of inter-spin scattering. As shown in the full-wave numerical simulations in Figure 2c, the selective excitation of 1/1+ /1/1- using proper combination of electric and magnetic dipole point sources (.JsoE$_z$ = #0 Hz or Fa E$_z$ = - #0 H$_z$) proves the pseudo-spin configuration to be uniquely defined by the direction of the mode wavevector (q). In addition, as indicated by the power flux within the hexagonal unit cells in the vicinity of the interface in Figure 2b, the spatial profile of the forward propagating 1/1+ mode is clockwise-rotating (counter-clockwise) in the left (right) region. Meanwhile, this sense of rotations is reversed for the backward-propagating 1/1- mode. This apparent linkage between the spin state and the orbital state in the metasurface emulates spin-orbit coupling in electronic QSHE systems .[12,5] Furthermore, the electric and magnetic field distributions over the cross section of the interface waveguide, which are plotted in Figure 2d, show that the edge mode is concentrated along the line intersection of the thin metasurface films and decays rapidly into the surrounding bulk/surfaces. Uniquely, this characterizes the edge states as lD line waves[3 4 ,35] in contrast to the typical **2D** surface edge states in previously reported PTis,

Edge states can also emerge at the boundary between topologically nontrivial and trivial systems. Hence, we expect to observe the edge modes on the external boundary (side edges) of

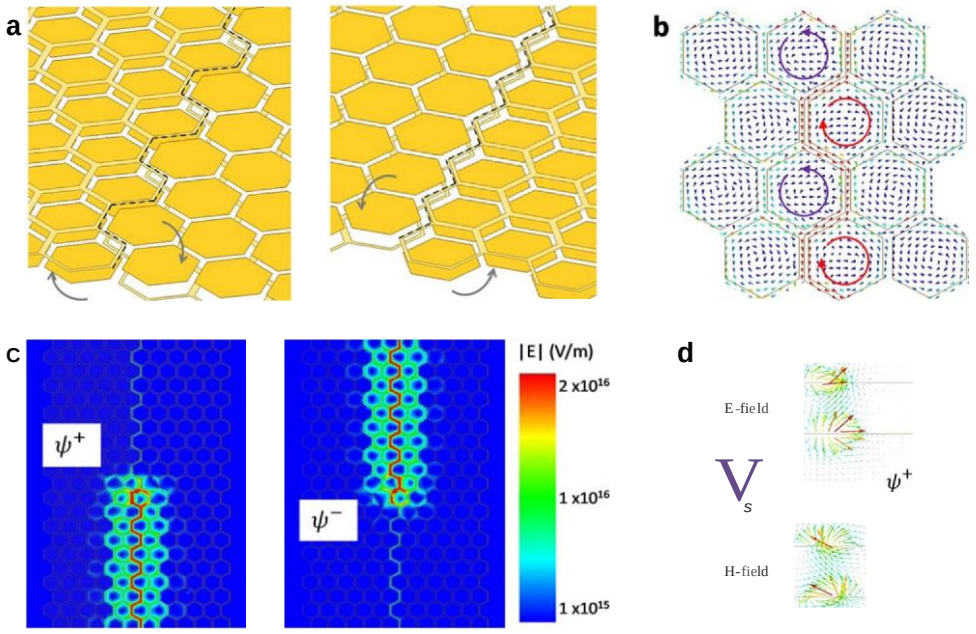

Figure 2. Edge states between topological dual-metasurfaces with opposite signs of effective bianisotropy. a) Schematic of the domain wall between dual-metasurfaces with inverted orientation in the normal (z) direction. Choice of either armchair (left) and zigzag (right) edge boundary is appropriate. b) In-plane power flux (pointing vector) on both sides of the domain wall illustrating the orbital state of the spin-up mode propagating in the forward direction. c) Selective excitation of the spin-polarized edge mode with appropriate electric and magnetic dipole sources showing spin-momentum locking. d) Electric and magnetic vector fields distributions over a cross section of the domain wall showing high localization of the edge mode along the line interface between the inverted dual-metasurfaces.

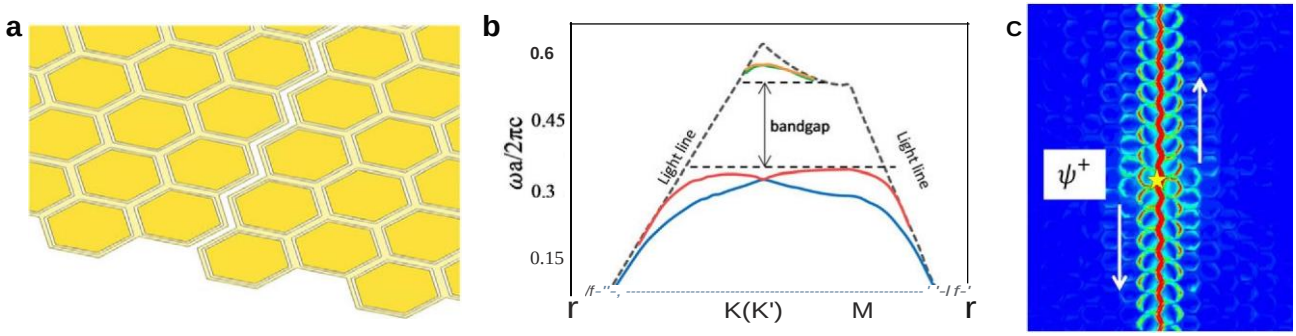

Figure 3. Edge states between topologically nontrivial (dual-metasurface) and trivial (air) domains. a) Schematic of metasurface-air interface made using two identical flat dual-metasurfaces placed side by side with a finite gap in between. b) The band structure of the flat dual-metasurface's unit cell on either side. Large topologically nontrivial bandgap is present despite the patch-layer and aperture-layer not being perfectly complementary to each other. c) Planar surface field distribution across the slot showing excellent localization of the edge modes. The spin state is excited here bidirectionally due to the opposite orientation of the metasurface-air interface across the slot.

the dual-metasurface with air. However, in contrast to electronic systems, the free-space domain does not possess a bandgap as its spectrum is filled with the electromagnetic continuum. Consequently, such modes are not confined and could readily scatter into to the radiative continuum by arbitrary perturbations. To reduce this leakage, we consider introducing a bandgap into the external boundary by placing the metasurface approximately next to another identical metasurface, as illustrated in **Figure 3a.** The two dual-metasurfaces are on the same level (z-coordinate) and are separated from each other by a small slot. Moreover, the metasurfaces are made completely flat (zero thickness) by diminishing the distance between the associated inductive and capacitive metallic layers. This configuration supports two pairs of $y,+/i\dot{f},$, similar to the configuration in Figure 2a, with a pair at each edge across the slot. Here, however, the spin states are excited bidirectionally, as shown in Figure 3c, as the reversal of the air-metasurface interface orientation across the slot entails the reversal of the spin states' propagation direction at the respective edges of the two metasurfaces.

Note that the dimensions of the constituent patch and aperture of the unit cells in the case of the flat dual-metasurface are slightly altered to avoid their spatial overlap. While this makes the inductive and capacitive layers not have the exact band dispersion (i. e., not have perfect EM duality), it is found

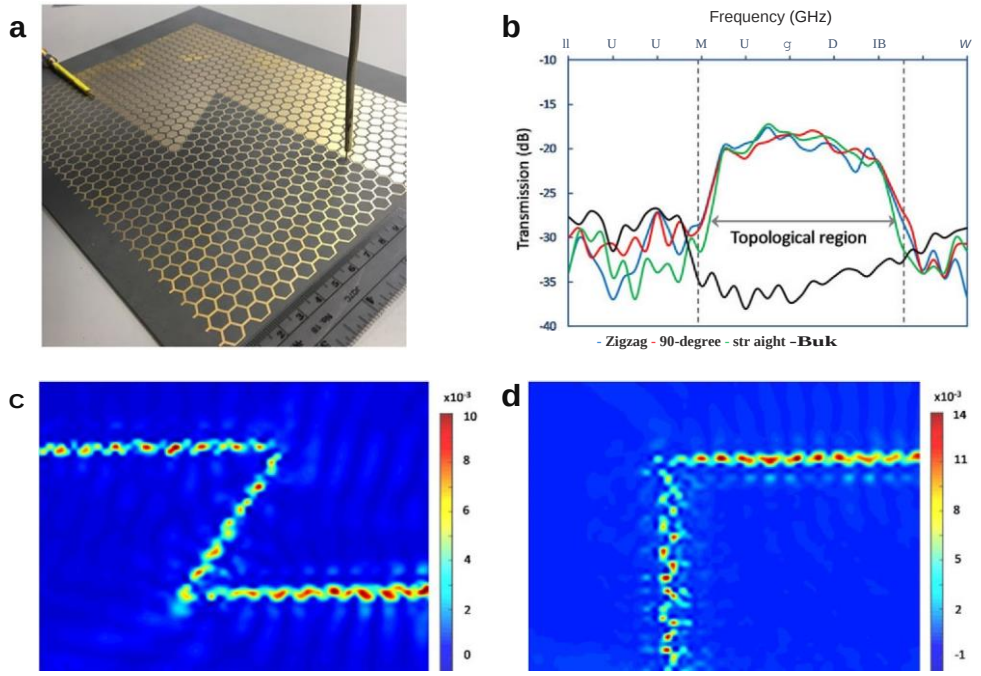

Figure 4. Measured transmission of robust edge states and direct observation via near-field mapping of the surface field distribution. a) Photograph of the fabricated prototype of the dual-metasurface PTI waveg uide , which is made by interfacing two structures with opposite sign of bianisotropy, along with the excitation and detection antennas. b) Transmission data of bulk and edge modes showing the existence of bulk bandgap and the enhanced transmission of edge modes within the bandgap. Here, similar transmission values are observed for straight, zigzag, and 90° waveguides, verifying the robustness of the PTI against sharp bends. c) Measured E_z field distribution at 16 GHz over the surface of a PTI with zigzag interface showing localization of the edge mode at the domain wall and the successful transmission of the edge mode with roughly constant field intensity. d) Measured E_z field distribution at 16 GHz over the surface ofa PTI with sharp 90° corner showing similar localization and transmission features to the zigzag case.

that the compound metasurface remains topologically non-trivial. As can be seen from Figure 3b, the metasurface has a bandgap that covers a wide frequency range (""35% bandwidth), which separates twofold mode degeneracy at K/K' valleys at both the lower and upper bands. The relatively wider bandgap here, which is a manifestation of synthetic gauge field in the system,[12,6] is expected due to the stronger interaction between the surface modes over the constitutive layers, which is inversely proportional to the inter-layer spacing. In addition, this case demonstrates the immunity of the proposed dual-metasurface structure to perturbations to the meta-cells design. In general, the edge modes maintain their topological gapless character as long as the frequency detuning between the Dirac cones of the independent TE and TM modes remains smaller than the topological bandgap opened by the magneto-electric coupling.

2.3. Realization and Observation of Robust Edge Transport

The stability of edge states based on QSHE, as in the proposed system, is generally warranted by the time-reversal symmetry in the absence of spin-flipping processes. This in addition to the spin-chirality feature of the edge states makes PTis attractive for making waveguides that are robust against defects and disorder such as sharp bends. To verify the existence of topological edge states in the dual-met asurface and confirm their robustness, a prototype based on standard printed-circuit-board (PCB) technique was fabricated and tested. The prototype is configured such that the orientation of the complementary metallic patterns is inverted in both lateral and vertical directions across the waveguide interface, as shown in **Figure** 4a (only top layer is visible). The sample has 35-µm-thick copper layers on a 1.57-mm-thick Rogers/Duroid 5880 substrate with permittivity of 2.2 and tangent loss factor of 0.002. The unit cell size (periodic constant) is 7 mm and the width of the slit (strip) of the patch (aperture) is 0.6 mm. The design has a center operating frequency of 16.25 GHz , making the total thickness about 1/12 of the wavelength. Note that the substrate thickness is chosen to provide adequate mechanical support but, in principle, thinner design can be realized instead , which would have advantageously wider bandgap as discussed above.

First, we tested the existence of the topological bandgap by exciting bulk modes with an antenna source placed far from the domain wall. Figure 4b clearly reveals the gap spanning the frequency range 13.9-18.6 GHz, that is, 28.9% bandwidth (marked by dashed lines), which corresponds to the topological region of the unit cell's band structure from numerical simulations (see Section 4). Next, we tested the presence of the topological edge mode by placing the excitation source at the domain wall and measuring the transmission spectrum. We notice enhanced transmission within the bandgap, which is attributed to the excitation of the edge mode. Here, the transmission is roughly steady throughout the middle of the bandgap and decreases toward the lower and upper bulk bands frequencies. The measured results were found to be in good agreement with the full-wave frequency-domain simulations of the entire sample (see Section 4).

Finally, to demonstrate the robustness of the proposed PTI metasurface, we tested waveguides featuring sharp corners of 120° (photographed in Figure 4a) and 90°. The transmission data of the bent waveguides are compared to the straight waveguide case in Figure 4b, which depicts similar performances. To directly visualize the edge modes, we scanned the near-field distribution of electric-field intensity over the upper surface *(xy* plane) of the entire sample area. As shown in Figure 4c, the measured amplitude ratios of E_z show good contrast at 16 GHz (i.e., within the bulk bandgap), with minimum energy away from the domain wall and simultaneously roughly constant amplitude along the zigzag path. This map proves that the wave is indeed guided by the interface line between the two inverted dual-metasurfaces with good localization and negligible scattering losses at the bends. Note that the edge modes are also robust against 90° bends, as demonstrated in Figure 4d, since they could also occur along the armchair edge of the hexagonal metasurface, unlike the so-called valley topological insulators [44–47].

2.4. Discussion

PTis are preferably robust also against lattice perturbations, that is, displacements in the local arrangements of unit cells, which are a common uncertainty in photonic crystals fabrication. Since the topological phase in the proposed system stems from EM duality, which is tied to the local response and basic design of the unit cell,[29] it is immune to such perturbations. This is unlike crystalline topological insulator structures,[19–23] in which lattice disorder and improper edge cuts may break topological protection and open a gap in the edge mode spectrum. In general, breaking the underlying symmetry behind the system's topology leads to the removal of essential degeneracies in the band structure. In our system the same would happen if the duality is violated. However, as discussed earlier, the proposed dual-metasurface is insensitive to perturbations to the meta-cells design as long as the spectral detuning between the Dirac cones of the independent TE and TM modes remains smaller than the topological bandgap open by the magneto-electric coupling.

Compared with other PTis, the proposed metasurface does not require external magnetic field[11,12,15,48] nor bulky structures[14–16,18] for realizing robust edge modes, thus benefiting both large-scale production and applications. Note that the reported design is easily reproducible up to terahertz frequencies,[48–50] where metallic dissipation losses are relatively low. In addition, the planar geometry and ultrathin thickness of the metasurface will facilitate its integration with existing electronic systems. This includes electronic topological insula- tors as well as PTis based on lumped-circuit components.[12,50,51,52] Attractively, the addition of electrical elements to the proposed PCB-compatible design would enable tunable/switchable topological states and reconfigurable pathways.[53] Other elements including mechanical resonators and superconducting Josephson junctions, which are useful for advanced informa- tion processing, could also be included.[54] Furthermore, the considered open boundary nature here is attractive due to the possible interaction between topological modes and free-space waves, which paves a way to metasurface designs with unique topologically endowed scattering characteristics.[55] Additionally, the demonstrated feasibility for scanning the near fields over the metasurface generally allows more direct experimental studies on topological phenomena of classical waves.

Notably, unlike the majority of existing PTis, our design approach relies on engineering surface waves rather than **bulk** waves. Uniquely, the reported edge states are confined along a 1D line rather than a surface interface. Note that common PTis structures are 2D systems, where their interface modes are either free to travel in two dimensions or have an enclosing structure such as parallel plate waveguide for vertical confinement. This makes the proposed design in comparison appealing for energy confinement and transport applications, as a **1D** object being potentially the smallest waveguide possible. Advantageously, this potentially enables topological modes with strong field enhancement, which is beneficial for light-matter interactions. Moreover, the enhanced effective bianisotropy of the dual-metasurface, which stems from the strong coupling between surface waves, creates a bandgap with bandwidth greater than 25% compared to previously reported topological bandgap ofless than 10%.[12,25,31]

3. Conclusion

In summary, we have demonstrated an ultrathin topologically nontrivial metasurface based on EM duality, which emulates QSHE and exhibits directional gapless edge modes. Specifically, we have shown how the EM duality underpinning the necessary spin degeneracies is restored by combining complementary metallic patterns of hexagonal symmetry. We have also shown experimentally by near field mapping robust edge states transport through sharp corners with negligible scattering, a critical concern in conventional waveguides. Unlike existing PTis, our design approach is straightforward and enables broad operating bandwidth and edge states that are notably confined along 1D line interface. This paves the way for planar, compact, and efficient routing and concentration of EM energy endowed by topological properties. The reported metasurface is attractive as a table-top platform for the study of photonic topological phases, as well as for applications benefiting the compactness and versatility of metasurfaces and the potential of topological insulators.

4. Experimental Section

Simulations: All of the full-wave simulations and numerical calculations presented here were performed using commercial software ANSYS HFSS, in which the eigenmodal and driven-modal setups were used. When calculating the bulk (edge) band structure, periodic boundary conditions were imposed on periodic surfaces of the unit cell (supercell). In case of domain wall simulation, the structure was surrounded by vacuum with sufficient distance comparable to the wavelength at the low frequency end.

Calculations of Berry Curvature: When numerically calculating Berry curvature of a point in the reciprocal space, Berry connection was integrated along an infinitesimal square contour around the point. Then, according to Stokes ' theorem, the line integral is equal to the surface integral of Berry curvature over the infinitesimal square that includes the point. Hence, the Berry curvature of the point was the line integral divided by the area of the infinitesimal square. In our numerical calculations , the path integrals were discretized into summations and the side length of the square contour was chosen to be $\delta k = 1/40a$, where a is the period constant .

Measurement Set-Up: A near-field 2D scanning system was used for measu rements. A probe antenna centered at the interface line and

oriented in the direction of propagation of the edge mode was used as the excitation source. Another probe, which is oriented vertically to the surface, was used to scan the relative intensity of normal component of electric-field (E_z) in close proximity to the top surface of the PCB board. In measurements, the source and detector were connected to port l and port 2 of a vector network analyzer and the scattering parameter S2l was recorded, which was proportional to the E_z. The scan resolution in the xy plane was 0.5 x 0.5 mm ^{2}. The total area of the fabricated dual-metasurfaces on both sides of the domain wall was 18 x 24 cm ^{2}.

Acknowledgements

This work has been supported in part by AFOSR grant FA9550- l6- l-0093, and by DARPA contract W9l l NF-17-1-0580.

Conflict ofl nterest

The authors declare no conflict of interest.

Keywords

l D waves, bianisotropy, electromagnetic duality, metasurfaces, topological photonics

Received: April 9, 2019
Revised: June 12, 2019
Published online:

[l] J.E. Moore, *Nature* **2010,** *464,* 194.
[2] X.-L. Qi, S.-C. Zhang, *Rev. M od. Phys.* **2011,** *83,* 1057.
[3] Z. Yang, F. Gao, X. Shi, X. Lin, Z. Gao, Y. Chong, B. Zhang, *Phys. Rev. Lett.* **2015,** *114,* 114301.
[4] X. Zhang, M. Xiao, Y. Cheng, M.-H Lu, J. Christensen, *Comm. Phys.* **2018,** 1, 97.
[5] A. B. Khanikaev, R. Fleury, S. H. Mousavi, A. Alu, *Nat. Commun.* **2015,** *6,* 8260.
[6] S. H . Mousavi, A. B. Khanikaev, Z. Wang, *Nat. Commun.* **2015,** *6,* 8682.
[7] R. Fleury, A. B. Khanikaev, A. Alu, *Nat. Commun.* **2016,** 7, 11744.
[8] L. Lu, J. Joannopoulos, M. Soljacic, *Nat. Phys.* **2016,** 72, 626.
[9] A. B. Khanikaev, G. Shvets, *Nat. Photonics* **2017,** 11, 763.
[10] T. Ozawa, H. M. Price, A. Amo, N. Goldman, M. Hafezi, L. Lu, M. C. Rechtsman, D. Schuster, J. Simon,0 . Zilberberg, I. Carusotto, *Rev. Mod. Phys.* **2019,** 91, 015006.
[II] Z.Wang, Y. Chong, J. Joannopoulos, M. Soljacic, *Nature* **2009,** *461,* 772.
[12] Y. Poo, R. Wu, Z. Lin, Y. Yang, C. T. Chan, *Phys. Rev. Lett.* **2011,** *106,* 093903.
[13] K. Fang, Z. Yu, S. Fan, *Nat. Photonics* **2012,** *6,* 782.
[14] M. C. Rechtsman, J. M. Zeuner, Y. Plotnik, Y. Lumer, D. Podolsky, F. Dreisow, S. Nolte , M. Segev, A. Szameit, *Nature* **2013,** *496,* 196.
[15] B. Bahari, R. Tellez-Limon, B. Kante, *Appl. Phys. Lett.* **2016,** 109, 143501.
[16] M. Hafezi, E. A. Demler, M. D. Lukin, J.M. Taylor, *Nat. Phys.* **2011,** 7, 907.
[17] G. Q. Liang, Y. D. Chong, *Phys. Rev. Lett.* **2013,** 110, 203904.
[18] F. Gao, Z. Gao, X. Shi, Z. Yang, X. Lin, J. D. Joannopoulos, M. Soljacic, H. Chen, L. Lu, Y. Chong, B. Zhang, *Nat. Commun.* **2016,** 7, 11619.
[19] S. Yves, R. Fleury, T. Berthelot, M. Fink, F. Lemoult, G. Lerosey, *Nat. Commun.* **2017,** *8,* 16023.
[20] Y. Li, Y. Sun, W.W. Zhu, Z. W. Guo, J. Jiang, T. Kariyado, H. Chen, X. Hu, *Nat . Commun.* **2018,** 9, 4598.
[21] L.-H . Wu, X. Hu, *Phys. Rev. Lett.* **2015,** *114 ,* 223901.
[22] S. Barik, H. Miyake, W. DeGottardi, E. Waks, M. Hafezi, *New J. Phys.* **2016,** *18,* 113013.
[23] Y. Yang, Y. F. Xu, T. Xu, H. X. Wang, J. H. Jiang, X. Hu, Z. H. Hang, *Phys. Rev. Lett.* **2018,** *120,* 217401.
[24] J.-W. Dong, X.-D. Chen, H. Zhu, Y. Wang, X. Zhang, *Nat. Mater.* **2017,** 16,298.
[25] A. B. Khanikaev, S. H. Mousavi, W.-L. Tse, M. Kargarian, A. H. MacDonald, G. Shvets, *Nat. Mater.* **2013,** 12,233.
[26] W.-J. Chen, S.-J. Jiang, X.-D. Chen, B. Zhu, L. Zhou, J.-W. Dong, C. T. Chan, *Nat. Commun.* **2014,** 5, 5782.
[27] T. Ma , A. B. Khanikaev, S. H. Mousavi, G. Shvets, *Phys. Rev. Lett.* **2015,** *174,* 127401.
[28] A. Slobozhanyuk, S. H . Mousavi, X. Ni, D. Smi rnova, Y. S. Kivshar, A. B. Khanikaev, *Nat. Photonics* **2017,** 17, 130.
[29] A. Slobozhanyuk, A. V. Shchelokova, X. Ni, S. H. Mousavi, D. A. Smirnova, P. A. Belov, A. Alu, Y. S. Kivshar, A. B. Khanikaev, *Appl. Phys. Lett.* **2019,** *114,* 031103.
[30] X.-D. Chen, Z.-L. Deng, W.-J. Chen, J.-R. Wang, J.-W Dong, *Ph ys. Rev. 8* **2015,** 92, 014210.
[3 l] X.-D. Chen, W.-M. Deng, F.-L. Zhao, J.-W. Dong, *Laser Photonics Rev.* **2018,** 12, 1800073.
[32] S. A. H. Gangaraj, M. G. Silveirinha, G. W. Hanson, *IEEEJ. Multiscale Multiphys. Comp. Tech.* **2017,** *2,* 3.
[33] F. Wilczek, A. Shapere, *Geometric Phases in Physics,* World Scientific, Singapore **1989.**
[34] D. J. Bisharat, D. F. Sievenpiper, *Phys. Rev. Lett.* **2017,** 119, 106802.
[35] X. Kong, D. J. Bisharat, G. Xiao, D. F. Sievenpiper, *Phys. Rev. A* **2019,** 99, 033842.
[36] S. A. R. Horsley, I. R. Hooper,). *Phys. 0: Appl. Phys.* **2014,** *47,* 435103.
[37] D. J. Bisharat, D. F. Sievenpiper, *Nanophotonics* **2018,** 7,893.
[38] D.R. Mason, S. G. Menabde, S. Yu, N. Park, *Sci. Rep .* **2015,** *4,* 4536.
[39] W.-J. Chen, Z. Q. Zhang, J.-W. Dong, C. T. Chan, *Nat . Commun.* **2015,** *6,* 8183.
[40] K. van Kruiningand, J.B. Gotte,J. *Opt.* **2016,** *18,* 085601.
[4l] T. Zentgraf, T. P. Meyrath, A. Seidel, S. Kaiser, H. Giessen, C. Rockstuhl, F. Lederer, *Phys. Rev. B* **2007,** *76,* 033407.
[42] H. U. Yang, R. L. Olmon , K. S. Deryckx, X. G. Xu, H. A. Bechtel , Y. Xu, B. A. Lail, M. B. Raschke, *ACS Photonics* **2014,** 1, 894.
[43] M. G. Silveirinha, *Phys. Rev. B* **2017,** 95, 035153 .
[44] T. Ma, G. Shvets, *Newj. Phys.* **2016,** *18,* 025012.
[45] Z. Gao, *Phys. Rev. B* **2017,** 96, 201402(R).
[46] X. Wu, Y. Meng, J. Tian, Y. Huang, H. Xiang, D. Han, W. Wen, *Nat. Commun.* **2017,** *8,* 1304.
[47] J. Noh, S. Huang, K. P. Chen, M. C. Rechtsman, *Phys. Rev. Lett.* **2018,** *120,* 063902.
[48] S. A. H. Gangaraj, A. Nemilentsau , G. W. Hanson, *Sci. Rep .* **2016,** *6,* 30055.
[49] B. S. Williams, S. Kumar, H. Callebaut, Q. Hu, J. L. Reno, *Appl. Phys. Lett.* **2003,** *83,* 2124.
[50] G. Kumar, S. Pandey, A. Cui, A. Nahata, *NewJ. Phys.* **2011,** *13,* 033024.
[5 l] C. H. Lee, S. Imhof, C. Berger, F. Bayer, J. Brehm, L. W. Molenkamp, T. Kiessling, R. Thomale, *Comm. Phys.* **2018,** 1, 39.
[52] Y. Wang, L.-J. Lang, C. H. Lee, B. Zhang, Y. D. Chong, *Nat. Commun.* **2019,** 10, 1102.
[53] X. Cheng, C. Jouvaud, X. Ni, S. H. Mousavi, A. Z. Genack, A. B. Khanikaev, *Nat. Mater.* **2016,** 15,542.
[54] V. Yannopapas, *Newj. Phys.* **2012,** *14,* 113017.
[55] M.A. Gorlach, X. Ni, D. A. Smirnova, D. Korobkin, D. Zhirihin, A. P. Slobozhanyuk, P.A. Belov, A. Alu, A. B. Khanikaev, *Nat. Commun.* **2018,** 9, 909.

Adiabatic Mode-Matching Techniques for Coupling Between Conventional Microwave Transmission Lines and One-Dimensional Impedance-Interface Waveguides

Zhixia Xu,[1,2] Xiaoxing Yin,[1] and Daniel F. Sievenpiper[2]

[1] *State Key Laboratory of Millimeter Waves, Southeast University, Nanjing 210096, China*

[2] *Electrical and Computer Engineering Departm ent, Univ ersity of California, San Diego, California 92093, USA*

(Received 13 March 2019; revised manuscript received 3 April 2019; published 22 April 2019)

Waveguides consisting of artificial media based on periodic stmctures at the subwavelength scale are a major open topic in contemporary applied physics and engineering. Recent research efforts focus on the prope1iies of guided modes in artificial stmctures. However, as the cornerstone of applications, matching techniqu es between these interesting waveguides and traditional wave guides deserve more attention. We report a broadband adiabatic mode-matching technique for efficient coupling between conventional microwave transmission lines (a coplanar waveguide and a slotline) and one-dimensional (ID) interface waveguides consisting of transverse-electric (TE) and transverse-magnetic (TM) artificial imped ance surfaces. The transverse electromagnetic (TEM) mode is adiabatically transfonned to the line wave mode at the ID impedance-interface. Proposed matching techniques open up avenues for applications of various impedance-interface waveguides.

DOI: 10.1103 /PhysRevA pplied.l l.044071

I. INTRODUCTION

As solutions of Maxwell' s equations, guided waves at the interface of two different materials that decay away from the interface have been studied for decades [1]. Surface plasmons, Dyakonov-Tamm waves, and Zenneck waves can all be treated in a unified form [2,3]. With a peak field bound at the interface, these waves are attractive for communication and sensing applications [4]. In order to utilize waves at interfaces of different media, various waveguides have been invented. Goubau lines [5- 7] as well as spoof surface plasmons [8- 11] support waves at the interface of metals and dielectrics. Dielectric waveguides [12,13], such as fibers, support waves at the interface of dielectrics with different pennittivity. Based on the concept that the local intensity of guided waves can control the wavevector, nonlinear waveguides have been attractive for decades for their multiplicity of applications to all-optical signal processing systems [14--17]. Photonic crystals support waves along the interface of two photonic crystals with overlapping band gaps [18,19]. Topological insulators support waves at the interface of trivial and nontrivial materials in topological space [20,21]. In the past several years, researchers have found a different one-dimensional (1D) impedance-interface mode called a line wave (LW) mode at the interface of two planes with different surface impedances from microwave to optical bands [22- 24]. Further research focusing on similar waveguides has been reported recently [25,26]. LW modes show robustness with wave-vector-locked states as well as field confinement ability. Compared to photonic crystals based on overlapping narrow energy gaps, LW modes have a very broadband transmission feature. However, this also brings a drawback: without overlapped band gaps, surface waves can propagate in any direction on the two surrounding impedance surfaces. Thus, it is difficult to excite a pure LW mode with suppressed surface waves on both sides. Previous methods to excite and detect the LW mode were based on probes fabricated at the interface with a weak coupling efficiency [23]. Therefore, it is meaningful to develop mode-matching techniques for coupling LW modes with higher efficiency in order to further implement these impedance-interface waveguides into systems.

Coupling techniques based on interference theory or adiabatic gradual changes are widely used to solve coupling tasks between different waveguides. Interference-based methods utilize multiple reflections in several matching stages, where destructive interference of reflected waves is achieved [27- 30]. The physical size of each matching stage determines the working frequency. Thus, a main concern to utilizing these interference-based approaches is the limited working bandwidth. Gradual changes, also known as adiabatic transitions, slightly modify the structure between two different modes [31- 33]. Passing through

*230l 59363@seu.edu.cn

10l 010074@seu.edu.cn

t dsievenpiper @eng.ucsd.edu

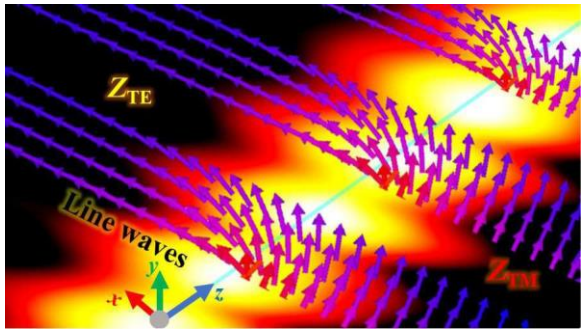

FIG. 1. The schematic of the LW mode propagating along the interface between Zrn and ZrM impedance surfaces, arrows represent the electric vectors. Metallic patches (grids) are designed to realize a Zrn (Zr M) impedance surface.

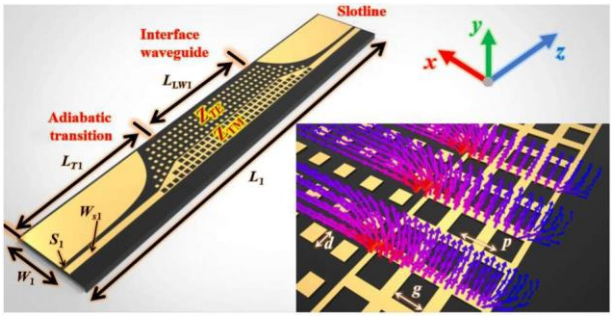

FIG. 2. Schematic of adiabatic transitions between a slotline and a TE-TM impedance interface waveguide (LW guide), where the inset shows the detail of the structure and the electric field vector distribution characteristic.

these structures, initial modes gradually transform into the target modes with low reflection within a wide bandwidth. When the unperturbed waveguides have continuous structure, the adiabatic condition could be easily fulfilled by continuously varying the waveguide structures along the propagation direction. However, when facing a complex waveguide with periodically distributed unit cells at the subwavelength scale, it is not clear how one could achieve the required smooth transitions. In the past, pioneers have solved matching tasks between guided modes in photonic waveguides [34,35] and spoof surface plasmons [5,9,36], as well as surface waves on arbitrary impedance surfaces [37].

In this work, adiabatic matching transitions between conventional transmission lines, a slotline, a coplanar waveguide (CPW), and a 1D transverse-electric (TE) and transverse-magnetic (TM) impedance-interface waveguide is proposed. The smooth bridge consists of gradually changing TE-TM impedance surfaces and a flaring ground plane, matching the momentum and impedance of the transverse electromagnetic (TEM) mode and the LW mode. Samples are fabricated and measured. Simulated and measured S parameters and near-field distributions, as well as the dispersion diagram, demonstrate the existence of the LW mode after adiabatic transitions. Our research paves the way to implement LW modes into systems with hybrid guiding structures. Although the proposed designs operate at microwave bands, some recent work on LW modes based on plasmonic and flat graphene structures has been reported at higher frequency bands [22,26]. Therefore, the proposed methodology can also open a door to develop mode-matching techniques in integrated circuits at terahertz and optical bands.

II. RESULTS AND DISCUSSION

A. Physical concept of the LW mode

As shown in Fig. 1, we start by briefly introducing LW modes. Additional details about LW modes have been discussed before [23]. An electromagnetic mode can be supported by an impedance surface with an exponential decay e^{-ay} away from the surface and a propagation function e^{-ikz}. The surface impedances for TE and TM polarized waves are [18,24,37]

$$Z_{TE} = -j\eta_0 \frac{k}{\alpha}, \tag{1}$$

$$Z_{TM} = j\eta_0 \frac{\alpha}{k}, \tag{2}$$

where η_0 is the intrinsic impedance of free space, k is the wave number in free space, and α is the decay rate away from the surface. At a perfect electric and magnetic

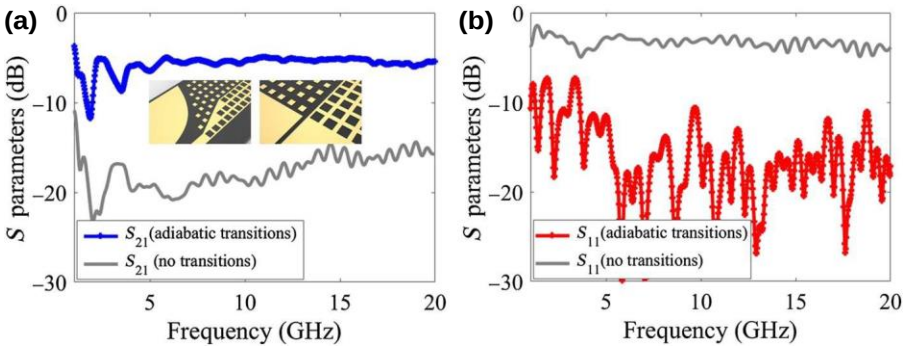

FIG. 3. (a) Simulated S_{21} and (b) S_{11} with and without adiabatic transitions between the slotline and LW guide.

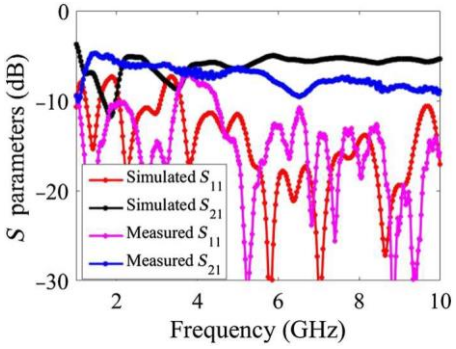

FIG. 4. S parameters of the slotline-LW guide.

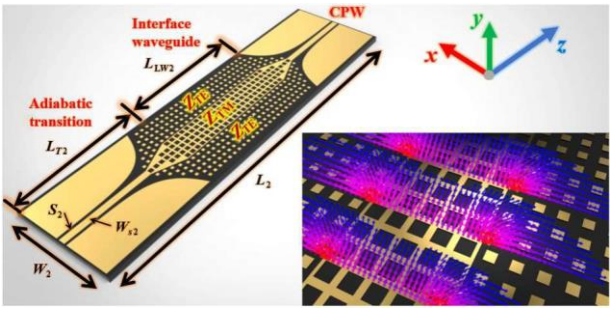

FIG. 6. Schematic of the adiabatic transition between a CPW and a LW guide, where the inset shows the detail of the structme and the electric vector distribution characteristic.

boundary condition, the tangential electric and magnetic fields vanish separately. Thus, only the TE and TM surface modes exist and the hybrid localized mode, the LW mode, appears at the interface of two surfaces with different impedances . Using cylindrical coordinates, the wave form of the LW mode can be deduced based on Bessel functions as

$$Ez = E_0 K_{1;2}(ap)\sin(\quad) \quad e\text{-}.if3z, \tag{3}$$

$$H_{z} = \frac{E_o}{ryo} K_{1\ 2}(ap)\cos\left(\frac{f}{2}\right) e\text{-}.if3z\_ \tag{4}$$

Figure 1 clearly indicates features of the electric field of the LW mode. The field decays away from the interface at different angles with a similar rate. Note that the electric field on the ZTM surface has a strong component toward the *y* axis, and the electric field on the Zrn surface has strong components toward the *x* axis, while at the interface, the electric field shows a rotational distribution.

B. Adiabatic transitions between the slotline and the impedance-interface waveguide

According to the field distribution characteristics at the interface of two impedance surfaces, it is natural to choose the TEM mode suppmted by a slotline as the unperturbed original mode. The electric fields of both modes at the interface are distributed along the *x-o-y* plane. The main difference is the field penetrating into both sides of the impedance surfaces, which could be matched smoothly. In quantum physics, when the Hamiltonian of a system changes slowly, eigenmodes at any instant of time can be adiabatically transformed into different eigenmodes at a later time. Similar concepts can be applied in the electromagnetic field. When the geometry of a waveguide is gradually changed along the propagation direction, the fundamental mode can be adiabatically changed into another fundamental mode with a slightly different field distribution. Using this concept, we design a transition to match the slotline to the TE-TM impedance-interface waveguide, as shown in Fig. 2. The transition is designed to have a flaring ground plane on one side, described as $x = C1\ e^{\ 2} + C2$ where $C1 = (x2 - x1)/(e^{22} - e^{21})$ and $C2 = (x1e^{22} - x2ea^{21})/(ez^{2} - e^{21})$, a=0.1, and (z1, X1) and (z_2, x2) are the starting and ending points, respectively. The total length of the strncture L_I is 240 mm, the length of transition Ln is 76 mm, the length of the interface waveguide *LLw1* is 88 mm, the total width *W,* is 32 mm, the slot width S_1 is 0.08 mm, and the patch width Ws_1 is

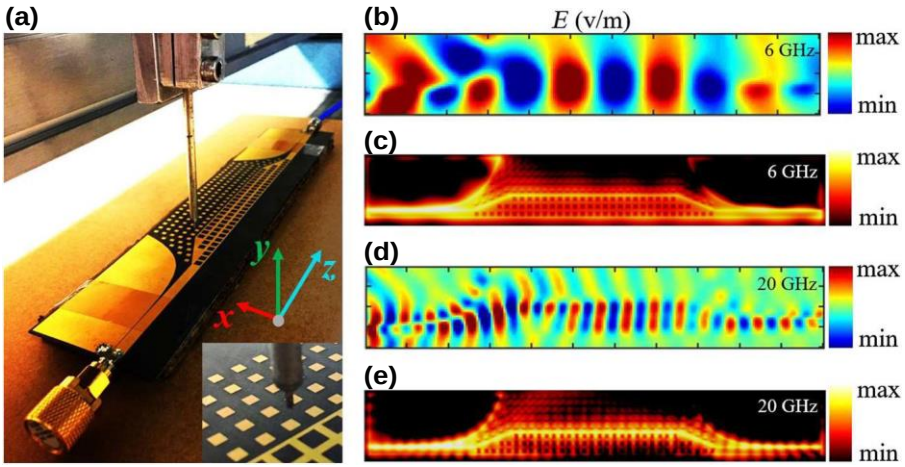

FIG. 5. (a) Photograph of the near-field scan where the electric probe is positioned 1 mm above the sample, and the inset at the comer shows the detail of the probe. (b) Measured £, distributions at 6 GHz. (c) Simulated electric field distributions at 6 GHz. (d) Measured £ 2 distributions at 20 GHz. (e) Simulated electric field distributions at 20 GHz.

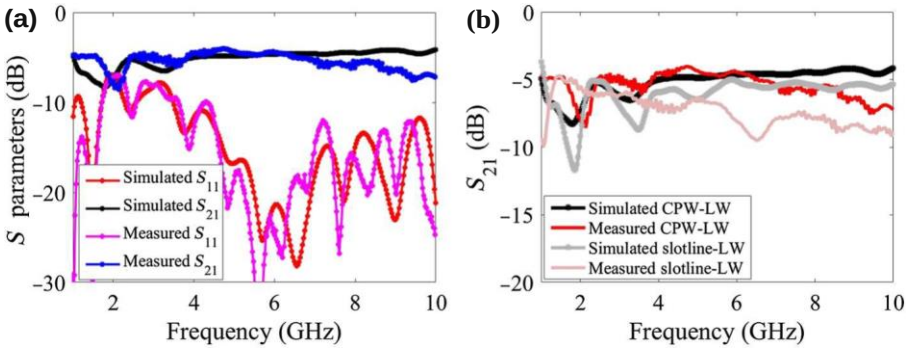

FIG. 7. (a) Simulated and measured S parameters of the CPW-LW guide. (b) Comparisons of s 21 between CPW-LW and slotline-LW guides.

4 mm. We design periodic grid and patch arrays to realize inductive and capacitive responses, supporting TM and TE modes, respectively, as labeled in Fig. 2. The lattice constant p is 4 mm, the geometric parameters of the unit cells d and g are 1.8 and 2.8 mm, respectively. The substrate is 0.8-mm thick Rogers 5880 whose pennittivity is 2.2 with 0.035-mm thick copper above it.

We show the simulated S parameters of the proposed structures in Fig. 3. As a comparison, results of structures without adiabatic transitions (directly connecting the slotline with the interface waveguide) are also shown. Without adiabatical transitions, most of the energy is reflected back at the abrupt connections with very low transmission efficiency. While using the adiabatic transitions, the reflection is suppressed and the transmission efficiency is increased dramatically, providing the smooth transfonnation from the TEM mode to the LW mode by adiabatic pe1turbation. S parameters measured by a network analyzer (Agi- lent Technologies E5071) are shown in Fig. 4. At low frequencies, simulations and measurements match well, but as the frequency increases the transmission efficiency decreases gradually due to errors likely brought on by fabrication tolerances. In order to achieve the 50-Ohm characteristic impedance of the slotline, the width of the slot is only 0.08 mm and the impedance is very sensitive when soldered to the connectors, especially at high frequencies.

Although only S parameters below IO GHz are presented due to the limitation of connectors, we can still further estimate field distributions at higher frequency bands within the desirable area, ignoring the reflection loss from connectors on both sides. Figure 5(a) shows the photograph of the near-field scan. One port of the sample is connected to a broadband matching load and the other port of the sample is connected to the first port of the network analyzer whose second port is connected to the electric probe d1iven by a motor to scan the target area. Measured and simulated electric field distributions at 6 and 20 GHz are shown in Figs. 5(b}-5(e). It is difficult to discern the LW mode at 6 GHz from measurements, while the simulated profile of the total electric field indicates the existence of the LW mode along the ID interface. In order to better understand the difference, investigatin g the electric vector distributions of the LW mode in Fig. 2 is instructive. The probe detects the electric field primarily toward the y axis. Therefore, more energy above the TM

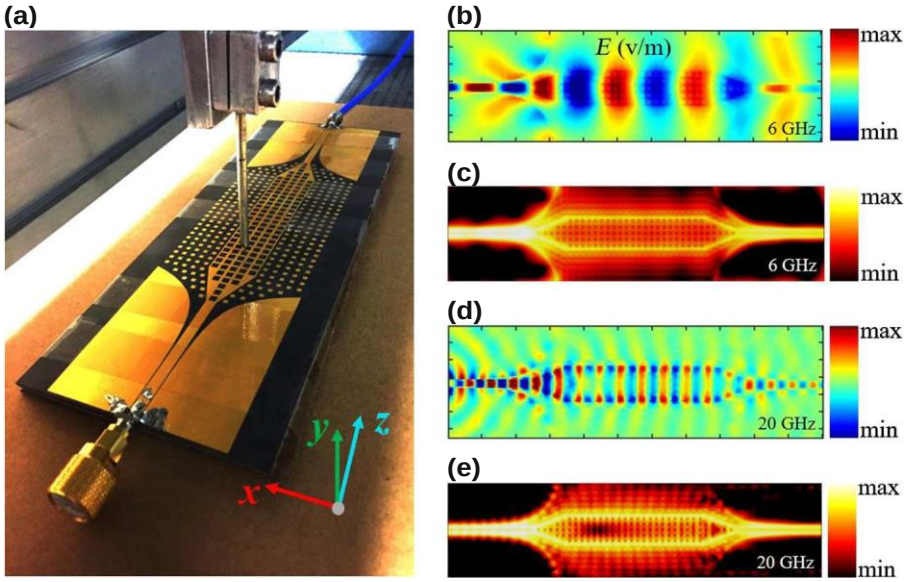

FIG. 8. (a) Photograph of a near-field scan where the electric probe is positioned 1 mm above the sample, and the inset at the corner shows the detail of the probe. (b) Measured £ ₂ distJi bution s at 6 GHz. (c) Simulated electric field distributions at 6 GHz. (d) Measured £₂ distributions at 20 GHz. (e) Simulated electric field distribution s at 20 GHz.

impedance surface with a mainly *y* axis-polarized electric vector field will be detected than above the TE impedance surface with a mainly *x* axis-polarized electric field. This makes it more difficult to identify the LW mode at the lD interface through experiments, especially at low frequencies when the decay rate into both sides remains low. It should also be mentioned that the transition acts as a planar horn antenna. Thus, part of the energy is radiated out during the adiabatic procedure, which is the main cause of the transmission loss.

C. Adiabatic transitions between the CPW and the impedance-interface waveguide

In order to suppress the radiation loss, it is natural to consider designing a symmetric structure with fields distributed in opposite directions during the adiabatic procedure. The TEM mode of a CPW is an ideal candidate as the starting unperturbed state. The structure is shown in Fig. 6. The width Ws_2 is 4 mm and the width of slot S_2 is 0.17 mm. Other geometric parameters are the same as with the slotline-LW design. The adiabatic transitions are the same as the transitions discussed previously. At the middle section, there is a sandwich-like structure consisting ofTE-TM-TE impedance surfaces where two mirror-symmetric LW modes will be transported along two lD impedance-interface waveguides. The electric field vector distribution characteristic of the sandwich-like structure is shown in the inset.

The measured and simulated *S* parameters are shown in Fig. 7(a) and we further compare it with the proposed slotline-LW guide structure in Fig. 7(b). Due to the suppression of radiation loss from transitions, the CPW-LW structure shows higher transmission efficiency.

We also conduct near-field scans at 6 and 20 GHz, as shown in Fig. 8. Similar to the previous results in Fig. 5, it is somewhat difficult to recognize the LW mode at 6 GHz for the same reason as explained before. However, through simulations, we can analyze the total electric field to verify the existence of the LW mode. We also use Fourier transform to analyze the near-field distribution every 0.5 GHz from 1 to 20 GHz to obtain the dispersion diagram of the LW mode in Fig. 9, where eigenrnode-simulated results are also plotted as a comparison. The results match well, further proving the existence of the LW mode.

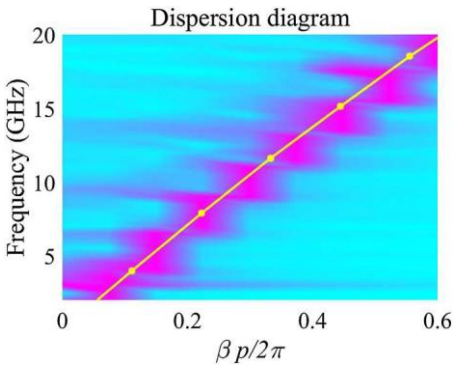

FIG. 9 The dispersion diagram of the LW mode where the background is deduced by Fourier transform of the measured near-field distributions and the yellow line is the simulated results from the eigenmode solver.

III. CONCLUSION

To summarize, this work shows that the principle of adiabatic matching can be used to design transitions for transform TEM modes, which are common modes in traditional waveguides , into the recently discovered LW modes at a ID interface of artificial impedance surfaces. Two matching tasks starting from a slotline and a CPW are provided as examples of the technique. The proposed adiabatic matching strategy shows a high robustness in broadband applications, opening the door to implement LW modes into systems from microwave bands all the way to optical bands.

ACKNOWLEDGMENTS

This work was supported by National Natural Science Foundation of China (Grants No. 61771127 and No. 61427801), Scientific Research Foundation of Graduate School of Southeast University (Grant No. YBJJl 814), and Postgraduate Research & Practice Innovation Program of Jiangsu Province (Grant No. KYCX18_0098) as well as AFOSR Grant No. FA9550-16-l -0093.

[l] J. Polo, T. Mackay, and A. Lakhtakia, *Electromagnetic Surface Waves: A Modern Perspective* (Elsevier Inc., London, 2013).

[2] S. A. Maier, *Plasmonics: Fundamentals and Applications* (Springer Science & Business Media, New York, 2007).

[3] J. D. Jackson, *Classical Electrodynamics* (Wiley, New York, 1962).

[4] R. B. M. Schasfoort, *Handbook of Surface Plasmon Resonance* (Royal Society of Chemistry, Croydon, 2017), 2nd ed.

[5] S. Laurette, A. Treizebre, and B. Bocquet, Corrugated Goubau lines to slow down and confine THz waves, IEEE Trans. Terahertz Sci. Technol. **2,** 340 (2012).

[6] G. Goubau, Open wire lines, IRE Trans. Mierow. Theory Tech. **4,** 197 (1956).

[7] G. Goubau, Waves on interfaces, IRE Trans. Antennas Propag. 7, 140 (1959).

[8] J. B. Pendry, L. Mai1in-Moreno, and F. J. Garcia-Vidal, Mimicking surface plasmons with structured surfaces, Science **305,** 847 (2004).

[9] H. F. Ma, X. Shen, Q. Cheng, W. X. Jiang, and T. J. Cui, Broadband and high-efficiency conversion from guided waves to spoof surface plasmon polaritons, Laser Photonics Rev. **8,** 146 (2014).

[10] W. L. Barnes, A. Dereux, and T. W. Ebbesen, Surface plasmon subwavelength optics, Nature **424,** 824 (2003).
[11] Z. Xu, S. Li, X. Yin, H. Zhao, and L. Liu, Radiation loss of planar surface plasmon polaritons transmission lines at microwave frequencies, Sci. Rep. 7, 6098 (2017).
[12] E. A. J. Marcatili, Dielectric rectangular waveguide and directional coupler for integrated optics, Bell Syst. Tech. J. **48,** 2071 (1969).
[13] Y. G. Smirnov and D. V. Valovik, Guided electromaguetic waves propagating in a plane dielectric waveguide with nonlinear pe1mittivity, Phys. Rev. A **91,** 013840(2015).
[14] U. Langbein, F. Lederer, and H.-E. Ponath, Generalized dispersion relations for nonlinear slab-guided waves, Opt. Commun. 53,417 (1985).
[15] D. Mihalache, M. Bertolotti, and C. Sibilia, in *Progress in Optics* (Elsevier, Oxford, 1989), vol. 27, pp. 227- 313.
[16] U. Langbein, F. Lederer, T. Peschel, U. Trutschel, and D. Mihalache, Nonlinear transmission resonances at stratified dielectric media, Phys. Rep. **194,** 325 (1990).
[17] A. D. Boardman, P. Egan, F. Lederer, U. Langbein, and **D.** Mihalache, in *Modern Problems in Condensed Matter Sciences*, edited by H.-E. Ponath and G. I. Stegeman (Elsevier, Amsterdam, 1991), vol. 29 of *Nonlinear Surface Electromagnetic Phenomena*, pp. 73- 287.
[18] D. Sievenpiper, L. Zhang, **R.** F. J. Broas, N. G. Alexopolous, and E. Yablonovitch, High-impedance electromagnetic surfaces with a forbidden frequency band, IEEE Trans. Mierow. Theory Tech. **47,** 2059 (1999).
[19] J. D. Joannopoulos, P.R. Villeneuve, and S. Fan, Photonic crystals, Solid State Commun. **102,** 165 (1997).
[20] M. Z. Hasan and C. L. Kane, Colloquium: Topological insulators, Rev. Mod. Phys. **82,** 3045 (2010).
[21] A. B. Khanikaev, S. Hossein Mousavi, W.-K. Tse, M. Kargarian, A. H. MacDonald, and G. Shvets, Photonic topological insulators, Nat. Mater. **12,** 233 (2013).
[22] D.R. Mason, S. G. Menabde, S. Yu, and N. Park, Plasmonic excitations of lD metal-dielectric interfaces in 2D systems: 1 D surface plasmon polaritons, Sci. Rep. **4,** 4536(2014).
[23] D. J. Bisharat and D. F. Sievenpiper, Guiding Waves Along an Infinitesimal Line between Impedance Surfaces, Phys. Rev. Lett. **119,** 106802 (2017).
[24] X. Kong, D. J. Bisharat, G. Xiao, and D. F. Sievenpiper, Analytic theory of an edge mode between impedance surfaces, Phys. Rev. A **99,** 033842 (2019).
[25] E. Martini, M. G. Silveirinha, and S. Maci, Exact solution for the protected TEM edge mode in a PTD-symmetric parallel-plate waveguide, IEEE Trans. Antennas Propag. **67,** 1035 (2019).
[26] D. J. Bisharat and **D.** F. Sievenpiper, Manipulating line waves in flat graphene for agile terahertz applications, Nanophotonics **7,** 893 (2018).
[27] T. Baba and D. Ohsaki, Interfaces of photonic crystals for high efficiency light transmission, Jpn. J. Appl. Phys. **40,** 5920 (2001).
[28] J. Witzens, M. Hochberg, T. Baehr-Jones, and A. Scherer, Mode matching interface for efficient coupling of light into planar photonic crystals, Phys. Rev. E **69,** 046609 (2004).
[29] H. Iizuka and N. Engheta, Antireflection structure for an effective refractive index near-zero medium in a two-dimensional photonic c1ystal , Phys. Rev. B **90,** 115412 (2014).
[30] Z. Yao, J. Luo, and Y. Lai, Photonic crystals with broadband, wide-angle, and polarization-insensitive transparency, Opt. Lett. **41,** 5106 (2016).
[31] E. Verhagen, M. Spasenovic, A. PoIman, and L. (Kobus) Kuipers, Nanowire Plasmon Excitation by Adiabatic Mode Transformation, Phys. Rev. Lett. **102,** 203904 (2009).
[32] B. Momeni and A. Adibi, Adiabatic matching stage for coupling of light to extended Bloch modes of photonic c1ystals, Appl. Phys. Lett. **87,** 171104 (2005).
[33] R. Dangel, A. L. Porta, D. Jubin, F. Horst, N. Meier, M. Seifried, and B. J. Oflrein, Polymer waveguides enabling scalable low-loss adiabatic optical coupling for silicon photonics, IEEE J. Sel. Top. Quantum Electron. **24,** 8200211 (2018).
[34] Y. Xu, R. K. Lee, and A. Yariv, Adiabatic coupling between conventional dielectric waveguides and waveguides with discrete translational symmehy , Opt. Lett. **25,** 755 (2000).
[35] S. G. Johnson, P. Bienstman, M. A. Skorobogatiy, M. Ibanescu, E. Lidorikis, and J. D. Joannopoulos, Adiabatic theorem and continuous coupled-mode theory for efficient taper transitions in photonic crystals, Phys. Rev. E **66,** 066608 (2002).
[36] A. Kianinejad, Z. N. Chen, and C. Qiu, Design and modeling of spoof surface plasmon modes-based microwave slow-wave transmission line, IEEE Trans. Mie row. Theory Tech. **63,** 1817 (2015).
[37] **J.** Lee and **D. F.** Sievenpiper, Patterning technique for generating arbitrary anisotropic impedance surfaces, IEEE Trans. Antennas Propag. **64,** 4725 (2016).

Analytic theory of an edge mode between impedance surfaces

Xianghong Kong,[1,2] Dia'aaldin J. Bisharat,[2] Gaobiao Xiao,[1] and Daniel F. Sievenpiper [2]
[1] *Department of Electronic Engineering, Shanghai Jiao Tong University, Shanghai 200240, China*
[2] *Electrical and Computer Engineering Department, University of California, San Diego, California 92093, USA*

(Received 25 October 2018; published 21 March 2019)

An eigenmode analysis is presented of the electromagnetic field which occurs between two complementary surface impedances. The analysis is based on the generalized reflection method which is a generalization of the Sommerfeld-Maliuzhinets technique. Numerical results are presented and validated against independent COMSOL simul ations . Also, the characteristic impedance and phase velocity are defined and calculated for further investigation of the structure.

DOI: 10.1103/PhysRevA.99.033842

I. INTRODUCTION

Edge modes can be widely found in quantum phenomena [1,2], optics [3- 6], and acoustics [7,8]. Because of the complexity of such structures, it is almost impossible to obtain the exact closed-form solutions of the edge modes. However, a simple structure has been discovered which confines the energy along the interface between two planar surfaces recently [9- 11]. It has been shown that the line wave occurs when the surface impedances on the two sides are complementary, which means one is inductive while the other is capacitive. Both numerical simulation and experimental verification have demonstrated these line waves, but an analytical solution has only been found for the limiting case where the two surfaces are perfect electric and pe1fect magnetic conductors.

In this paper, we apply the generalized reflection method to the eigenmode solution of a wedge with two different impedance boundary conditions. The generalized reflection method is developed by Vaccaro to study the scattering from an impedance wedge excited by an obliquely incident plane wave as shown in Fig. l(a) [12,13]. The generalized reflection method is the generalization of the Sommerfeld-Maliuzhinets method, which is applied to solve the problem of the scattering wave of a wedge with impedance surfaces excited by a nonnally incident plane wave [14]. The **TM** and TE polarized wave are coupled for the oblique incidence, which makes the Maliuzhinets method no longer valid. Based on the Sommerfeld-Maliuzhinets technique, the diffraction of an electromagnetic skew-incident wave by a wedge with anisotropic impedance boundary condition is solved analytically [15,16]. The scattered wave generated by a Hertzian dipole placed over an impedance wedge can be calculated by expanding the dipole field into plane waves and extending to complex angles of incidence [17].

However, to the best of the authors' knowledge, no satisfactory analytic solution to the eigenmode on an impedance wedge exists. Knowing the eigenmode solution not only helps us to understand the driven mode such as the scattered wave of a wedge excited by plane wave or dipole, but also gives a deeper understanding on the edge mode between impedance surfaces.

II. THEORETICAL ANALYSIS

A. Structure description

Similar to the driven mode analysis, we have two semi-infinite surfaces with complementary surface impedances Z_1 and Z_2 as shown in Fig. l (b), which means $\mathrm{Im}(Z_1)\mathrm{Im}(Z_2) < 0$. However, instead of solving for scattering by an incident wave, we find the eigenmode solution . For simplicity, we assume the surface is lossless, so $\mathrm{Re}(Z_1) = \mathrm{Re}(Z_2) = 0$. We also assume the angle between two surfaces is rr, which is the same as in Ref. [9]. All the fields in the following discussion have the e^{-iwt} time dependence, which is suppressed. The surfaces of the wedge satisfy the Leontovich boundary condition [18]:

$$\hat{E} \times \hat{\phi}(\hat{\phi} \cdot \hat{E}) = \text{efJ} \times HZ1, \tag{1a}$$

$$\hat{E} \times \hat{\phi}(\hat{\phi} \cdot \hat{E}) = -\hat{\phi} \times HZ2, \tag{1b}$$

where $\hat{\phi}$ is the unit vector as shown in Fig. l (a).

B. Generalized reflection method

By applying the Sommerfeld-Maliuzhinets technique, we can transform the electromagnetic field from real space to the spectral domain:

$$\bar{f}_z(\rho, \phi, z) = \frac{e^{ik_0 z \cos\beta}}{2\pi i} \int_\gamma \bar{F}_z\left(\alpha + \frac{\pi}{2} - \phi\right) e^{-ik_0 \rho \sin\beta \cos\alpha} d\alpha, \tag{2}$$

where $\bar{f}_z(\rho, \phi, z) = [Z:h)$ and Z_0 is the free space intrinsic impedance. The column vector $F'z(a)$ represents the spectral function for Ez and ZoH z. For the driven mode, fJ is the angle between the incident wave and the Z axis, which is a

*klovek @ sjtu.e du.cn
t dbisharat@eng.ucsd.edu
*gaobiaoxiao@sjtu .edu.cn
§ dsievenpiper@eng . ucsd.edu

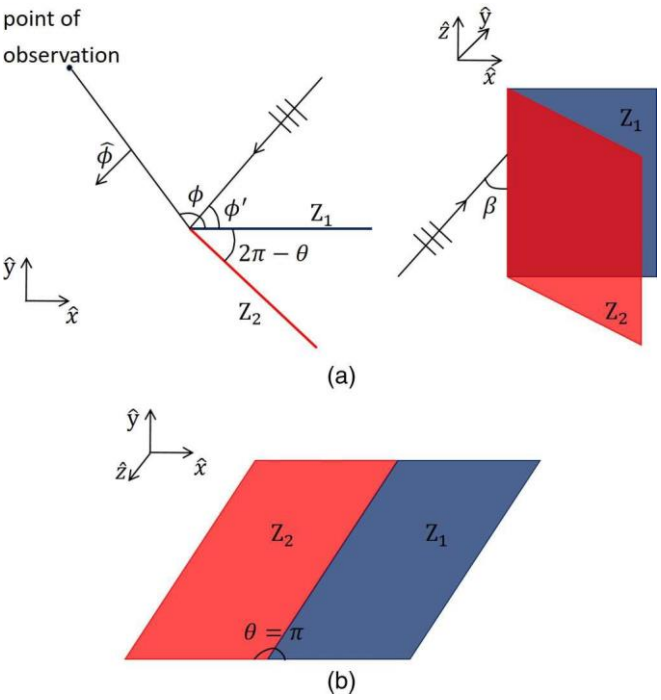

FIG. 1. (a) Impedance wedge with obliquely incident plane wav e. The angle between imp edance faces is *0.* (b) Lin e wave structure shown in Ref. [9] when *o* = *n.*

given parameter. However, for the eigenmode case, *f3* is the eigenvalue that we need to find by solving Maxwell equations. It is proven that for the wedge structure the *z* components of the electric and magnetic fields are bounded at the edge, *I Ez (P* = 0)1 < oo and *IH z(P* = 0)1 < oo, while IE p l, IE 1> I, IH p l, and IH ¢ I will tend to infinity [19]. The behavior of *.fz (p, ¢, z)* at *p* ---+ 0 is related to the behavior of the spectral function *F'z(a)* at IIm(a)I ---+ oo:

$$\lim_{\mathrm{Im}(a)\to\infty} Fz(a) = \text{constant.} \quad (3)$$

Applying the impedance boundary condition as shown in Eqs. (l a) and (l b) to the spectral expression Eq. (2), we can get [18]

$$(J \sin a + \sin V1)C(a)Fz(a +) = (-J \sin a + \sin V_1)C(- a)Pz(- a +), \quad (4a)$$

$$(J\sin a - \sin V2)C(a)Fz(a -) = (-Jsina - \sin V2)C(- a)P_2(- a -), \quad (4b)$$

where

$$\bar{C}a = \begin{bmatrix} cosa & -\sin a \cos /3 \\ \sin a \cos f3 & \cos a \end{bmatrix} \quad (5)$$

$$\sin \nu_{e_{1,2}} = \begin{bmatrix} \sin \nu_{e_{1,2}} & 0 \\ 0 & \sin \nu_{h_{1,2}} \end{bmatrix} = \begin{bmatrix} Yo \sin \beta & 0 \\ 0 & Zo \sin \beta \end{bmatrix}, \quad (6)$$

and I is the 2 x 2 identity matrix. $Yo = 1/Zo$ is the free-space admittance and $Y_{1,2} = 1/2_{1,2}$.

As shown in Eqs. (4a) and (4b), !he two components in $F_z(a)$ are coupled since the matrix C(a) is nondiagonal. In order to solve *F'z(a)* efficiently, we rewrite Eqs. (4a) and (4b) by variable substitution:

$$\bar{F}_z(\alpha) = \bar{\bar{C}}^{-1}\left(\alpha - \frac{\pi}{2}\right)\bar{G}_z(\alpha). \quad (7)$$

Then we have

$$([\sin a + \sin vi)c\, z\,(a +) = (-T\sin a + \sin v1)G_2(- a +), \quad (8a)$$

$$(J \sin a - \sin V2)\, Gz\,(a -) = (- J \sin a - \sin v2)Gz(- a -)- \quad (8b)$$

For Eqs. (8a) and (8b), the two components of *Gz* are decoupled and are solved by Maliuzhinets [14]:

$$\bar{G}_z(\alpha) = \begin{bmatrix} \Psi_e(\alpha) & 0 \\ 0 & \Psi_h(\alpha) \end{bmatrix}\begin{bmatrix} a_1^0 \\ a_2^0 \end{bmatrix}, \quad (9)$$

where $a?$ and a are arbitrary constants, and

$$\backslash V\, e,h(a) = 1/f(a + vf\cdot h)i/f(a + TC - vf\cdot h) \text{ x } 1/f(a + V;\cdot'' - n)i/f(a - v;\cdot''). \quad (10)$$

The Maliuzhinets function *1/f* (a) of wedge with angle *n* is defined as

$$1/f(a) = \exp\left(\frac{1}{4n}\int_0^a \frac{2u\, n \sin u}{\cos u}\, du\right). \quad (11)$$

The asymptotic behavior of *1/f* (a) is

$$\lim_{|\mathrm{Im}(a)|\to\infty} 1/f(a) = o[\exp(|\mathrm{Im}(a)|)]\cdot \quad (12)$$

Combining Eqs. (9) and (7), we can get the expression for the spectral function *F'z(a*).

It was first discovered by Vaccaro that if *Gz(a)* in Eq. (9) is the solution to Eq. (8), *G'z(a)a (a)* where a(a) satisfies $a(a \pm f) = a(-a \pm f)$ will also be the solution [12]. It is easy to show that sin"(a), where *n* is an integer is a solution of *a(a).* Hence, Eq. (9) can be generalized as [18]

$$\bar{G}_z(\alpha) = \begin{bmatrix} \Psi_e(\alpha) & 0 \\ 0 & \Psi_h(\alpha) \end{bmatrix}\left(\begin{bmatrix} a_1^{-1} \\ a_2^{-1} \end{bmatrix}\frac{1}{\sin\alpha - \cos\phi'} + \begin{bmatrix} \cdot \\ \cdot \end{bmatrix} + \begin{bmatrix} \cdot \\ \cdot \end{bmatrix}\sin\alpha + \ldots\right) \quad (13)$$

where ¢ ' is the incident angle as shown in Fig. l(a) and $a_{1,2}$ are constants we need to figure out. From Eqs. (12) and (10), we know that $\lim_{\mathrm{Im}(a)\to\infty} Ve,l,(a) = O(\exp(|\mathrm{Im}(a)|))$ and $\lim_{\mathrm{Im}(a)\to\infty} 1/f(a - f) = O(\exp(-|\mathrm{Im}(a)|))$. Combining that with Eq. (3), we can conclude that $a_{1,2} = 0$ for n ? l. The first-order pole caused by $a;-1$ is produced by the incident wave in the driven mode. For the eigenmode case, we can set

$a\,1$ = 0 directly. The spectral function E'z(a) can be expressed as

$$F\,z(a) = c\text{-}\ ^{1}(a\ -\ )\,[wet\ )\qquad 1,a)\,]\,[:n \tag{14}$$

$a?_{,2}$ and eigenvalue $f3$ are calculated by removing the poles introduced by -c ^{1} $(a$ -),which have no physical interpretation. The poles at can be defined as

$$\cos(at\ -\ ) = f\sin(at\ -\ )\quad \cos/3 = 0. \tag{15}$$

The process of removing the poles at is to find appropriate eigenvalue $/3$ and eigenvector $a?_{,2}$ that satisfied the equations $Fz(at)[\cos^2(at\ -\ ) + \sin^2(at\ -\ )\cos^2/3) = 0$. It can be further expressed as

$$\begin{bmatrix} i\Psi_e(\alpha_0^+) & \Psi_h(\alpha_0^+) \\ -i\Psi_e(\alpha_0^-) & \Psi_h(\alpha_0^-) \end{bmatrix}\begin{bmatrix} a_1^0 \\ a_2^0 \end{bmatrix} = 0. \tag{16}$$

In order to have nonzero solution of $a?_{,2,}$ it requires

$$\det\left(\begin{bmatrix} i\Psi_e(\alpha_0^+) & \Psi_h(\alpha_0^+) \\ -i\Psi_e(\alpha_0^-) & \Psi_h(\alpha_0^-) \end{bmatrix}\right) = 0. \tag{17}$$

Keep in mind that $'lie.h(at)$ as defined by Eq. (10) are functions of $\{3$. By solving Eq. (17), we can get the eigenvalue $/3.$ It is shown in Ref. [9] that the energy of the electromagnetic wave is confined near $p = 0$ and decays exponentially as p grows. Hence, it is intuitive to predict that the eigenvalue $f3$ should satisfy I cos /31 > 1, which means l kz l > *ko*. Plugging $f3$ into Eq. (16), we can solve $a?_{,2}$ and finally get the spectral function $F_2(a)$.

Once the spectral function *Fz(a)* is achieved, we can figure out E_2 and H_2 in real space by applying Eq. (2). The integral path as shown in Fig. 2 is symmetric to the origin in the a plane [20). The ends of $Y\pm$ are located in those regions where $Re(-ikop \sin/3\cos a) < 0$ so that the factor $e^{ikoR\,n\,fJ\cos a}$ decays as IIm(a)I -+ oo. Since I cos /31 > 1 and the impedance

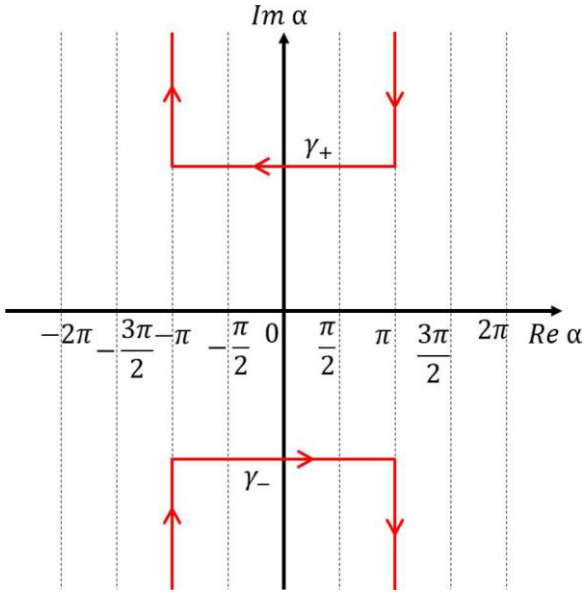

FIG. 2. Integration path *y*.

surface is lossless, we know that sin $f3$ is purely imaginary. Without loss of generality, we assume Im(s in /3) > 0. To ensure the fastest decay of $e^{ikop\,s\,in\ fJ\,co\ ",\ it}$ is assumed that the ends of $Y+$ are located at rr + *ioo* and -rr + *ioo* and the ends of $y\_$ are at -rr - *ioo* and rr - *ioo*. Although the poles introduced by $\epsilon^{1}(a\ -\ )$ which have no physical interpretation have been removed, the poles introduced by e,1,(a) still exist. The poles of the Maliuzhinets function *1/f* (a) are all on the real axis of the a plane. According to the definition of $e,J,(a)$ given in Eq. (10), the poles are shifted to the region with Im(a) #- 0 due to the fact that Im(vr) may be nonzero. In order to ensure that no singularities of' the integrand function are located in the regions bounded by $Y\pm$ above $Y+$ and below $y\_$, the integral path should be chosen sufficiently far from the real axis. For simplicity, we choose $Y+ =$ (ioo + rr , *id* + rr] U *[id* + *n, id* - *JT]* U *[id* - *n , ioo* - *n*), where d can be any constant that satisfies $d > \Vert m(v\ :\ )\vert$.

III. NUMERICAL RESULTS AND DISCUSSION

Numerical results will be presented in the section to verify the accuracy of proposed analytical representation. The two-dimensional (2D) model in COMSOL is chosen for compatison since we neglect the z dependence of field, which is in the form of $e^{ikozcos\ fJ}$ when showing the result.

A. Eigenvalue verification

Since we assume the su·rtace impedance Z_1 and Z_2 are constants and the structure is invariant under the scaling transform, *kz / ko* should be a constant that will not vary with *ko* , which means cos $f3$ should be a constant only related to Zt and Z_2. The method to figure out cos $f3$ is to solve Eq. (17). By sweeping the value of cos *{3*, we can easily find the correct solution as shown in Fig. 3. Comparing with the result simul ated by COMSOL, we find the high accuracy of our method when calculating the eigenvalue cos $f3.$ Here the surface impedances Z_1 and Z_2 are inductive and capacitive impedance respectively. When they are both inductive or capacitive, no eigenmode will exist. Because of the inversion symmetry in the z axis, if cos $f3$ is one solution for the eigenvalue, then - cos $f3$ will also be a solution. For simplicity, we only focus on the positive cos $f3.$ As shown in Fig. 3, I cos /31 > 1 is satisfied for different values of Z_1 and Z_2, which in dic ates the energy of the electromagnetic field is confined near the inte·rtace between the two surt·aces. Also, larger values of I cos /31 represent better confinement of the eigenfield. Hence, the case when $Z_1 =$ - $iZ_0/\sqrt{3}$, $Z_2 = \sqrt{3}iZ_0$ in Fig. 3(a) decays faster in the p direction than the case when $Z_1 =$ - $iZ_0/2$, $Z_2 = 2./5.iZo$ in Fig. 3(c).

B. Eigenfield verification

When Eq. (17) is satisfied, Eq. (16) will have a nonzero solution for $('h.$ We will take $[\_ij[\,'\,c]\,]$ in the following derivation. Assuming the case when $Z_1 = -i/2./5.Zo$ and $Z_2 = 2iZ_0$, we can achieve the eigenvalue cos $f3 = 1.7205$ by sweeping the parameter as mentioned. Also, we can get $a? =$ - 0.1143 + 0.3244i and $a = 0.1359$ - 0.3858i. By inserting the values of $a?$ and a into Eq. (14), we have

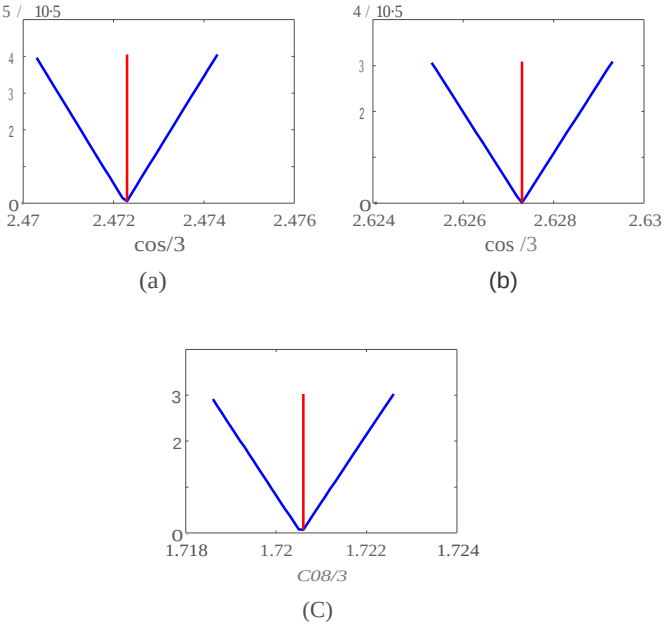

FIG. 3. Absolute value of the determinant defined in Eq. (17) when sweeping cos *f3* (blue line) and eigenvalue cos *f3* calculated by COMSOL (red line) for (a) Z_1 = -iZo/./3, *2i* = ./3 iZ0; (b) Z_1 = - iZo/ v'2 , Z2 = 2iZo; and (c) Z1 = - iZ 0/ 2, Z2 = 2v'2iZo.

completely solved the spectral function *Fz' (a*). One last step is to define the integration path *y* in order to calculate *Ez* and *Hz* in real space as shown in Eq. (2). We choose *Y+* = (ioo+n, *id + n] U [i d + n , id-n]U[id-n,* ioo-n) where *d* satisfies the condition *d* > ‖ m(vf·;)‖. Here we have *Vf* = JT/2 - l.3286i, *V\'* = -0.2553, 2 = - 0.36 52, *v* = JT/2 - 0.8955i. We set *d* = JT and the integration path becomes *Y+* = *(ioo* + JT, *in+* n] U *[in+* JT, *in* - n] U [in -JT, ioo -n), *y_* = *(-ioo* - JT, *-in* -n] U [-in - *n, -in+* n]U [-in+ rr, *-ioo* + n).

As shown in Fig. 4, we set ¢ = Jr / 3 as a constant and sweep the value of *kop* from 0.1 to 1.0. Both *Ez* and *ZoH z* are normalized by *Ez(k0 p* = 0.1) so we can compare the analytic solution with the COMSOL simulation result. Figure 4(a) shows that both IEzl and IHzl decrease with the increase of k_0 *p* and the analytic solution matches well with the simulation result.

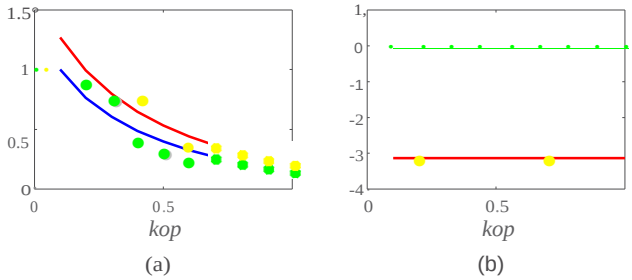

FIG. 4. (a) Absolute value and (b) phase of normalized electric field *Ezf Ez(k0 p* = 0.1) (blue line for analytic solution and green dots for COMSOL simulation) and normalized magnetic field *Z0 H, / E,(ko p* = 0.1) (red line for analytic solution and yellow dots for COMSOL simulation) , when¢ = *n* / 3.

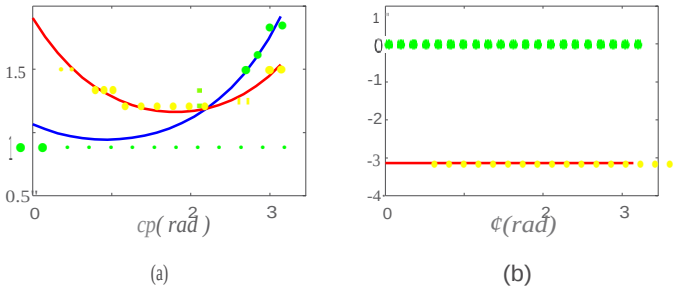

FIG. 5. (a) Absolute value and (b) phase of n01malized electric field *E, / E,(cp* = *n* / 2) (blue line for analytic solution and green dots for COMSOL simulation) and normalized magnetic field *Z0H, / E,(cp* = *n* / 2) (red line for analytic solution and yellow dots for COMSOL simulation) when k_0 *p* = 0.5.

The phase of the eigenfield along the *p* axis is a constant which can be concluded from Fig. 4(b).

Similar to Fig. 4, we set k_0 *p* = 0.5 as a constant and sweep ‹› from 0 to Jr in Fig. 5. Divided by *E,(‹›* = JT/2), the normalized eigenfield calculated by the analytic method shows high accuracy. From Fig. 5(a), we can conclude that the absolute value of *Ez* and *H,* will not vary monotonically with the increase of¢, but instead they increase after reaching a minimum at a particular value of¢. Figure 5(b) shows that the phase is also a constant when k_0p is fixed. Combined with result in Fig. 4(b), we predict that both *Ez* and *Hz* have same phase throughout the *xy* plane.

The absolute values of the normalized electric field *lEz / Ez(kop* = 0)1 and normalized magnetic field *lHzZo/ E,(kop* = 0)1 are plotted in Figs. 6 and 7 respectively. The phases are neglected here since we can conclude from Figs. 4(b) and 5(b) that the phases of *Ez* and *Hz* are uniformly distributed in the *xy* plane. As we can see, the field is concentrated at the interface between two complementary surfaces where *p* = 0 and decays exponentially as *p* grows. Both *Ez* and *Hz* are finite at *p* = 0, which satisfies the boundary condition while *Ep, E‹›, Hp,* and *H‹›* can have a singularity at the edge [9,19]. The field is not symmetrically distributed about axis ¢ = Jr / 2 since for *E,* the left part Jr/2 < </> < JT is larger while for *Hz* the right part O < </> < JT / 2 is larger. It is more clear in Fig. 8, where the ratio of electric field and magnetic field ‖ z/ (H, Z0)‖ is plotted. The value will increase as ¢ varies from O to Jr for a constant *p.*

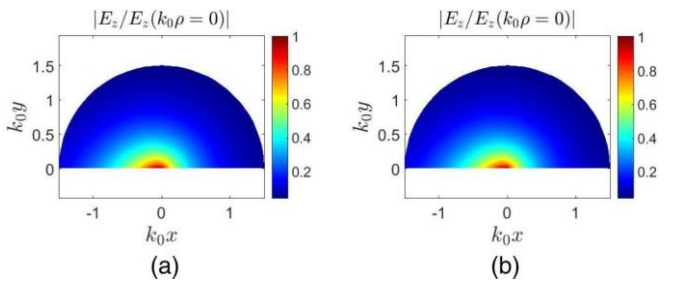

FIG. 6. Nonnalized electric field *lE, /E,(k0p* = 0)1 calculated by (a) analytic method and (b) COMSOL simulation.

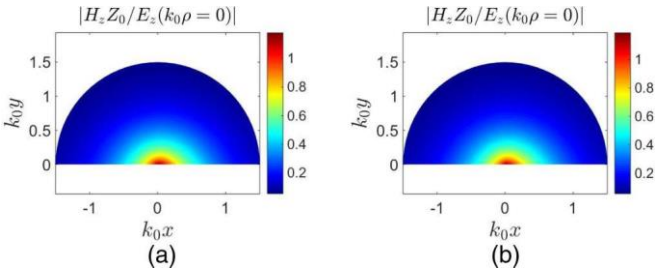

FIG. 7. Normalized magnetic field $|H_zZ_0/E_z(k_0\rho=0)|$ calculated by (a) analytic method and (b) COMSOL simulation.

Once we figure out the value of E_z and H_z, it is easy to get the value of transverse electric field E_ρ, E_ϕ by applying (similarly for transverse magnetic field)

$$E_\rho = \frac{i}{k_0 \sin^2\beta}\left(\cos\beta\frac{\partial E_z}{\partial\rho}+\frac{1}{\rho}\frac{\partial Z_0H_z}{\partial\phi}\right), \tag{18a}$$

$$E_\phi = \frac{i}{k_0 \sin^2\beta}\left(\cos\beta\frac{1}{\rho}\frac{\partial E_z}{\partial\phi}-\frac{\partial Z_0H_z}{\partial\rho}\right). \tag{18b}$$

Alternatively, we can also solve them by the Sommerfeld-Maliuzhinets technique and the derivative in Eq. (18) turns into multiplication in the spectral domain through $\partial/\partial\rho$ $-ik_0\sin\beta\cos\alpha$, $\partial/\partial\phi$ $ik_0\rho\sin\beta\sin\alpha$. Equation (18) can be rewritten as

$$E_\rho = \frac{1}{2\pi}\int_{-\infty}^{+\infty}\frac{e^{ik_z\cos\beta}}{\sin\beta}[\cos\beta\cos\alpha, -\sin\alpha]F_z\left(\alpha+\frac{\pi}{2}\right) \times e^{-ik_0\rho\sin\beta\cos\alpha}d\alpha, \tag{19a}$$

$$E_\phi = -\frac{1}{2\pi}\int_{-\infty}^{+\infty}\frac{e^{ik_z\cos\beta}}{\sin\beta}[\cos\beta\sin\alpha, \cos\alpha]F_z\left(\alpha+\frac{\pi}{2}\right) \times e^{-ik_0\rho\sin\beta\cos\alpha}d\alpha. \tag{19b}$$

The spectral functions of E_ρ ($[\cos\beta\cos\alpha, -\sin\alpha]F_z/\sin\beta$) and E_ϕ ($-[\cos\beta\sin\alpha, \cos\alpha]F_z/\sin\beta$) tend to infinity when $\beta\to 0$, which indicates E_ρ and E_ϕ will tend to infinity at $\rho = 0$ in real space. However, the volume integrals of $|E_\rho|^2$ and $|E_\phi|^2$ are still finite for finite volume around $\rho = 0$ since the energy should be finite for any practical physical system. As shown in Fig. 9, the transverse electric field decays when ρ increases, which also matches the simulation results in Ref. [9].

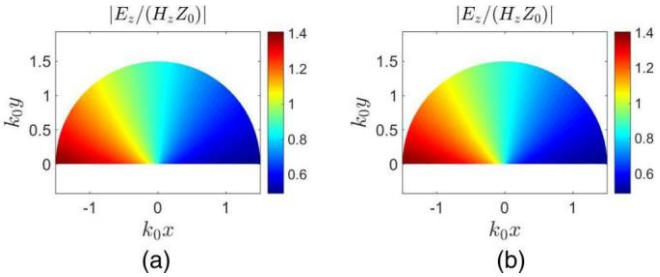

FIG. 8. $|E_z/(H_zZ_0)|$ calculated by (a) analytic method and (b) COMSOL simulation.

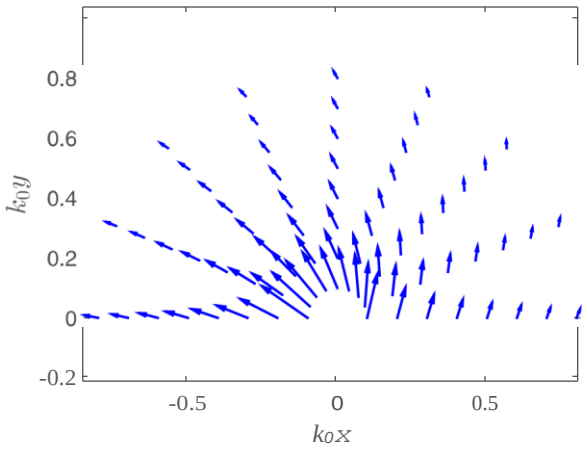

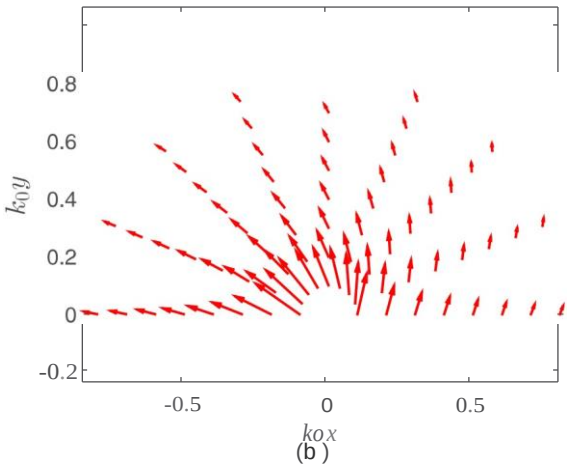

FIG. 9. Real pait of the transverse electric field calculated by (a) applying Eq. (19) and (b) COMSOL simulation is plotted.

C. Characteristic impedance and phase velocity of the waveguide

The phase velocity of the structure shown in Fig. 1(b) can be calculated by

$$V_p = \frac{\omega}{k_z} = \frac{c}{\cos\beta}, \tag{20}$$

where c is the speed of light in vacuum and $\cos\beta$ is the eigenvalue mentioned above.

Also, we can follow the definition given in Ref. [21] and define the characteristic impedance as

$$Z_c = \frac{2P}{|I|^2}, \tag{21}$$

where

$$P = \frac{1}{2}\mathrm{Re}\left[\iint(E_t\times H_t^*)_z dxdy\right] \tag{22}$$

and

$$I = \int_{-\infty}^{+\infty} J_z dx = \int_{-\infty}^{+\infty} -H_x dx. \tag{23}$$

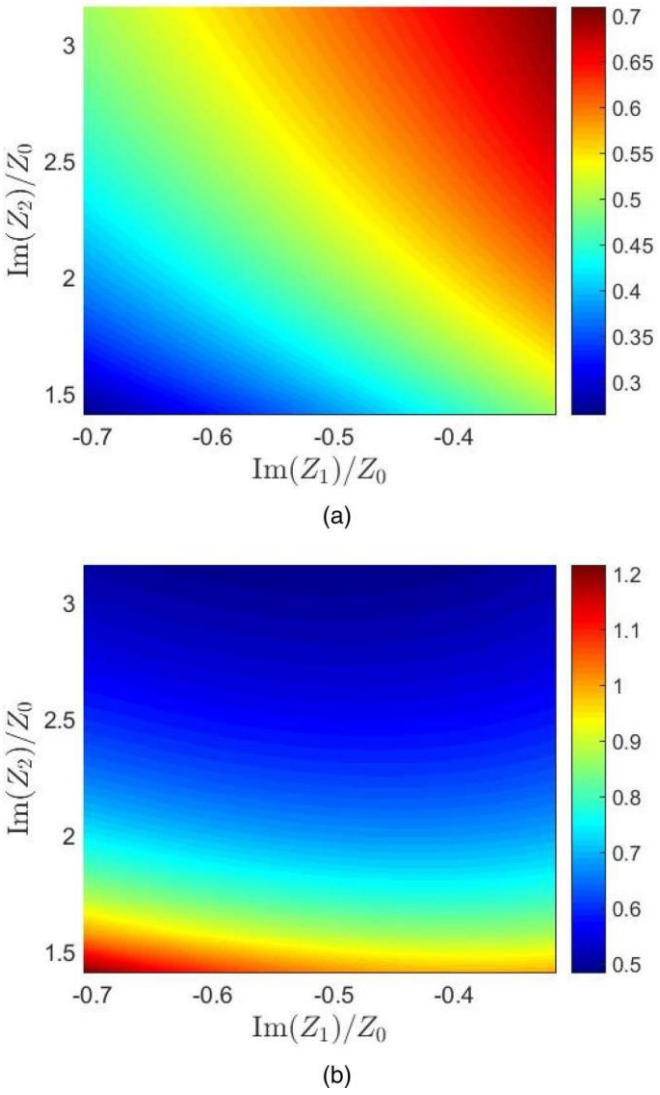

FIG. 10. (a) Normalized phase velocity v_p/c and (b) nonnalized characteristic impedance Z_c/Z_0 are plotted as functi ons of Z_1 and Z_2.

The integrand in Eq. (22) is the z component of the Poynting vector and the integral domain is the cross section above the impedance surface. J_z in Eq. (23) is the current density on the surface, which has the same value as $-H_x$ on the impedance surface.

As shown in Fig. 10, since we assume the complementary impedance surfaces are lossless, both Z_1 and Z_2 are purely imaginary with opposite sign. With the increase of $\mathrm{lm}(Z_1)$ and $\mathbf{lm(Z_2)}$, the phase velocity will increase monotonically, which means the energy will be less confined near $p = 0$ according to the definition in Eq. (20). Besides, the phase velocities have an upper bound since they cannot exceed the speed of light, which is also shown in Fig. lO(a). Similarly, we can achieve larger characteristic impedance for smaller $\mathrm{lm}(Z_1)$ and $\mathrm{lm}(Z_2)$ as shown in Fig. l0(b).

IV. CONCLUSIONS

An analytic solution of the eigenmode of a wedge structure with two complementary surface impedances has been carried out by using the generalized reflection method which is developed from the Sommerfeld-Maliuzhinets technique. Compared with the driven mode which can also be solved by generalized reflection method , both spectral function $F_{z(a)}$ and integration path γ have to be modified in order to make the method effective. The analytic theory not only proves the existence of an edge mode but also provides the theoretical support for understanding the relation between edge modes and diffraction from a wedge structure. The results are useful because we have also calculated the waveguide properties such as characteristic impedance and phase velocity for the structure.

ACKNOWLEDGMENTS

This work was suppmted in pait by Air Force Office of Scientific Research Grant No. FA9550-16-l-0093 and in part by the China Scholarship Council (No. 201706230113).

[l] B. A. Bemevig, T. L. Hughes, and S.-C. Zhang, Science **314** , 1757 (2006).
[2] C. L. Kane and E. J. Mele, Phys. Rev. Lett. **95** , 146802 (2005).
[3] A. B. Khanikaev, S. H. Mousavi, W.-K. Tse, M. Kargar ian, A.H. MacDonald, and G. Shvets, Nat. Mater. 12, 233 (2013).
[4] T. Ma, A. B. Khanikaev, S. **H.** Mousavi, and G. Shvets, Phys. Rev. Lett. **114** , 127401 (2015).
[5] L. Lu, J. D. Joann opoul os, and M. Soljacic, Nat. Photon. **8**, 821 (2014).
[6] S. Raghu and F. D. M. Haldane, Phys. Rev. A **78** , 033834 (2008).
[7] C. He, X. Ni, H. Ge, X.-C. Sun , Y.-B. Chen, **M .-H .** Lu, X.-P. Liu, and Y.-F. Chen, Nat. Phys. **12**, 1124 (2016).
[8] **R.** Siisstrunk and S. D. Huber, Proc. Natl. Acad. Sci. USA **113** , E4767 (2016).
[9] J. B. Dia'aaldin and D. F. Sievenpiper, Phys. Rev. Lett. **119**, 106802 (2017).
[10] D. J. Bisharat and D. F. Sie venpiper , Nanophotonics 7, 893 (2018).
(11] D. R. Mason, S. G. Menabde, S. Yu, and N. Park, Sci. Rep. **4**, 4536 (201 4).
[12] V. Vaccaro, AEU-Archiv Electronik Ubertragungstechnik- Int. J. Electronics Commun. 34,493 (1980).
[13] V. G. Vaccaro, Optica Acta: Int. J. Optics **28** , 293 (1981).
[14] G.D. Maliuzhinets, Soviet Phys. Doklady **3**, 752 (1958).
(15] J. Bernard , J. Phys. A: Math. Gen. **31** , 595 (1998).

[16] A. Vallecchi, Electromagnetics **33,** 73 (2013).
[17] M. A. Lyalinov and N. Y. Zhu, IEEE Trans. Antenna s Propag. **61,** 329 (2013).
[18] R. G. Rojas, IEEE Trans. Antennas Propag. **36,** 956 (1988).
[19] J. Meixner, IEEE Trans. Antennas Propag. 20, 442 (1972).
[20] A. V. Osipov and S. A. Tretyakov, *Modern Electromagnetic Scattering Theory with Applications* (John Wiley & Sons, New York, 2017).
[21] W. Marynowski, P. Kowalczyk, and J. Mazur, Prog. Electromagn. Res. 110, 219(2010).